Universidade do Minho
Escola de Engenharia

José Pedro Freitas da Cunha

MODELLING OF BALLASTED RAILWAY TRACKS FOR HIGH-SPEED TRAINS

Fevereiro de 2013

MODELLING OF BALLASTED RAILWAY TRACKS FOR HIGH-SPEED TRAINS
José Pedro Freitas da Cunha
UMinho | 2013

Universidade do Minho
Escola de Engenharia

José Pedro Freitas da Cunha

MODELLING OF BALLASTED RAILWAY TRACKS FOR HIGH-SPEED TRAINS

Tese de Doutoramento
Engenharia Civil

Trabalho efectuado sob a orientação do
Professor Doutor António Gomes Correia

Fevereiro de 2013

The miracle of the appropriateness of the language of mathematics for the formulation of the laws of physics is a wonderful gift which we neither understand nor deserve.

The Unreasonable Effectiveness of Mathematics in the Natural Sciences
Eugene Wigner

Acknowledgements

The author would like to thank all institutions and persons who made this thesis possible, namely:

- Professor A. Gomes Correia for supervising this thesis and for all the relevant suggestions made to improve the developed work. I would also like to acknowledge his continuous support and care.
- Professor Geert Degrande for receiving me so well and providing all the necessary conditions at the Katholieke Universiteit Leuven to improve my knowledge in relevant matters. Also for is guidance, important remarks and shared knowledge related to subjects such as 2.5D modelling and seismic wave propagation. I would also like to acknowledge the toolboxes shared that made possible part of the work in this thesis.
- The Portuguese Foundation for Science and Technology (FCT) for the financial support given through the individual doctoral grant SFRH/BD/46850/2008.
- My colleagues at the University of Minho João Paulo Martins, Nuno Araújo and Sandra Ferreira, with whom shared informations contributed to improve the works.
- All those at the Katholieke Universiteit Leuven who provided important support: Professor Geert Lombaert, Professor Matthias Schevenels, Sayed Ali Badsar and most especially Stijn François.
- My colleagues at FEUP, Nuno Santos and Pedro Alves Costa, for all the relevant discussions and shared knowledge regarding modelling of railway tracks.
- Ana Catarina Teixeira and Joaquim Tinoco for reading and providing important remarks upon the thesis.
- My friends and colleagues Nuno Mendes and Rui Silva, for more than a decade of important Engineering discussions.

- Finally I would like to thank all my friends and family. Most especially to my parents who discarded a more comfortable life in order to support our studies; and to my wife Claudia, for everything.

Abstract

Ballasted railway tracks are one of the most common structures travelled by high-speed trains. The high circulation speeds of these trains lead to increased vibrations in the tracks and nearby structures, which can affect the serviceability and maintenance costs of the tracks. There is a growing demand for a means of accurately predicting the performance of ballasted railway tracks in train circulation. Numerical simulations are a highly effective means of predicting track response and the propagation of vibrations to the free field. However, numerical simplifications often prevent these models from performing additional in-depth analyses of three-dimensional track response or non-linear behaviour of the track ballast and foundation soil. This thesis aims to expand the knowledge of ballasted railway track response by performing 3D non-linear railway track simulations and investigating the importance of non-linear material behaviour in numerical predictions.

The first part of the thesis concentrates on the elastodynamics of railway track response to moving loads and the numerical accuracy of 3D Finite Element meshes of railway tracks. The advantages and disadvantages of 3D Finite Element simulations for these structures are highlighted and the cases for which they are suitable are identified.

The second part of this thesis focuses on non-linear ballast and soil response using time-domain simulations. The study of ballast behaviour is performed using a constitutive model in which the separated consideration of yield surfaces and pressure dependent Young's modulus, facilitates the identification of their individual influences on track response. The 3D nature of the model also enables the study of the stress and strain distribution in ballast, in the transversal and longitudinal directions of the track, which provide insight into the difference in behaviour between ballast under a sleeper and ballast between two sleepers. The evaluation of the non-linear soil response is conducted using a cyclic non-linear model that was implemented in the Finite Element software. This model examines the spatial distribution and time history of the stiffness degradation experienced by the soil during the passage of a train axle. Finally, the simulation of the integrated non-linear soil and ballast material models demonstrates the influence

of non-linear behaviour at different circulation speeds.

Keywords: Ballasted railway track, high-speed train, Finite Element Method, response to moving loads, non-linear analyses, cyclic non-linear model.

Sumário

Vias férreas balastradas são uma das principais estruturas nas quais circulam os comboios de alta velocidade. A grande velocidade de circulação destes veículos induz acrescidas vibrações na via-férrea e estruturas circundantes, que podem afetar a eficácia e custos de manutenção da via. Consequentemente é cada vez maior a procura de meios precisos de previsão da resposta de vias férreas à passagem de comboios de alta velocidade. As simulações numéricas são bastante eficientes para prever a resposta da via e a propagação de ondas no solo. No entanto algumas simplificações numéricas impedem muitas vezes estes modelos de permitir análises mais detalhadas sobre a resposta tridimensional da via e o comportamento não-linear do balastro e do solo de fundação. Este trabalho contribui para aprofundar o conhecimento existente do comportamento de vias férreas através de análises 3D não-lineares e do estudo da importância do comportamento não-linear dos materiais nas previsões numéricas.

A primeira parte do trabalho visa essencialmente o estudo do comportamento elastodinâmico das vias férreas e da precisão numérica de malhas em Elementos Finitos 3D para a simulação das vias. As vantagens e desvantagens das simulações em Elementos Finitos 3D são discutidas e são identificados os propósitos para os quais estas simulações são mais adequadas.

A segunda parte do trabalho foca-se no estudo da resposta não-linear de balastro e solo de fundação através de simulações no domínio do tempo. O estudo do comportamento do balastro é feito através de um modelo constitutivo no qual a consideração em separado de superfícies de cedência e da variação do módulo de Young com a tensão média permitiu identificar a influência de cada na resposta da via. A análise tridimensional permitiu também estudar a distribuição de tensões e deformações na direção transversal e longitudinal da via, facultando uma análise do diferente comportamento de balastro debaixo de uma travessa e de balastro situado entre duas travessas. O estudo do comportamento não-linear do solo é feito através de um modelo não-linear cíclico que foi implementado no software de Elementos Finitos. Isto permitiu o estudo da distribuição espacial e temporal da degradação da rigidez que o solo sofre durante a passagem de um eixo de um comboio. Finalmente a simulação integrada do comportamento não-linear do solo e do balastro permitiu compreender a importância do comporta-

mento não-linear em função da velocidade de circulação do comboio.

Palavras-Chave: Via-férrea balastrada, comboio de alta velocidade, Método dos Elementos Finitos, resposta a cargas rolantes, análise não-linear, modelo não-linear cíclico.

Contents

List of Figures

List of Tables

Glossary

General Symbols

(x, y, z) . . . . . .Cartesian Coordinates

ω . . . . . .Circular frequency

λ . . . . . .Wavelength

t . . . . . .Time

T . . . . . .Period

k_y . . . . . .Wavenumber domain representation of y

k_x . . . . . .Wavenumber domain representation of x

$\mathcal{F}(\square)$ . . . . . .Fourier transform of $\square$

$\widetilde{\square}$ . . . . . .Frequency domain representation of $\square$

$\widehat{\square}$ . . . . . .Frequency-wavenumber domain representation of $\square$

$\dot{\square}$ . . . . . .First order time derivative of $\square$

$\ddot{\square}$ . . . . . .Second order time derivative of $\square$

$\sin \square$ . . . . . .Sine of angle $\square$

Elastodynamics

C_p . . . . . .Primary wave speed

C_r . . . . . .Rayleigh wave speed

C_s . . . . . .Shear wave speed

D_{ijkl} . . . . . .Constitutive tensor

E . . . . . .Young's Modulus

P . . . . . .Generic vertical load

Γ . . . . . .Domain boundary

Γ_t . . . . . .Interface portion of the domain boundary

Γ_u . . . . . .Free portion of the domain boundary

Ω . . . . . .Generic domain

Φ . . . . . .Generic scalar function

Ψ . . . . . .Generic vector function

δ_{ij} . . . . . .Kronecker delta

λ . . . . . .First Lamé coefficient

$\mathcal{B}$ . . . . . .Generic body

$\mathbf{x}$ . . . . . .Generic point

μ . . . . . .Second Lamé coefficient

ν . . . . . .Poisson's ratio

ρb_i . . . . . .Body force

ρl . . . . . .Mass per unit length

σ_{ij} . . . . . .Stress tensor

ε_{ij} . . . . . .Strain tensor

$a(\mathbf{x})$ . . . . . .Generic field variable

c . . . . . .Moving load speed

c_d . . . . . .Viscous damping

k . . . . . .Stiffness

t . . . . . .Stress vector

u_i . . . . . .Displacement vector

v_i . . . . . .Generic scalar funcion

Soil-structure interaction in the frequency domain

A_b . . . . . .Area of the track section

K_b . . . . . .Ballast impedance

Ω . . . . . .Domain

Ω_{b} . . . . . .Track sub-domain

Ω_{s} . . . . . .Soil sub-domain

Σ_{bs} . . . . . .Track-soil interface

β_{bs} . . . . . .Rotation of the rigid track-soil interface

β_{sl} . . . . . .Rotation of the rigid sleeper

$\mathbf{K}_{\mathrm{bb}}$ . . . . . .Dynamic track stiffness matrix

$\mathbf{N}_{\mathrm{bs}}$ . . . . . .Shape function at the track-soil interface

$\mathbf{f}_{\mathrm{b}}$ . . . . . .Track force vector

$\mathbf{h_{zi}}$ . . . . . .Track-soil transfer functions

$\mathbf{u}^{\mathbf{G}}_{\mathbf{zi}}$ . . . . . .Green's functions

$\mathbf{u}_{\mathrm{bs}}$ . . . . . .Wavefield in the soil

$\mathbf{u}_{\mathrm{b}}$ . . . . . .Track displacement vector

$\mathbf{u}_{\mathrm{s}}$ . . . . . .Soil displacements

$\mathbf{u}_{\mathrm{t}}$ . . . . . .Rail displacement

$\mathbf{u}_{\mathrm{w/r}}$ . . . . . .Rail unevenness

$\hat{\mathbf{C}}^{\mathrm{v}}$ . . . . . .Compliance matrix

$\hat{\mathbf{g}}_{\mathrm{d}}$ . . . . . .Vehicle-track interaction forces

ϕ_{bs} . . . . . .Imposed displacement at the track interface

$\tilde{\mathbf{t}}_{\mathrm{bs}}$ . . . . . .Soil traction at the track-soil interface

$\tilde{u}_{\mathrm{bs}}$ . . . . . .Soil displacements at the track-soil interface

u_{r1} . . . . . .Displacement of rail 1

u_{r2} . . . . . .Displacement of rail 2

Numerical Analyses

F . . . . . .Modulus of the moving load

$G_{tan\gamma_a}$ . . . . . .Tangent shear modulus at the maximum shear strain

N_i . . . . . .Global interpolation function of node i

$N_i^{(e)}$ . . . . . .Interpolation function associated to node i

R_1 . . . . . .Contorting parameter for the shape of the yield surface in the modified Mohr-Coulomb model

R_2 . . . . . .Second cap shape factor in the modified Mohr-Coulomb model

Γ . . . . . .Second pre-consolidation variation shape parameter in the modified Mohr-Coulomb model

Ω . . . . . .Finite element model domain

Ω^e . . . . . .Domain of a finite element

α . . . . . .First Rayleigh damping coefficient

α . . . . . .First cap shape factor

α_b . . . . . .Parameter for the determination of the characteristic length

α_r . . . . . .Ramberg-Osgood first calibration parameter

β . . . . . .Second Rayleigh damping coeffient

β_1 . . . . . .First parameter of the Newmark time integration

β_2 . . . . . .Second parameter of the Newmark time integration

$\mathbf{B}$ . . . . . .Strain-displacement matrix

$\mathbf{D}$ . . . . . .Elasticity matrix

$\mathbf{K}$ . . . . . .Global stiffness matrix

$\mathbf{M}$ . . . . . .Mass matrix

α . . . . . .Array of user state variables

σ . . . . . .Array of stress components

$\mathbf{f}$ . . . . . .Global vector of nodal forces

$\mathbf{u}$ . . . . . .Displacement vector

$\mathbf{u}$ . . . . . .Global vector of nodal displacements

$\mathbf{v}_\mathrm{i}$ . . . . . .Virtual displacements

$\mathbf{K}_\mathrm{tan}$ . . . . . .Global tangent stiffness matrix

$\mathbf{N}$ . . . . . .Global interpolation matrix

ε . . . . . .Array of engineering strains

$\ddot{\mathbf{u}}$ . . . . . .Vector of nodal accelerations

γ^p . . . . . .Plastic shear strain

κ_1 . . . . . .Equivalent plastic shear strain

λ' . . . . . .Modified first Lamé coefficient

$\mathbf{x}^i$ . . . . . .Coordinate of node i

$\mathbf{C}$ . . . . . .Rayleigh damping matrix

f_i . . . . . .Rail node force

μ' . . . . . .Modified second Lamé coefficient

n_{point} . . . . . .Number of nodes in the finite element mesh

ε_v^p . . . . . .Plastic volumetric strain

${}^h a$ . . . . . .Interpolation of filed variable a

d_i . . . . . .Multiplication factor to account for the wave velocity at mesh boundaries

f^{int} . . . . . .Vector of internal forces

f_{sec} . . . . . .Reduction factor of the second shear modulus

l . . . . . .Distance between two consecutive rail nodes

l_i . . . . . .Caracteristic length of the bounding elements

m . . . . . .First pre-consolidation variation shape parameter in the modified Mohr-Coulomb model

n_{k} . . . . . .Number of elements in the Iwan model

p_c . . . . . .Pre-consolidation pressure in the modified Mohr-Coulomb model

p_{c0} . . . . . .Pre-consolidation stress at the beginning of the non-linear step

p_{ref} . . . . . .Reference pressure in the modified Mohr-Coulomb model

r . . . . . .Ramberg-Osgood second calibration parameter

$u(\mathbf{x})$ . . . . . .Displacement at generic point $\mathbf{x}$

v . . . . . .Moving load velocity

x_0 . . . . . .Initial position of the moving load

n_{node} . . . . . .Number of nodes in a generic finite element

Track properties

$E_{\square}$ . . . . . .Young's modulus of track component $\square$

$k_{\square}$ . . . . . .Stiffness of track component $\square$

$A_{\square}$ . . . . . .Area of track component $\square$

$I_{\square}$ . . . . . .Moment of inertia of track component $\square$

$\rho_{\square}$ . . . . . .Volumetric mass of track component $\square$

$m_{\square}$ . . . . . .Mass of the of track component $\square$

$h_{\square}$ . . . . . .Height of track component $\square$

$l_{\square}$ . . . . . .Length of track component $\square$

$\nu_{\square}$ . . . . . .Poisson's ratio of track component $\square$

$\xi_{\square}$ . . . . . .Damping ratio of track component $\square$

$b_{\square}$ . . . . . .Width of track component $\square$

$\square_{\mathrm{r}}$ . . . . . .Parameter $\square$ of the rail

$\square_{\mathrm{rp}}$ . . . . . .Parameter $\square$ of the railpad

$\square_{\mathrm{sl}}$ . . . . . .Parameter $\square$ of the sleeper

$\square_{\mathrm{b}}$ . . . . . .Parameter $\square$ of the ballast

$\square_{\mathrm{sb}}$ . . . . . .Parameter $\square$ of the sub-ballast

$\square_{\mathrm{cl}}$ . . . . . .Parameter $\square$ of the capping layer

$\square_{\mathrm{s_i}}$ . . . . . .Parameter $\square$ of the soil layer i

$\square_{\mathrm{bs}}$ . . . . . .Parameter $\square$ of the track-soil interface

b_{r} . . . . . .Distance from the rail to the track centre

d_{sl} . . . . . .Sleeper spacing

Geotechnical Symbols

D . . . . . .Diameter of triaxial specimen

F_{bb} . . . . . .General function describing the backbone curve

G_0 . . . . . .Small strain shear modulus

$G_{\tan}$ . . . . . .Tangent shear modulus

G_{sec} . . . . . .Secant shear modulus

H . . . . . .Height of triaxial specimen

M_ϕ . . . . . .Slope of the line representing the yield condition

R_γ . . . . . .Maximum to effective shear strain ratio

ΔW . . . . . .Area of the hysteresis curve

γ . . . . . .Shear strain

γ_a . . . . . .Effective shear strain of a complete load cycle

γ_r . . . . . .Reference shear strain

γ_{eff} . . . . . .Effective shear strain

M . . . . . .Magnitude

ϕ . . . . . .Friction angle

ψ . . . . . .Dilatancy angle

σ_1 . . . . . .Major principal stress

σ_2 . . . . . .Intermediate principal stress

σ_3 . . . . . .Minor principal stress

σ_a . . . . . .Axial stress in triaxial compression

τ . . . . . .Shear stress

τ_a . . . . . .Effective shear stress of a complete load cycle

τ_r . . . . . .Reference shear stress

τ_{eff} . . . . . .Effective shear stress

ε_1 . . . . . .Major principal strain

ε_3 . . . . . .Minor principal strain

ε_a . . . . . .Axial strain in triaxial compression

c . . . . . .Cohesion

t_n . . . . . .Degradation parameter

p . . . . . .Isotropic stress

q . . . . . .Deviatoric stress

Optimization

$F(\mathbf{x})$ . . . . . .Objective function values

H(x) . . . . . .Hessian of F(x)

S . . . . . .Two-dimensional sub-space

N . . . . . .Trust-region

g . . . . . .Gradient of F(x)

m . . . . . .Array of lower limit values for the optimization parameters

n . . . . . .Array of lower higher values for the optimization parameters

x . . . . . .Array of optimization parameters

H . . . . . .Hessian matrix

$\mathbf{s_1}$ . . . . . .Direction of **g**

$\mathbf{s_2}$ . . . . . .Approximate Newton direction or direction of negative curvature in $F\mathbf{x}$

$\mathbf{x_0}$ . . . . . .Array of initial values of the optimization parameters

σ^* . . . . . .Array of standard deviation of parameters

σ^{*min} . . . . . .Array of standard deviation corresponding to the minimum known objective function

x^k . . . . . .Tentative array of parameter values

x^{min} . . . . . .Array of parameter values corresponding to the minimum known objective function

σ_0 . . . . . .Stress scaling factor

σ_k^e . . . . . .Experimental stress value

σ_k^n . . . . . .Numeric stress value

ε_0 . . . . . .Strain scaling factor

ε_k^e . . . . . .Experimental strain value

ε_k^n . . . . . .Numeric strain value

$g(\mathrm{x})$ . . . . . .Gradient of $F(\mathrm{x})$

n . . . . . .Number of optimization parameters

q_0 . . . . . .Deviatoric stress scaling factor

q_k^e . . . . . .Experimental deviatoric stress

q_k^n . . . . . .Numeric deviatoric stress

r . . . . . .Aproximation to $F(\mathrm{x})$

s . . . . . .Trial step

u_0 . . . . . .Pore pressure scaling factor

u_k^e . . . . . .Experimental pore pressure

u_k^n . . . . . .Numeric pore pressure

w_s . . . . . .Scaling factor

Acronyms

BE . . . . . .Boundary Element

BEM . . . . . .Boundary Element Method

CPT . . . . . .Cone Penetration Test

DE . . . . . .Discrete Element

DEM . . . . . .Discrete Element Method

DSM . . . . . .Direct Stiffness Method

FE . . . . . .Finite Element

FEM . . . . . .Finite Element Method

PML . . . . . .Perfectly Matching Layers

RMS . . . . . .Root Mean Square

SASW . . . . . .Spectral Analysis of Surface Waves

SCPT . . . . . .Seismic Cone Penetration Test

SPT . . . . . .Standard Penetration Test

Chapter 1

Introduction

Railway tracks for high-speed trains are significant innovations for development and communication in countries that invest in this type of infrastructure. Significant advancements in this area have been achieved in Europe and Asia; however, France and Japan are internationally recognised for their substantial technological investments. Portugal is also exploring the possibility of constructing a high-speed network that connects Portugal with Spain and the rest of Europe. This issue has become the main focus of national debate over the last decade.

Quality criteria for high-speed tracks must be significantly more restrictive than quality criteria for conventional railway tracks. In some locations with soft-ground conditions, very high levels of displacement have been observed (Holm et al., 2002). Faulty track behaviour may lead to increased vibration in neighbouring structures, discomfort to passengers or even risk of derailment in extreme cases. Thus, the development of tools and methodologies that can accurately predict the behaviour of high-speed tracks when subjected to traffic loads, and the study and development of mitigation countermeasures, has become a primary focus of research over the past few decades. There are four main approaches to this problem: field measurements, empirical models, analytical models and numerical models.

The field measurements are used to develop the empirical, analytical and numerical models. These measurements are also used to calibrate the analytical and numerical models, which result in improved agreement regarding the behaviour of the railway tracks.

The empirical methods still exhibit strong influence in track design, decision making and maintenance planning. However, such methods are subject to miscalculations that are due to a lack of input, which is caused by a lack of understanding of the mechanical processes that are involved in railway track response. From this perspective, the analytical and numerical models are better research contributions.

The analytical approaches use theoretical models to represent the com-

ponents of track and soil. Because of the necessary simplifications involved in modelling, analytical solutions are not usually adequate for practical problems. However, they can offer a better understanding of well-defined theoretical problems and provide useful references for validating numerical simulation results. The need to overcome these limitations led to the development of the numerical models, which is reinforced by the increase in processing capacity of computers.

The overall objective of this thesis is to study and develop advanced numerical models that provide detailed insight into critical physical and mechanical aspects of ballasted railway tracks for high-speed trains. The study is mainly confined to ballasted track response to the passage of high-speed trains, and considers non-linear material models and their influence in the prediction of railway track behaviour.

The thesis is structured in such a way that it demonstrates the increasing complexity of the studies, informs the reader of the models and phenomena, and enables better comprehension of the complex considerations that are described in the following sections. The thesis is outlined as follows:

- **Chapter 1** presents the theme and thesis outline.
- **Chapter 2** describes state-of-the-art railway track modelling. The components of a typical ballasted railway track and various available methods for response prediction are discussed. By focusing on the numerical models, the most common numerical techniques used to simulate railway tracks are examined. Finally, the objectives of this thesis are derived from advancements in the models and by identification of specific fields in which developments are less profound .
- **Chapter 3** explores linear analyses of railway track behaviour and the validation of the 3D Finite Element (FE) mesh methodology. The FE model is used to simulate a track whose response has been experimentally obtained. Two 2.5D models, which were developed and validated at the Katholiek Universiteit Leuven, are employed and compared. The track dynamics and the models are examined to understand the elastodynamics of the track-soil system and the models. These models are also used to validate the 3D FE models and to highlight their advantages and disadvantages for the simulation of railway tracks for high-speed trains.
- **Chapter 4** explores non-linear railway track behaviour, which is the main focus of this study. This investigation is initially performed through separate studies of the non-linear behaviour of ballast and the non-linear behaviour of soil. The non-linear behaviour of ballast is achieved through the utilisation of a modified Mohr-Coulomb constitutive model, which was calibrated to simulate the experimental

behaviour in the literature. A synthetic case is used to obtain relevant information about the differences between the consideration of linear ballast behaviour and the consideration of non-linear ballast behaviour, and about the differences between the consideration of a constant Young's modulus and consideration of equivalent linear pressure-dependent Young's modulus. To simulate non-linear soil behaviour, a cyclic non-linear model that is based on Iwan's parallel model is implemented, which facilitates simulation of the soil's hysteresis curve and consequent stiffness and damping variation with shear strain. The implementation of the model is presented and its behaviour is validated with experimental results from related research. Later, a synthetic case is formulated in which the track and soil responses are evaluated by considering this non-linear soil behaviour. The differences among consideration of linear, equivalent-linear and non-linear soil behaviour are presented and discussed. Finally, the real case of the Ledsgard site in Sweden is simulated by simultaneously considering the non-linear behaviour of ballast and soil. The differences in the accuracy of the linear and non-linear considerations are discussed in view of the different circulation speeds.

- **Chapter 5** discusses the main conclusions and contributions of the thesis and suggests research topics for future development.

- **Appendix A** details the definition of the material properties in the implemented cyclic non-linear model and presents the Fortan code developed to implement the model in the FE software.

- **Appendix B** discusses the challenges in determining the eigenvalues of a matrix, and describes the numerical methods and algorithms that are employed in the implemented cyclic non-linear model to determine the principal strains.

Chapter 2

State of art

2.1 The railway track infrastructure

2.1.1 Railway track superstructure

The railway track structure provides the necessary conditions for the circulation of trains. There is a great variety of track structures throughout the world of which the ballasted railway track is one of the most common. Since the focus of this thesis relies on the simulation of ballasted railway tracks, the description of track components is mainly restricted to this track type. Usually, the track components are divided into the superstructure and the substructure (Figure 2.1).

The superstructure is composed by the rails, rail pads, fastening system and sleepers. The rails are a pair of longitudinal steel beams which are in contact with the train wheels. Their function is to support the wheels as smoothly as possible and provide a stable platform for the wheels to circulate. The cross section of the rail can be very varied throughout the world but it is usually "I" shaped as this provides good flexural strength and is economically effective. The rails should transmit the vertical forces to the sleepers as well as any accelerating/breaking and lateral forces. They should have such stiffness so that they distribute the forces to the nearby sleepers without suffering too much deflection. They should also be as smooth as possible because irregularities in the rail (as well as in the train wheels) will generate dynamic interaction forces between the rail and the wheel. The union of the several rail sections is usually made either by bolted joints or by welding. As Selig and Waters (1994) pointed out, bolted joints have been a source of problem in railway tracks because they create a discontinuity in the rail surface thus generating unwanted vibrations. Although the procedure of bolting the rails has been improved to minimize this problem, it has been pointed out that continuously welded rails are a better solution, especially for high-speed tracks (Selig and Waters, 1994).

In ballasted tracks the rails are discretely supported by sleepers that are

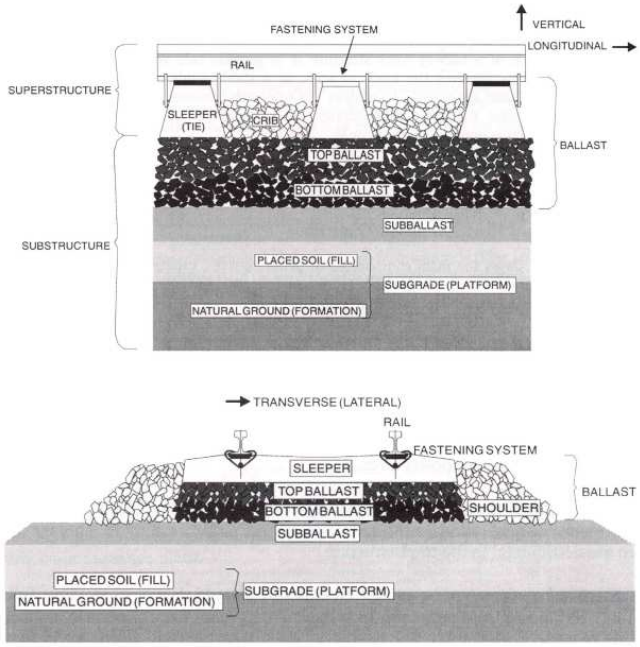

Figure 2.1: Ballasted railway track (Selig and Waters, 1994).

periodically placed in the longitudinal direction of the track. The connection between the rail and the sleeper is usually done by a fastening system (Figure 2.2). This consists in a mechanical clip that keeps the rail connected with the sleeper. The rail does not rest directly on top of the sleeper, instead a rail pad is used, which consists in an elastic material of 10 to 15 mm that is placed between the two surfaces.

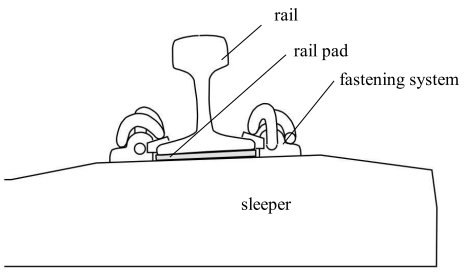

Figure 2.2: Connection between rail and sleeper (adapted from Dahlberg (2003)).

The sleeper distributes the vertical load of the wheels in the transversal direction of the track to the ballast, secures the fastening system and

anchorages the superstructure to the ballast preventing lateral and longitudinal movements. It can be made of wood for the case of conventional or older railway tracks. For the case of tracks for high-speed trains, pre-stressed concrete mono-blocks (Figure 2.3) are more commonly used as these provide more secure fastening of the rails, and are more durable. A disadvantage of mono-block sleepers is their handling as these are very heavy in comparison to wood sleepers. Another type of sleeper is more common in France which is the twin-block sleeper (Figure 2.3). These sleepers consist of two concrete reinforced blocks joined together by a steel bar. This is a type of sleeper that is considerably lighter than the mono-block sleeper but its handling is still limited because of its tendency to twist when lifted. Sleepers may also be of steel (Bonnett, 2005) providing very low weight, although this option has been hardly used due to the fear of corrosion and high cost.

Figure 2.3: Concrete mono-block (bottom) and twin-block (top) sleepers.

2.1.2 Railway track substructure

The railway track substructure includes the ballast, sub-ballast and subgrade.

Ballast is a crushed granular material where the sleepers rest. It has many functions, namely retaining track position, distributing the sleeper pressure to the lower layers of the track, restitution of original geometry during track maintenance, track drainage, to name a few. According to Bonnett (2005), to ensure lateral and longitudinal stability of the track, ballast material should be taken up to the level of the sleepers and a good lateral zone (ballast shoulder) should also be placed. Bonnett (2005) also states that the depth of good ballast material that should be used in railway tracks depends upon the magnitude and frequency of the traffic load, suggesting that even for a lightly loaded railway a minimum of 150 mm should be used.

Several materials are used as ballast, such as granite, limestone or basalt. The choice usually depends on local availability. The particle size should be between 28 mm and 50 mm because a finer grade than this does not provide adequate drainage and larger particles do not provide adequate stress distribution (Bonnett, 2005). It is also preferable that particles present great angularity as this provides better particle interlocking which results in higher resistance to longitudinal and lateral movement under dynamic loading. Although the ballast is usually considered a uniformly graded material, several different gradations are commonly used such as the AREMA, the Australian and French gradations (Tutumluer et al., 2009).

In the past, most attention was focused into studying the superstructure. However, according to Selig and Waters (1994), ballast contributes the most to track settlement, as shown in Figure 2.4. In recognition of its importance in the track behaviour, ballast has been recently one of the main focus of study in railway track engineering.

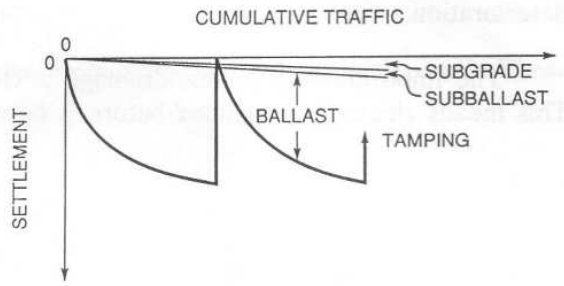

Figure 2.4: Contribution of the materials to track settlement (Selig and Waters, 1994).

Many researchers have performed experimental and laboratory measurements aiming at providing insight into ballast behaviour. The most usual laboratory experiments to determine ballast behaviour are box tests and large triaxial tests. In the later ones, large triaxial chambers (300 mm diameter) are required because a minimum sample size ratio (diameter of the triaxial specimen divided by the maximum particle dimension) of approximately 6 should be ensured in order to keep the sample size effects negligible (Indraratna et al., 1993).

Indraratna et al. (1998) performed a series of large triaxial tests on uniformly graded latite basalt which was being used by the Railway Services Authority of New South Wales, Australia in the construction of new railway tracks. They noted that the deformation and shear behaviour of the latite basalt at low confining pressures (< 100 kPa) departed significantly from the behaviour at high confining pressures. This is confirmed in a literature review on the resilient behaviour of unbound aggregates, where Lekarp et al.

(2000a) refer that all studied investigations showed without exception that the stress level is the factor that has the most impact on the resilient behaviour of granular materials. The resilient modulus increases considerably with confining pressure and is also affected to a much smaller extent by the magnitude of the deviatoric stress. Experimental measurements have shown that for each deviatoric stress there is an optimum confining pressure that minimizes the ballast degradation (Indraratna et al., 2005a, Lackenby et al., 2007), usually the optimum confining pressure is above the confining pressure of ballast in railway tracks. It is therefore vital that in laboratory experiments on ballast material the confining pressure at which the material is subjected in practice is dully known and reproduced. Raymond and Davies (1978) demonstrated that when a maximum wheel load of 150 kN could treble due to wheel or rail effects, the confining stress would hardly develop over 140 kPa.

Brown and Hyde (1975) suggested that it was not necessary to cycle the confining pressure in triaxial tests since they obtained similar resilient results when cycling the axial stress and maintaining the confining pressure equal to the mean of the cyclic value. However, Nataatmajda (1995) would later reconsider this assumption that either constant or cyclic confining pressure could be used. The author presented the results of a comprehensive experimental program of 200 mm diameter crushed rock in which it was shown that the pattern of volumetric change differed in the cases of constant and cycling confining pressure.

Besides confining pressure, other factors affect the behaviour of unbound granulates in general and railway ballast in particular. Higher particle angularity leads to higher resilient modulus and smaller plastic deformations due to better particle interlocking (Indraratna et al., 1998, Lekarp et al., 2000a,b). Indraratna et al. (2005b) also suggest that higher particle breakage leads to a reduction of the void ratio, thus increasing the inter-particle contact area and the resilient modulus. The general view regarding the impact of load duration and frequency on the resilient behaviour of granular materials is that these parameters are of little or no significance (Lekarp et al., 2000a). However, the stress history does have direct implication on the permanent strain development. Brown and Hyde (1975) obtained less permanent deformations when applying increasing successive stress levels than when the maximum stress level was immediately applied to the aggregates. This occurs as a result of gradual material stiffening by each load application, causing a reduction in the proportion of permanent to resilient strains during subsequent loading cycles. Although this relation between stress history and permanent deformation has been recognized, it has been seldom acknowledged and studied as most laboratory experiments use new specimens for each stress path applied (Lekarp et al., 2000b). Suiker et al. (2005) performed a series of static and cyclic triaxial tests on ballast and sub-ballast material at stress levels relevant for railway

structures. They concluded that the application of cyclic loading can lead to material compaction which leads to a considerable increase in material strength and stiffness.

The degradation of ballast material usually occurs due to traffic load, track maintenance and intrusion of external materials. Past studies on the long-term behaviour of tracks have shown that this degradation is related to a great reduction in the track's serviceability. Track maintenance is mostly made on ballast level by mechanical means. There are two mechanical procedures applied to correct track irregularities with medium to long wavelengths: ballast tamping and stoneblowing. Tamping (Figure 2.5) consists in lifting the sleepers separately to a prescribed level, after which a tamping unit of steel tools vibrates and squeezes the underlying ballast particles to all the voids beneath the lifted sleepers. This is repeated at each sleeper in the segment of track needing smoothing.

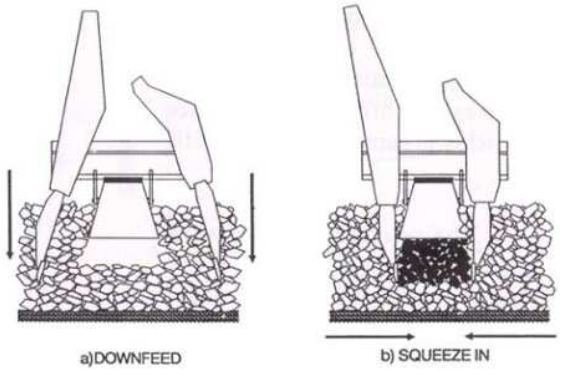

Figure 2.5: Ballast tamping (Selig and Waters, 1994).

According to Esveld (1989), this procedure breaks particles and thus diminishes the effectiveness of the material. Wright (1983) had reached similar conclusions. He noticed that 2 to 4 kg of finer content than 14 mm would be generated in the tamping process of a single sleeper. Another disadvantage of this process is that the ballast that fills the space below the sleeper is loose and will settle very fast under traffic loading. This originates the called "ballast memory" in which the track will in short time return to its pre-maintenance profile. In Figure 2.6 this effect is exemplified.

In the procedure of stoneblowing (Figure 2.7), instead of squeezing the ballast particles, a predetermined quantity of small stones is pneumatically injected into the void created by the lifted sleeper. In contrast to tamping, stoneblowing causes the original ballast layer to be minimally disturbed. Esveld (1989) suggested that this may result in an improved post-maintenance performance if the size and type of the stone and the thickness of the injected layer are chosen adequately.

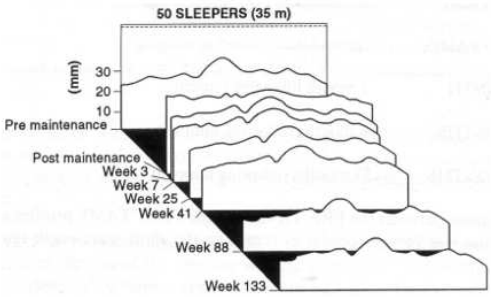

Figure 2.6: Ballast memory (Selig and Waters, 1994).

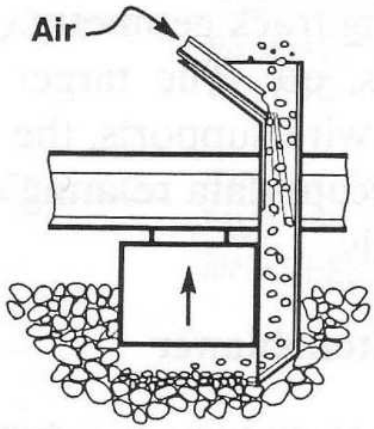

Figure 2.7: The stoneblowing process (Selig and Waters, 1994).

Wright (1983) showed that both tamping and stoneblowing caused ballast breakage during the insertion into the ballast layer. However, stoneblowing produced up to eight times fewer particles smaller than 14 mm than tamping. Suiker et al. (2005), amongst others, suggest that stoneblowing is preferable to tamping because, from the viewpoint of track stabilization, track maintenance procedures should aim at preserving consolidated granular substructures as much as possible.

Sub-ballast is the layer that usually separates the ballast and the subgrade, serving as a medium through which the stress from the ballast is further distributed to the lower layers. However, according to Lim (2004) the most important function of the sub-ballast is to prevent interpenetration between the subgrade and the ballast and thus, sub-ballast materials are broadly-graded sand-gravel mixtures. Because of this, sub-ballast must

fulfil the filter requirements for the ballast and the subgrade. As long as these filter requirements are fulfilled, any sand or gravel materials will usually serve as sub-ballast material. However, depending upon the conditions of the subgrade below, it may be necessary to construct the sub-ballast layer using asphalt concrete, geo-synthetic materials or cement/lime stabilized soils (Selig and Waters, 1994). According to Brandl (2004) the seasonal variation of road stiffness and bearing capacity (Figure 2.8) is analogous to that of sub-ballast. Consequently, he suggests that in zones exposed to temporary frost periods, the sub-ballast of railway tracks must exhibit sufficient freezing-thawing resistance.

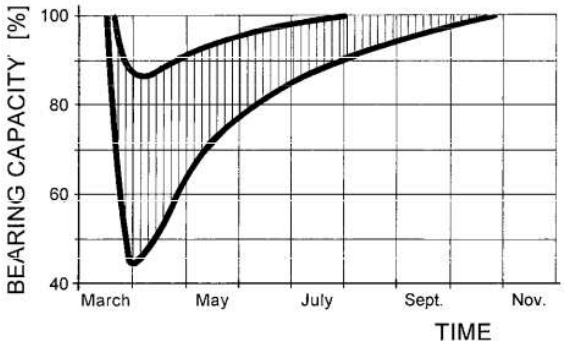

Figure 2.8: Seasonal fluctuation of the bearing capacity of unbound road layer, analogous to sub-ballast (Brandl, 2004).

The subgrade is the foundation upon which the track structure is constructed, its main requirement is to provide a stable foundation upon which the sub-ballast and ballast layers may rest upon. Upon the consideration of the vertical stiffness of the full soil-track system, a large component is due to the subgrade, or foundation soil. Selig and Waters (1994) stressed that subgrade has also been pointed out as influencing the ballast and sub-ballast deterioration as well as rail differential settlement. As a consequence, the subgrade has a very important influence in the rail deflection and the track response in general. On a related phenomenon, the track-soil critical speed is highly dependent of the soil and with the increasing circulation velocities of high-speed trains, the critical speeds may be easily reached in cases of soft subgrade. An example occurred shortly after the Gothemburg-Malmö line was opened. It was noticed that in some stretches with soft soil, excessive vibrations occurred in the track, surrounding soil and nearby power-line pylons when the X-2000 trains circulated at speeds around 200 km/h. The immediate consequence was that the circulation speed in these stretches had to be reduced (Madshus and Kaynia, 2000). This example illustrates how the subgrade conditions may critically condition the track serviceability. Thus, any prediction model attempting to simulate the track response

must incorporate the track-soil interaction.

When the upper subgrade material is unsuitable, it may be replaced with soil obtained from nearby formations, but anything beyond soils existing locally is expensive. This upper subgrade layer of higher mechanical properties than the rest of the subgrade, either existing originally or purposely placed is usually called the capping layer, although some authors may also refer the sub-ballast material as capping layer. It is also possible to improve the subgrade of an existing track without removing the structure. Kouby et al. (2010) suggested such a method that consists in building vertical soil-cement columns under the sub-ballast layer. This method was performed in a site in the north of France without impregnating the ballast and sub-ballast materials. The method also allowed for reduced maintenance works and thus limited traffic interruption.

2.2 Analytical railway track modelling

The analytical approach uses theoretical models to describe each component of the system. Concerning the evaluation of wave propagation, Lamb (1904) included in his work most of the elements that are essential to analytical studies on the vibration sources and transmission paths in soils. His work focused on studying the influence of an impulsive load applied in a point or across a line on the surface of an infinite half-space or inside an unbounded full space (Figure 2.9). After the pioneering work of Lamb (1904) many authors further developed the analytical determination of the half and full space response to point and line loads, amongst them Ewing et al. (1957), Achenbach (1973), Graff (1975), Gutowski and Dym (1976), Dawn and Stanworth (1979).

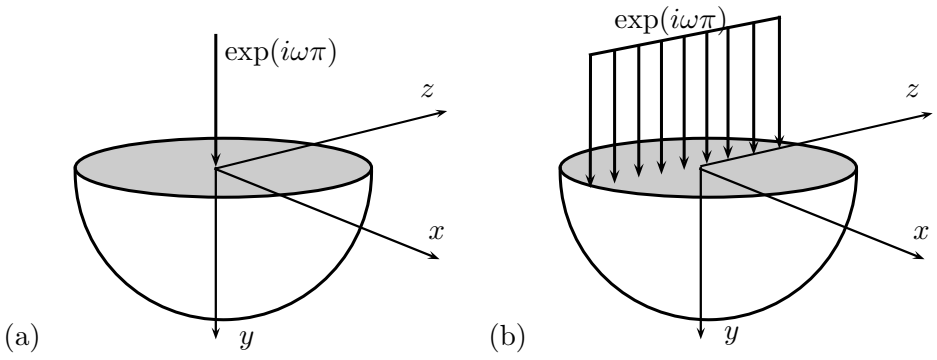

Figure 2.9: Classical Lamb's problems with harmonic a) point load and b) line load.

A generic understanding of the response states that an harmonic load on a full space generates two types of waves propagating away from the load: primary waves or P-waves generate particle movement in the direction of the wave propagation, secondary or S-waves generate particle movement in a plane normal to the direction of the propagation of the wave. The P-waves speed C_p is higher than the speed of the S-waves C_s. In elastic half-spaces a third type of wave called Rayleigh or R-Waves appear at the surface. The amplitude of Rayleigh waves attenuate exponentially in the normal direction of the free surface and their speed C_r is lower than the speed of S-waves.

After the problem of the elastic response to harmonic loads was well established, researchers began to study the response to moving loads, a problem that had increasing interest with the increasing speed of the means of transportation. Fryba (1973) used a triple Fourier integral transformation to obtain the displacements due to a moving point load. The expressions were determined for three different cases of the moving load problem: the subsonic case is when the moving load speed is lower than the speed of S-waves in the medium ($c < C_s$), the transonic case occurs when the moving load speed is higher than the speed of S-waves and lower than the speed of P-waves ($C_s < c < C_p$) and the supersonic case occurs when the load moves at higher speed than the speed of P-waves in the medium ($c > C_p$).

Concerning a moving load on an elastic half-space, Eason (1965) studied the three-dimensional steady state problem of moving point loads and of moving loads distributed along circular and rectangular areas. Fryba (1973) also determined the steady state response of a moving point load at the free surface, presented in an integral form.

Concerning the response of the track, a very useful analytical model is the beam on Winkler foundation. This model approximates the response of the track by considering a moving load on a beam discretely supported by springs and dashpots (Figure 2.10).

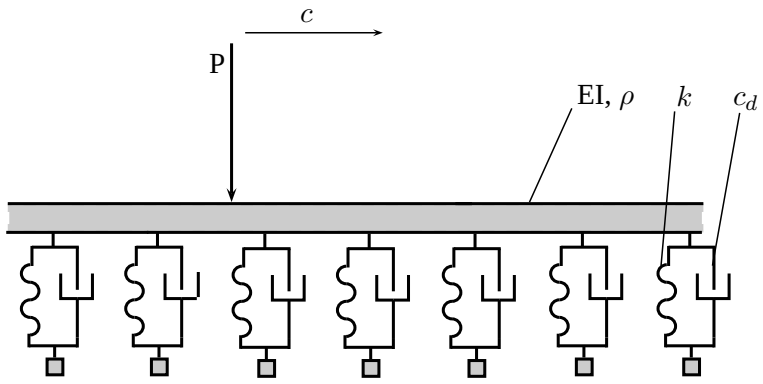

Figure 2.10: Beam on Winkler foundation.

The differential equation of this problem is given by:

$$EI\frac{d^4u(x,t)}{\partial x^4} + \rho_l\frac{d^2u(x,t)}{\partial x^2} + 2c_d\frac{du(x,t)}{\partial x} + kdu = P\delta(x-ct) \qquad (2.1)$$

where EI is the flexural stiffness of the beam, u is the vertical displacement, ρ_l is the mass per unit length of the beam, k is the stiffness coefficient of the Winkler foundation, c_d is the viscous damping of the foundation, P is the vertical load and $\delta(x-ct)$ is the Dirac delta function of the moving load at speed c.

The determination of the these properties will depend upon which components of the structure are considered for the beam and which are considered for the Winkler foundation. One common approach consists in considering only the rails for the beam of the model and all other components of the track and subgrade in the Winkler foundation. However, this is not a universally accepted approach as it is also possible to consider the beam as representing the whole track structure and the Winkler foundation representing only the track subgrade. For the determination of the Winkler stiffness k, many authors have suggested different formulations, amongst them Biot (1937). Terzaghi (1955) demonstrated that the stiffness of any given soil layer is not an intrinsic property of the layer, but rather varies from case to case. Heelis et al. (1999) suggested the utilization of a FE model to compare deflections under a known applied load.

Despite the usefulness of the beam on Winkler foundation model to estimate track deflection and critical speed of the track, the simplifications it assumes have been pointed out as the cause of some errors, a very highlighted disadvantage is that model cannot transmit shear stresses, although modified models have been suggested to overcome this drawback (Sadrekarimi and Akbarzad, 2009).

Because of the necessary simplifications and sub-divisions involved, analytical solutions are not usually adequate for practical problems. However, they can give a better understanding of well defined theoretical problems and provide useful references for the validation of numerical simulation tools.

2.3 Numerical railway track modelling

2.3.1 Introduction

The necessity to overcome the limitations of empirical and analytical models led to the development of the numerical models, which were backed up by the increasing processing capacity of computers. Different approaches have been used to make numerical predictions in the scope of railway tracks for high-speed trains. The main differences regard the numerical method that

is used (mainly the FEM, Boundary Element Method (BEM), Discrete Element Method (DEM) and hybrids). Each numerical method was originally proposed based on assumptions that are further elaborated and developed until the framework of the method is revealed. These assumptions allow to develop the method toward the desired framework but also ensure that the method will be implicitly limited into complying with them. Consequently each method will have numerical advantages and short comes making them more or less suitable for numerical simulations depending on the assumptions or simplifications that the user is willing to make.

The purpose of this subsection is to describe in a general way the most common numerical approaches in the literature to simulate railway track response, giving a general understanding of their relative advantages and short comes.

2.3.2 2D and 3D FE models

The FEM has the advantage of being very widespread amongst engineers and such when choosing which numerical method to use in the approach of the problem, it becomes a first choice for many. Regarding the prediction of track response and wave propagation to outer zones, the FEM has the advantage of allowing a detailed definition of the track geometry and the possibility to consider non-linear material behaviour.

On the other hand, one of the major problems concerns soil modelling with finite elements, because the soil is an infinite half-space. If the FE mesh is constrained in its outer limits, the waves generated by the dynamic loading spuriously reflect on the fixed constrains instead of continuously propagating to outer regions. Consequently the results of the numerical simulation will be affected by this numerical short come. To overcome this drawback, the models must become larger than those used for static analyses and include a methodology that mitigates or prevents these spurious wave reflections. Lysmer and Kuhlemeyer (1969) and White et al. (1977) have proposed the introduction non-reflecting viscous boundaries to absorb incoming waves and avoid reflections. These viscous boundaries are perfectly absorbing if aligned in the same direction of the incoming wave, thus it is a perfect solution for one dimensional problems but only mitigates this problem in 2D and 3D models (see sub-section 3.3.4). Another way to address this problem is by introducing infinite elements, these were proposed by Bettess (1992) for static and steady-state problems. These elements are derived from standard finite elements and modified to represent a decay type behaviour as one or more dimensions approach infinity. Wolf and Song (1996) suggested the consistent infinitesimal finite-element cell method also called the Scaled Boundary Finite Element Method (SBFEM). The method is derived from the similarity of the unbounded domain and is used in a substructure method. The discretization is limited to the structure-medium interface resulting in a one

dimension reduction of the spatial dimension that, unlike the BEM, does not require a fundamental solution. Ekevid and Wiberg (2002) applied the SBFEM to simulate the dynamic response of a typical railway track stretch (Figure 2.11). The results suggested that the usage of the SBFEM resulted in very small or no reflections of waves even when constraints were used in the nodes of the soil-structure interface. The calculated time-history plot of the vertical displacements of a point in the track agreed very well with experimental measurements.

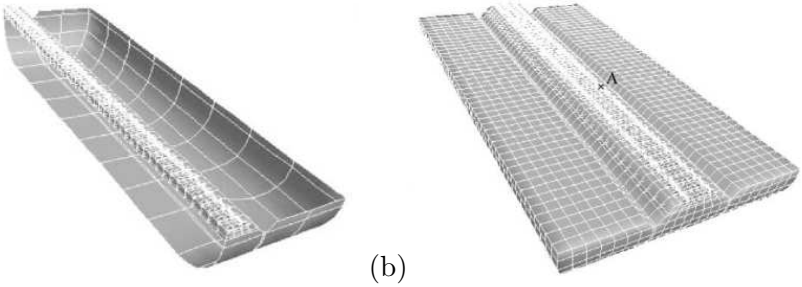

(a) (b)

Figure 2.11: Coupling of FEM and SBFEM for simulation of a rail road section: (a) discretization of the structure-unbounded media interface, (b) the FE model (adapted from Ekevid and Wiberg, 2002).

In the context of the simulation of electromagnetic waves, Bérenger (1994) introduced the concept of Perfectly Matching Layers (PML) that consists in modelling an outer layer of the same material, but having attenuation characteristics that damp the outgoing and reflected waves within the layer thickness. Later, the concept of a PML has been developed for elastodynamics wave equations (Chew and Liu, 1996, Collino and Tsogka, 2001).

Even taking into account the fact that the wave propagation to outer zones in FE models has been studied by many authors and mitigated through different modelling techniques, it is still necessary to include in the FE mesh a considerable part of the foundation soil, which makes the models computationally demanding, although in most cases it is possible to consider symmetry conditions and thus reduce the computational efforts to approximately 50%.

The approach to modelling railway track behaviour using the FEM is usually done in one of the two following ways: 2D plane strain modelling and 3D modelling. Figure 2.12 presents a 2D plane strain mesh used by Suiker (2002). The 2D plane strain modelling requires the simplification assumption that the transversal profile of the track is invariable in the longitudinal direction, which, does not correspond to the reality in the case of ballasted tracks where the rail is discretely supported by the sleepers.

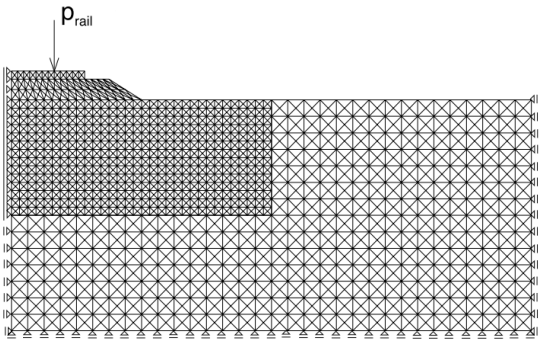

Figure 2.12: Example of a 2D plane strain FE model of the track and soil (adapted from Suiker (2002)).

Another requirement of these 2D models concerns the assumption of the longitudinal load distribution. In order to accurately account for the load time history in the transversal section of the track, the load distribution in the longitudinal direction of the track must be previously accounted for. An approach was proposed by Gardien and Stuit (2003) studying soil vibrations from railway tunnels. These authors, instead of creating a three-dimensional model for the dynamic analysis built three complementary models: the first one is three-dimensional, where static loads were applied to obtain equivalent beam parameters, which were used in the second model to calculate the under-sleeper force in time; this force was then introduced in the third, a plane strain model of the tunnel cross section.

The 3D FE models do not require such simplifying assumptions. The load distribution in the longitudinal direction of the track is done by the model itself invalidating the need to previously account for this. 3D FE models also eliminate the necessity to consider continuous support of the rail in the longitudinal direction of the track as the discretely support system can be discretized in the 3D FE mesh. This usually includes beam elements to simulate the rails and spring-dashpot elements to simulate the rail pads, although this is not necessarily the case for all models: Araújo (2011) and Hall (2003) did not include the rail pads in their simulation, instead having the rail rest directly on the sleepers. The remaining model, including the sleepers and all other track and soil layers are usually modelled using brick or wedge elements (Figure 2.13).

Usually only the quasi-static moving load of the train is considered in these models. As was previously mentioned a disadvantage of these 3D FE models concerns the numerical demand associated with such a large number of degrees of freedom. Furthermore, the amount of soil that must be simulated in the transversal direction and in the depth of the model is

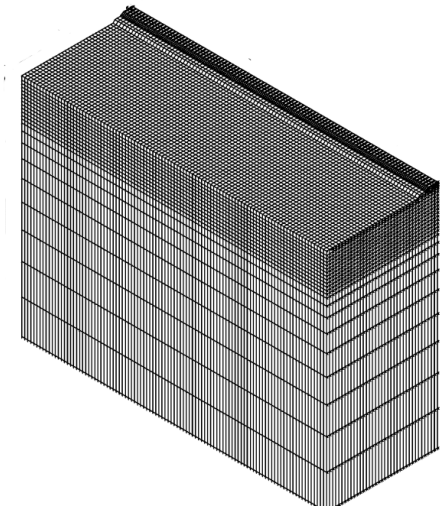

Figure 2.13: Example of a 3D FE model of the track and soil (adapted from Hall (2003)).

not clear. Users of these models usually rely on trial and error or their own experience to decide upon the size of the model.

Some spurious numerical disturbances in 3D FE modelling were referred by Hall (2003). The author noted that the entrance and exit of the axle loads in the FE model created some disturbances in the model. Another remark by the author was that the stress waves in the free field were not fully developed when they entered the FE model. This stems from the fact that the load does not come from infinity but instead begins its movement at the limit of the FE mesh. Consequently the results that the author obtained were more accurate closest to the track and farther away from the entry point.

2.3.3 2.5D and 3D FE-BE models

A very efficient way to model the propagation of waves in the soil is to use the BEM. This consists in a method to solve partial differential equations in a boundary integral form. This method requires the definition of a fundamental solution which, in the particular case of modelling wave propagation in the soil, are very often the Green's functions in the free field. The Green's functions are obtained as numerically precise solutions of an elastodynamics problem of a load in a homogeneous or layered half-space (full-spaces may be also considered in other cases). The BEM has the advantage of correctly accounting for wave propagation in the half-space but is not appropriate to deal with geometrical complexities and non-linearities (Kausel,

1981, Domínguez, 1993). Usually in these situations the soil definition is restricted to vertical soil layering. Because of its advantages and short comes, in the context of railway track simulations, the BEM is almost exclusively used to simulate the foundation soil, while the track is simulated using different numerical methods, with the two components of the model interacting in order to obtain a true track-soil response. On top of correctly accounting for wave propagation to outer zones, the BEM has another advantage over FEM in the computational effort as the Direct Stiffness Method (DSM) pioneered by Kausel and Roësset (1981) allows to do straightforward computations of the Green's functions in the soil. Consequently, only the desired free field locations need to be computed, while in the FEM the system of equations must be solved for the whole mesh.

A common and efficient way to implement the track-soil model with the soil modelled with the BEM, is by defining the model in 2.5D. The designation comes from the fact that the geometry of the problem is only defined in 2D, i.e. only the transversal section of the track is discretized. However, a true 3D response is obtained in these models. This occurs because the problem is formulated in the frequency-wavenumber domain, which implies a double Fourier transform, from the time domain into frequency domain and from the longitudinal direction into wavenumber domain. These transformations imply that only linear material properties can be admitted and also that the transversal geometry of the model is invariant in the longitudinal direction. The definition of the model in this 2.5D formulation allows to efficiently implement the BEM using as fundamental solution the 2.5D Green's functions of the soil, which are more efficiently evaluated in frequency-wavenumber domain than in space-time domain. Sheng et al. (1999) defined a model in which the track is simulated as an infinite layered beam and the soil as a layered half-space. Following these developments, the model was adapted to account for train-track interaction (Sheng et al., 2003, 2004). Lombaert et al. (2006) applied a similar methodology with Boundary Element (BE) formulation for the soil.

Evolving from modelling the track as an infinite layered beam, Sheng et al. (2006) modelled the track-soil interaction by coupling 2.5D Finite Element (FE) and 2.5D BE formulations. Other authors (Galvín et al., 2010, Costa et al., 2012, Fiala et al., 2007) have used similar formulations to model track response and wave propagation in the soil due to high-speed trains (Figure 2.14).

Clouteau et al. (2000) developed an approach in which periodicity in one direction, instead of invariance, is assumed. The Fourier transform of the 2.5D models is replaced by a Floquet transform in these models. The FE-BE discretization is reduced to one single reference cell (Figure 2.15). Within the context of railway track simulation, the approach has been mostly used to simulate vibration from underground railway traffic (Degrande et al., 2003, Chatterjee et al., 2003, Clouteau et al., 2004, Gupta et al., 2006a,b).

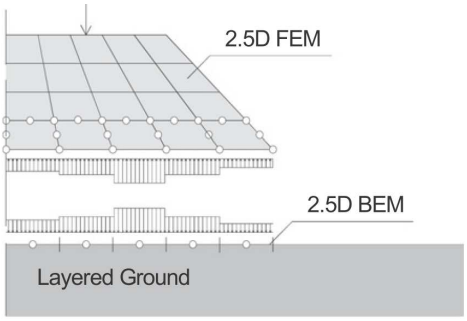

Figure 2.14: Example of a 2.5D FE-BE model of the track and soil (adapted from Costa et al. (2012)).

Araújo (2011) used this approach to model train passage in a railway line between Paris and Brussels obtaining good correspondence between measurements and numerical results.

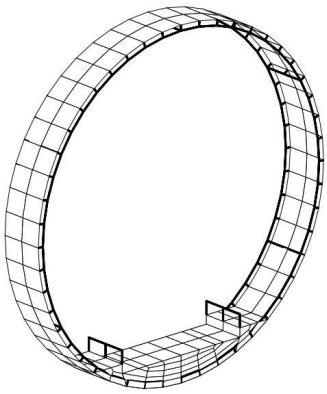

Figure 2.15: Example of a reference cell in a periodic model (Gupta et al., 2006b).

It is also possible to couple FE-BE methodologies in 3D conditions. The computation of BE solutions in a 3D environment is more computationally expensive but it can be coupled to 3D FE model of the track in time domain allowing for more detailed geometric and material properties. O'Brien and Rizos (2005) proposed a 3D FE-BE methodology (Figure 2.16) for the simulation of high-speed train induced vibrations where the time marching scheme is adapted to provide the FE and BE solvers with different time steps to ensure stability of both solvers. The communication of data between solvers is then done at a time step where the results of one solver

are computed and the results of the other solver are linearly interpolated.

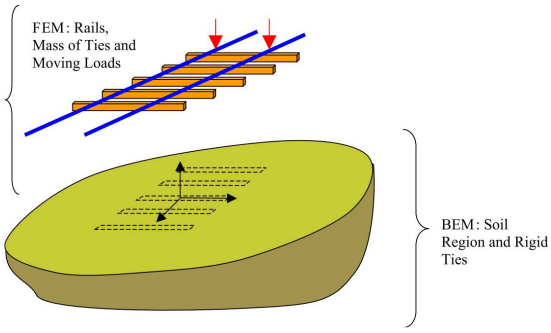

Figure 2.16: Example of a 3D FE-BE model of the track and soil (O'Brien and Rizos, 2005).

2.3.4 DEM models

Due to the large size of ballast particles, there is an increasing trend to try to reproduce ballast behaviour through the DEM. An increasing number of authors have used this method in order to reproduce experimental results from triaxial tests (Lu and McDowell, 2008, Hossain et al., 2007) and box tests (Lim and McDowell, 2005, Lu and McDowell, 2007).

In general the Discrete Element (DE) codes simulate simple interactions between a great number of micro-particles that combined result in a much more complex macro-behaviour. Although usually referred as the (more general) DEM, the Distinct Element Method is the most commonly used discrete code in the study of the ballast behaviour.

In the DEM, there are usually only two basic entities: particles and walls. Walls usually represent containers for the particle assemblies allowing them to be constrained to a defined volume region. A wall will only interact with particles and not with other walls. Also, the position of the walls may be constant or time-dependent but will usually not depend upon the interaction forces with the balls. A particle is subject to gravity loads or contact forces with other particles and walls and its movement within each time step is computed with the consideration of all applied forces. The calculations within a single cycle alternate between the computation of the particles movements and the computation of the interaction forces between all elements. For instance, the calculation cycle of the Distinct Element Code PFC2D is represented in Figure 2.17. The particle movements are usually computed with the Newton's second law while a force-displacement law is applied to compute the interaction forces. As a result, contacts that may form or break between the particles are automatically accounted for in the

computational scheme. The complex behaviour of the materials then arise from the combination of a great number of (usually) simpler particle-particle or particle-wall interactions.

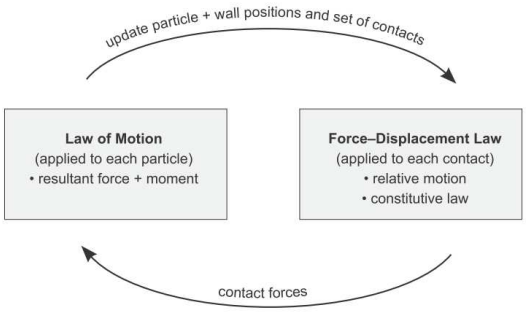

Figure 2.17: Calculation cycle in PFC2D (Itasca).

Due to the large computational effort that DEM requires, seldom has this method been used to try to reproduce the ballast behaviour in a numerical model of the track. Those track models that have been constructed in which the ballast is modelled with DEM only reproduce a small part of the track, and the interaction with the subgrade is not simulated. Also, the longitudinal length of the model is reduced spanning 1 to 5 sleepers in 2D (Lobo-Guerrero and Vallejo, 2006, Saussine et al., 2006) or a single sleeper in 3D (Tutumluer et al., 2007). The limited longitudinal length of these models limits the simulation of the moving loads, which is done usually by the consideration of a single load with time-dependent modulus.

2.4 The achievements of numerical railway track modelling

From the various approaches that have been applied to simulate track and subgrade response to high-speed train passage, various models are now available which have been proved to be very accurate. The possibility to predict the railway track response and/or propagation of waves to the free field is by itself an important achievement. However, numerical models may provide detailed insight into the phenomenons at hand that even experimental measurements are not able to show. A validated numerical model is also an invaluable tool to study different case scenarios where the railway track response may be obtained for alternative geometry/material configurations. Thus in this section a general overview is presented of the achievements that the different numerical tools have obtained in further advancing the knowledge of railway track and subgrade behaviour. From the understanding of

the various approaches presented previously and their achievements herein presented, a better comprehension of the state of art in numerical railway track modelling is possible. This allows for a clearer realization of which niches of knowledge have been well established and which have not been so thoroughly studied, thus highlighting the reasons why the works presented in this thesis are valuable contributions.

Even though the non-linear behaviour of the track and soil layers may have significant influence in the track-soil response, very good results have been obtained with numerical models that disregard this complex behaviour. This may be explained by the fact that the influence of the non-linear material behaviour may be reduced in some cases. Also the dynamic properties obtained from optimization of the rail receptance are in many cases obtained from the loaded railway track, thus the model is calibrated to simulate the track response using the stiffness that the materials present when the track is loaded.

The consideration of non-linear behaviour in railway track modelling has been seldom done due to its limited applicability in some cases or due to the extended computational demands that these models require. In general, non-linear behaviour is studied in the track components such as ballast and sub-ballast or the foundation soil.

2.4.1 Linear modelling

The 2.5D model presented by Lombaert et al. (2006) for the prediction of train induced vibrations presented very good correspondence with experimental results of the free field transfer functions and the response to the passage of the Thalys high-speed train. The model was elaborated in order to account for the dynamic interaction between the vehicle and the track. From this experimental validation, the numerical model was further used (Lombaert and Degrande, 2009) to study the influence of the quasi-static and the dynamic components of the load at several speeds in the track and soil response. A major remark made was that the quasi-static component of the load resulting from the weight per axle moving along the track has large influence in the track behaviour and the very near vicinity. On the other hand, the dynamic component of the load that is generated due to the rail and wheel unevenness dominates the free field response. The authors also remarked that the vertical sleeper velocity due to the quasi-static axle load increases moderately with speed and becomes shorter in time, also the response shifts to higher frequencies with increasing speed. The dynamic component of the load only dominates the sleeper response at high frequencies. It also has higher duration in time than the static component, and it increases slightly with increasing speed. In the free field, the dynamic response also increases with increasing speed while the high frequency component is attenuated due to the soil damping.

Other works have successfully modelled the track with FEM and the semi-infinite zone through BEM (Andersen and Nielsen, 2005, Celebi, 2006, Adam et al., 2000, Madshus and Kaynia, 2000, Galvín et al., 2010, Costa et al., 2012).

Fiala et al. (2007) used a 2.5D model of the track and soil as a source model for the ground induced vibrations. Using a receiver model with a BE formulation of the soil and FE of the building they were able to study the structural and acoustic response of the building due to railway traffic. The numerical simulations also allowed to simulate the effectiveness of several vibration countermeasures. Galvín and Domínguez (2009) were also able to predict railway induced vibrations in a a nearby structure using a 3D FE-BE model.

The coupled FE-BE model of O'Brien and Rizos (2005) allowed to demonstrate that the vibration characteristics depend on the relative speed between soil wave velocities and the train speed and that the relative stiffness of the soil with respect to the rail affects the distribution of the wheel load on the sleepers. Similar conclusions were obtained by Yang et al. (2003) using a 2.5D finite-infinite element model to perform parametric studies on the soil configuration and its influence in the track response. It was observed that for layered soils the critical speed at locations near the source can be determined from the Rayleigh wave speed of the top layer soil. But at locations away from the source, the critical speed might be higher.

Closely related to the conclusions obtained by Lombaert and Degrande (2009), the 3D FE model by Ju et al. (2010) allowed to obtain some information regarding the influence of the rail unevenness on train-induced ground vibrations. The authors confirmed that the ground vibrations are dominated by the dynamic component of the load, however, they noted that this dominance only occurs at subsonic speeds. At supersonic train speeds the ground vibrations in the model were not very different with or without rail unevenness. The Vibtrain program, based on sub-structuring in which the ground is represented by discrete Green's functions for layered half-space and the track is represented as a beam by finite elements, allowed Kaynia et al. (2000) to demonstrate that embankment stiffening may be an effective measure to limit ground vibration for trains running near or in transonic regime.

After analysis with 3D finite difference models, González-Nicieza et al. (2008) remarked that the existence under one and the same sleeper of very different properties leads to the appearance of micro deformations in the sleeper of more than $150\,\eta$m/m, which is a value above which cracks would start to appear in the concrete.

Galvín and Domínguez (2007) used a 3D time domain BE model to simulate the track and soil. The analysis allowed the authors to state that the ballast layers do have significant influence in the system response, and thus should not be disregarded. Also they suggest that the presence of these lay-

ers may be considered in a half-space with equivalent properties, however, an assessment of these properties is difficult.

2.4.2 Non-linear ballast modelling

Due to its key role in the track response, ballast has been the increasing focus of interest in railway track modelling. Because the particle size is close to 10% the average ballast width, it can be an exaggerated simplification to simulate the ballast layer as a continuous medium. Regardless of that, due to the large processing demands of discrete calculations, many authors model the ballast as a continuous media, considering elastic linear behaviour or more complex material behaviour. Even those that consider non-linear continuous modelling of the ballast material, often opt to do so in reduced models, 2D plane strain or axisymmetric models due to the high demands of a full 3D non-linear model.

Continuous approach

Nguyen et al. (2003) have proposed a no-tension constitutive law for continuum modelling of granular materials. Unlike many other no-tension models previously written, mainly for the purpose of modelling masonry structures, the model proposed in this paper has been derived directly from a strain-energy function which is evaluated by means of a modified function of stretches. The model has been applied to a quasi-static test on ballast materials in a 3D FE analysis, the compressive stresses found in the no-tension model were approximately 15% higher than those in the non-linear elastic case. These numerical results revealed that the influence of the no-tension effect in a granular structure with the configuration of the ballast layer can be significant.

Suiker and de Borst (2003) proposed an elasto-plastic material model to simulate the cyclic deterioration of ballast and sub-ballast. The model captures the envelope of the maximum plastic deformations, allowing to evaluate the deformation accumulation by means of relatively large load cycle increments. The plastic deformation is controlled by two mechanisms, frictional sliding and volumetric compaction. The frictional shakedown surface is represented by a Drucker-Prager cone which is limited by a cap representing the compaction shakedown surface. The frictional failure level under static loading may not be exceeded and is also represented by a Drucker-Prager cone. The combination of this surfaces with the tensile failure surface divide the p-q plane into four zones that represent the four response regimes of the model (Figure 2.18): the shakedown regime where the response of the material is purely elastic; the cyclic densification regime in which the cyclic loading leads to plastic strain accumulation; the frictional failure regime in which the frictional collapse occurs; and the tensile failure regime in which

the material disintegrates. The parameters of the cyclic densification model were calibrated for experimental data of cyclic triaxial tests on ballast and sub-ballast materials. The model was able to represent with good accuracy the development of permanent deviatoric and volumetric shear strain with number of cycles, for the ballast and sub-ballast materials. Only for cases where the cyclic stress levels were close to the static failure level, the model prediction was inaccurate for a number of cycles inferior to 100. The model was also used to predict the development of permanent deformations in a ballasted railway track under a large number of train axle passages. This was done in a FE simulation of a moving axle on the track. The predictions did not match the experimental results with great accuracy but this was justified by the consideration of plane strain behaviour of the track.

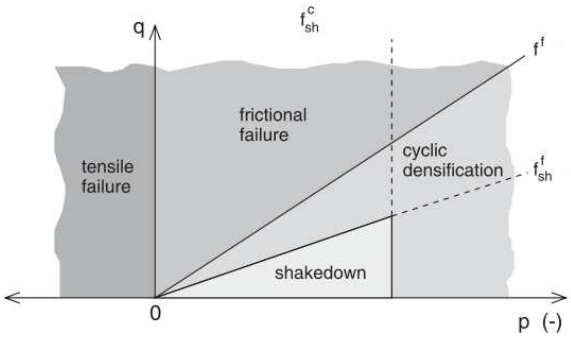

Figure 2.18: Map of various response regimes in p - q plane during cyclic loading in the cyclic densification model (adapted from Suiker and de Borst (2003)).

Al Shaer et al. (2008) presented one approach in which the ballast behaves linearly but accounts for the fact that ballast below the sleeper is more confined than in the crib or shoulder. The method was applied in simple FE model in order to compare numerical results to experimental ones obtained in a reduced scale experiment with three sleepers. All experiment components were considered as linear elastic materials. Ballast was decomposed into two regions of different physical and mechanical characteristics. Ballast in the zones under the blocks at an angle of 45° was considered compacted while ballast elsewhere was considered uncompacted. A correct agreement was observed between the measurements and the computations in most cases.

Indraratna and Nimbalkar (2011) performed numerical simulations using 2D axisymmetric and plane-strain FE analysis in which the behaviour of ballast was simulated using a hardening soil model with a non-associative modified flow rule capable of capturing the effects of the confining pressure and ballast breakage. The models showed that increased track confinement

leads to significant reduction in vertical stresses and deformations, confirming that the optimum confining pressure is usually above those present in the railway track.

In a rare example of non-linear ballast behaviour modelled in a large scale 3D FE model, Araújo (2011) used the linear elastic, Mohr-Coulomb and Hujeux non-linear models in order to study the stress paths in the ballast during the passage of a high-speed train boogie. The Hujeux law is an elasto-plastic continuum approach model developed to simulate 3D cyclic soil behaviour. The model is developed in a multi-mechanism with four plastic elementary mechanisms: three plastic mechanisms for the deviatoric deformations and one plastic mechanism for the isotropic deformation. It was detected that with the linear elastic models, characteristic stress-path range from a slope parallel to the natural state line on the ballast layer to a practically vertical one in the capping layer. This effect, however, was not found in the non-linear models. In those cases the slope remains almost constant and far from the failure envelope. From the comparison of the linear and non-linear simulations the author suggested that a linear elastic model is able to reproduce the vertical displacement and velocity induced by the passage of a high-speed train but its capability quantify the stress evolution seems questionable.

Discrete approach

Due to the large ratio between particle size and ballast thickness, most authors feel that modelling this material with a continuous formulation is an exaggerated simplification that can hardly provide insight into the ballast behaviour in service conditions. Consequently, an increasingly number of researchers have adopted techniques where particle interactions are taken into account. More so than in the continuous case, the consideration of discrete ballast behaviour is mainly constrained to reduced models, either in 2D or 3D.

The tensile strength of ballast as measured by single particle crushing tests has been correlated with ballast degradation on oedometer and box tests (Lim, 2004). However, most DEM implementations do not allow particle breakage. One way to circumvent this short come is to simulate each particle as an agglomerate of several smaller particles (Cheng et al., 2003). The individual particle breakage can occur when a predefined condition is met or by using bonds with limited resistance. Hossain et al. (2007) simulated angular ballast breakage under cyclic biaxial loading at various confining pressures in 2D DEM. They observed that the breakage of particles has significant influence on the settlement and volumetric strains. The analysis also demonstrated that breakage is a function of confining pressure. Lim and McDowell (2005) performed 3D simulations of single particle crushing tests using bonded particle agglomerates. The distribution of strengths

correctly followed the Weibull distribution, and the size effect on average strength was also consistent with that measured in the laboratory.

Another solution to the particle breakage problem is to replace the particles fulfilling a predefined failure criterion with an equivalent group of smaller particles. Lobo-Guerrero and Vallejo (2006) studied the effect of particle crushing using the DEM. They simulated a track section subject to cyclic load and the the values of permanent deformation as a function of number of cycles were recorded. The simulation was done twice for the same idealized material but in one of the simulations particle crushing was allowed whereas in the other it was not. Crushing was simulated by replacing the particle with smaller ones. The obtained results showed that the induced permanent deformation strongly increased when considering particle crushing even though only a few particles were broken. Moreover, it was found that crushing concentrated underneath the simulated sleepers (Figure 2.19).

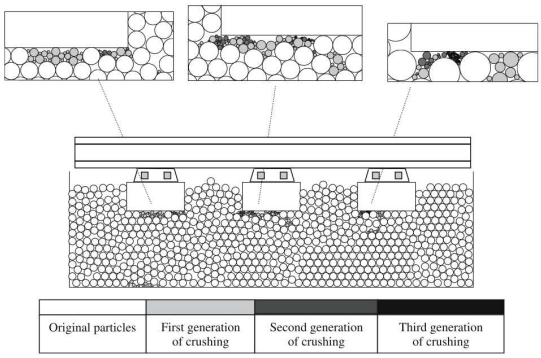

Figure 2.19: Ballast crushing after 200 cycles of 62 kN (Lobo-Guerrero and Vallejo, 2006).

Soon, it became evident that modelling each ballast particle as a sphere did not provide the necessary interlocking between particles to allow for a good ballast simulation. The implementation of more angular particles in DEM simulations of ballast behaviour leads to a greater degree of homogeneity in the stress distribution (Lu and McDowell, 2007), in accordance to experimental data. The simulation of angular particles in DEM software that only allows spherical elemental particles is implemented by the simulation of a single ballast particle with multiple spheres. The particles can be assembled as an agglomerate of bonded spheres, this increases significantly the computational cost of the model, but as previously explained allows to consider ballast breakage. Another solution consists in grouping the spheres in clumps. A clump consists in an agglomerate of overlapping balls. It is rigid internally, which allows the calculation mechanism of the DEM simulation to skip computing internal forces between spheres of the same clump,

but is deformable at the outer boundaries. One disadvantage of the clump is that in the spacial zone where balls overlap the density will be the sum of the overlapping balls densities, thus the clump has non-uniform density throughout its volume.

Lu and McDowell (2007) simulated ballast material using spheres and using clumps with different angularities in a box test consisting of one cycle of sleeper load after compaction. The simulation showed that the angularity of clumps increased particle interlocking thus diminishing the displacement and rotations of sphere particles. For the spheres, the deformation of the ballast material in the box test simulation concentrated on the corners and sides of the sleeper where ballast particles flew upwards, even on unloading. For the clumps the deformation of the ballast material occurred directly under the sleeper.

Lu and McDowell (2008) remarked that previously the DEM had been successfully used to simulate granular materials with crushable particles by several authors. Despite that, the authors were not aware of any work where the simulation of ballast under a range of confining pressures captured with detail both the deviatoric and the volumetric behaviour. In addition they were unaware of any simulation of triaxial tests on ballast where particle abrasion was considered. To suppress these gaps, they modelled each ballast particle using a clump consisting of ten spheres. Eight smaller spheres were bonded to each clump using contact bonds and parallel bonds (Figure 2.20). The authors remarked that the addition of weak bonded asperities allowed to enhance the particle shear resistance as well as simulate particle abrasion. Monotonic triaxial tests on ballast material were simulated in DEM using the particle definition that was described. By comparison of numerical response and experimental measurements, it was shown that by including bonded asperities, approximately the correct response in terms of shear stress and volumetric strain can be observed.

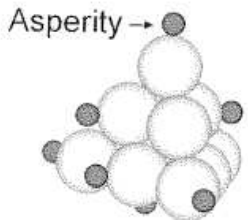

Figure 2.20: Small spheres are added to clumps in order to simulate particle asperities (Lu and McDowell, 2008).

Tutumluer et al. (2009) used the DEM in order to study the effect of gradation on ballast settlement. This numerical method allowed the authors to determine which gradation, of several that were studied, presented least

settlement. Furthermore, the study suggested that the gradations could be improved by employing a minimum particle size of 36 mm which would provide large enough air voids for drainage and minimize the settlement potential of ballast.

It is shown that non-linear ballast modelling in DEM has earned great interest and developments in the past few years. This method allows for a very thorough study of the material behaviour, with the great innovations of allowing to study the inter-particle interaction forces and particle crushing (Lim and McDowell, 2005). In general, good correspondence has been obtained in ballast behaviour with triaxial tests (Lu and McDowell, 2008, Hossain et al., 2007) and box tests (Lim and McDowell, 2005, Lu and McDowell, 2007). Despite these advantages the DEM has a very high computational demand and modelling of DEM ballast in a railway track is mainly confined to a few sleepers (Lobo-Guerrero and Vallejo, 2006, Saussine et al., 2006). The full track-soil system is not yet possible to model with DEM due to limitations in the computational capabilities of current computers.

2.4.3 Non-linear soil modelling

In the context of geotechnical engineering, many numerical material models have been developed in order to simulate soil behaviour for a long range of applications. The many available material models can be used to simulate cohesive or cohensionless materials, account for the no-tension effect and friction failure, and accurately simulate monotonic or cyclic behaviour of soils. Despite the large attention that soil numerical modelling has had for many decades, very seldom has its non-linear response been taken into account in the simulation of railway tracks under high-speed trains.

Hall (2003) achieved good agreement between the measured and calculated responses close to the track in three-dimensional analysis with a FE linear model. The model featured dashpots in the boundaries of the mesh in order to account for outgoing waves. The agreement between the measured and calculated response from the three-dimensional analysis was achieved after a reduction in the soil stiffness directly below the track. This reduction was compliant with the induced shear strain, thus an equivalent linear approach for the soil was used. From the motion orbits calculated in the 3D FE analysis the author suggested that the Rayleigh wave was the dominating wave type outside the embankment.

Banimahd and Woodward (2007) used a non-linear elastic behaviour to model the soil in a 3D FE model to study the speed effect on railway track response and correlate these results with anticipated track maintenance level. According to the study, ballasted tracks with speeds from 50% to 70% of the critical track velocity were classified as high maintenance and those with speeds of 70% of the critical track velocity were associated with the rapid de-

terioration of the railway track and a potential risk of derailment. The study confirmed that the subgrade properties highly influence the critical speed in the track. Also, the study of the non-linear subgrade behaviour showed that it has small influence at low speeds ($\approx 50\,\mathrm{m/s}$), but for increasing speeds it has a substantial effect.

2.4.4 Integrated non-linear modelling

The non-linear consideration of either the track components or subgrade in the track behaviour is in itself seldom done, even more rare are cases in which both the track and subgrade non-linearities are considered simultaneously. One of such examples is the work by Costa et al. (2010) in which the authors applied a linear equivalent method to account for the large strain response of the embankment and the soil in a 2.5D Finite-Infinite Element Method. This approach allowed to obtain a very good simulation of measurements of an experimental case in which it is suspected that the non-linear soil response contributed for very high displacements in the track and soil. The authors also remarked that the error of the predicted displacements in the linear model was directly connected with the train circulation speed: for low speeds the error was neglectable, but for high-speeds the error was very high. The numerical model was also used to predict the response at supercritical speed for which it was found that the linear and linear equivalent models predicted almost the same response. This led the authors to suggest that at these high-speeds the dynamic properties of the soil are closer to those of the small strain range.

2.5 Conclusions

The processes of generation and propagation of waves in railway tracks for high-speed trains are continuously being studied. This chapter presents an overall understanding of the phenomena that occur in a track during the passage of high-speed trains, and the developed methodologies to predict track response. Due to the high standards of high-speed railway tracks, the tools that facilitate predictions of track behaviour are essential for adequate decision making in planning, construction or maintenance of the tracks.

A general description of the components in ballasted railway tracks was prepared initially to provide a better understanding of the study tools, which are later discussed. This description is followed by a general overview of the approaches that are adopted in this study.

A detailed examination of the numerical models was performed to determine which areas are lacking in knowledge and numerical tools; this helped to identify which paths should be pursued for an original contribution. From a numerical point of view, some distinctive methodologies have been de-

veloped and proven that provide an adequate prediction of track and soil vibration levels.

The BE based models allow us to efficiently model soil response and avoid any spurious reflection, these models are usually coupled with different numerical methods that simulate the track. Although 3D FE-BE models may better represent complex geometries, railway track modelling has primarily focused on the more computationally efficient 2.5D models. The researches of Lombaert et al. (2006), Galvín et al. (2010) and Costa et al. (2012), amongst others, have proven that these 2.5D models provide very good predictions of vibrations in the track and soil. The limitations of these models are based on the mandatory assumption of linear behaviour.

FE models within a time domain have been successfully employed to predict track response and, to some extent, soil response. The problem of wave reflection in the limits of the model must be addressed. Although solutions have been developed, the necessity of modelling a considerable part of the soil with finite elements greatly increases the computational costs associated with such models. 2D FE models of plane strain have been predominantly utilised in preliminary simulations. 3D FE models are computationally demanding but have been validated with experimental measurements (Hall, 2003, Araújo, 2011). The advantage of 3D FE models is that geometry complexities, such as the discrete rail-sleeper support in the longitudinal direction of the track, may be included. Because the FEM has been extensively employed in many scientific and engineering applications of non-linear analysis, the possibility of explaining this complex behaviour is one of the main incentives for using FE models. Some authors have modelled non-linear material behaviour in simplified FE track models, but the consideration of non-linear material behaviour in full track models is a concept seldom explored, especially concerning soil non-linearity.

The DEM may be the most accurate model for simulating ballast behaviour; however, simulation of a track stretch remains cost-prohibitive.

The analysis of modern railway track modelling indicates that the study of non-linear track and soil behaviour, especially the latter, during the passage of high-speed trains is a problem that should be further explored. Although analytical methods provide quick solutions for well-defined cases, they do not allow for analyses of complex cases. The numerical models of the BEM only consider linear equivalent simulations, and the DEM is still too computationally expensive to be integrated in a model of the full track. As a result, the FEM is the best method for studying the non-linear response of ballast and subgrade. The study of how non-linear behaviour influences the model results may reveal its importance. In addition, a comprehensive study of how stresses are distributed along the track and soil may provide insight into railway track design to improve vehicle stability or limit costly maintenance. By considering these aspects and without disregarding its limitations, this thesis implements and validates a 3D FE model to model

non-linear subgrade and track behaviour, study the influence of this non-linear consideration and gain knowledge of track and soil responses during the passage of high-speed trains.

Chapter 3

Application of linear railway track modelling

3.1 Introduction

This chapter introduces the application of two common models to simulate railway track response under high-speed trains in linear behaviour: 3D FE models and 2.5D models. The purpose is to broaden the knowledge not only of these two tools, thus gaining insight into the cases for which they present advantages and limitations, but also to further enrich the knowledge of the dynamic phenomenons themselves that are at the heart of the railway track response during the passage of a high-speed train and to validate the 3D FE model that will be later used to study non-linear ballast and subgrade behaviour. The chapter begins by a general overlook of the governing elastodynamics equations that are at the genesis of both formulations, the specific formulations of each modelling technique are further referred in the corresponding sections.

The FE models herein presented are developed using the commercial software Diana (TNO, 2005). A case study is defined for which the track response has been measured and further on, the 3D FE mesh is used to simulate the passage of the high-speed train. Through comparison of numerical and experimental results, the method's accuracy is discussed.

Subsequently, two 2.5D models are studied and discussed. Both models use the BEM to simulate the soil but they differ in the track formulation. One model considers undeformable sleeper and track-soil interface in the transversal plane whereas the other considers deformable track components. The comparisons are used to further enrich knowledge on the dynamics of the tracks and establish deeper knowledge of the 2.5D models, which are latter used to validate the 3D FE model. The 2.5D models herein used are modelled using numerical toolboxes developed for the MATLAB (Mat, 2005) commercial software by the Structural Mechanics Division of the Civil

Engineering Department at the Katholieke Universiteit Leuven. These toolboxes have been validated with field results by the authors and were gently made available to be used in the scope of this thesis in order to obtain better knowledge of the phenomenons and also to serve as validation tools for the FE models.

Finally in a third part of the chapter the 3D FE and 2.5D models are used to simulate study cases and compared with each other. The purpose is to further enrich the knowledge of the dynamic response and also to better understand the advantages and limitations of the FE model. Considering that often experimental measurements are limited in their availability and in location, it is very useful to have a tool such as the 2.5D models, whose numerical accuracy has been previously validated, to judge the numerical accuracy of the 3D FE model. With that purpose, the various components of the soil-track system are initially simulated separately with both models and compared, allowing to better understand the similarities and the differences that the full models exhibit when predicting railway track response.

3.2 Elastodynamics

The governing equations of elastodynamics serve as foundation by which the linear FEM and BEM are developed. It is not the purpose of this thesis to detail the formulations of these numerical methods. However, an overview is provided in order to give a general understanding of both methods.

Considering a domain Ω, occupied by a generic body $\mathcal{B}$, with a boundary Γ, a linear elastodynamic problem is defined on Ω by the linearised strain-displacement relation, the equilibrium equations and the Hooke constitutive equations.

The linearised strain-displacement relation relates the components of the displacement vector $u_i(\mathbf{x}, t)$ and the components of the strain tensor ε_{ij}:

$$\varepsilon_{ij} = \frac{1}{2}(u_{i,j} + u_{j,i}) \tag{3.1}$$

The Hooke law relates the stress σ_{ij} and the strain ε_{kl} through the constitutive tensor D_{ijkl}:

$$\sigma_{ij} = D_{ijkl}\varepsilon_{kl} \tag{3.2}$$

For an elastic, isotropic material the constitutive tensor is given by:

$$D_{ijkl} = \lambda\delta_{ij}\delta_{kl} + \mu(\delta_{ik}\delta_{jl} + \delta_{il}\delta_{jk}) \tag{3.3}$$

where λ and μ are the Lamé coefficients that can be related to the Young's modulus E and Poisson's ratio ν of the material:

$$\lambda = \frac{E\nu}{(1+\nu)(1-2\nu)} \tag{3.4}$$

$$\mu = \frac{E}{2(1+\nu)} \tag{3.5}$$

and δ_{ij} is the Kronecker Delta:

$$\delta_{ij} = \begin{cases} 1, & \text{if } i = j \\ 0, & \text{if } i \neq j \end{cases} \tag{3.6}$$

the constitutive equation then becomes:

$$\sigma_{ij} = \lambda \varepsilon_{kk} \delta_{ij} + 2\mu \varepsilon_{ij} \tag{3.7}$$

The equilibrium equation is given by:

$$\sigma_{ji,j} + \rho b_i = \rho \ddot{u}_i \tag{3.8}$$

where $\ddot{u}_i$ is the second derivative of the displacement with respect to time, ρ is the density of the elastic medium and ρb_i is the body force.

The linear elastodynamic problem is complemented by the initial conditions and the boundary conditions.

The initial conditions specify the displacement and velocity at every point $\mathbf{x}$ of the problem domain Ω:

$$u_i(\mathbf{x}, t = 0) = u_{i0}(\mathbf{x}) \text{ in } \Omega \tag{3.9}$$

$$\dot{u}_i(\mathbf{x}, t = 0) = \dot{u}_{i0}(\mathbf{x}) \text{ in } \Omega \tag{3.10}$$

The boundary conditions specify the components $u_i(t)$ of the displacement vector on a portion Γ_u of the boundary Γ and the components $t_i(t)$ of the stress vector on a portion Γ_t of the boundary Γ:

$$u_i(\mathbf{x}, t) = \overline{u}_i(\mathbf{x}) \text{ on } \Gamma_u \tag{3.11}$$

$$t_i(\mathbf{x}, t) = \overline{t}_i(\mathbf{x}) \text{ on } \Gamma_t \tag{3.12}$$

Using Cauchy's stress formula, the components $t_i(t)$ of the stress vector can be written as a function of the elements σ_{ij} of the stress tensor and the components n_i of the unit outward boundary Γ_t:

$$\sigma_{ji} n_j = \bar{t}_i(\mathbf{x}) \text{ on } \Gamma_t \tag{3.13}$$

The equilibrium equations (3.8) can be defined in terms of the displacement only. These are called the Navier equations and result from introducing the strain-displacement equation (3.1) and the constitutive equation (3.7) in the equilibrium equation (3.8). The resulting Navier equation can be written:

$$(\lambda + \mu) u_{j,ij} + \mu u_{i,jj} + \rho b_i = \rho \ddot{u}_i \tag{3.14}$$

or alternatively:

$$(\lambda + \mu) \nabla \nabla . \mathbf{u} + \mathbf{u} \nabla^2 \mathbf{u} + \rho \mathbf{b} = \rho \ddot{\mathbf{u}} \tag{3.15}$$

The displacement vector $\mathbf{u}$ can be conveniently decomposed into two components, the gradient of a scalar function Φ and the rotor of a vector function $\mathbf{\Psi}$:

$$\mathbf{u} = \nabla \Phi + \nabla \times \mathbf{\Psi} \tag{3.16}$$

Re-writing the Navier equation (3.15) in terms of the decomposed displacement vector (3.16) and further elaborating results:

$$\nabla \left[(\lambda + 2\mu) \nabla^2 \Phi - \rho \ddot{\Phi} \right] + \nabla \times \left[\mu \nabla^2 \mathbf{\Psi} - \rho \ddot{\mathbf{u}} \right] = 0 \tag{3.17}$$

This equation is satisfied if the terms inside the brackets equal 0, thus:

$$(\lambda + 2\mu) \nabla^2 \Phi = \rho \ddot{\Phi} \tag{3.18}$$

$$\mu \nabla^2 \mathbf{\Psi} = \rho \ddot{\mathbf{\Psi}} \tag{3.19}$$

The Helmholtz decomposition expressed by equation (3.16) allowed to obtain the elastodynamics solution expressed as the sum of two complementary responses of the body $\mathcal{B}$. Equation (3.18) represents the propagation of longitudinal or primary waves characterized by the wave velocity:

$$C_{\mathrm{p}} = \sqrt{\frac{\lambda + 2\mu}{\rho}} \tag{3.20}$$

Equation (3.19) represents the propagation of shear or secondary waves characterized by the wave velocity:

$$C_{\mathrm{s}} = \sqrt{\frac{\mu}{\rho}} \tag{3.21}$$

The ratio of primary to secondary wave velocity can be written in terms of the Poisson's ratio only:

$$\frac{C_{\mathrm{s}}}{C_{\mathrm{p}}} = \sqrt{\frac{1 - 2\nu}{2 - 2\nu}} \tag{3.22}$$

3.3 Finite Element modelling of high-speed tracks

3.3.1 Finite Element Method

The FEM is one of the most used computational techniques for the evaluation of boundary value problems. Its application to multiple physical problems, the possibility for dynamical and non-linear problems and the increasing availability of multiple commercial and open-source software have all contributed to its popularity. It is a computational technique that allows to obtain an approximate result for a boundary value problem. A boundary value or field problem is a mathematical problem in which one or two variables must satisfy a differential equation everywhere within a known domain of independent variables and satisfy specific conditions on the boundary of the domain (Hutton, 2004). Depending on the type of physical problem being analysed, the field variables may include physical displacement, temperature, heat flux, and fluid velocity, to name only a few.

Figure 3.1 features a domain Ω in which the field variable $a(\mathbf{x})$ is to be determined at every point $\mathbf{x}$ such that a known governing equation (or equations) is satisfied in every point. The figure also shows a representative FE mesh of the domain, composed of an assembly of 3-node triangular finite elements. The vertices of the triangular elements are the mesh nodes. Nodes are points of the domain where the field variable is explicitly computed. The field variables at non-nodal points of the domain are obtained by interpolation of the solution at the nodes using shape functions. The different elements share nodes where the field variables are computed and that ensures that field continuity is respected between the various elements.

This continuity is also ensured in the non-nodal boundaries of the elements because the interpolation functions of the elements are consistent.

The utilization of several elements to model a domain has two main reasons: to accurately reproduce the geometry of the domain because the utilization of a single element would very inaccurately reproduce the domain's geometry for the vast majority of problems; also to increase the density of mesh nodes, in which the field variables are accurately computed.

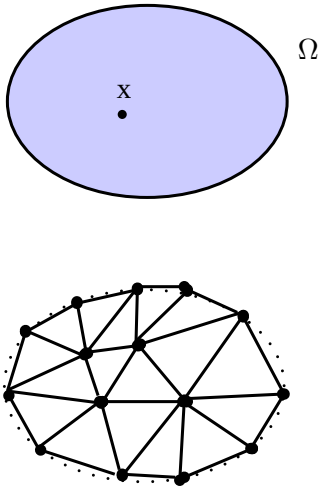

Figure 3.1: General technique of the FEM: a general two-dimensional domain Ω of field variable $a(\mathbf{x})$ (top) and representative FE mesh (bottom).

In the particular case of structural mechanics, the FEM is a very useful tool. Since it relies on a meshing scheme, it allows for the consideration of complex structural geometries and loading conditions, allowing for the determination of the structure's response to a particular solicitation scenario, for example. The method is also applicable to dynamic problems, in which modal analysis, frequency response and time integration analysis are possible.

3.3.2 FEM framework

Weak form of the equilibrium equations

Defining arbitrary scalar functions v_i and $\overline{v}_i$ such that $v_i = 0$ and $\overline{v}_i = 0$ on Γ_u, the equilibrium equations (3.8) and the natural boundary conditions (3.13) can be stated in the following form:

$$v_i \int_{\Omega} \left(\sigma_{ji,j} + \rho b_i - \rho \ddot{u}_i\right)\, d\Omega + \overline{v}_i \int_{\Gamma_t} \left(\sigma_{ji} n_j - \overline{t}_i\right)\, d\Gamma = 0 \tag{3.23}$$

For any v_i and $\overline{v}_i$ the above equation satisfies the equilibrium equations and the natural boundary conditions. Integrating the term $\int_\Omega \sigma_{ji,j} v_i \, d\Omega$ by parts:

$$\int_\Omega \sigma_{ji,j} v_i \, d\Omega = -\int_\Omega \sigma_{ji} v_{i,j} \, d\Omega + \int_\Gamma v_i \sigma_{ji} n_j \, d\Gamma \tag{3.24}$$

allows to write equation (3.23) in a "weak" form:

$$-\int_\Omega \sigma_{ji} v_{i,j} \, d\Omega + \int_\Gamma v_i \sigma_{ji} n_j \, d\Gamma + \int_\Omega v_i \rho b_i \, d\Omega - \int_\Omega \rho \ddot{u}_i v_i \, d\Omega + \overline{v}_i \int_{\Gamma_t} \sigma_{ji} n_j - \overline{t}_i \, d\Gamma = 0 \tag{3.25}$$

Taking $\overline{v}_i = -v_i$ equation (3.25) becomes:

$$-\int_\Omega \sigma_{ji} v_{i,j} \, d\Omega + \int_{\Gamma_u} v_i \sigma_{ji} n_j \, d\Gamma + \int_\Omega v_i \rho b_i d\Omega - \int_\Omega \rho \ddot{u}_i v_i \, d\Omega + \int_{\Gamma_t} v_i \overline{t}_i \, d\Gamma = 0 \tag{3.26}$$

and remembering that $v_i = 0$ on Γ_u the term $\int_{\Gamma_u} v \sigma_{ji} n_j \, d\Gamma$ vanishes:

$$\int_\Omega v_i \rho b_i \, d\Omega + \int_{\Gamma_t} v_i \overline{t}_i \, d\Gamma = \int_\Omega \sigma_{ji} v_{i,j} \, d\Omega + \int_\Omega \rho \ddot{u}_i v_i \, d\Omega \tag{3.27}$$

The "weak form" represented by equation (3.27) is usually referred as the Principle of Virtual Work. The importance of this result to the definition of the FEM and other numerical methods is that the derivatives in the partial differential equations of equilibrium are replaced with equivalent integrals, which are easier to treat numerically.

Finite element interpolation

In a FE discretization of domain Ω, a generic finite element is defined by n_{node} nodes with one interpolation function $N_i^{(e)}(\mathbf{x})$ associated with each node i whose coordinate is $\mathbf{x}^i$. Each interpolation function takes the unity value at $\mathbf{x}^i$ and zero at every other nodes of the element.

For a generic field $a(\mathbf{x})$ defined over the domain Ω^e of the element, its FE interpolation ${}^h a$ over the element is obtained

$${}^h a(\mathbf{x}) = \sum_{n=1}^{n_{node}} a^i N_i^{(e)}(\mathbf{x}) \tag{3.28}$$

where a^i is the value of a at node i.

The generic field $a(\mathbf{x})$ is defined over the entire domain Ω by the discretization of the domain in a mesh of $n_{element}$ elements. In each element the generic field $a(\mathbf{x})$ is interpolated as stated in equation (3.28). The generic field is obtained over the domain Ω:

$$a(\mathbf{x}) = \sum_{n=1}^{n_{point}} a^i N_i(\mathbf{x}) \tag{3.29}$$

where N_i is the global interpolation function of the global node i and n_{point} is the total number of nodal points in the FE mesh. Defining a global interpolation matrix $\mathbf{N}$:

$$\mathbf{N}(\mathbf{x}) = \left[\mathbf{N}_1(\mathbf{x}), \mathbf{N}_2(\mathbf{x}) \; ... \; \mathbf{N}_{n_{point}}(\mathbf{x})\right] \tag{3.30}$$

where $\mathbf{N}_1(\mathbf{x})$ is the diagonal $n_{dim} \times n_{dim}$ matrix:

$$\mathbf{N}_i = \begin{bmatrix} N_i & 0 & ... & 0 \\ 0 & N_i & ... & 0 \\ & & \ddots & \\ 0 & 0 & ... & N_i \end{bmatrix}$$

Any displacement $u(\mathbf{x})$ can be determined

$$u(\mathbf{x}) = \mathbf{N}\mathbf{u} \tag{3.31}$$

where $\mathbf{u}$ is the global vector of nodal displacements. The strain-displacement matrix $\mathbf{B}$ is defined such that

$$\boldsymbol{\varepsilon} = \mathbf{B}\mathbf{u} \tag{3.32}$$

where $\boldsymbol{\varepsilon}$ is the array of engineering strains:

$$\boldsymbol{\varepsilon} = \{\varepsilon_x, \varepsilon_y, \varepsilon_z, \gamma_{xy}, \gamma_{yz}, \gamma_{xz}\}^{\mathrm{T}} \tag{3.33}$$

in three dimensions the strain-displacement matrix $\mathbf{B}$ has the format:

$$\mathbf{B} = \begin{bmatrix} \frac{\partial \mathbf{N}_1}{\partial x} & 0 & 0 & \frac{\partial \mathbf{N}_2}{\partial x} & 0 & 0 & ... & \frac{\partial \mathbf{N}_{n_{point}}}{\partial x} & 0 & 0 \\ 0 & \frac{\partial \mathbf{N}_1}{\partial y} & 0 & 0 & \frac{\partial \mathbf{N}_2}{\partial y} & 0 & ... & 0 & \frac{\partial \mathbf{N}_{n_{point}}}{\partial y} & 0 \\ 0 & 0 & \frac{\partial \mathbf{N}_1}{\partial z} & 0 & 0 & \frac{\partial \mathbf{N}_2}{\partial z} & ... & 0 & 0 & \frac{\partial \mathbf{N}_{n_{point}}}{\partial z} \\ \frac{\partial \mathbf{N}_1}{\partial y} & \frac{\partial \mathbf{N}_1}{\partial x} & 0 & \frac{\partial \mathbf{N}_2}{\partial y} & \frac{\partial \mathbf{N}_2}{\partial x} & 0 & ... & \frac{\partial \mathbf{N}_{n_{point}}}{\partial y} & \frac{\partial \mathbf{N}_{n_{point}}}{\partial x} & 0 \\ \frac{\partial \mathbf{N}_1}{\partial z} & 0 & \frac{\partial \mathbf{N}_1}{\partial x} & \frac{\partial \mathbf{N}_2}{\partial z} & 0 & \frac{\partial \mathbf{N}_2}{\partial x} & ... & \frac{\partial \mathbf{N}_{n_{point}}}{\partial z} & 0 & \frac{\partial \mathbf{N}_{n_{point}}}{\partial x} \\ 0 & \frac{\partial \mathbf{N}_1}{\partial z} & \frac{\partial \mathbf{N}_1}{\partial y} & 0 & \frac{\partial \mathbf{N}_2}{\partial z} & \frac{\partial \mathbf{N}_2}{\partial y} & ... & 0 & \frac{\partial \mathbf{N}_{n_{point}}}{\partial z} & \frac{\partial \mathbf{N}_{n_{point}}}{\partial y} \end{bmatrix}$$

Defining the array of stress components $\boldsymbol{\sigma}$:

$$\boldsymbol{\sigma} = \{\sigma_x, \sigma_y, \sigma_z, \tau_{xy}, \tau_{yz}, \tau_{xz}\}^{\mathrm{T}} \tag{3.34}$$

it can be related with the array of engineering strains $\boldsymbol{\varepsilon}$ by the elasticity matrix $\mathbf{D}$:

$$\boldsymbol{\sigma} = \mathbf{D}\boldsymbol{\varepsilon} \tag{3.35}$$

For isotropic materials the three dimensional elasticity matrix $\mathbf{D}$ takes the form:

$$\mathbf{D} = \begin{bmatrix} \lambda+2\mu & \lambda & \lambda & 0 & 0 & 0 \\ \lambda & \lambda+2\mu & \lambda & 0 & 0 & 0 \\ \lambda & \lambda & \lambda+2\mu & 0 & 0 & 0 \\ 0 & 0 & 0 & \mu & 0 & 0 \\ 0 & 0 & 0 & 0 & \mu & 0 \\ 0 & 0 & 0 & 0 & 0 & \mu \end{bmatrix}$$

Taking the virtual work equation (3.27), writing in matrix notation with the virtual displacements in evidence, it becomes:

$$\mathbf{v}_{\mathrm{i}} \left[\int_\Omega \mathbf{N}^{\mathrm{T}} \rho \mathbf{N} \ddot{\mathbf{u}} \, d\Omega + \int_\Omega \mathbf{B}^{\mathrm{T}} \mathbf{D} \mathbf{B} \mathbf{u} \, d\Omega - \int_{\Gamma_t} \mathbf{N}^{\mathrm{T}} \mathbf{t} \, d\Gamma - \int_\Omega \mathbf{N}^{\mathrm{T}} \mathbf{b} \, d\Omega \right] = 0 \tag{3.36}$$

where $\mathbf{v}_{\mathrm{i}}$ is the virtual displacement and $\ddot{\mathbf{u}}$ is the vector of nodal accelerations. Since the above equation must hold for any virtual displacement, the term inside the brackets must equal 0 and the equation represents a linear system that can be expressed in the form:

$$\mathbf{M}\ddot{\mathbf{u}} + \mathbf{K}\mathbf{u} - \mathbf{f} = 0 \tag{3.37}$$

where:

$$\mathbf{K} = \int_\Omega \mathbf{B}^{\mathrm{T}} \mathbf{D} \mathbf{B} \, d\Omega \tag{3.38}$$

$$\mathbf{f} = \int_\Omega \mathbf{N}^{\mathrm{T}} \mathbf{b} \, d\Omega + \int_{\Gamma_t} \mathbf{N}^{\mathrm{T}} \mathbf{t} \, d\Gamma \tag{3.39}$$

$$\mathbf{M} = \int_\Omega \mathbf{N}^{\mathrm{T}} \rho \mathbf{N} \, d\Omega \tag{3.40}$$

where $\mathbf{K}$ is the global stiffness matrix, $\mathbf{f}$ is the global vector of nodal forces and $\mathbf{M}$ is the mass matrix.

3.3.3 Newmark time integration

The Newmark time integration method is used in the 3D FE time domain response computations. This is one of the most popular time integration schemes in numerical methods. The time integration problem can be summarized as: knowing the displacement u and the velocity $\dot{u}$ at some time t, one wishes to determine the same variables at a slightly different time $t + \Delta t$.

Supposing that the displacement vector $\mathbf{u}(t)$ and velocity vector $\dot{\mathbf{u}}(t)$ are known at time step t and that it is possible to obtain estimates for the acceleration vectors $\ddot{\mathbf{u}}(t)$ and $\ddot{\mathbf{u}}(t + \Delta t)$, the displacement vector $\mathbf{u}(t + \Delta t)$ and velocity $\dot{\mathbf{u}}(t + \Delta t)$ can be estimated with a Taylor series expansion:

$$\mathbf{u}(t + \Delta t) \approx \mathbf{u}(t) + \Delta t\dot{\mathbf{u}}(t) + \frac{\Delta t^2}{2}\left[(1 - \beta_2)\ddot{\mathbf{u}}(t) + \beta_2\ddot{\mathbf{u}}(t + \Delta t)\right] \quad (3.41)$$

$$\dot{\mathbf{u}}(t + \Delta t) \approx \dot{\mathbf{u}}(t) + \Delta t\left[(1 - \beta_1)\ddot{\mathbf{u}}(t) + \beta_1\ddot{\mathbf{u}}(t + \Delta t)\right] \quad (3.42)$$

where β_1 and β_2 are two adjustable parameters that determine the nature of the time integration scheme. For $\beta_1 = \beta_2 = 0$ the displacement vector $\mathbf{u}(t + \Delta t)$ and velocity vector $\dot{\mathbf{u}}(t + \Delta t)$ are evaluated using the acceleration vector at time step t. This is known as an explicit time integration scheme. Alternatively, for $\beta_1 = \beta_2 = 1$ the displacement vector $\mathbf{u}(t+\Delta t)$ and velocity vector $\dot{\mathbf{u}}(t + \Delta t)$ are evaluated using the acceleration vector at time $t + \Delta t$ and the scheme is known as an implicit time integration. Recalling equation (3.37), the accelerations at t are determined:

$$\ddot{\mathbf{u}}(t) = \mathbf{M}^{-1}\left[-\mathbf{K}\mathbf{u}(t) + \mathbf{f}(t)\right] \quad (3.43)$$

then, replacing equation (3.42) into equation (3.37):

$$\begin{aligned}&\mathbf{M}\ddot{\mathbf{u}}(t + \Delta t)\\ &+\mathbf{K}\left\{\mathbf{u}(t) + \Delta t\dot{\mathbf{u}}(t) + \frac{\Delta t^2}{2}\left[(1 - \beta_2)\ddot{\mathbf{u}}(t) + \beta_2\ddot{\mathbf{u}}(t + \Delta t)\right]\right\} - \mathbf{f}(t + \Delta t) = 0\end{aligned} \quad (3.44)$$

which can be re-written as:

$$\begin{aligned}&\mathbf{M}\ddot{\mathbf{u}}(t + \Delta t) + \beta_2\Delta t^2\mathbf{K}\ddot{\mathbf{u}}(t + \Delta t) =\\ &\qquad - \mathbf{K}\left[\mathbf{u}(t) + \Delta t\dot{\mathbf{u}}(t) + \frac{\Delta t^2}{2}(1 - \beta_2)\ddot{\mathbf{u}}(t)\right] + \mathbf{f}(t + \Delta t)\end{aligned} \quad (3.45)$$

the above system of equations can be solved for $\ddot{\mathbf{u}}(t+\Delta t)$. The displacement vector $\mathbf{u}(t + \Delta t)$ and velocity vector $\dot{\mathbf{u}}(t + \Delta t)$ are evaluated using equations (3.41) and (3.42).

3.3.4 Viscous Boundaries

Considering a soil element (Figure 3.2) in which dilatational waves are propagating in the x direction, the equilibrium equation is:

$$\frac{\partial \sigma_{\mathrm{xx}}}{\partial x} + \rho b = \rho \frac{\partial^2 u_{\mathrm{x}}}{\partial t^2} \tag{3.46}$$

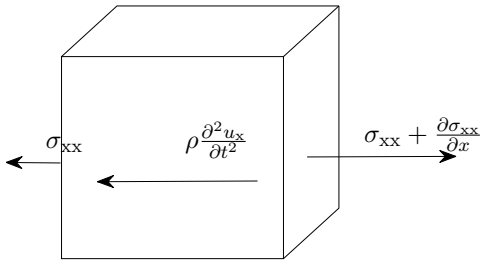

Figure 3.2: Wave propagation through a soil element.

The corresponding Navier equation is:

$$(\lambda + 2\mu)\frac{\partial^2 u_{\mathrm{x}}}{\partial x^2} + \rho b = \rho \frac{\partial^2 u_{\mathrm{x}}}{\partial t^2} \tag{3.47}$$

Neglecting the body forces the equation reduces to:

$$\frac{\partial^2 u_{\mathrm{x}}}{\partial x^2} = \frac{1}{C_{\mathrm{p}}^2}\frac{\partial^2 u_{\mathrm{x}}}{\partial t^2} \tag{3.48}$$

where C_{p} is again the dilatational wave velocity in the material. The solution to the partial differential equation is given by:

$$u_{\mathrm{x}}(x,t) = U\left[\sin(\omega t - \frac{\omega x}{C_{\mathrm{p}}}) + \cos(\omega t - \frac{\omega x}{C_{\mathrm{p}}})\right] \tag{3.49}$$

Differentiating the above equation with respect to t:

$$\dot{u}_{\mathrm{x}}(x,t) = U\omega\left[\cos(\omega t - \frac{\omega x}{C_{\mathrm{p}}}) - \sin(\omega t - \frac{\omega x}{C_{\mathrm{p}}})\right] \tag{3.50}$$

and differentiation the same equation with respect to x:

$$\partial = U\frac{\omega}{C_\mathrm{p}}\left[\cos(\omega t - \frac{\omega x}{C_\mathrm{p}}) - \sin(\omega t - \frac{\omega x}{C_\mathrm{p}})\right] \tag{3.51}$$

Thus, considering (3.50) and (3.51):

$$\frac{-\dot{u}_{\mathrm{x}(x,t)}}{C_\mathrm{p}} = \frac{\partial u_\mathrm{x}}{\partial x} = \varepsilon_{\mathrm{xx}} \tag{3.52}$$

Considering that the stress σ_{xx} is given by:

$$\sigma_{\mathrm{xx}} = (\lambda + 2\mu)\varepsilon_{\mathrm{xx}} \tag{3.53}$$

then:

$$\sigma_{\mathrm{xx}} = -{C_\mathrm{p}}^2\rho\frac{\dot{u}_\mathrm{x}(x,t)}{C_\mathrm{p}} = -\rho C_\mathrm{p}\dot{u}_\mathrm{x} \tag{3.54}$$

Multiplying the stress by the area A of the soil elements, the force is obtained:

$$F_{\mathrm{xx}} = -\rho C_\mathrm{p}\dot{u}_\mathrm{x}A \tag{3.55}$$

From equation (3.55) it is demonstrated that the force in the x direction due to the propagation of dilatational waves is identical to the force by a viscous damper with coefficient $c = \rho C_\mathrm{p}A$. It can be proved in an analogous way that the force due to shear waves propagation is identical to the force of a viscous damper with coefficient $c = \rho C_\mathrm{s}A$. Lysmer and Kuhlemeyer (1969) proposed the introduction of such dampers in the boundaries of the mesh in order to mitigate spurious wave reflection.

This can be achieved in the FE software Diana through the definition of "bounding elements" (TNO, 2005) in the boundaries of the mesh. These consist in the introduction of a set of spring/damper elements in all the nodes that belong to the boundary surface (Figure 3.3).

In each node i the spring/damper element is configured taking into account the area A. The individual spring stiffness is computed by Diana:

$$k = \frac{AE}{l_i} \tag{3.56}$$

where l_i is a characteristic length in one of the local axes directions. The characteristic length is computed from a user-specified parameter α_b:

$$l_i = \frac{1}{\alpha_b} \tag{3.57}$$

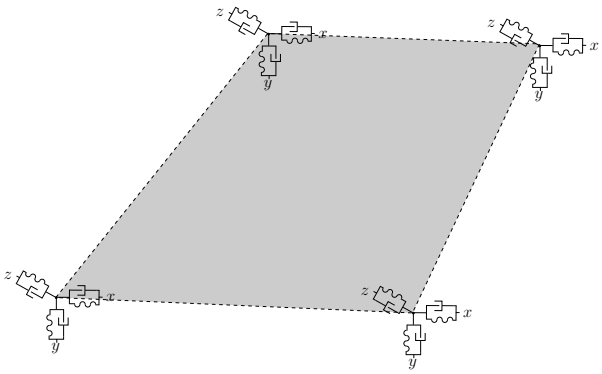

Figure 3.3: Bounding elements on a mesh element.

The damping coefficients are defined by Diana:

$$c = d_i A \tag{3.58}$$

where d_i is a multiplication factor that takes into account the wave velocity to occur at the end of the mesh:

$$d_{xy} = \rho C_s \tag{3.59}$$

$$d_z = \rho C_p \tag{3.60}$$

The "Bounding elements" correspond to the viscous quiet boundaries of Lysmer and Kuhlemeyer (1969) when $\alpha = 0$.

3.3.5 Case study and experimental data

The experimental data herein used to validate the model is obtained from the literature (Degrande and Schillemans, 2001) with material parameters summarized in Table 3.1.

Experimental measurements are a crucial component to understand railway track behaviour as they are the best source of information for the response of the track and the wave propagation to outer zones. Additionally the experimental measurements may be used to calibrate and validate numerical models which may themselves serve as invaluable tools to better understand the phenomenons at work in these study cases. Over the last decade, an effort has been made by several authors (Degrande and Lombaert, 2000, Degrande and Schillemans, 2001, Chebli et al., 2008, Galvín and Domínguez, 2009, Martins et al., 2009, Kouroussis et al., 2011, Costa et al., 2012, Shuangyang et al., 2012) to obtain and share the results of experimental measurements in high-speed tracks providing an increasing database for others to understand the railway track behaviour and/or test their numerical tools.

The experimental data herein used to validate the model is obtained from the literature (Degrande and Schillemans, 2001) with material parameters summarized in Table 3.1.

Table 3.1: Case study properties.

Element	Parameter	Value
Sleeper	E_{sl}	3.0×10^{10} Pa
	ρ_{sl}	2054 Kg/m^3
Rail pad	h_{rp}	1×10^{-2} m
	k_{rp}	1×10^{8} N/m
Rail	A_{r}	7.684×10^{-3} m^2
	I_{r}	3.055×10^{-5} m^4
	ρ_{r}	7800 Kg/m^3
	E_{r}	2.1×10^{11} Pa
Ballast	ρ_{b}	1800 Kg/m^3
	υ_{b}	0.1
	E_{b}	2×10^{8} Pa
	ξ_{b}	0.01
Sub-Ballast	ρ_{sb}	2200 Kg/m^3
	υ_{sb}	0.2
	E_{sb}	3×10^{8} Pa
	ξ_{sb}	0.01
Capping Layer	ρ_{cl}	2200 Kg/m^3
	υ_{cl}	0.2
	E_{cl}	2×10^{8} Pa
	ξ_{cl}	0.01
Soil Layers	ρ_{s}	1850 Kg/m^3
	υ_{s}	0.3
	ξ_{s}	0.03
	h_{s1}	1.4 m
	$C_{p\mathrm{s1}}$	187 m/s
	$C_{s\mathrm{s1}}$	100 m/s
	h_{s2}	1.9 m
	$C_{p\mathrm{s2}}$	249 m/s
	$C_{s\mathrm{s2}}$	133 m/s
	h_{s3}	∞
	$C_{p\mathrm{l3}}$	423 m/s
	$C_{s\mathrm{l3}}$	226 m/s

These data correspond to vibration measurements made during the passage of a Thalys high-speed train at 314 km/h on a track between Brus-

sels and Paris, more precisely near Ath, 55 km south of Brussels. The track is a classical ballasted railway track with continuously welded UIC 60 rails, pre-stressed concrete mono-block sleepers of length $l_{\mathrm{sl}} = 2.5\,\mathrm{m}$, width $b_{\mathrm{sl}} = 0.285\,\mathrm{m}$, height $h_{\mathrm{sl}} = 0.205\,\mathrm{m}$ (under the rail) and mass $m_{\mathrm{sl}} = 300\,\mathrm{kg}$. The flexible rail pads have thickness $h_{\mathrm{rp}} = 0.01\,\mathrm{m}$ and a static stiffness $k_{\mathrm{rp}} = 100\,\mathrm{MN/m}$, for a load varying between 15 and 90 kN. The track is supported by ballast and sub-ballast layers, capping layer and the subgrade.

For the determination of the soil properties many experimental techniques are available, either by in situ testing or by collecting samples for posterior analysis at the laboratory. As the properties of the soil materials depend largely on their condition it is often preferable to perform in situ tests as the laboratory characterizations require that samples are obtained and transported in an undisturbed state which is often not easy to do. From the in situ tests available the SASW test is often used to complement other tests like Cone Penetration Tests (CPT), Standard Penetration Tests (SPT), Seismic Cone Penetration Tests (SCPT), downhole or crosshole methods.

The dynamic soils characteristics for this case study were determined by Degrande and Schillemans (2001) through a Spectral Analysis of Surface Waves (SASW). The basis of this test are the dispersive characteristics of the Rayleigh waves when travelling through a layered medium. In this test, impact solicitations through a hammer or a falling weight are done at a surface point in the soil in order to excite several frequencies. At several distances from this point, also at the soil surface, the vertical soil response is measured using accelerometers or geophones. From these measurements, the theoretical dispersion curve of the soil is obtained, usually through the the Haskell-Thomson approach (Nazarian and Desai, 1993, Yuan and Nazarian, 1993). An inverse problem is then formulated in which the variation of the shear wave velocity with depth is calibrated in a numerical model in order to minimize the error of the numerical dispersion curve of the soil. It should be noted that this is an ill-posed problem which implies that a given experimental dispersion curve may correspond to more than one shear wave velocity profile. From the data obtained in the test it is also possible to obtain the attenuation curve of the soil, solving a similar inverse problem allows to estimate the shear damping profile of the soil.

The main experimental campaign was carried out by measuring the vibrations in the track and soil during the passage of the train. Usually, the measurements in the track are restricted to the rail or most commonly the sleeper, as these are solid, compact elements thus making it easier to fix the measuring instruments. Measurements in the ballast or sub-ballast materials are seldom done because its discrete nature makes it hard to obtain a representative measure of the material response. The soil makes for an easier medium to measure the vibrations, usually these measurements are made at the surface by craving a stake in which the measurement equipment is attached. The measurements in the soil were made at 10 different

distances from the track ranging from a 4 m to 72 m . The location of the measurement points (accelerometers) used for this work is presented in Figure 3.4. The first measurement point is at the sleeper, next to the rail, this allows to obtain the track response to the passage of the train. The second measurement point is located in the soil surface at a horizontal distance of 7.25 m from the rail. As the main purpose of this work is to test modelling accuracy at the track and its vicinity, other measurement points at larger distances from the track are not considered.

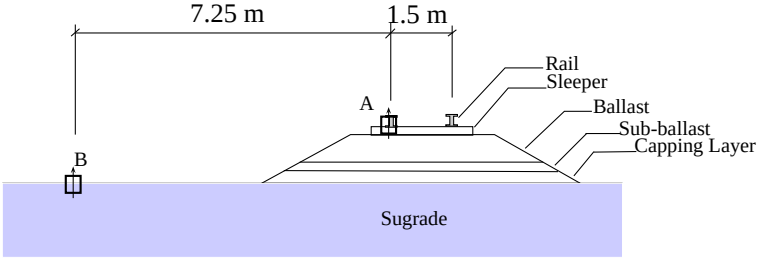

Figure 3.4: Geometry and measurement points of the track.

Figure 3.5 shows the configuration of the Thalys high-speed train consisting of 2 locomotives and 8 carriages. The total length of the train is 200.18 m. The locomotives are supported by 2 bogies and have 4 axles. The carriages next to the locomotives share one bogie with the neighbouring carriage, while the 6 other carriages share both bogies with neighbouring carriages. The total number of bogies is 13 and, consequently, the number of axles on the train is 26.

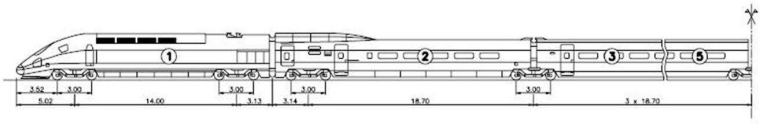

	# carriages	# axles	L_t [m]	L_b [m]	L_a [m]	M_t [kg]
Locomotives	2	4	22.15	14.00	3.00	17000
Side carriages	2	3	21.84	18.70	3.00	14500
Central carriages	6	2	18.70	18.70	3.00	17000

Figure 3.5: Geometry and load characteristics of the Thalys high-speed train (Lombaert et al., 2006).

3.3.6 FE Mesh

The 3D FE mesh is defined in order to simulate the case presented in section 3.3.5. Solid elements of 6 and 8 nodes are used to simulate the subgrade, capping layer, sub-ballast, ballast and sleepers. Each rail pad is simulated as a spring-dashpot duo separated 0.6 m from each other, the rail is modelled with beam elements of 3 nodes. The inferior limit of the model is constrained, the upper limit is unconstrained and the others are assigned with the bounding elements presented in sub-section 3.3.4.

Due to the great number of degrees of freedom involved, the size of the model was kept to a minimum. In this case using a computer with 2 Gb of memory it was noted that at nearly 50.000 mesh nodes there was a threshold where the computational time for each time step was greatly increased. It is assumed that the software uses the memory of the computer to store the matrices of the model but when the memory is not sufficient the software uses the hard drives of the computer where the access to data is much slower and thus the computational time is greatly increased. Because of this an effort was made to keep the model below this threshold. The mesh is achieved by firstly creating a longitudinal module of the track (Figure 3.6.a). This allows to easily change the dimensions and refinement of the mesh. Once the desired module is achieved it is then copied a set number of times until it achieves the intended length (Figure 3.6b).

The dimensions of the FE mesh are: 30 m of track length, 40 m wide and 20 m of soil depth. These depth dimension was used as previous models in FEM have been validated with 20 m of soil depth. Also, the longitudinal length of the model was subject to a parametric study in order to find the minimum length for which the track model is representative.

3.3.7 Simulation of the moving load

The moving quasi-static load is simulated through the definition of stationary loads at the rail nodes with time dependent modulus. Suiker et al. (1998) have demonstrated that the moving load problem can be analysed using the FEM in which the moving load is modelled by a sequence of discrete pulses.

Considering a moving load with constant modulus F, its position $x(t)$ can be computed at any time t provided that the initial position x_0 and the constant speed c are known. At any given time t in which the load is passing at a node of the rail, that node will be solicited by a force of modulus F, and all other nodes will be solicited with loads of modulus 0. At any given time t in which the load is acting in the rail span between two nodes, these will be solicited according to the representation of Figure 3.7.

All nodes are solicited by a force with modulus 0, except those nodes (n_{i-1} and n_i) that limit the span of the rail where the moving load is in-

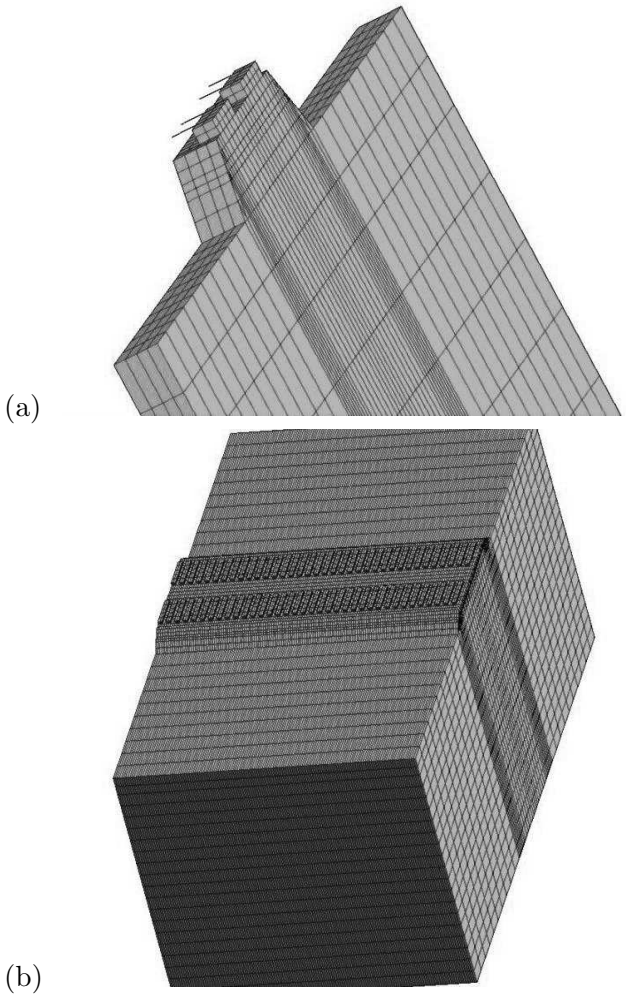

Figure 3.6: FE mesh of the 3D model constructed through copying a a) module to achieve the b) final mesh.

stantly acting. For each of these nodes the instant force applied is inversely proportional to the distance between node and the position of the moving load. Thus for node n_{i-1} the instant force $\mathrm{f}_{i-1}(t)$ is:

$$\mathrm{f}_{i-1}(t) = \left(1 - \frac{x(t)}{l}\right) F \tag{3.61}$$

where $x(t)$ is the distance between node n_{i-1} and the position of the moving load and l is the distance between nodes n_{i-1} and n_i. For node n_1 the instant force $\mathrm{f}_i(t)$ is:

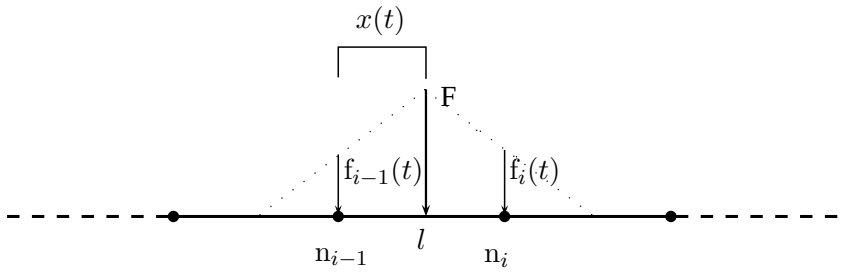

Figure 3.7: Simulation of the moving load with time dependent stationary loads.

$$\mathrm{f}_i(t) = \left(\frac{x(t)}{l}\right) F \tag{3.62}$$

Taking advantage of the linear behaviour of the model, the passage of a single axle with unitary load is computed and the effect of the whole train is determined in post-processing. Araújo (2011) and Hall (2003) have successfully used similar load schemes to simulate moving loads in 3D FE models.

3.3.8 Results discussion

The results obtained from the moving load are processed to represent the response due to the passage of the Thalys high-speed train, taking into account the Thalys axle load, the distance between axles and the circulation speed of 314 km/h. In Figure 3.8 the experimental and numerical vertical accelerations in the sleeper are compared.

The computed response agrees very well with the experimental measurements. The downward accelerations are higher than measurements and the upward accelerations are very well predicted by the 3D FE mesh. Some of the measured peak values are significantly higher than the rest, this is probably explained by some random occurrence in site like the presence of dirt on the rail or an uneven distribution of weight or wheel unevenness more pronounced in those axles. These are obviously unaccounted for in the numerical model, therefore differences occur between some of the computed peak values and the corresponding measurements. The numerical simulation of the response at the track vicinity is also studied (Figure 3.9).

The computational and measurement results agree reasonably well. The upper and downer peak values have similar values although the computed values are much "cleaner" in a sense that the contribution of the axles is still perceptible while the measurements show a cloud of results where the contribution of each set of axles is not noticeable. As Lombaert and Degrande

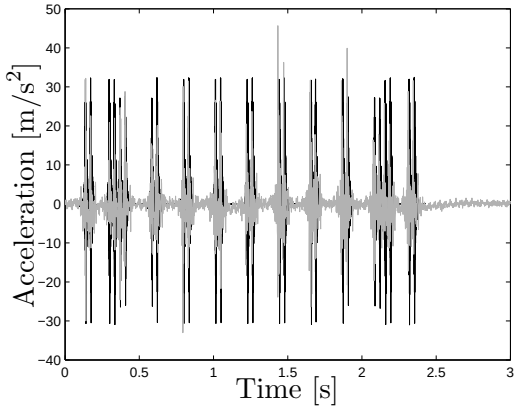

Figure 3.8: Computed (black) and measured (grey) response at measurement point A due to the passage of a Thalys high-speed train at 314 km/h.

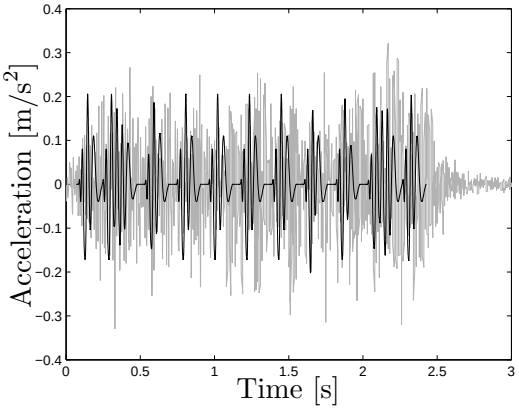

Figure 3.9: Computed (black) and measured (grey) response at measurement point B due to the passage of a Thalys high-speed train at 314 km/h.

(2009) concluded, the quasi-static contribution of the load dominates the track response and the field response is dominated by the dynamic contribution. Therefore, a numerical model, like the 3D FE model presented, that only accounts for the quasi-static contribution is only suited to predict the response in the immediate vicinity of the track. The numerical predictions seem to confirm that since the track response agrees well with experimental results while the response in the soil at 7.25 m from the rail is less accurate.

3.3.9 Partial remarks

3D FE models were presented and a simple case in which the response to the passage of a Thalys high-speed train, at the track and its vicinity, were computed and compared with the experimental measurements.

Taking advantage of the linear elastic properties of the model, only the response to unitary wheel loads was computed and the consideration of a full train passage was calculated in post processing. The loading plan consisted in a pair of loads that solicited both rails and whose application point was time dependent to take into account the train velocity. The computed response at the sleeper agreed very well with the experimental measurements. While still showing some appreciative agreement, the response at the soil was not so accurate. This is explained by the consideration of the quasi-static component of the load.

Due to the many uncertainties related to experimental campaigns and to the limited amount of data that is obtained, experimental results might not always be the best tools to validate in detail the numerical models for all the components of the structure and all distances from the track, as this extensive data is usually not available. To that extend, although the numerical case studied shows some encouraging results, the FE model should be further validated. For that purpose, numerically validated 2.5D models are used in the following. In section 3.4 these 2.5D models are presented and studied and later used to validate the 3D FE model in section 3.5

3.4 2.5D Models

3.4.1 Introduction

In this section two 2.5D models are explored and compared. The aim is to get better knowledge of these validated numerical models and into the track-soil dynamics. This allows for a better understanding of the FE validation in the following section.

The formulation for the soil is similar in both 2.5D models, however, a rigid transversal track model is considered in model A and flexible track model is considered in model B. The comparison is made phase by phase beginning by exploring the soil formulations and explaining the similarities between both models. This is followed by a comparison of the track formulation coupled from the soil, highlighting the major differences in the track dynamics of both formulations. Finally the track-soil coupled systems are compared accounting for the track and the free field responses, in light of the isolated soil and track comparisons, the differences and similarities of the full system responses are discussed.

3.4.2 Direct Stiffness Method

In the 2.5D models used in this work, the soil is simulated through the BEM. The Green's functions are used as fundamental solutions of the BEM and are computed through the DSM. The DSM is based on the solution of the wave propagation in an elastic medium in the frequency-wavenumber domain.

Considering a function formulated in the time-space domain, its frequency-wavenumber domain representation is obtained with a double Fourier transform. A Fourier transform of the time dimension of a function $f(x, y, z, t)$ formulated in the time-space domain determines its frequency domain representation $\hat{f}(x, y, z, \omega)$:

$$\hat{f}(x, y, z, \omega) = \mathcal{F}\left[f(x, y, z, t), \omega\right] = \int_{-\infty}^{\infty} \exp(-i\omega t) f(x, y, z, t) dt. \quad (3.63)$$

Another Fourier transform of one of the spacial dimensions of the function $\hat{f}(x, y, z, \omega)$ determines its frequency-wavenumber representation $\tilde{f}(k_x, y, z, \omega)$:

$$\tilde{f}(k_x, y, z, \omega) = \mathcal{F}\left[\hat{f}(x, y, z, \omega), k_x\right] = \int_{-\infty}^{\infty} \exp(ik_x x) \hat{f}(x, y, z, w) dx. \quad (3.64)$$

The DSM is based on a stiffness matrix formulation proposed by Kausel and Roësset (Kausel and Roësset, 1981). The method relies on an assembly of element matrices similarly to the FEM, but the formulation in the frequency-wavenumber domain allows for the computation of exact solutions of the Navier equations. These exact solutions are used as shape functions in the DSM. Consequently, the simulation of wave propagation in homogeneous layers, half-spaces or full spaces is treated exactly. Each homogeneous medium can be simulated with a single element and there is no need for subdivision as occurs in other methods. For the case of layered media the DSM is restricted to layering in one direction (p.e. an horizontally layered soil).

3.4.3 General solution

The general solution of both models is formulated in a similar way. The dynamic soil-structure interaction problem is decomposed into two subdomains: the structure Ω_b and the semi-infinite layered soil Ω_s. The dynamic soil-structure interaction problem is solved by enforcing continuity of displacements and equilibrium of stresses on the interface Σ_bs between both sub-domains. The section A_b of the structure is invariant with respect to the longitudinal coordinate y. The dynamic soil-structure interaction problem is assumed to be linear and all equations are elaborated in the frequency domain. The invariance of the geometry with respect to the longitudinal

coordinate y allows to perform a Fourier transformation of the coordinate y to the wavenumber k_y. This results in a solution procedure in the frequency-wavenumber domain, where the equations of motion of the coupled track-soil system can be written in the following general form:

$$\left[\tilde{\mathbf{K}}_{\mathrm{bb}}(k_y,\omega)+\tilde{\mathbf{K}}_{\mathrm{s}}(k_y,\omega)\right]\tilde{\mathbf{u}}_{\mathrm{b}}(k_y,\omega) \;=\; \tilde{\mathbf{f}}_{\mathrm{b}}(k_y,\omega) \tag{3.65}$$

where $\tilde{\mathbf{K}}_{\mathrm{bb}}(k_y,\omega)$ and $\tilde{\mathbf{K}}_{\mathrm{s}}(k_y,\omega)$ are the dynamic stiffness matrices of the track and the soil respectively, while $\tilde{\mathbf{u}}_{\mathrm{b}}(k_y,\omega)$ is the track displacement vector and $\tilde{\mathbf{f}}_{\mathrm{b}}(k_y,\omega)$ is the force vector applied to the track. The solution of the track-soil interaction (3.65) provides the soil displacements $\tilde{\mathbf{u}}_{\mathrm{bs}}$ at the track-soil interface, which allows for the computation of the soil tractions $\tilde{\mathbf{t}}_{\mathrm{bs}}(x,k_y,z=0,\omega)$ at this interface:

$$\tilde{\mathbf{t}}_{\mathrm{bs}}(x,k_y,z=0,\omega) \;=\; \tilde{\mathbf{t}}_{\mathrm{bs}}(\mathbf{u}_{\mathrm{bs}}(\mathbf{N}_{\mathrm{bs}}))\tilde{u}_{\mathrm{bs}} \tag{3.66}$$

where $\mathbf{N}_{\mathrm{bs}}$ are the shape functions related to the degrees of freedom $\mathbf{u}_{\mathrm{bs}}$ at the track-soil interface.

The dynamic reciprocity theorem is used for the calculation of the track-soil transfer functions $\tilde{\mathbf{h}}_{zi}(k_y,\omega)$:

$$\tilde{\mathbf{h}}_{zi}(k_y,\omega) \;=\; \int_{\Sigma_{\mathrm{bs}}} \tilde{\mathbf{u}}^{G}_{zi}(x-x',k_y,z,\omega)\tilde{\mathbf{t}}_{\mathrm{bs}}(x',k_y,z'=0,\omega)\,d\Gamma \tag{3.67}$$

where $\tilde{\mathbf{u}}^{G}_{zi}(x-x',k_y,z,\omega)$ are the Green's functions between the BE mesh at the track-soil interface and the receiver locations in the soil.

The dynamic load is obtained using a compliance formulation in the frame of reference that moves with the vehicle (Clouteau et al., 2001), the contact between the axles and the rails is approximated as a point contact. A perfect contact is assumed between the vehicle and the railway track. The displacement vector $\hat{\mathbf{u}}_{\mathrm{a}}(\omega)$ that contains the vehicle displacements at the vehicle-track contact points is equal to:

$$\hat{\mathbf{u}}_{\mathrm{a}}(\omega) \;=\; \hat{\mathbf{u}}_{\mathrm{r}}(\omega)+\hat{\mathbf{u}}_{\mathrm{w}/r}(\omega) \tag{3.68}$$

where $\hat{\mathbf{u}}_{\mathrm{r}}(\omega)$ is the rail displacement and $\hat{\mathbf{u}}_{\mathrm{w}/r}(\omega)$ is the rail unevenness, evaluated at a fixed position in the moving frame of reference.

The vehicle's compliance matrix $\hat{\mathbf{C}}^{\mathrm{v}}(\omega)$ relates the displacements $\hat{\mathbf{u}}_{\mathrm{a}}(\omega)$ to the vehicle-track interaction forces $\hat{\mathbf{g}}_{\mathrm{d}}(\omega)$:

$$\hat{\mathbf{u}}_{a}(\omega) \;=\; -\hat{\mathbf{C}}^{\mathrm{v}}(\omega)\hat{\mathbf{g}}_{\mathrm{d}}(\omega) \tag{3.69}$$

In the case of a longitudinally invariant track, the displacements $\hat{\mathbf{u}}_{\mathrm{r}}$ at the contact points between the vehicle and the track can be calculated in a similar way:

$$\hat{\mathbf{u}}_{\mathrm{r}}(\omega) \;=\; \hat{\mathbf{C}}^{\mathrm{t}}(\omega)\hat{\mathbf{g}}_{d}(\omega) \tag{3.70}$$

The track compliance matrix is computed using the transfer function between forces and displacements on the rail:

$$\hat{\mathbf{C}}^{\mathrm{t}}_{kl}(\omega) = \frac{1}{2\pi}\int_{-\infty}^{+\infty} \tilde{\mathbf{h}}_{zi}(k_y, \omega + k_y v)\exp\left[-ik_y(y_{k0} - y_{l0})\right]\, dk_y \qquad (3.71)$$

Introducing (3.69) and (3.70) in equation (3.68) results:

$$\left[\hat{\mathbf{C}}^{\mathrm{v}}(\omega) + \hat{\mathbf{C}}^{\mathrm{t}}(\omega)\right]\hat{\mathbf{g}}_{\mathrm{d}}(\omega) \quad = \quad -\hat{\mathbf{u}}_{\mathrm{w}/r}(\omega) \qquad (3.72)$$

This equation allows to compute the vehicle-track interaction forces $\hat{\mathbf{g}}_{\mathrm{d}}(\omega)$ from the track unevenness $\hat{\mathbf{u}}_{\mathrm{w}/r}(\omega)$.

The 2.5D models have been presented and validated by the authors and it is not in the scope of this thesis to detail the formulations of these models. The reader may be referred to Lombaert et al. (2006) or Galvín et al. (2010) for more information on the formulations.

Model A

This model has been previously studied and validated by the authors (Lombaert et al., 2006) and is compared with model B. It relies on an analytical formulation of the track (Figure 3.10).

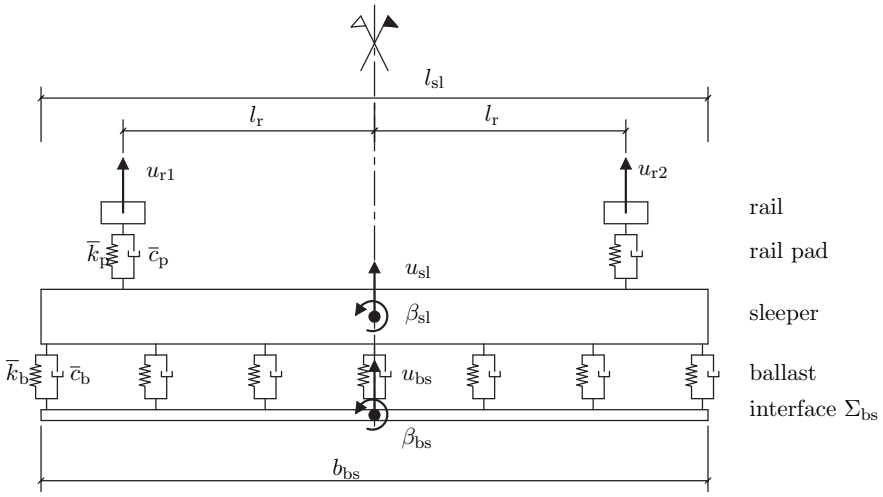

Figure 3.10: Cross section of model A (Lombaert et al., 2006).

The rails are modelled as Euler-Bernoulli beams whose displacements are denoted as $u_{\mathrm{r1}}(y,t)$ and $u_{\mathrm{r2}}(y,t)$. The rail pads are modelled as longitudinally continuous spring-dashpot elements with an equivalent stiffness $\overline{k}_{\mathrm{rp}}$:

$$\overline{k}_{\mathrm{rp}} = \frac{k_{\mathrm{rp}}}{d_{sl}} \tag{3.73}$$

where k_{rp} is the single rail pad stiffness and d_{sl} is the sleeper distance. Similarly, the equivalent damping $\overline{c}_{\mathrm{rp}}$ is obtained:

$$\overline{c}_{\mathrm{rp}} = \frac{c_{\mathrm{rp}}}{d_{sl}} \tag{3.74}$$

where c_{rp} is the single pad damping coefficient.

The sleepers are assumed to be rigid in the transversal plane and thus the displacement of any point along the sleeper is a combination of only two basic motions: displacement u_{sl} at the centre of gravity of the sleeper and rotation β_{sl} about this centre. To account for the fact that the sleepers in the track are not connected with each other, the sleeper elements in the model do not contribute for the longitudinal stiffness of the track and are modelled only as a uniformly distributed mass along the track. The distributed mass $\overline{m}_{\mathrm{sl}}$ per unit length is obtained from the total mass of a single sleeper m_{sl} and the sleeper distance d_{sl}

$$\overline{m}_{\mathrm{sl}} = \frac{m_{\mathrm{sl}}}{d_{sl}} \tag{3.75}$$

The ballast is modelled as a set of distributed, independent linear springs and dampers. The ballast stiffness $\overline{k}_{\mathrm{b}}$ is obtained assuming that only the ballast portion directly below the sleeper contributes for the vertical stiffness of the model:

$$\overline{k}_{\mathrm{b}} = \frac{l_{\mathrm{sl}} b_{\mathrm{sl}} k_{\mathrm{b}}}{d_{sl}} \tag{3.76}$$

where l_{sl} is the sleeper length, b_{sl} is the sleeper width and k_{b} is the ballast stiffness. The ballast viscous damping is accounted for in the ballast impedance $\overline{k}^{*}_{\mathrm{b}}$:

$$\overline{k}^{*}_{\mathrm{b}} = \overline{k}_{\mathrm{b}} + i\omega\overline{c}_{\mathrm{b}} \tag{3.77}$$

The ballast mass is determined in a similar way, accounting for the discrete support of the sleepers and the sleeper length. The width b_{bs} of the track-soil interface is taken equal to the sleeper length l_{sl}.

The track-soil interface is also assumed to be rigid in the transversal plane of the track. Thus, the vertical displacements u_{bs} at the track-soil interface Σ_{bs} are determined as in the sleeper, by the vertical displacement u_{bs} at the centre of the interface and the rotation β_{bs} about this centre.

Only a generalized displacement and rotation of the track-soil interface is allowed. This restriction is imposed on the computation of the soil stiffness matrix:

$$\tilde{\mathbf{K}}_{\mathrm{s}ij}(k_y,\omega) \;=\; \int_{\Sigma} \phi_{\mathrm{bs}i}\tilde{\mathbf{t}}_{sz}(\mathbf{u}_{\mathrm{bs}}(\phi_{\mathrm{bs}j}))\,d\Gamma \tag{3.78}$$

where $\mathbf{u}_{\mathrm{bs}}(\phi_{\mathrm{bs}j})$ is the wavefield in the soil due to an imposed displacement $\phi_{\mathrm{bs}j}$ at the track-soil interface Σ_{bs} in the frequency-wavenumber domain, $\tilde{\mathbf{t}}_{\mathrm{s}z}(\mathbf{u}_{\mathrm{bs}}(\phi_{\mathrm{t}j}))$ is the vertical component of the soil tractions $\tilde{\mathbf{t}}_{\mathrm{s}} = \tilde{\sigma}_{\mathrm{s}}\mathbf{n}$ on a boundary with a unit outward normal $\mathbf{n}$ due to this scattered wavefield $\mathbf{u}_{\mathrm{bs}}(\phi_{\mathrm{bs}j})$. The BEM is used to calculate the soil tractions $\tilde{\mathbf{t}}_{\mathrm{s}z}(\mathbf{u}_{\mathrm{bs}}(\phi_{\mathrm{bs}j}))$ at the track-soil interface, assuming that the track is located at the soil's surface. The BE formulation is based on the boundary integral equations in the frequency-wavenumber domain, using the Green's functions of a horizontally layered soil (Lombaert et al., 2006).

Model B

This model relies on the 2.5D FE formulation in order to represent the ballast of the track. It allows the deformation of the sleeper and track-soil interface providing a wider range of interactions between the track and the soil.

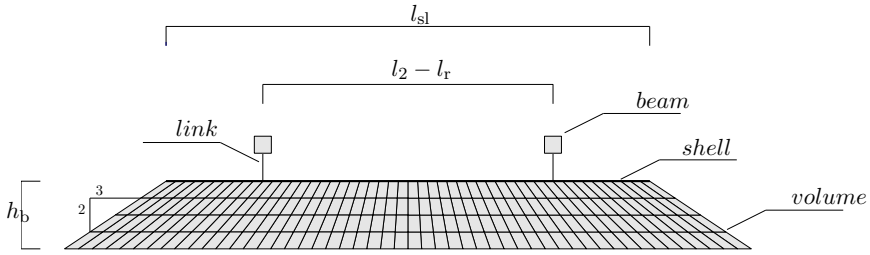

Figure 3.11: Cross section of model B.

The rails and rail pads are modelled with Euler-Bernoulli beams and continuous spring-dashpot elements respectively, as in model A. The sleeper is modelled with 2-node 2.5D shell elements and is considered to contribute to the in plane stiffness of the track only. The equivalent Young's modulus $\overline{E}_{\mathrm{sl}}$ of the sleeper is determined from the original Young's modulus E_{sl}, the width of the sleeper b_{sl} and the distance between sleepers d_{sl}:

$$\overline{E}_{\mathrm{sl}} = \frac{E_{\mathrm{sl}} b_{\mathrm{sl}}}{d_{\mathrm{sl}}} \tag{3.79}$$

The sleeper mass m_{sl} is used to calculate a uniformly distributed mass

$$\overline{m}_{\mathrm{sl}} = \frac{m_{\mathrm{sl}}}{d_{\mathrm{sl}}} \tag{3.80}$$

The ballast is modelled as a mesh of 2.5D 4-node volume elements. The equivalent ballast mass $\overline{m}_{\mathrm{b}}$ in the continuous model is calculated from the part of the ballast that is in contact with the sleepers:

$$\overline{m}_{\mathrm{b}} = \frac{\rho_{\mathrm{b}} h_{\mathrm{b}} l_{\mathrm{sl}} b_{\mathrm{sl}}}{d_{sl}} \tag{3.81}$$

The formulation of the volume finite elements in 2.5D is presented by François et al. (2010).

3.4.4 Case study

Soil profile

The case study relies on a test site, located in Lincent along the track Brussels-Köln. In order to determine the soil layering, two SASW tests (Pyl and Degrande, 2001) and five SCPT (Haegeman, 2001) have been performed. The SCPT tests proposed by Robertson et al. (1986) result from the combined methods of the borehole test and the CPT. A cone penetrometer is pushed into the soil and in usual CPT tests the cone end resistance, the sleeve side friction and the pore pressure are measured. These results are then correlated with the mechanical properties of the soil through empirical relations, analytical or numerical models. The main innovation of the SCPT consisted in adding a geophone in the cone penetrometer and generating a shear wave at the surface of the soil. The time the shear wave takes to reach the geophone is measured and through it the shear wave velocity is determined.

It was found that the site consists of a layer with a thickness of 3.0 m and a shear wave velocity between 150 m/s and 160 m/s and a layer with a shear wave velocity between 250 m/s and 280 m/s (Pyl and Degrande, 2001). Table 3.2 summarizes the dynamic soil characteristics of the site in Lincent.

Table 3.2: Dynamic soil characteristics.

Layer	d	C_{s}	C_{p}	E	ν	ρ	ξ
	[m]	[m/s]	[m/s]	[$\times 10^6$N/m^2]	[-]	[kg/m^3]	[-]
1	3	150	300	120	0.333	2000	0.03
2	∞	280	560	418	0.333	2000	0.03

Track properties

The track in Lincent is a ballasted railway track with UIC 60 rails supported every 0.60 m by concrete mono block sleepers. With very similar characteristics to those presented in sub-section 3.3.5.

The distributed sleeper mass per unit length is $\overline{m}_{\mathrm{sl}}$ equals 500 kg/m. The dynamic stiffness $\overline{k}_{\mathrm{b}}$ and damping $\overline{c}_{\mathrm{b}}$ of the ballast and the equivalent stiffness $\overline{k}_{\mathrm{rp}} = k_{\mathrm{rp}}/d$ and damping $\overline{c}_{\mathrm{rp}} = c_{\mathrm{rp}}/d$ of the rail pad were obtained by Lombaert et al. (2006) by means of a rail receptance test. In this test, an impulse hammer was used to induce an impact load on the track, the rail response was measured and through an optimization procedure, the unknown characteristics were calibrated in the numerical model A in order to minimize the error of the track receptance. The optimized ballast stiffness $\overline{k}_{\mathrm{b}}$ and damping $\overline{c}_{\mathrm{b}}$ corresponded $1534.5 \times 10^6\,\mathrm{N/m^2}$ and $27.7 \times 10^3\,\mathrm{Ns/m^2}$, respectively. The equivalent rail pad stiffness $k_{\mathrm{rp}} = 153.4 \times 10^6\,\mathrm{N/m}$, as for medium to stiff rail pads, and a damping $c_{\mathrm{rp}} = 13.5 \times 10^3\,\mathrm{Ns/m}$ (Lombaert et al., 2006).

The Young's modulus of the ballast in model B is tuned with model A in the 2D static case. The displacement of the rails due to a unitary load in one rail is the comparison parameter. Model A presents a displacement of 3.434×10^{-8}m and 2.374×10^{-8}m for the loaded and not loaded rail respectively. Using this optimization, the Young's modulus in model B is tuned to $128.9 \times 10^6\,\mathrm{N/m^2}$, for which it presents displacements of 3.446×10^{-8}m and 2.353×10^{-8}m.

3.4.5 Models' comparison

Mathematical verification

The two models presented have different kinematics of the track. In both cases a BE formulation is used to determine the dynamic stiffness of the soil. In Model A only the generalized degrees of freedom corresponding to a vertical translation and a rotation of the whole soil-track interface are considered, in model B the shape functions of the degrees of freedom at the interface are used. These models also use different tools for the computation of the soil's stiffness, model A uses Traffic (Lombaert, 2001), while model B uses Bemfun (François et al.). To ensure the consistency of both tools, the Bemfun toolbox is adjusted to compute the stiffness matrix of the soil for the two generalized degrees of freedom. Figure 3.12 shows one term of the dynamic stiffness matrix of the soil. For a comparison in the full wavenumber range, a frequency of 100 Hz is chosen from which the stiffness is compared (Figure 3.12a). The inverse wavenumber transform allows an easier comparison in the frequency range. The results at the load source are indeterminable and the dynamic stiffness is compared at 0.01 m from the source.

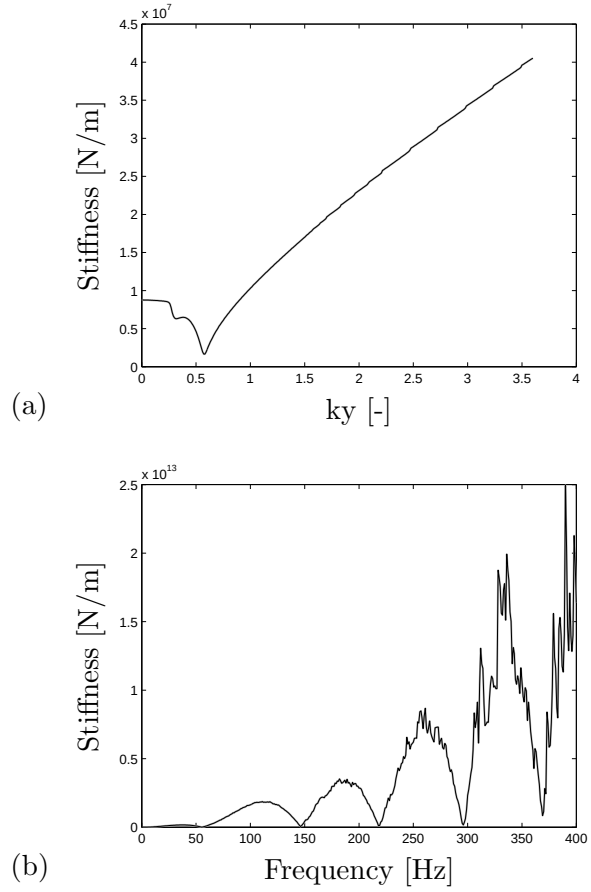

Figure 3.12: One term of the dynamic stiffness matrix of the soil for model A (grey line) and model B (black line) a) in the wavenumber domain at 100 Hz and b) in the frequency domain at 0.01 m from the source.

The dynamic stiffness of both formulations fully matches. This good correspondence is found in the whole wavenumber-frequency range ensuring that both formulations for the soil are numerically equivalent.

Dynamic track behaviour

The track dynamics in model B allows for better insight into ballast behaviour of high-speed train tracks. Attention must be given to how this different track modelling affects the overall behaviour of the track. The comparison with model A allows to perceive how these different approaches affect the final outcome. Taking into account the differences in the track formulations, a thorough comparison and discussion of their respective behaviour is done in the following.

The dispersion curves of both free track models are computed and shown

in Figure 3.13 and Figure 3.14. For model A all 6 modes are shown, these

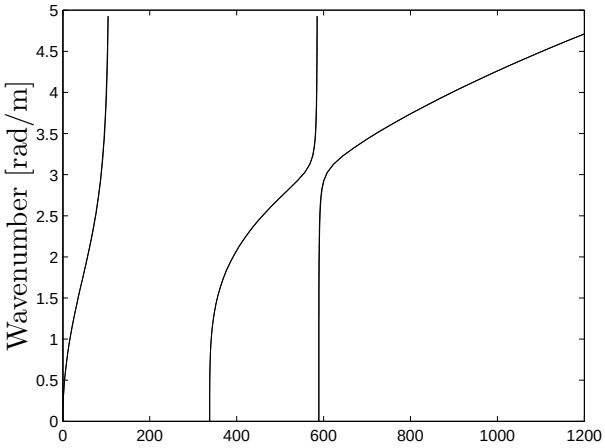

(a)

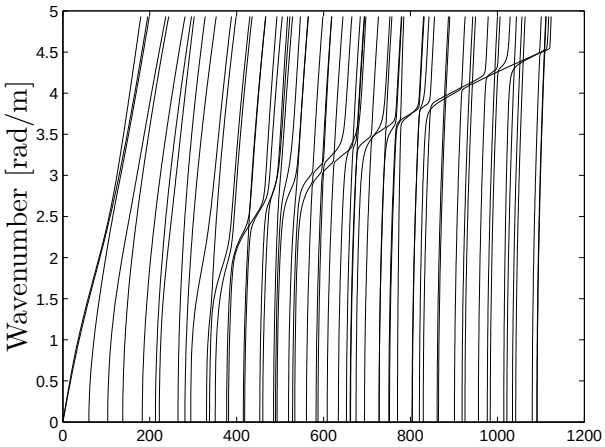

(b)

Figure 3.13: Dispersion curves of the track model of a) model A and b) model B in frequency-wavenumber domain.

are coupled in pairs and each mode is undistinguishable from its pair in the graphical representation. The first pair starts at 0 Hz, the second pair has a cut-on frequency at 338 Hz and the third pair has a cut-on frequency at 589 Hz. For model B the representation is restricted to the first 60 modes due to the large number of degrees of freedom of the track model. This more elaborate model incorporates the kinematics of model A, since the rigid behaviour of the interface and sleeper are specific cases of the flexible behaviour in model B.

The first pair in model A corresponds to the rigid modes, a translation and a rotation of the whole track, with a slight resonance of the rails without

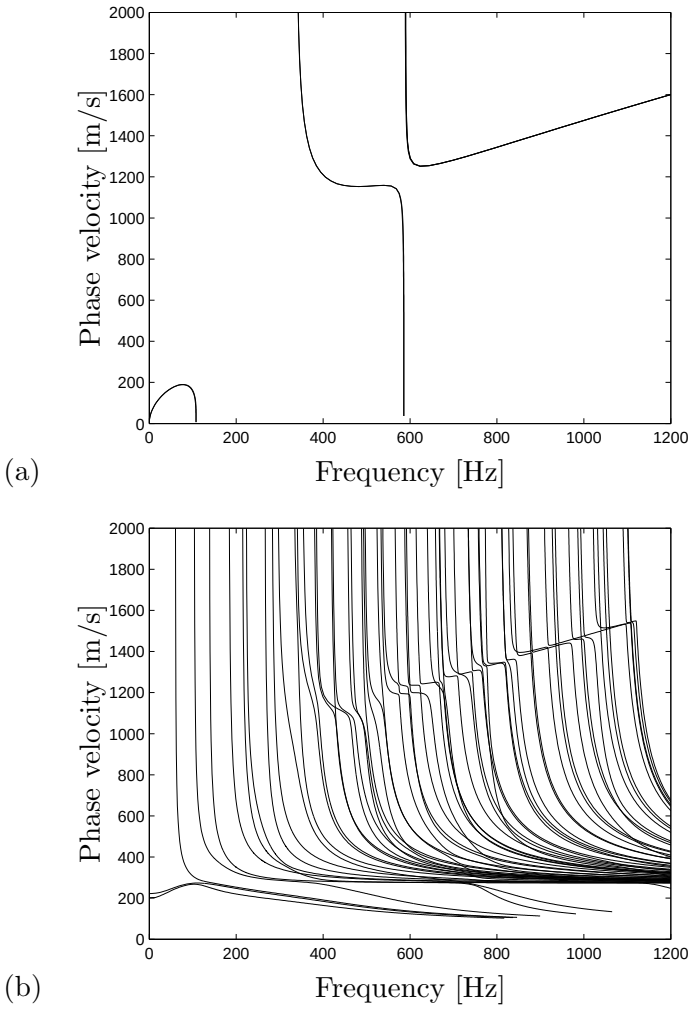

Figure 3.14: Dispersion curves of the track model of a) model A and b) model B in frequency-phase velocity domain.

vertical deformation of the ballast. The first two modes of model B, starting at 0 Hz, are represented in Figure 3.15 and Figure 3.16, the translation and rotation of the track provokes a bending of the ballast and sleeper that is not possible in model A. As the wavenumber increases, so does the bending of the track and thus these modes appear at increasingly distant frequencies.

The second pair of modes in model A corresponds to the in and out of phase resonance of the rails. The resonance frequency of the rail pad and rail is 326.3 Hz at 0 rad/m, considering $f = \sqrt{\bar{k}_{\mathrm{rp}}/\rho A_{\mathrm{r}}}$. The connection with the track makes a frequency shift of the resonance to higher frequency, thus making these modes appear at 338 Hz. These modes are not closely followed by any pair of modes in model B, but by a combination of a bigger

(a)

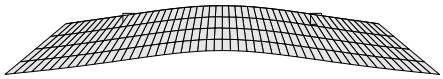

(b)

Figure 3.15: First mode of the track model B at a) 1 rad/m and b) 3 rad/m.

(a)

(b)

Figure 3.16: Second mode of the track model B at a) 1 rad/m and b) 3 rad/m.

number of these. The dispersion curves of the track model A are noticeable as a trend formed by a great number of modes in model B (Figures 3.13 and 3.14)

The third pair of modes in model A corresponds to the resonance of the ballast. The resonance of the free ballast occurs at 578 Hz in the 2D case, the coupling with the rails makes the mode shift to 589 Hz. These

modes have no influence in the model's behaviour since calculations for the trains passage are done at lower frequencies. Again, a combination of several modes in model B includes the dispersion curves of the third pair of modes of model A.

Dynamic track-soil system behaviour

The dynamic stiffness matrices $\tilde{\mathbf{K}}_{\mathrm{s}}$ and $\tilde{\mathbf{K}}_{\mathrm{bb}}$ are assembled and the response of the track-soil coupled system of both models is compared. Figure 3.17 shows the displacement of the rails due to a unitary load equally distributed through both rails at frequencies up to 100 Hz.

The receptance at this frequency range is the same in both cases. This is due to the fact that in the considered frequency-wavenumber range, the response of the model is dominated by the soil. This high receptance occurs mainly due to the dispersion properties of the soil. At low frequencies, the high wavelength reflects the properties of the half-space, and the peak response is obtained for wave velocities close to the shear wave velocity (280 m/s). At higher frequencies, the lower wavelength reflects the properties of the top layer and so the peak response occurs at velocities close to the shear wave velocity of the top layer (150 m/s).

Figure 3.18 presents the rail receptance for a broader frequency range, along with the dispersion curves of each model. The growing influence of the track at higher frequencies is noticeable in both models.

For a better understanding of the tracks behaviour, the soil receptance computed with model A (either model computes the same receptance) is shown in Figure 3.19. The differences with Figure 3.18 are due to the track component. The rail receptance is not considerably affected by the differences in the track models A and B. In both cases, besides the response governed by the soil, peaks of response appear at higher frequencies. The appearance of these peaks does not occur in the soil receptance and are due to the track coupling with the soil. These peaks occur due to the fact that some resonance can occur at the track-soil interface at frequencies where the following equation is valid:

$$l_{\mathrm{bs}}/\lambda = \mathrm{a} + 0.5 \tag{3.82}$$

where l_{bs} is the length of the soil/track interface, λ is the wavelength of the shear wave and a is an integer number.

When $\mathrm{a} + 0.5$ wavelengths fit the soil track interface, the deformation of the soil surface tends to be symmetric, which, combined with the symmetric loading of the rails induces amplification of the response. The combination of the soil and track makes these peaks appear at approximately 105 Hz, 162 Hz, 222 Hz and 283 Hz, for model A and 2 to 10 Hz less for model B. These are similar frequencies to those predicted by equation (3.82) with an interface of 2.5 m: 90 Hz, 150 Hz, 210 Hz, 270 Hz. The kinematics of model B makes

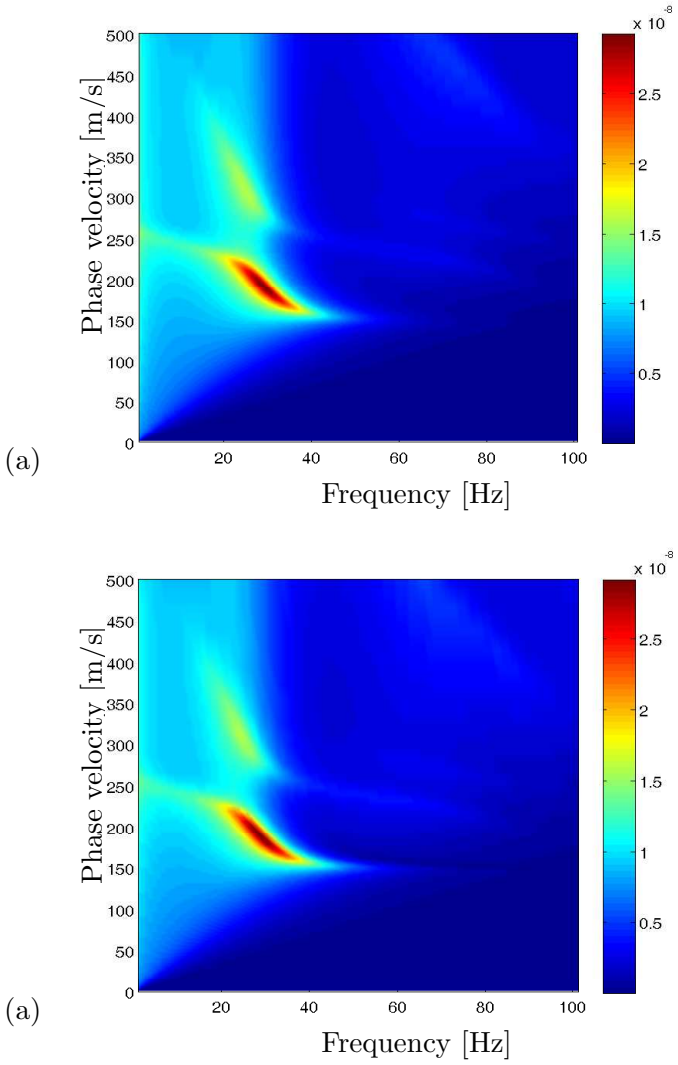

Figure 3.17: Receptance (m/N) of the track-soil coupled system at the rail for a) model A and b) model B.

it flexible, which explains why these peaks are more pronounced and at lower frequencies. An inverse wavenumber transform is used to compute the track receptance from the frequency-wavenumber domain to the frequency domain. Figure 3.20 shows this comparison between both models.

The comparison of the receptance of both formulations in the frequency domain confirms the previous conclusions. First, a higher peak appears due to the soil response that dominates at these lower frequencies. This is followed by a series of lower peaks due to the soil's symmetrical deformation, the last peak occurs due to the rail's resonance at 338 Hz for model A and

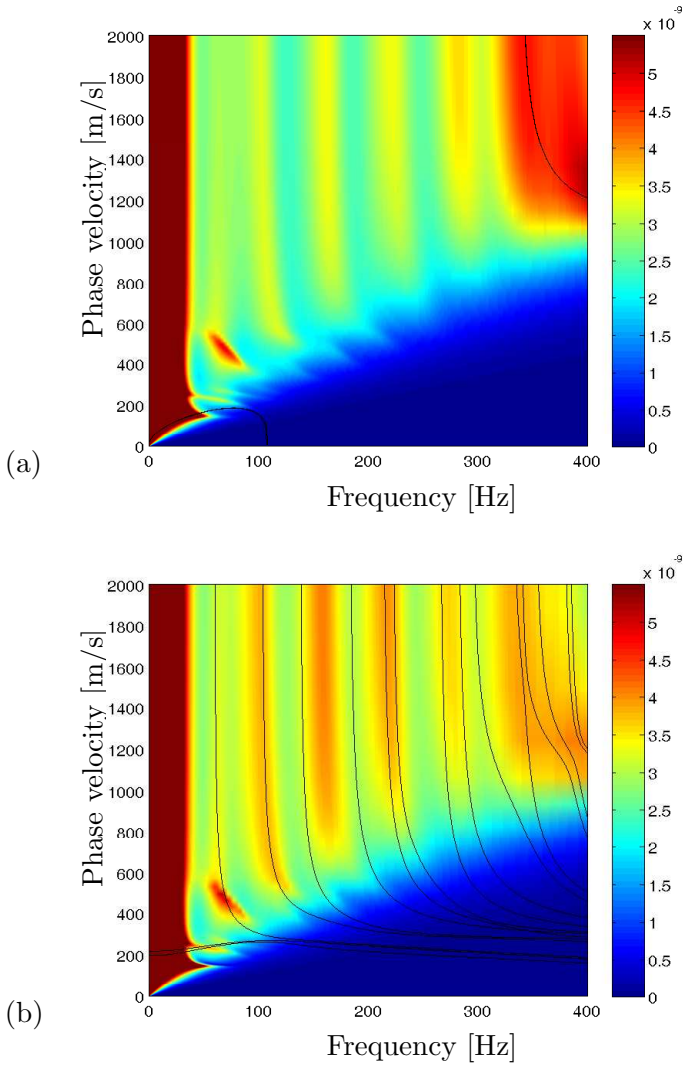

Figure 3.18: Receptance (m/N) and dispersion curves of a) model A and b) model B.

at a wider range of frequencies in model B, thus making this effect more distributed. At lower frequencies, both models behave similarly, due to the fact that the soil response dominates the overall behaviour and the ballast stiffness in model B is tuned to match with the model A in the 2D static case. At higher frequencies, the behaviour of both models differs due to the increased influence of the track kinematics. Model B accounts for wave propagation through the ballast that consequently increases with the frequency. As seen in the comparison of the dispersion curves, different definitions of the interface kinematics leads to different modes of interaction

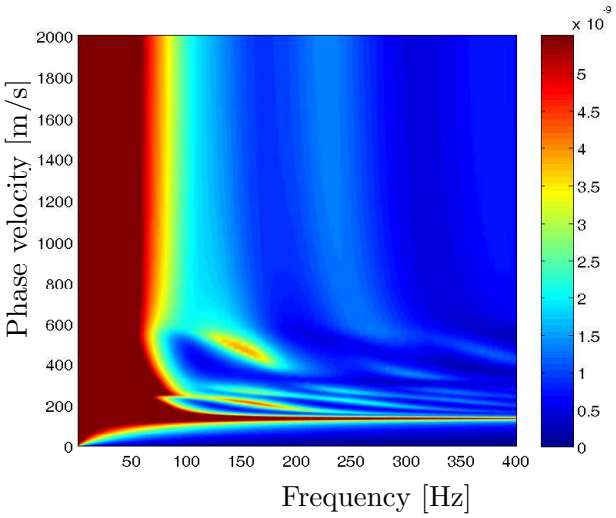

Figure 3.19: Soil receptance (m/N) of both models.

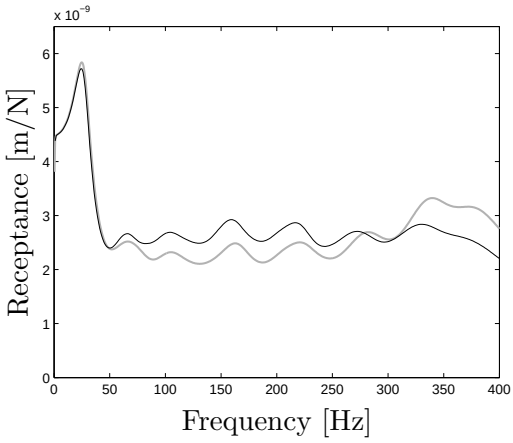

Figure 3.20: Track receptance computed with model A (grey) and model B (black).

between the track and the soil, which are reflected in different receptance values at higher frequencies.

The overall response in both models has good correspondence. At lower frequencies the higher correspondence is a consequence of the tuning and another proof that the soil formulations are consistent. At higher frequencies the receptance is considerably different.

Transfer functions

For the comparison of the free field response of both models, the mobility is compared in the frequency domain at several distances from the track ranging from 8 m to 64 m. Figure 3.21 shows the mobility obtained with both formulations at the considered distances from the track.

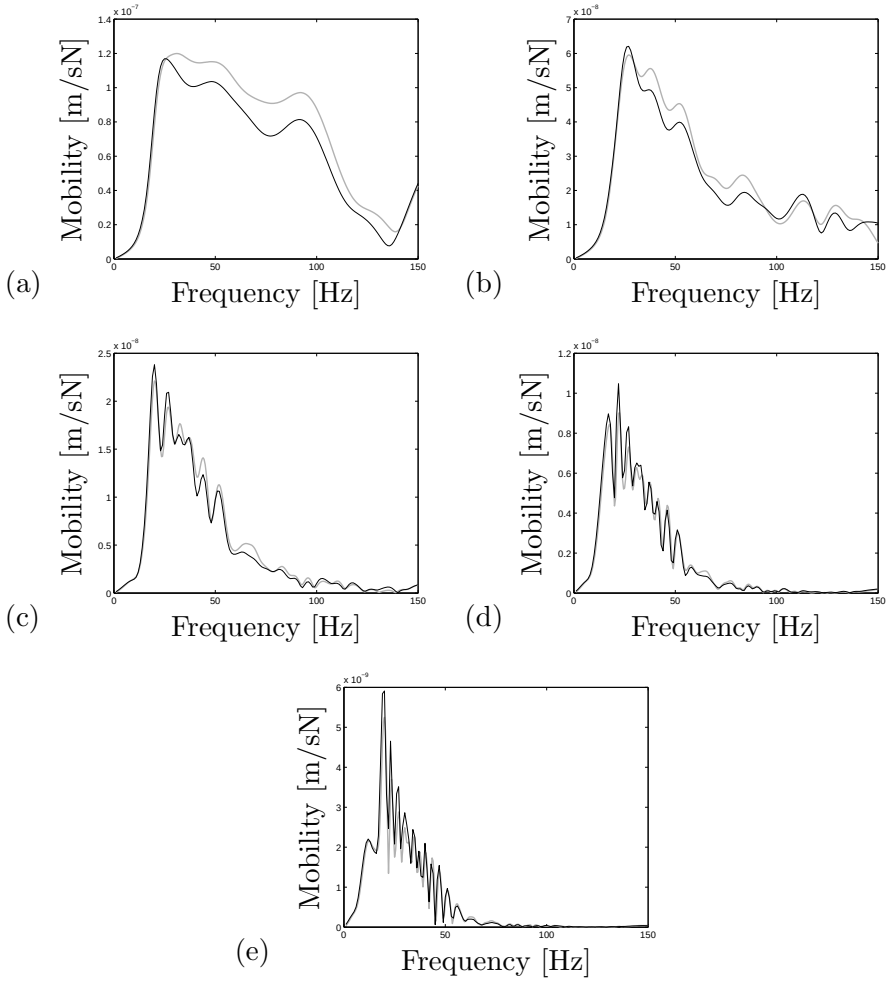

Figure 3.21: Vertical mobility computed with model A (grey) and model B (black) at (a) 8 m, (b) 16 m, (c) 32 m, (d) 48 m, and (e) 64 m.

In both models the frequency range of the mobility is broader at 8 m than at higher distances. At this distance there is a small tendency for a decrease of the mobility with increasing frequency. At 16 m this tendency is higher although the frequency range of the mobility is still broad. As the distance to the track increases, the frequency content of the mobility becomes more concentrated at a frequency range between 10 Hz and 50 Hz and the peak mobility at around 20 Hz. The reason for this is that at

higher distances the soil works as a natural filter for higher frequencies and the mobility concentrates on low frequencies where the models shows good correspondence.

Although showing a general accordance, the trend is that model B underestimates the mobility at closer distances, especially at a frequency range between 25 Hz and 50 Hz. At lower frequencies there is a very good agreement. The differences in the mobility predicted by both models are explained by the tractions at the interface. Figure 3.22 shows the tractions at the track-soil interface in both models at the frequency of 100 Hz. This ex-

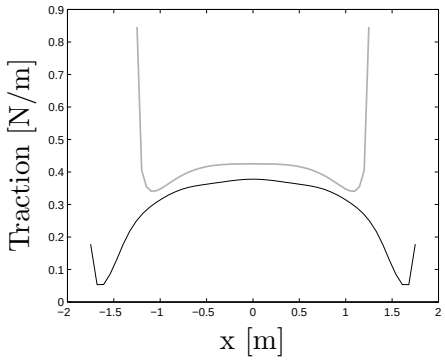

Figure 3.22: Tractions at the interface at 100 Hz and $y = 0.01$ m computed with model A (grey line) and model B (black line).

emplifies how the distribution of the tractions is done through the interface in both cases. The stiff interface of model A implies a more regular distribution of the tractions through its length with higher values at the centre, and a great disparity of the tractions at the extremities of the interface. This is reminiscent of the stress distribution in the soil for strip foundations found in the theory of soil mechanics and geotechnical engineering. In model B the interface is longer allowing a bigger distribution of the tractions. The possibility to deform the interface allows for more localized traction concentration provoking a bigger traction variation along its length. The extremities of the interface are not localized directly below the sleeper and are subject to much less tractions than in model A.

These differences in the track-soil interaction explain the differences in the track mobility in both models.

Free field vibrations

As the final goal of these models is to simulate the effects of the passage of a high-speed train, the final comparison between the models incorporates a full run to check the influence that the identified differences have in the free field results. The simulation adopted is the passage of a Thalys high-speed

train at 300 km/h. The track compliance is computed for both models and compared in Figure 3.23.

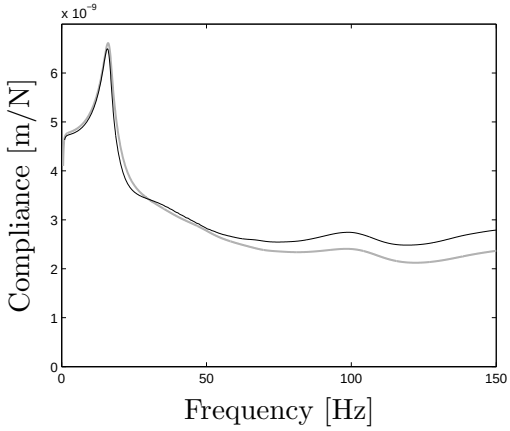

Figure 3.23: Track compliance computed with model A (grey line) and model B (black line) at the first axle .

The compliance of the track is very close in both models for the diagonal elements (track displacement at a point due to a load in the same point). The good correspondence is consistent with that of the track receptance, with higher correspondence at low frequencies.

Using a randomly generated rail unevenness, the frequency content of the dynamic moving load is determined. Figure 3.24 shows the one-third octave band Root Mean Square (RMS) spectra of the dynamic load in both models. The dynamic axle loads computed with both models are very near

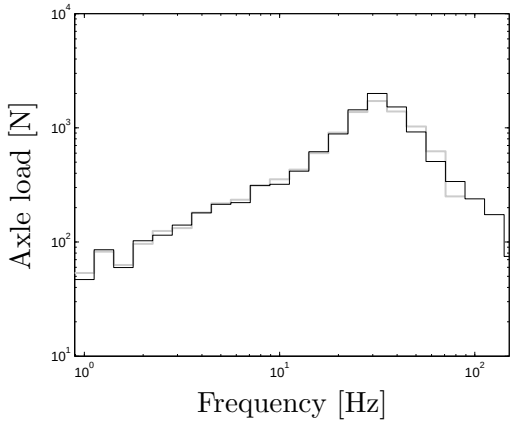

Figure 3.24: One-third octave band RMS spectra of the dynamic load of the first axle in model A (grey) and model B (black).

through the whole frequency range, again the best fit occurs at up to 25 Hz.

Some noticeable yet acceptable differences occur from 60 Hz onward, which is consistent with the comparison of the track compliance in Figure 3.23.

Afterwards, the response to the passage of the Thalys high-speed train is computed using both models. The vertical velocities in the soil at several distances from the track are compared in Figure 3.25 and Figure 3.26.

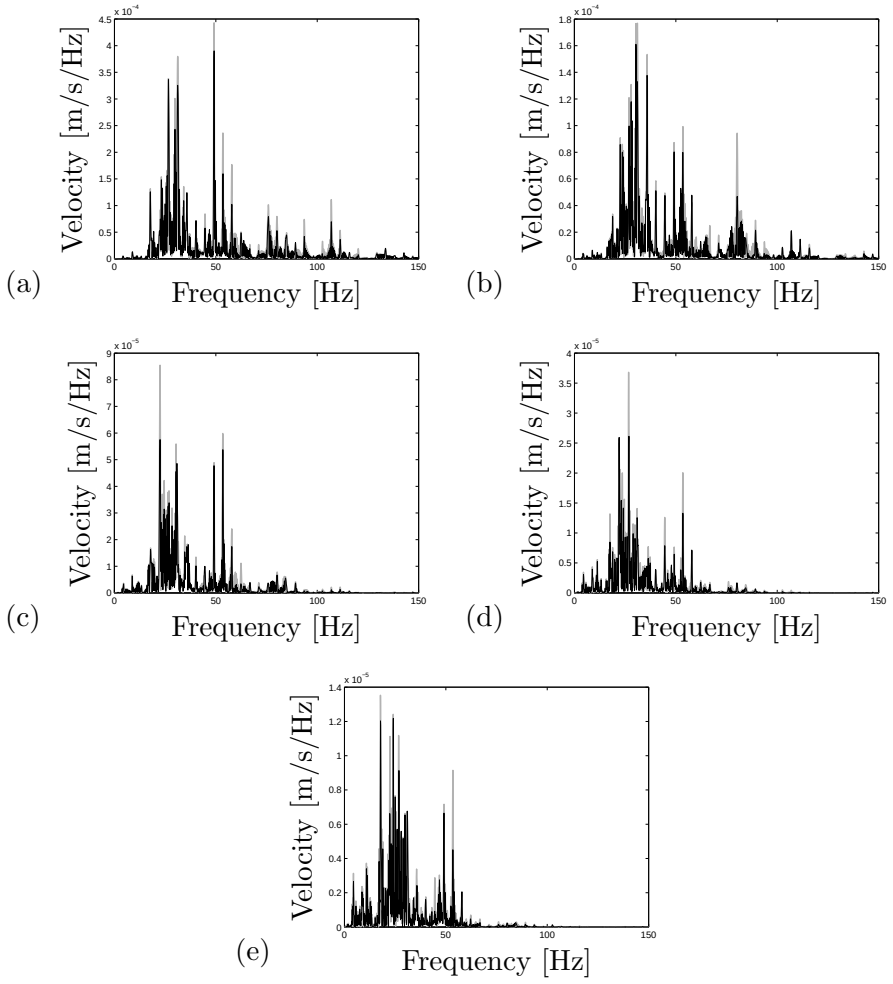

Figure 3.25: Frequency content of the vertical velocity in the free field computed with model A (grey) and model B (black) at (a) 8 m, (b) 16 m, (c) 32 m, (d) 48 m, and (e) 64 m from the track.

The overall trend of the response in the frequency domain is not much different than the mobility analysis, i.e. an increasing shift to lower frequencies as the distance from the track increases. The models behave alike in the sense that they show peaks at the same frequencies, although these might show slightly different peak values. Model B tends to underestimate the peak values of the response. This happens at all distances from the track.

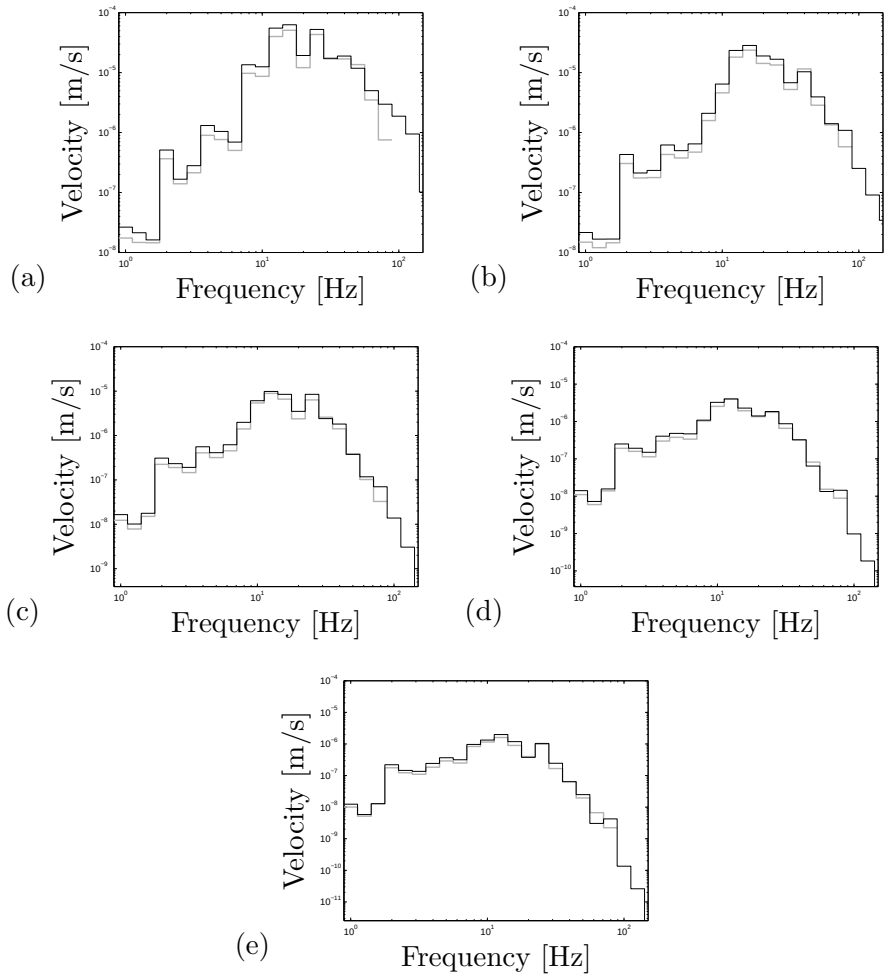

Figure 3.26: One-third octave band RMS spectra of the vertical velocity in the free field computed with model A (grey) and model B (black) at (a) 8 m, (b) 16 m, (c) 32 m, (d) 48 m, and (e) 64 m from the track.

Besides these peaks, the computed response is very similar in both cases. The one-third octave band RMS spectra of the response shows a very good agreement between both models at all distances (Figure 3.26).

Finally the time response at the receptance points and the RMS over a 4 s window is shown in Figure 3.27 and Figure 3.28 respectively. The velocities tend naturally to decrease with the distance to the track due to geometric and material damping. The response in Model B tends be lower than in model A which can be explained by the lower tractions at the soil-track interface.

The general trend is that both models behave similarly, especially at low frequencies where the soil dominates the response. Some small differences do

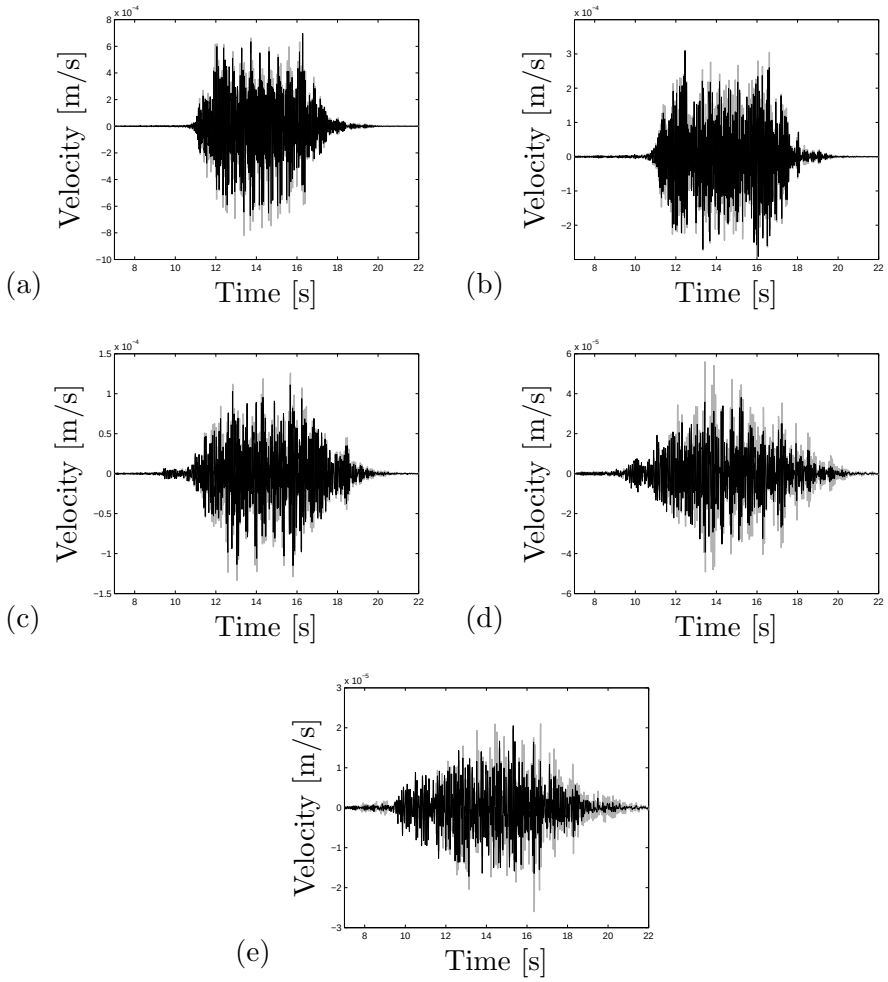

Figure 3.27: Time history of the vertical velocity in the free field computed with model A (grey) and model B (black) at (a) 8 m, (b) 16 m, (c) 32 m, (d) 48 m, and (e) 64 m from the track.

occur due to the different soil-track interaction especially at high frequencies. Galvín et al. (2010) reached similar results, also comparing 2.5D models featuring stiff and flexible track-soil interface. The authors stated that the models corresponded very well at low frequencies. At high frequencies the study presented higher differences between the models than those herein found. However, the comparison by Galvín et al. (2010) was done for a case of a double tracked embankment where there is no load symmetry and thus the influence of the track deformability is higher.

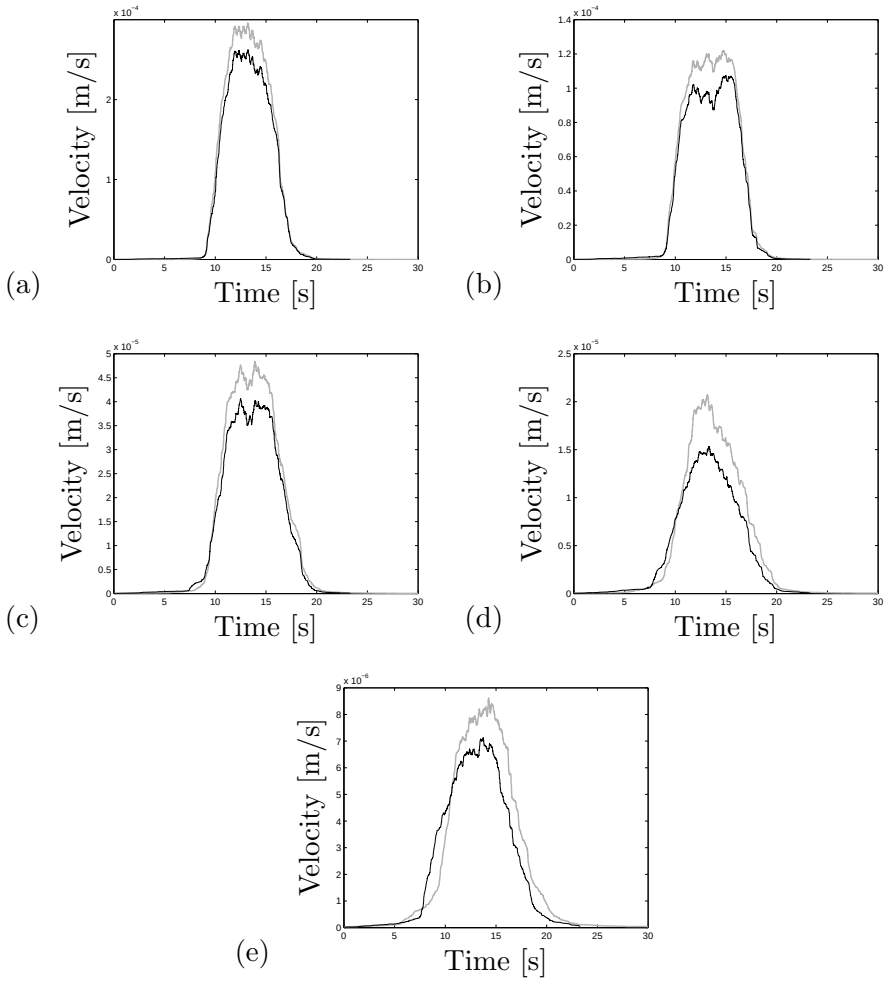

Figure 3.28: Running RMS of the vertical velocity in the free field computed with model A (grey) and model B (black) at (a) 8 m, (b) 16 m, (c) 32 m, (d) 48 m, and (e) 64 m from the track.

3.4.6 Partial remarks

The comparison between two 2.5D models was presented in this section. The formulation common to both models was presented as well as the specific characteristics of each. The two models differ in the track's kinematics.

The mathematical verification of the soil formulations was done by changing the formulation of model B into a formulation similar of the one in model A. The values of the soil stiffness are numerically equal proving the coherence of the formulations. The comparison between both track models done through their dispersion curves showed that their behaviour at low frequencies is very similar and the kinematics of the model A are shown to be a specific case of the more general model B. There is a very good cor-

respondence of the full models response at those low frequencies where the response is governed mainly by the soil. The receptance of the models at higher frequencies shows higher differences because it is influenced by the track-soil interface and by the resonance of the rails.

The differences at the track-soil interfaces result in different distribution of tractions along the interfaces. Model A has a stress distribution similar to that of the stiff foundations which results in high tractions at the edges. Model B allows deformation of the track-soil interface and has lower tractions along all its length. These differences result in slightly different transfer functions between the track and the soil.

The track compliance is computed for both models using the rail receptance. The compliance differences are coherent with those found in the track receptance, with better correspondence at lower frequencies. The dynamic axle loads due to the passage of a Thalys high-speed train at 300 km/h were computed using the compliance of models A and B and show very good correspondence. The response in the free field due to the dynamic loads although not exactly the same is very consistent, both in the frequency and time domain. RMS values revealed very good agreement of the results.

The different track formulations are shown to have influence in the results obtained by the models, although these are not major differences. Model A is much less computationally expensive due to the reduced number of degrees of freedom. Model B allows for a better insight into ballast behaviour and track-soil interactions. For the determination of the rail response and free field vibration, both models compute similar results.

Throughout the analyses herein presented a better insight into these models and the dynamics of the track-soil system were obtained. These 2.5D models are used in the following to study the accuracy of 3D FE models.

3.5 Comparison between 3D FE and 2.5D models

3.5.1 Introduction

In the scope of the final objective of incorporating non-linear subgrade and ballast modelling in the rail track response simulations, it is necessary to further validate the FE models. In section 3.3.1 the FE model was successfully used to reproduce track response to the passage of a high speed train, however, experimental results are often scarce and a thorough exploration of the model's accuracy using only experimental measurements is limited. Because of this, the 3D FE and the 2.5D FE models explored in the previous section are herein compared. The 2.5D model A that has been thoroughly developed and validated at K.U. Leuven allows to perform a more thorough examination of the FE model's numerical accuracy. With that purpose, the various components of the soil-track system are initially analysed separately which allows to better understand the similarities and the differences that the full models exhibit when predicting railway track response. Finally the track response to a moving load is simulated in both cases and compared.

3.5.2 Computation of Green's functions

Axisymmetric FE Green's functions

In a first instance, the computation of the FE 3D Green's functions is done in the frequency domain, allowing a direct comparison with the frequency domain Green's functions of the DSM. The soil is modelled as a semi-infinite homogeneous layered half space whose dynamic properties are represented in Table 3.3. The solicitation is a vertical load on the soil surface and the response is observed at several distances from the load, also at the soil surface. Due to the homogeneity of the soil, the response to the vertical load is axisymmetric with respect to the vertical axis that includes the load point.

The Green's functions computed with the DSM are obtained using the elastodynamics toolbox EDT (Schevenels et al., 2008). This toolbox has been extensively used by the authors in didactic and research environments to compute the elastodynamics response of infinite or semi-infinite media.

Table 3.3: Soil profile adopted for the simulation of the half-space

Layer	d [m]	C_s [m/s]	C_p [m/s]	ρ [kg/m^3]	ξ_s	ξ_p
1	3	150	300	2000	0.03	0.03
2	∞	280	560	2000	0.03	0.03

The FE model is created with axissymmetry, which allows a reduction of the mesh to 2D and a consequent reduction in the computational cost. This enables the consideration of a FE mesh with small element size. The upper FE mesh is represented in Figure 3.29 where two zones in the horizontal direction x are distinguished. The first zone comprises the load point and its vicinity up to 15 m of distance in which the horizontal element size is 0.1667 m. The second zone expands the model 60 m in the horizontal direction up to a total of 75 m and the horizontal element size in this zone is 0.667 m. The aim of this second zone far from the load point is to provide improved accuracy at low frequencies. The total mesh size in the vertical y direction is 50 m anticipating that this is a sufficient depth to simulate with good accuracy the half-space, on the bottom the nodes of the mesh are clamped in the vertical y direction.

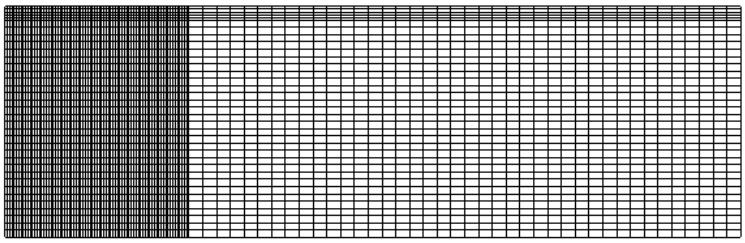

Figure 3.29: 2D mesh of the FE axisymmetric model of the soil.

The FE response is computed in the frequency domain considering hysteretic damping. Figure 3.30 compares the Green's functions obtained with the FE axisymmetric and DSM models. Since the purpose of the FE model is to obtain an accurate prediction of the response in the track and its vicinity, the comparisons are restricted to distances of 2 m, 4 m and 8 m from the source load.

The agreement between the models is very good. At low frequencies, the differences are very small and occur due to the limited mesh size of the FE model in the horizontal x direction. In the frequency range of $20 - 100$ Hz, the best agreement between both models is obtained, with the curves overlapping on most of this range. At high frequencies there are some disturbances in the axisymmetric model due to the the element size. From this observation it is proved that the FEM can be used to accurately simulate the dynamic soil response if a sufficiently large and detailed mesh is used.

Simplifications on the size and mesh discretization of the FE model are done in order to perceive if computational effort can be reduced without compromising the results. In the Green's functions obtained with the DSM it is considered that the second soil layer has an infinite thickness. This consideration can be done in the DSM with an accurate simulation of the

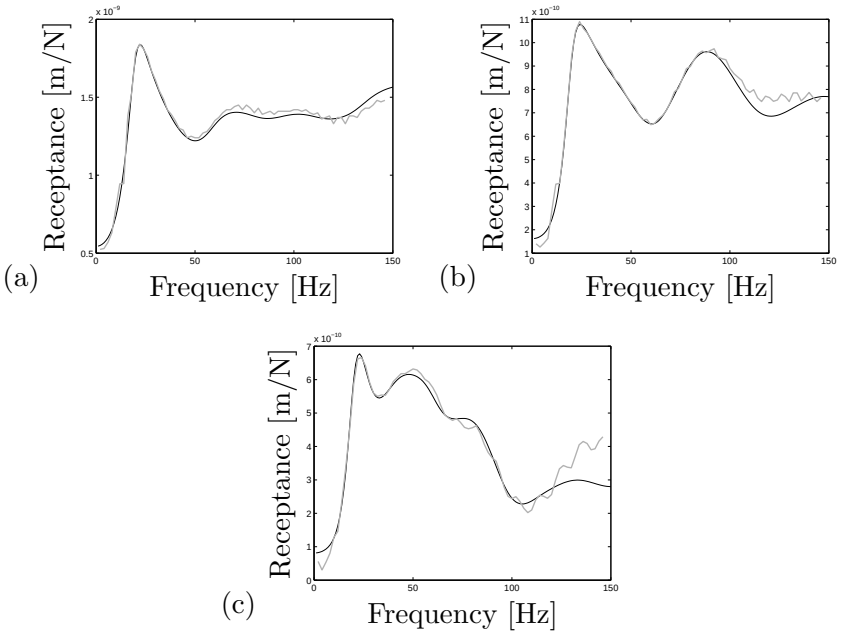

Figure 3.30: Comparison of the Green's functions computed in FE (grey) and DSM (black) at the soil surface a) 2 m, b) 4 m and c) 8 m from the source load.

soil stiffness and of the propagation of waves into infinity. In the FE models that is not possible and a lower limit is considered at 50 m of depth. From the soil response it is concluded that the consideration of 50 m of soil depth in the FE model ensures a good simulation of the soil response at the surface.

To study the influence of the depth of the FE mesh in the surface response, the Green's functions of the aforementioned mesh are compared with those obtained with a similar mesh where the full depth is reduced to 10 m and another mesh where the total depth is reduced to 5 m. Figure 4.57 compares the response of FE axisymmetric models representing the same soil profile, with the same element size but different mesh depth.

The reduction from 50 m to 10 m of depth results in some differences in the computed Green's functions, especially at low frequencies at which the wavelength is larger. These, however, are small differences and generally the model is still accurately representative of the soil behaviour. The reduction to 5 m has a more profound impact in the results, again with special differences at low frequencies.

A study is also done to perceive the influence of the mesh length in the horizontal x direction. The mesh of the axisymmetric model with 10 m of depth has a zone of 15 m of length and beyond that a second zone of 60 m. This second (outer) zone is reduced to 30 m and 20 m, while the zone in the vicinity of the load point is kept unchanged. The Green's functions are

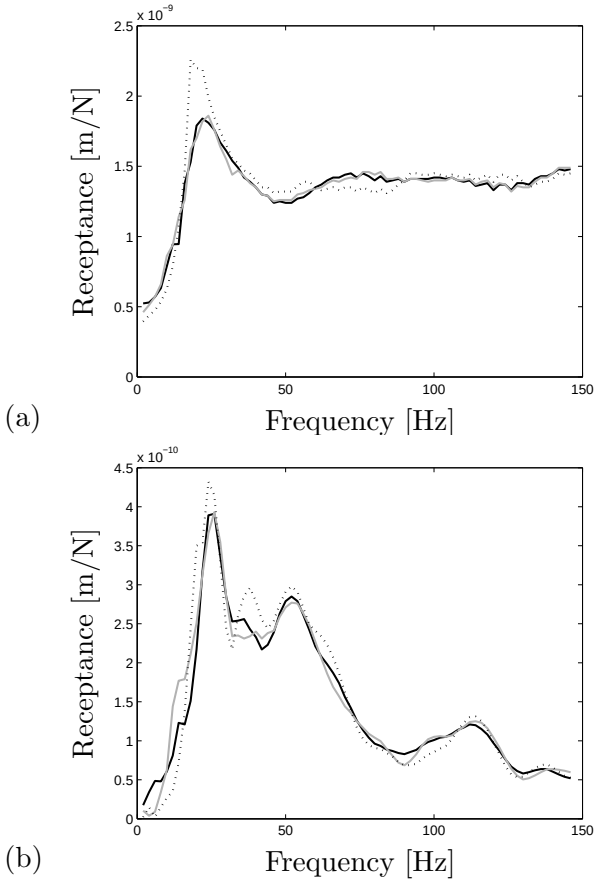

Figure 3.31: Comparison of the Green's functions computed with FE models with 50 m (black), 10 m (grey) and 5 m(doted) of depth at a) 2 m and b) 16 m from the source.

then computed. The results are compared in Figure 3.32.

When the total length of the mesh is reduced to 45 m, some noticeable changes occur in the model response at low frequencies. Even though, considering the fact that the number of elements was greatly reduced, the correspondence between the model with 45 m and the model with 75 m is appreciable. The model with a total length of 35 m presents less agreement with the previous models. It should be noticed that despite the differences that occur at low frequencies, the response of the various models at high frequencies is almost the same. Thus it can be concluded that an "outer zone" with larger element size in the horizontal direction can improve the model response at low frequencies, and has very limited influence in the mesh response at high frequencies.

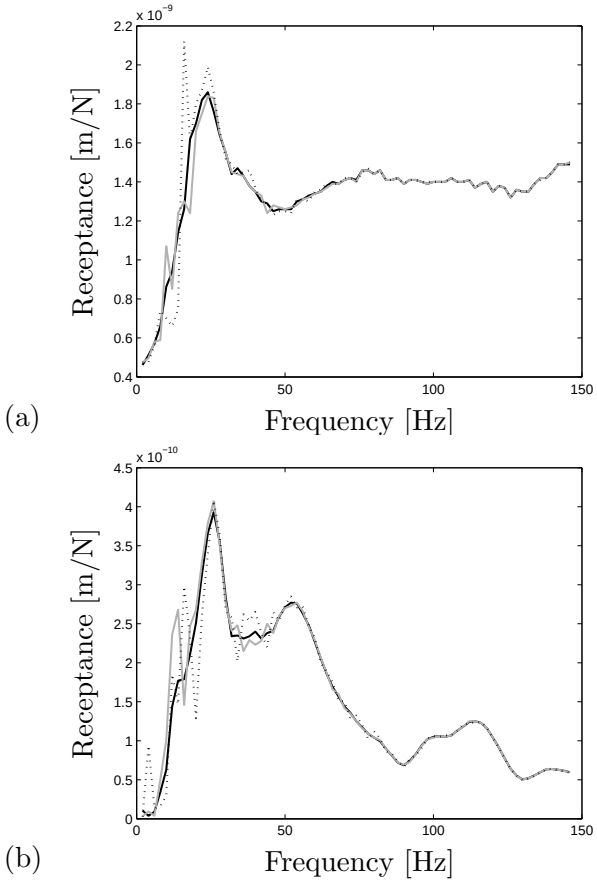

Figure 3.32: Comparison of the Green's functions computed with FE models with 75 m (black), 45 m (grey) and 35 m(doted) of total length at a) 2 m and b) 16 m from the source.

3D FE and 2.5D DSM Green's functions

For the computation of the Green's functions in FEM 3D, the FE mesh is modelled with 3D volumetric elements in order to simulate part of the soil. A soil profile is considered with dynamic properties represented in table 3.4.

Table 3.4: Soil profile for the computation of Green's functions in the soil.

Layer	d [m]	C_s [m/s]	C_p [m/s]	ρ [kg/m^3]	ξ_s	ξ_p
1	10	259.4	1852.4	2000	0.03	0.03
Bedrock	∞	-	-	-	-	-

FE mesh

The FE mesh is created to simulate the case study and includes the 10 m depth of soil (Figure 3.33). The nodes at the bottom are clamped in the vertical y direction to take into account the presence of the bedrock and bounding elements without spring stiffness are included in the limits of the mesh to absorb outgoing body waves. At the upper 5 m of soil, the vertical element edge size is 0.5 m and at the lower 5 m of soil the vertical element size is 1 m. Two zones are considered in the horizontal direction of the model, in a similar way as in the axisymmetric models. The first zone includes the load point and its vicinity in a total area of 20 m $\times$ 20 m, in which the edge length of each element is 0.44 m. The second mesh zone surrounds the first zone and is much less refined. The main objective of this second zone is to put the mesh boundaries far from the point load, and provide good simulation of the response at low frequencies. The dimensions of the full mesh are 60 m $\times$ 60 m $\times$ 10 m. The 10 m depth of the model is justified by the previous parametric study that showed this depth is enough to ensure numerical accuracy.

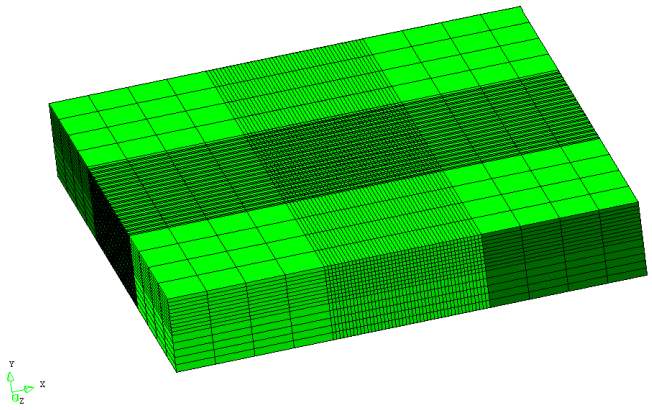

Figure 3.33: 3D mesh of the FE model of the soil

Damping

The different formulation of time domain and frequency domain calculations implies that inconsistent material damping formulations must be used. Usually, frequency domain models consider hysteretic damping which is frequency independent and regarded as more appropriate for soil modelling. Time dependent calculations generally rely on Rayleigh damping formulation which is frequency dependent.

In particular, the direct stiffness formulation admits the adoption of independent dilatational damping ξ_p and shear damping ξ_s through the definition of complex Lamé coefficients:

$$(\lambda^* + 2\mu^*) = (\lambda + 2\mu)(1 + 2i\xi_p) \tag{3.83}$$

$$\mu^* = \mu(1 + 2i\xi_s) \tag{3.84}$$

In the direct stiffness computation of the Green's functions, the dilatational damping $\xi_p = 0.03$ and shear damping $\xi_s = 0.03$ are defined.

In the FEM, Rayleigh damping is considered according to:

$$\mathbf{C} = \alpha\mathbf{M} + \beta\mathbf{K} \tag{3.85}$$

where $\mathbf{C}$ represents the damping matrix $\mathbf{M}$ the mass matrix and $\mathbf{K}$ the stiffness matrix. The parameters α and β are the damping coefficients. This defines a frequency-dependent damping ratio ξ_i:

$$\xi_i = \frac{1}{2}(\frac{\alpha}{\omega_i} + \beta\omega_i) \tag{3.86}$$

where ω_i is the angular velocity $\omega_i = 2\pi f_i$. In the FE model, the Rayleigh damping coefficients $\alpha = 3.406$ and $\beta = 6.45 \times 10^{-5}$ are computed in a least squares fitting of equation (3.86) with the hysteretic damping $\xi = 0.03$ in the frequency range of 20 Hz to 200 Hz. Figure 3.34 compares the damping of the FE and Direct Stiffness models.

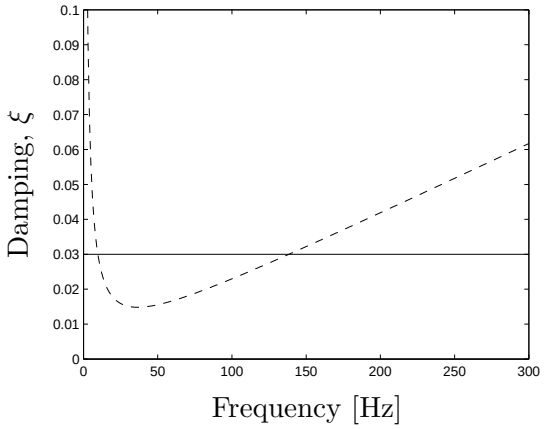

Figure 3.34: Damping of soil in the FE (dashed) and Direct Stiffness (full) models.

Due to the Rayleigh damping formulation, the FE model necessarily has very high damping at low frequencies. The damping of the FE model is lower than the damping of the DSM at frequencies between 10 Hz and 138 Hz, at other frequencies the damping is lower in the DSM model.

Dynamic load

Considering that the FE 3D soil response is computed in time domain, a procedure is adopted to compute the transfer functions. The FE mesh is solicited by a point load at the soil surface whose time history and frequency content are known. The time history response of the FE 3D model is then transformed into the frequency domain through a Fourier transform. Finally, the Green's functions are computed at each frequency as the quotient of the response and the load.

A source load is defined with a predominant frequency content on a range of 20 Hz to 250 Hz. The load is a Ricker pulse with the following time history:

$$t_y(t) = \left[2\left(\frac{\pi(t-t_s)}{T_{\mathrm{R}}}\right)^2 - 1\right] \exp\left[-\left(\frac{\pi(t-t_s)}{T_{\mathrm{R}}}\right)^2\right] \tag{3.87}$$

where $T_{\mathrm{R}} = 0.01$ s is the characteristic period and t_s =0.016 s is a time shift. The time history and frequency content of the load are shown in Figure 3.35.

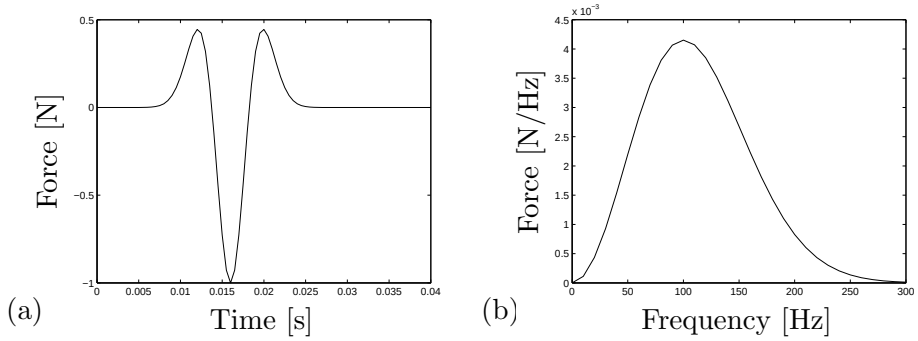

Figure 3.35: Load applied to the FE model: a) time history and b) frequency content.

Green's functions comparison

Figure 3.36 compares the soil receptance of the FE and DSM models at 2 m, 4 m and 8 m from the load point at the soil surface.

The response corresponds well at low frequencies but larger differences are found with increasing frequency and distance to the source load. The response at high frequencies degrades in the FE model because of the mesh element size.

The boundaries used were formulated to absorb incident dilatational and shear waves, however, they are ineffective in absorbing Rayleigh waves. This also explains the reason why the FE model results agree less with the DSM

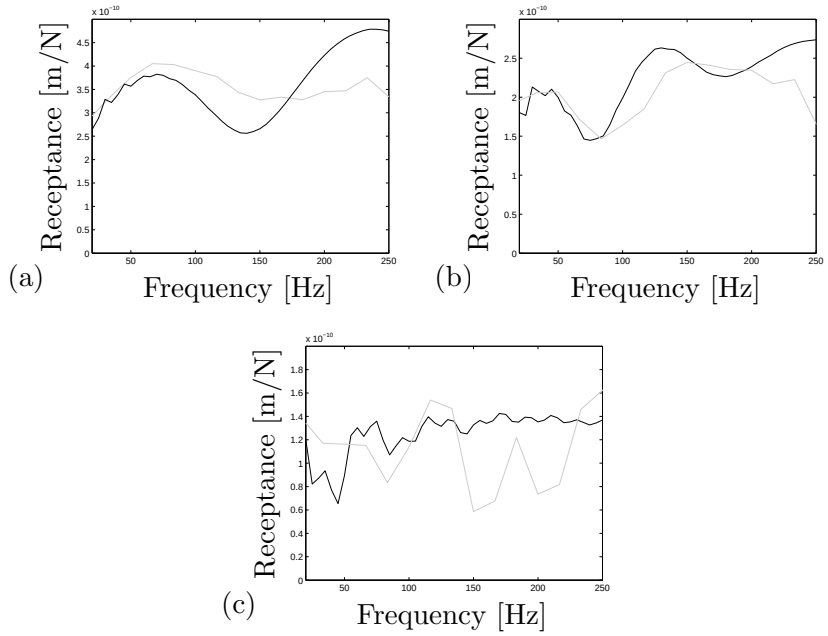

Figure 3.36: Soil receptance computed in FE (grey) and DSM (black) at the free surface a) 2 m, b) 4 m and c) 8 m from the source load.

model at increasing horizontal distances from the source load. This is a short come of the presented FE mesh that should be subject to subsequent study in order to be mitigated. Even so, since the simulation of the free field response at large distances from the track is not the goal of this work, this short come is not considered problematic.

Figure 3.37 compares the soil receptance of the FE and DSM models at 2 m, 4 m and 8 m depth below the load point.

In general, better agreement is found in the response of both models in the soil below the load point. The correspondence of the soil response at low frequencies is again good. There is a decrease in the correspondence of the responses with increasing frequency which is also explained by the element size. The response at 4 m depth computed with both models has better correspondence than the response at 2 m depth, which is surprising. At low frequencies the response is good at both depths but at higher frequencies the results at 4 m depth are very similar in both models, while at 2 m depth the FE model tends to increasingly overestimate the response with increasing frequency. At 8 m depth there is also a good agreement even though this node belongs to a zone where the FE mesh is less refined and has a bigger element size, thus making the response reliable at a narrower frequency range.

Figure 3.38 shows the accelerance of the FE and DSM models at 2 m, 4 m and 8 m from the load point at the soil surface.

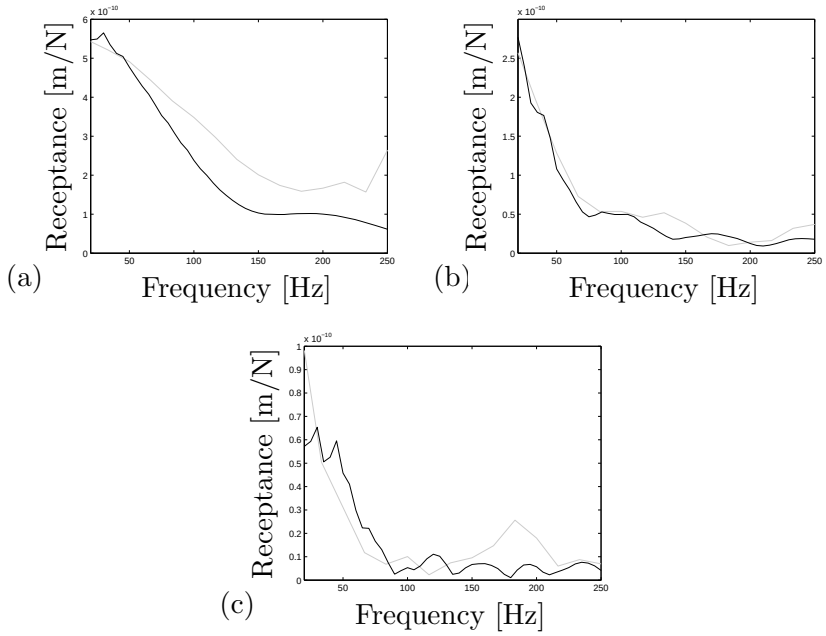

Figure 3.37: Soil receptance computed in FE (grey) and DSM (black) under the load at a) 2 m, b) 4 m and c) 8 m depth.

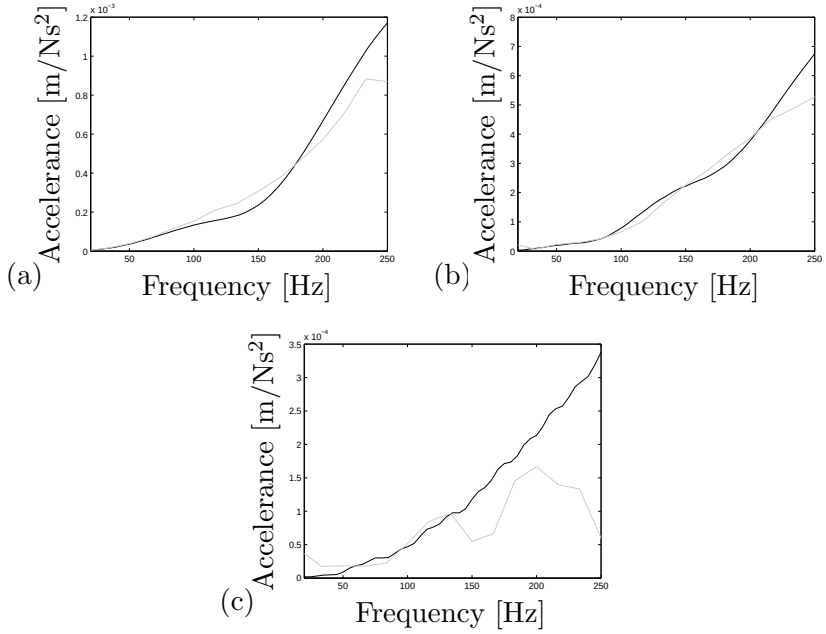

Figure 3.38: Soil accelerance computed in FE (grey) and DSM (black) at the free surface a) 2 m, b) 4 m and c) 8 m from the source load.

In general, the accelerance in the soil surface has correspondence at low

frequencies, although it is at high frequencies that higher accelerances are found. At 2 m from the source load the computed accelerance in the models agrees very well up to a frequency of 100 Hz. The accelerance computed with both models agrees well at 4 m from the source load throughout most of the frequency range, although at low frequencies the FE model tends to considerably overestimate the soil accelerance. At 8 m from the source load the correspondence is poorer demonstrating again that the FE mesh is less accurate to simulate the propagation of waves to regions far from the source load. Figure 3.39 shows the soil accelerance of the FE and Direct Stiffness models under the load.

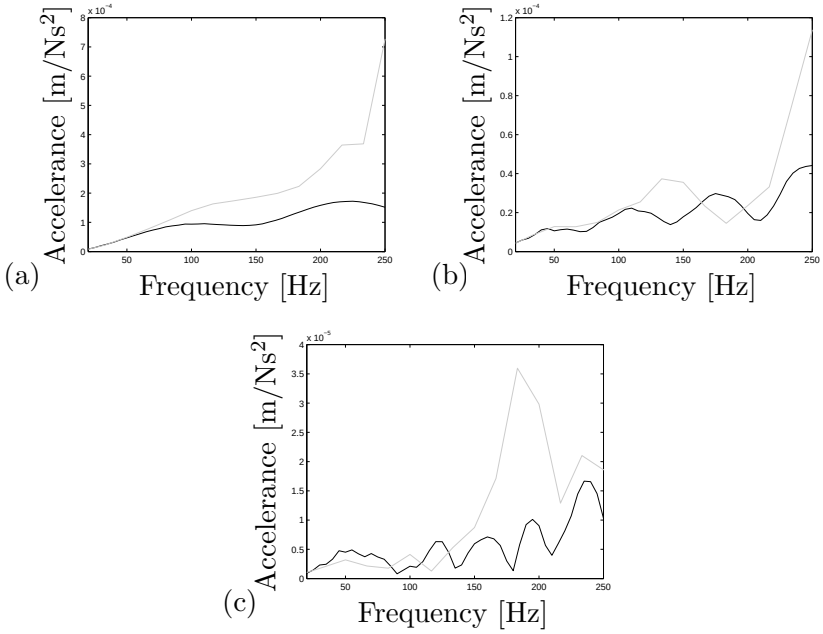

Figure 3.39: Soil accelerance computed in FE (grey) and DSM (black) in the soil at a) 2m, b) 4m and c) 8m depth.

Again, the point at 4 m depth shows the better correspondence of the three points showing good correspondence up to 110 Hz. At 2 m the correspondence is only good up to 75 Hz, at higher frequencies the FE model tends to overestimate the soil response. At 8 m of depth the correspondence between the accelerance computed with both models is only good at low frequencies.

3.5.3 Track-soil transfer functions

The 3D FE model

In this sub-section a railway track is presented and modelled using 2.5D and 3D FE. The transfer functions between the track and the soil are com-

puted and compared between both models. The 3D FE model allows the definitions of a more accurate reproduction of the track geometry because the consideration of invariable geometry in the longitudinal direction is no longer necessary consequently the discrete rail connection to the sleepers is considered. Equally, the sleepers are modelled in a discrete way instead of having their mass and stiffness smeared along the longitudinal direction of the track. The final aim of these models is to give better insight into the track response due to the passage of a high speed train. With a more detailed definition of the track geometry, the stress distribution along the ballast can be determined more accurately.

These are inevitably more elaborate models and computationally demanding, easily ascending to hundreds of thousands degrees of freedom. Because of this, much care must be taken into the mesh refinement so that no more computational effort is taken than the necessary.

The track is modelled to accurately simulate the geometry of ballasted railway tracks. The rail is modelled as a Mindlin-Reissner beam of 3 nodes and is discretely supported by a two-node translation spring/dashpot element that connects it with the sleepers

The sleepers are modelled with volumetric elements and embedded in the ballast. The ballast is modelled with volumetric elements, in transversal sections where no sleeper is present, the ballast top is at the same level as the top of the sleeper (crib), at transversal sections where a sleeper exists the top of the ballast layer is limited by the sleeper (Figure 3.40).

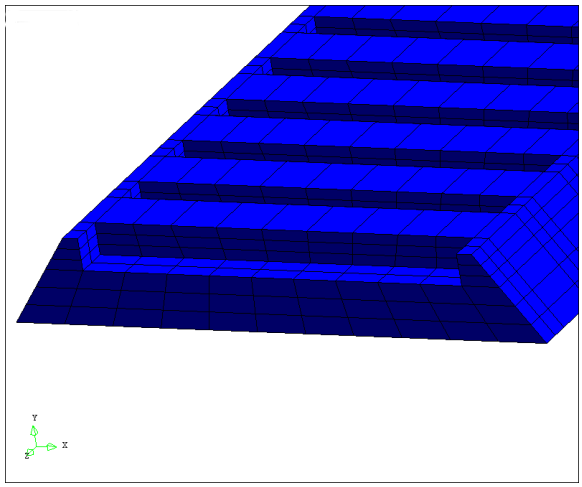

Figure 3.40: Ballast Mesh in the 3D FE model.

Track properties

The track properties are the same of section 3.4.4

The ballast Young's modulus of the 3D FE model is the same as in the 2.5D model. The sleeper has the dimensions $l_{\mathrm{sl}} \times b_{\mathrm{sl}} \times h_{\mathrm{sl}} = 2.5\,\mathrm{m} \times 0.235\,\mathrm{m} \times 0.205\,\mathrm{m}$ and a Young's modulus $E_{\mathrm{sl}} = 30 \times 10^9 \mathrm{N/m}^2$. The rail pad stiffness k_{rp} of the 3D FE model is calibrated with the 2.5D model using as optimization factor the rail receptance of the track clamped at it's bottom: at 1 Hz the 2.5D FE model with a rail pad stiffness of $k_{\mathrm{rp}} = 153.4 \times 10^6\,\mathrm{N/m}$ has a rail receptance of $2.362 \times 10^9\,\mathrm{m/N}$; the rail pad stiffness in the 3D FE model is calibrated for a value of $137 \times 10^6\,\mathrm{N/m}$ at which the rail receptance is $2.34 \times 10^9\,\mathrm{m/N}$.

Transfer functions between the track and the soil

The performance of the full 3D FE model and 2.5D model A, incorporating track and soil is evaluated. The soil profile is the same used in the computation of the 3D FE and Direct Stiffness computation of the Green's Functions (section 3.5.2). The 3D FE mesh incorporates the same soil mesh used for the computation of the Green's functions. To compute the transfer functions in the 3D FE model, the previous methodology is used, with a Ricker pulse with the characteristic period $T_{\mathrm{R}} = 0.01$ s and time shift t_s =0.016 s. Figure 3.41 compares the rail receptance computed in 3D FE and 2.5D models.

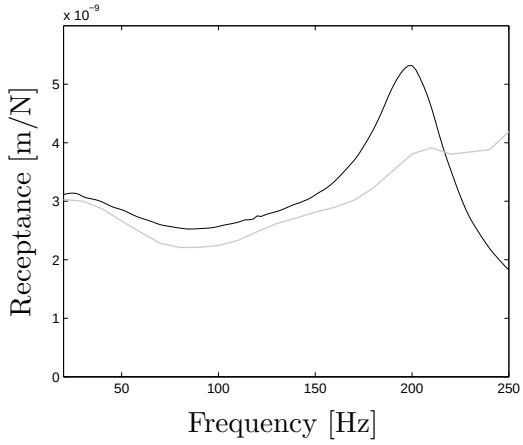

Figure 3.41: Rail receptance computed in 3D FE (grey) and 2.5D model (black).

The rail receptance shows good agreement, especially at low frequencies. The rail node of the 3D FE model where the results are computed is directly supported by a rail pad and thus all the transfer of stress from the rail at an effective zone of 0.6 m is transmitted to the sleeper and ballast through this node. The 3D FE model has lower receptance throughout almost all the considered frequency range. Again, the agreement between both models deteriorates with increasing frequency. The 3D FE receptance at 200 Hz is

a local peak, and the response at higher frequencies does not decrease, but rather increase. This is explained also by the element size in the FE mesh.

Figure 3.42 compares the receptance at the soil surface due to to a unitary axle load distributed through both rails.

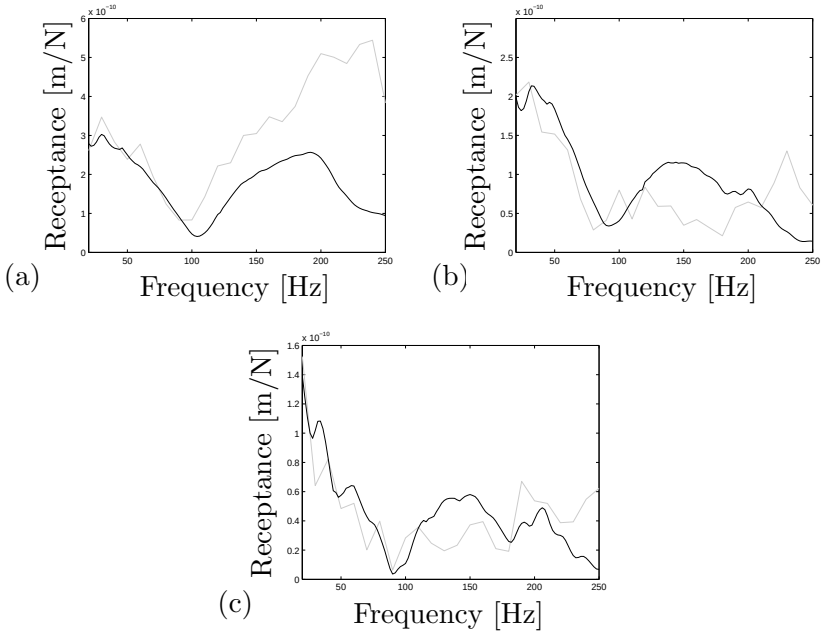

Figure 3.42: Soil receptance computed in FE (grey) and 2.5D model (black) at the free surface a) 2 m, b) 4 m and c) 8 m from the track.

There is generally good correspondence of the soil receptance at low frequencies. At high frequencies the agreement is poor. At 2 m from the track, the responses agree well up to a frequency of 100 Hz, at higher frequencies the soil receptance of the FE 3D model is higher than that of the 2.5D model. At 4 m from the track the 3D FE model has lower receptance than the 2.5D model throughout almost all the considered frequency range. At this distance from the track the response still agrees well up to a frequency of 100 Hz. At 8 m from the track the soil receptance computed with the 3D FE model also tends to be lower than the soil receptance of the 2.5D model, a good agreement is found again at frequencies up to 100 Hz.

It should be noticed that the soil receptance at the surface agrees well in these models incorporating track and soil, while the models incorporating only the soil showed much less correspondence. This is due to the fact that the point load is no longer applied at the soil surface but at the rail. The transmission of stresses to the soil is done through the ballast, thus in a more distributed way, and the Rayleigh wave reflection is less pronounced.

Figure 3.43 compares the receptance in the soil due to to a unitary axle load distributed through both rails.

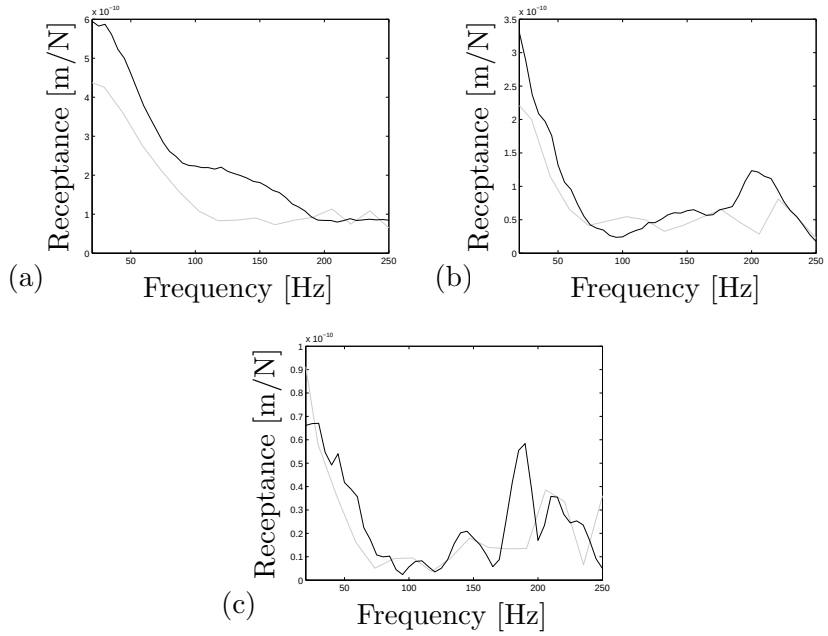

Figure 3.43: Soil receptance computed in 3D FE (grey) and 2.5D model (black) in the soil at a) 2 m, b) 4 m and c) 8 m depth below the track.

The soil receptances at 2 m depth computed with both formulations do not agree well. Throughout almost all the considered frequency range the 3D FE model computes a soil receptance that is lower than the soil receptance computed with the 2.5D model. At 4 m depth the 3D FE model also computes lower receptance than the 2.5D model although there is a better correspondence than the correspondence at 2 m depth. At 8 m depth there is a good correspondence up to a frequency of 150 Hz, although at low frequencies there is also the tendency of the 3D FE model to compute lower receptance than the 2.5D model.

Figure 3.44 compares the accelerance at the soil surface due to to a unitary axle load distributed through both rails.

The soil accelerance generally agrees well up to 100 Hz. It is shown very well by these comparisons that the 3D FE model loses accuracy at higher frequencies. At 2 m from the track the accelerance agrees well up to 100 Hz. At higher frequencies the 2.5D model presents a peak response at 200 Hz, which also occurs in the track response. The 3D FE model, however, presents very large accelerance. At 4 m from the track the accelerance of the 3D FE model at low frequencies is higher than the receptance of the 2.5D model. From 40 Hz to 110 Hz the accelerance of both models correspond very well, and at higher frequencies the correspondence is very poor. At 8 m from the track there is also a high accelerance at low frequencies in the 3D FE model that is followed by good agreement up to 90 Hz. Figure 3.45

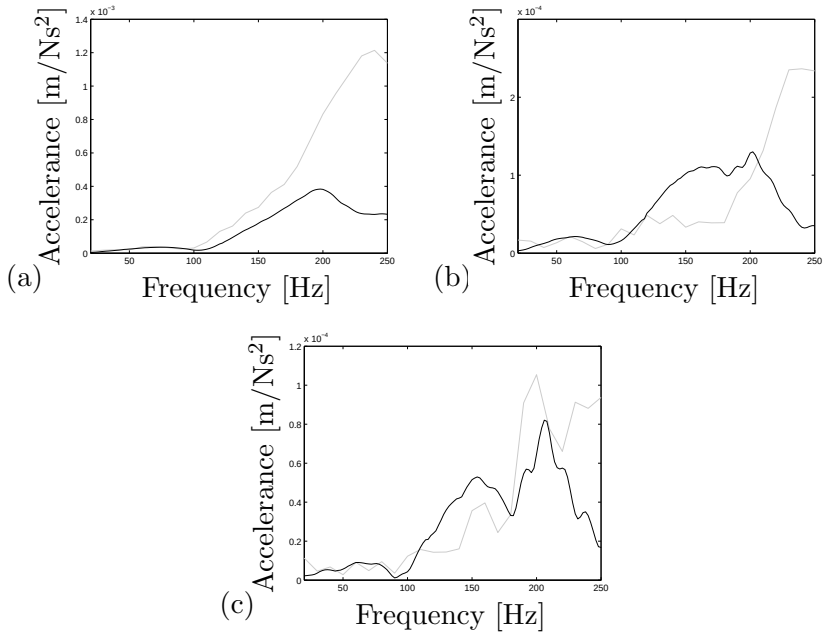

Figure 3.44: Soil accelerance computed in 3D FE (grey) and 2.5D model (black) at the free surface a) 2 m, b) 4 m and c) 8 m from the source load.

compares the accelerance in the soil due to to a unitary axle load distributed through both rails.

The soil accelerance at 2 m depth in the 3D FE model is highly underestimated in all the frequency range. At 4 m depth the soil accelerance agrees well at frequencies up to 90 Hz, with the exception of the lower frequencies at which there is again a tendency of the 3D FE model to overestimate the accelerance. At 8 m depth there is also an overestimation of the accelerance computed with the 3D FE mode, which is followed by good correspondence up to 90 Hz.

3.5.4 Response to a moving axle load

The response is obtained using the unitary axle load moving at 300 km/h, distributed through both rails. The response of the 3D FE model is obtained in time domain with the Newmark scheme while the response of the 2.5D model is obtained in the frequency domain and transformed into the time domain through an inverse Fourier transform. The methodology for the simulation of the moving load in the 3D FE model is presented in subsection 3.3.7 and the methodology for the simulation of the moving load in the 2.5D model can be consulted in Lombaert et al. (2006). The correspondence is very good, which is coherent with the good correspondence of the rail receptance. The time history of the rail vertical displacement (Figure

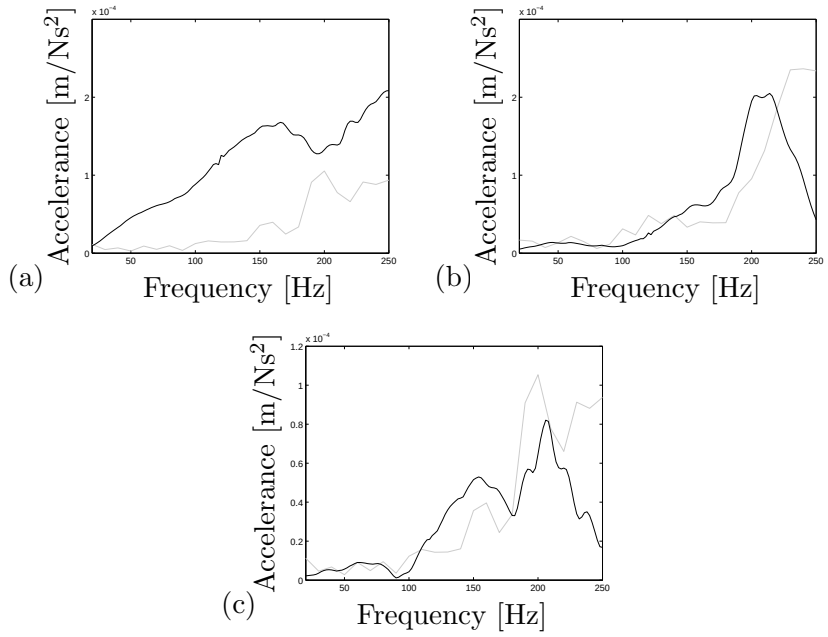

Figure 3.45: Soil accelerance computed in FE (grey) and 2.5D model (black) in the soil at a) 2 m, b) 4 m and c) 8 m depth below the track.

3.46) has almost the same time duration and the same peak value which, taking into account the different considerations of both models, is appreciable. This also proves that the simulation method of the moving load in the 3D FE model is appropriate, a remark that was already predictable by the good correspondence obtained of the sleeper response with experimental measurements in section 3.3. The frequency content of the displacement also corresponds very well at all the frequency range except at the very low frequencies.

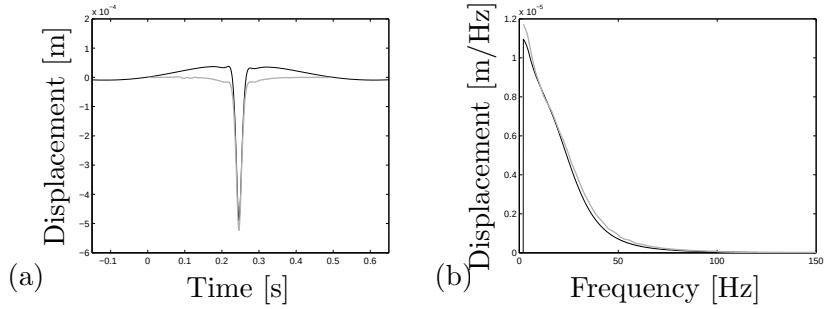

Figure 3.46: Rail displacement due to a moving axle load computed in 3D FE (grey) and 2.5D model (black).

The rail velocity (Figure 3.47) also corresponds very well in both models. The time history of the velocity is almost undistinguishable except for a peak

upwards value in the FE model. The frequency content of the velocity shows also that the models correspond very well, although there seems to be a shift of the response of approximately 5 Hz from the FE model to the BE model.

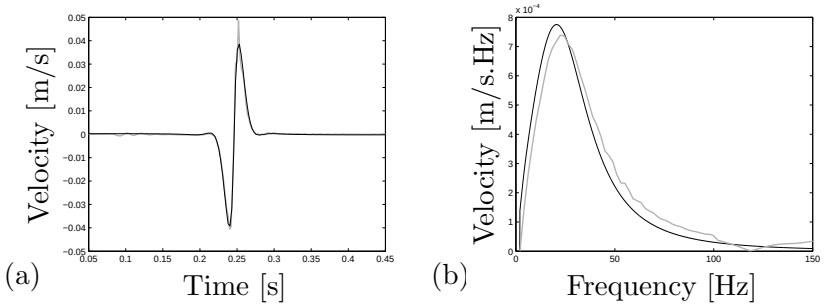

Figure 3.47: Rail velocity due to a moving axle load computed in 3D FE (grey) and 2.5D model (black).

The acceleration of the rail (Figure 3.48) shows a similar trend to the one presented by the velocity results. Some peak values do show in the FE model that are not present in the FE model. This occurs due to the previously mentioned limited capability of the FE model to reproduce accurate results at high frequency levels. These high frequency differences are amplified with the derivatives in order to time, and consequently the accelerations show more discrepancies between both models than velocities. The frequency content of the accelerations in the rail prove this, as it is clear that the FE model starts to lose accuracy at increasing frequency range.

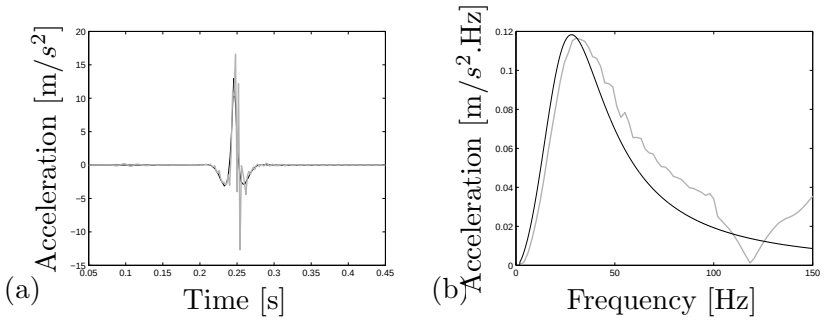

Figure 3.48: Rail acceleration due to a moving axle load computed in 3D FE (grey) and 2.5D model (black).

Despite the differences found mainly at the acceleration of the rail, the results correspond very well and allow to validate the FE model in the reproduction of the rail response due to the passage of a high-speed train. The limitation of the FE model to reproduce with accuracy high frequency response stems from the simplifications to the mesh related to the computation capabilities of nowadays PCs and not from numerical inaccuracies of the FE formulation. As shown previously with the axisymmetrical model,

when a small enough element size is adopted, the FE models simulate soil response with great accuracy even at high frequencies. The evolution of computational capabilities will most likely allow for 3D FE models with smaller element size and higher accuracy.

3.5.5 Partial remarks

A validation of the 3D FE model using the previously validated 2.5 model is done in this section. Initially the Green's functions in FE are computed in the frequency domain using an axisymmetric model. The computed Green's functions correspond very well up to frequencies of approximately 120 Hz. The decrease of correspondence at higher frequencies occurs due to the element size in the FE mesh. It is proved that the FEM can compute accurate results in the simulation of the soil dynamic response as long as the FE mesh is carefully considered.

Subsequently, the Green's functions are computed in a 3D FE mesh. Considering the utilization of the FEM is motivated by the possibility of the consideration of non-linear material models, the time-domain computations are essential, and thus the 3D Green's functions in the soil are computed in time domain. The Green's functions comparison reveals that the FE model generally simulates with accuracy the soil response at low frequencies. At higher frequencies the accuracy decreases due to the element size of the 3D FE mesh. At the soil surface the accuracy also decreases with increasing distance to the source load due to the inefficiency of the quiet boundaries in absorbing incoming Rayleigh waves. Generally the response computed with the 3D FE and 2.5D models below the load agree very well. A comparison of the transfer functions obtained between the track and the soil using the 2.5D model and the 3D FE model is also done. The rail receptance reveals good correspondence between the 3D FE and 2.5D models up to frequencies of 150 Hz. The response at the soil surface has generally very good agreement even at 8 m from the track. Below the track there is also a good agreement between the transfer functions computed with the 3D FE and 2.5D models.

Finally the comparison of the moving load response shows that the 3D FE mesh allows to obtain a very accurate simulation of the track displacements, velocities and accelerations.

3.6 Conclusions

This chapter presents the application of two distinct numerical tools for simulating high-speed track response to the passage of a high-speed train. The main goals include highlighting the dynamics of track-soil interaction and validating the 3D FE mesh computations.

A 3D FEM was initially employed to reproduce experimental measurements of a high-speed track. The results obtained are very promising because

the model was able to accurately predict the sleeper response. However, the soil response was not accurately simulated due to the lack of the dynamic load component. Because the results obtained are reasonable but not conclusive, it was decided to further validate the 3D FE models with a numerical tool whose accuracy was previously proven.

The 2.5D models were explored and two different track formulations were used and compared. The purpose of this study is to gain better insight of track behaviour and the 2.5D models. The track formulations mainly differ in two ways: one method considers undeformable sleepers and track-soil interfaces, whereas the other method allows the interfaces to deform. It was demonstrated that the model that allows more deformability of the track tends to induce less traction at the track-soil interface, whereas the final predictions of the free-field response are very similar in both formulations, especially at low frequencies.

Finally, the 3D FE mesh was validated using the 2.5D model. The FE mesh has the capability of simulating the dynamic soil response. Element size largely influences responses at high frequencies, whereas mesh size influences responses at low frequencies. Despite these findings, it was possible to obtain accurate track-soil transfer functions at low frequencies even with a 3D FE mesh. Although the models use different approaches to simulate the longitudinal geometry of the track and soil damping, the rail response due to the passage of a single axle corresponded well.

The main conclusion of this chapter is that the 3D FE mesh is numerically accurate in the simulation of track and soil responses to the passage of moving loads. This situation requires careful selection of the FE mesh, with regards to the length of the track stretch, the size of the FE soil simulation, and the absorbing boundaries.

Chapter 4

Application and development of non-linear models

4.1 Introduction

This chapter presents the study of the non-linear behaviour of ballast and subgrade using numerical models. From the study of the state of art in Chapter 2 it was concluded that, although the railway track numerical simulations have been subject to great development in the last few years, seldom have these simulations been used to study non-linear behaviour of the track components. In Chapter 3 the 3D FE models have been studied and validated so that in this chapter they can be used to study non-linear track response. The chapter includes studies of the non-linear ballast behaviour in section 4.2 and the non-linear behaviour of the soil is done in section 4.3.

Finally, in section 4.4the non-linear track and subgrade behaviour are simultaneously accounted for in the simulation of a railway track where it was demonstrated that the non-linear behaviour had a significant influence in the track serviceability.

4.2 Ballast stress analysis

4.2.1 Introduction

This sub-section presents the study of the non-linear ballast behaviour to the passage of a high-speed train. This study intends to determine how the consideration of non-linear ballast behaviour affects the track response in the numerical method. The study is done through the modelling of a case for which the 3D FE mesh is validated. The ballast stress-strain response is obtained from the literature in a case where the large triaxial apparatus was used. The experimental results are used to calibrate a modified Mohr-Coulomb model in which the hardening/softening is described as a multi-

linear curve specifying the variation of the friction angle ϕ. Due to the complexity of the model, the calibration procedure is done in three stages. Firstly, using a stochastic search for a broader search, secondly, using a more local search along with the Hessian method and thirdly using a parametric study to ensure that the objective function is minimized at the calibrated values for all parameters. The response to the passage of a train axle is analysed and the differences between linear, equivalent linear, non-linear and equivalent non-linear analyses are discussed, mainly considering the stress and strain in the ballast layer and the vertical displacements and velocities in the rail and sleeper of the track. The importance of pressure-dependent Young's Modulus and the yield surfaces are also studied and discussed.

4.2.2 Constitutive model

The constitutive model used to simulate the non-linear ballast behaviour is a Modified Mohr Coulomb model. It has been developed at Delft University of Technology (Groen, 1995) and is available in Diana software (TNO, 2005). The model is mostly suitable to model frictional materials like concrete or sand but it has been enhanced so it is suitable for all kinds of soil materials.

The model features a default smooth Mohr-Coulomb shear yield surface with optional pressure shift for initial cohesion. An optional hardening-softening multi-linear curve may be specified for the friction angle ϕ. The model allows the definition of associated plasticity ($\psi = \phi$) or the dilatancy angle may be explicitly defined or related to the friction angle via Rowe's Dilatancy rule. The elasticity may be directly defined or it can be related with the effective pressure using either an Exponential Law or a Power Law. Besides the shear yield surface, the model includes a cap shaped compression yield surface. Its initial position may be defined explicitly or can be derived from the initial stresses. A compression cap hardening rule may also be defined using either an Exponential Law or a Power Law. In the following, the model features that are used to simulate the ballast are more thoroughly discussed.

Shear Yield Surface

The shear yield surface follows the Mohr-Coulomb failure criteria. This states that failure of the soil mass will occur if the following condition applies:

$$\tau = \pm(c' + \sigma' \tan \phi') \tag{4.1}$$

Failure does not depend solely on the value of the shear stress τ but instead on its relation with the effective normal stress σ'. The component c' is often called cohesion and sets an initial shear resistance of the soil for 0 effective normal stress. For sandy materials the cohesion is commonly

considered equal to 0. In the $\sigma' : \tau$ stress plane, this failure criteria defines a pair of straight lines, if the Mohr's circle touches these lines then failure occurs.

This criteria states that the failure will be independent of the intermediate principal effective stress σ_2. The relation between the major principal stress σ_1 and the minor principal stress σ_3 is given by:

$$\frac{\sigma_1 + c' \cot \phi'}{\sigma_3 + c' \cot \phi'} = \frac{1 + \sin \phi'}{1 - \sin \phi'} \tag{4.2}$$

this can be also stated in terms of stress variables $p' : q$. Accounting for the fact that all considerations of the ballast material are done in drained conditions, the tilde denoting effective stresses will not be used onwards for simplification. The stress invariants p and q are given by:

$$p = \frac{\sigma_1 + \sigma_2 + \sigma_3}{3} \tag{4.3}$$

$$q = \sqrt{\frac{(\sigma_1 - \sigma_2)^2 + (\sigma_2 - \sigma_3)^2 + (\sigma_3 - \sigma_1)^2}{2}} \tag{4.4}$$

in the case of triaxial compression $\sigma_2 = \sigma_3$:

$$p = \frac{\sigma_1 + 2 \times \sigma_3}{3} \tag{4.5}$$

$$q = \sigma_1 - \sigma_3 \tag{4.6}$$

and σ_1 and σ_3 correspond to the axial stress and confining pressure, respectively. The critical state of equation (4.1) can then be written in terms of p and q:

$$M_\phi = \frac{q}{p} = \frac{6 \sin \phi}{3 - \sin \phi} \tag{4.7}$$

where M_ϕ is the slope of the line representing the yield condition in the $p : q$ space. Conversely, by knowing the value of M_ϕ at a particular critical state, the value of the friction angle ϕ can also be obtained:

$$\sin \phi = \frac{3M_\phi}{6 + M_\phi} \tag{4.8}$$

The failure yield surface in the $p : q$ space of the modified Mohr-Coulomb model is given by:

$$\frac{q}{R_1(\theta)} - \frac{6\sin\phi}{3-\sin\phi}(p+\Delta p) = 0 \tag{4.9}$$

where Δp is the pressure shift for cohesion and $R_1(\theta)$ is a parameter that controls the shape of the yield surface, by standard it is set so that the yield surface corresponds to the Mohr-Coulomb criteria.

Compression cap

Yield may also be defined as a function of the mean stress p. This is defined by a yield surface that is cap shaped (Figure 4.1) and is given by the equation

$$(p+\Delta p)^2 + \alpha\left(\frac{q}{R_2(\theta)}\right)^2 - p_c^2 = 0 \tag{4.10}$$

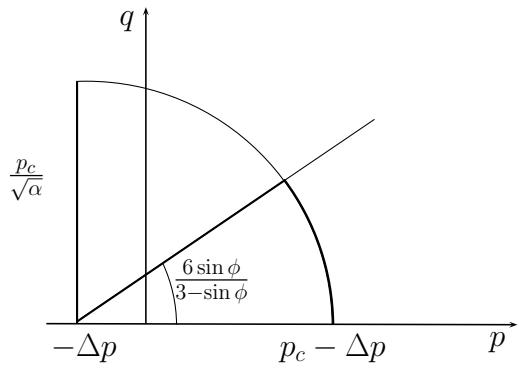

Figure 4.1: Shear yield surface and compression cap of the modified Mohr-Coulomb model, represented in the $p : q$ space.

p_c is the pre-consolidation pressure and α and $R_2(\theta)$ are cap shape factors.

Flow rule

The direction of the inelastic strain rate is determined by two plastic potential surfaces:

$$g(1) = q - \frac{6\sin\psi}{3-\sin\psi}(p+\Delta p) \tag{4.11}$$

$$g(2) = (p + \Delta p)^2 + \alpha q^2 - p_c^2 \tag{4.12}$$

This implies associative behaviour in $p : q$ space and non-associated flow in the deviatoric space. The dilatancy angle ψ may be related with the friction angle ϕ through Rowe's rule (Rowe, 1962):

$$\sin\psi = \frac{\sin\phi - \sin\phi_{cv}}{1 - \sin\phi\sin\phi_{cv}} \tag{4.13}$$

where ϕ_{cv} is the friction angle at constant volume.

Hardening behaviour

The modified Mohr-Coulomb model allows uncoupled hardening for both yield surfaces. For the shear yield surface, hardening is defined as a multi-linear variation of the mobilized friction angle ϕ (Figure 4.2) with deviatoric plastic strain:

$$\sin\phi = \sin\phi(\kappa_1) \tag{4.14}$$

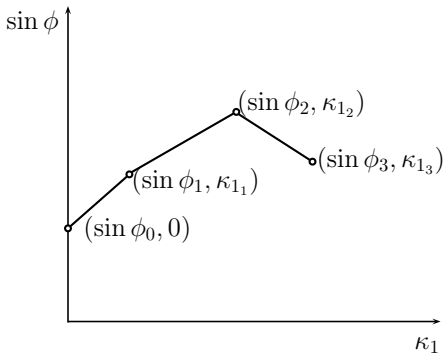

Figure 4.2: Definition of the shear yield surface hardening/softening through a $\phi : \kappa_1$ diagram.

where κ_1 is the equivalent plastic shear strain, that is related to the plastic shear strain γ^p:

$$\Delta\kappa_1 = \sqrt{\frac{2}{3}\Delta\gamma^{pT} R \gamma^p} \tag{4.15}$$

Hardening of the compressive cap is defined with a power law variation of the pre-consolidation stress:

$$p_c = p_{ref}\left(\left(\frac{p_{c0}}{p_{ref}}\right)^m - \frac{m}{\Gamma}\Delta\varepsilon_v^p\right)^{\frac{1}{m}} \tag{4.16}$$

m and Γ are parameters that shape the pre-consolidation variation with plastic volumetric strain ε_v^p, p_{ref} is a reference pressure and p_{c0} is the pre-consolidation stress at the beginning of the step.

4.2.3 Optimization technique

Procedure overview

An optimization strategy consists in the definition of a procedure that attempts to find the values of $\mathbf{x}$ so that $F(\mathbf{x})$ is minimized. Usually any optimization procedure requires the definition of a set of initial values for the variables $\mathbf{x}_0$, which the user obtains from an initial analysis of the experimental values or from his experience with similar materials or problems. It is important that $\mathbf{x}_0$ may be a set of variables that, in light of the constitutive model, defines a material with physical meaning, to which the numerical methods are oblivious. This prevents the definition of a set of variables $\mathbf{x}$ that may minimize $F(\mathbf{x})$ numerically but whose values are not related to the real physical properties of the material. To avoid the tendency to find spurious solutions it is also common to define a set of minimum $\mathbf{m}$ and maximum $\mathbf{n}$ values for the material parameters.

Starting from the initial values $\mathbf{x}_0$ and obeying to the condition

$$m_i \leq x_i \leq n_i, i = 1, 2, ..., n \tag{4.17}$$

where n is the number of parameters subject to calibration, the optimization strategy defines how the search for $\mathbf{x}$ is conducted.

Considering that $F(\mathbf{x})$ is twice continuously differentiable, the Gradient $g(\mathbf{x})$ and Hessian $H(\mathbf{x})$ may be defined as

$$\mathrm{g}(\mathbf{x}) = \frac{\partial F(\mathbf{x})}{\partial \mathbf{x}}, H(\mathbf{x}) = \frac{\partial^2 F(\mathbf{x})}{\partial \mathbf{x}^2} \tag{4.18}$$

Taking into account the possibility to compute $g(\mathbf{x})$ and $H(\mathbf{x})$ three general approaches may be used (Yang and Elgamal, 2003). Zero order strategies require only the evaluation of $F(\mathbf{x})$. These strategies generally require a large number of iterations to converge. First order strategies require the evaluation of $F(\mathbf{x})$ and $g(\mathbf{x})$, if $g(\mathbf{x})$ is not explicitly available, it may obtained through finite differences or semi-analytical methods. Second order strategies require the evaluation of $F(\mathbf{x})$, $g(\mathbf{x})$ and $H(\mathbf{x})$, these are more elaborate strategies with better convergence than the previous. Among the

second order strategies the Newton method is usually the most efficient (Gill et al., 1981). The evaluation of $g(\mathbf{x})$ and $H(\mathbf{x})$ when not explicitly available can be obtained through approximation algorithms, in this case the designation of "quasi-Newton" methods is common.

A major challenge in the optimization problems stems from the fact that often the optimization methods find local minimum for the objective function $F(\mathbf{x})$, while most often the objective is to find the global minimum. Given a function $F(\mathbf{x})$ and a local minimum, there is no general way to determine whether that corresponds to the global minimum (Yang and Elgamal, 2003). To circumvent this, usually the optimization strategy is repeated several times using different values of $\mathbf{x_0}$, assuming that with increased number for attempts starting at different points of the domain the probability of having determined the global minimum increases.

Other strategies consist in combining the utilization of global and local search algorithms. Cekerevac et al. (2006) developed the ParaID routine that combines stochastic and quasi-Newton methods. A similar strategy is herein adopted to calibrate the material model with the experimental results of ballast material. The general idea behind the combination of stochastic and quasi-Newton methods relies on the assumption that while the quasi-Newton method converges quickly to local minimum, it is usually the closest local minimum to the initial values of $\mathbf{x}$ and most often does not correspond to the global minimum; while the stochastic method, on the other hand, allows a more general search throughout the domain, finding where in the domain the objective function takes it's lower values. Therefore, the stochastic method is used to search the domain for zones of lowest values, and the quasi-Newton is used for a more thorough search in the zone to determine the local minimum that may correspond to the global minimum.

Objective function

The objective function is based on the function used by Cekerevac et al. (2006) to calibrate Hujeux constitutive model for a clay (Kaolin). A general objective function for optimization of triaxial results must incorporate the error found in the numerical computation of stress, strain and pore pressure in comparison with experimental values. Considering that the experimental results are discrete, the objective function for one point can be proposed:

$$f(\mathbf{x})_c = \frac{1}{\sum_{k,l=1}^{3} w_{kl}} \left\{ \sum_{k=1}^{3} \frac{1}{\sigma_0^2} (\sigma_k^e - \sigma_k^n) w_{k1} (\sigma_k^e - \sigma_k^n) + \sum_{k=1}^{3} \frac{1}{\varepsilon_0^2} (\varepsilon_k^e - \varepsilon_k^n) w_{k2} (\varepsilon_k^e - \varepsilon_k^n) + \sum_{k=1}^{3} \frac{1}{u_0^2} (u_k^e - u_k^n) w_{k3} (u_k^e - u_k^n) \right\} \tag{4.19}$$

where σ_k^e, ε_k^e and u_k^e are experimental values of stress, strain and pore pressure, respectively; σ_0, ε_0 and u_0 are the scaling factors of the variables which correspond to the maximum experimental values of stress, strain and pore pressure, respectively; and σ_k^n, ε_k^n and u_k^n are numerical values of stress, strain and pore pressure, respectively. The variables w correspond to weighting factors to account for the confidence in the various experimental results and also to account their correspondent importance in the calibration of the model.

For the case of triaxial results, it is more convenient to express the objective function in terms of deviatoric stress q, volumetric strain ε_v and pore pressure u:

$$f^k(\mathbf{x})_c = \frac{1}{\sum_{j,k=1}^{3} w_{jk}} \left\{ \sum_{j=1}^{3} \frac{1}{q_0^2} (q_j^e - q_j^n) w_{j1} (q_j^e - q_j^n) + \sum_{j=1}^{3} \frac{1}{\varepsilon_{v0}^2} (\varepsilon_{vj}^e - \varepsilon_{vj}^n) w_{j2} (\varepsilon_{vj}^e - \varepsilon_{vj}^n) + \sum_{j=1}^{3} \frac{1}{u_0^2} (u_j^e - u_j^n) w_{j3} (u_j^e - u_j^n) \right\} \tag{4.20}$$

In this case the response is calibrated for drained triaxial tests and thus the third term vanishes.

The calibration is done for various triaxial tests done with different confining pressures. Therefore, the final form of the objective function becomes:

$$F(\mathbf{x}) = \frac{1}{\sum_{s=1}^{n} w_s} \sum_{s=1}^{n} w_s f(\mathbf{x}) \tag{4.21}$$

where n is the number of experimental results to be calibrated and w_s is weighting factor to allow the inclusion of importance or confidence in the different experimental results.

Stochastic method

The stochastic method conducts a random search following the general algorithm:

1. A new set of variables $\mathbf{x}^k$ is randomly generated from a Gauss probability distribution with mean $\mathbf{x}^{min}$ and standard deviation σ^*.
2. For the set of variables $\mathbf{x}^k$ at iteration k the corresponding value of the objective function $F(\mathbf{x}^k)$ is determined.
3. If $F(\mathbf{x}^k) < F(\mathbf{x}^{min})$ then the best approximation parameters are updated: $\mathbf{x}^{min} = \mathbf{x}^k$ and $F(\mathbf{x}^{min}) = F(\mathbf{x}^k)$; otherwise no update is made to $F(\mathbf{x}^{min})$ and $\mathbf{x}^{min}$.
4. If the maximum number of iterations has been reached then stop the process, otherwise return to the first step.

It is a simple process in which the centre of the search is the point $\mathbf{x}^{min}$ at which the minimum value of the objective function $F(\mathbf{x}^{min})$ has been found. From this point, the direction and length of the new search is randomly generated. The advantage this has over first order and second order search algorithms is that even when falling on a local minimum, the process will not be deterred to jump to other zones of the domain in search of other minimum points. The disadvantage is that since the process is oblivious to the gradient and Hessian of the objective function, at any point the process may be close to the global minimum but not find it. The standard deviation should be chosen with criterion, if it is too large then the process may need an excessive number of iterations to find the global minimum, and if it is too small the large-scale advantage of this process may be lost. A procedure to scale the variance was proposed by Beckey and Masri (1983) and Pronzato et al. (1984). This method divides the stochastic search procedure into two phases: a phase where the variance is selected and a phase in which the variance is explored. A similar procedure is herein used to select the standard deviation of the stochastic optimization technique. Initially the standard deviation is selected:

$$\sigma^*{}_0 = \frac{\mathbf{n} - \mathbf{m}}{2} \tag{4.22}$$

starting at $\mathbf{x}_0$ and $\sigma^*{}_0$, 100 iterations of the stochastic search are done.

The standard deviation selection phase repeats the previous random searches. However, in this phase the mean of the Gauss probability distribution is constant and equal to the best approximation set of variables $\mathbf{x}^{min}$ from the previous phase; the standard deviation, on the other hand, is variable and consecutively corresponds to:

$$\sigma^*{}_i = \frac{\sigma_0^*}{10^i}; i = 0, 1, 2. \tag{4.23}$$

after 300 iteration steps each standard deviation is used 100 times and a new exploitation phase begins using $\mathbf{x}^{min}$ and the standard deviation that provides the best approximation σ^{*min}. This alternation between exploitation and selection phases is repeated until the best standard deviation is $\sigma_0/100$ for three consecutive times. After that the procedure moves to the Hessian method for a more thorough search in the vicinity of $\mathbf{x}^{min}$.

Hessian method

The Hessian method used is a subspace trust-region method based on an interior-reflective Newton method described by Coleman and Li (1994, 1996). Trust region methods reduce the complexity of the large-scale optimization problem by approximating the objective function with another function r which reasonably reflects the behaviour of $F(\mathbf{x})$ in a neighbourhood $\mathbf{N}$ around the current point $\mathbf{x}$. This neighbourhood is the trust region. The function $F(\mathbf{x})$ is approximated using the first two terms of the Taylor series with an expansion point $\mathbf{x} = \mathbf{s}$. The trust region sub-problem is then formulated:

$$\min\left\{\frac{1}{2}\mathbf{s}^T\mathbf{H}\mathbf{s} + \mathbf{s}^T\mathbf{g}, \mathbf{s} \in \mathbf{N}\right\} \tag{4.24}$$

where $\mathbf{H}$ is the Hessian matrix and $\mathbf{g}$ is the gradient of F at $\mathbf{x}$. Solving equation (4.24) allows to determine the trial step $\mathbf{s}$. For many of the accurate algorithms proposed (More and Sorensen, 1983), the solution of equation (4.24) in a large-scale problem can be computationally expensive. A simplification is then applied by reducing the trust-region sub-problem to a two-dimensional subspace S, defined:

$$S = < \mathbf{s_1}, \mathbf{s_2} > \tag{4.25}$$

where $\mathbf{s_1}$ is in the direction of $\mathbf{g}$ and $\mathbf{s_2}$ is computed to define either the approximate Newton direction

$$\mathbf{H}.\mathbf{s_2} = -\mathbf{g} \tag{4.26}$$

or the direction of negative curvature

$$\mathbf{s_2}^T.\mathbf{H}.\mathbf{s_2} < 0 \tag{4.27}$$

thus enforcing global convergence. Once the subspace S is determined, the solution to equation (4.24) becomes trivial and the trial step $\mathbf{s}$ is computed.

The iteration is then carried on by determining the value of $F(\mathbf{x}+\mathbf{s})$, if it is inferior to $F(\mathbf{x})$ then $\mathbf{x} = \mathbf{x}+\mathbf{s}$, if not then the trust region is shrunk, either way the procedure is repeated until the convergence is achieved.

Parametric study

The final phase in the optimization procedure is the evaluation of the objective function with the variation of each of the optimization variables. This is done by selecting a reasonable range within which each variable is changed while all the other variables remain equal to the previously optimized values in the trust region method. This allows to evaluate the relative influence of each variable around $\mathbf{x}$ and also to check the quality of the optimization by verifying if the objective function reaches a lower value than $F(\mathbf{x})$. If this happens then $\mathbf{x}$ is updated and the whole procedure (starting at the stochastic method) is repeated.

4.2.4 Calibration of the model

The cyclic triaxial results are obtained from the literature. Suiker et al. (2005), Suiker and de Borst (2003) performed a series of static and cyclic triaxial tests on ballast and sub-ballast material. The tests were done at constant confining pressures of 10.3 kPa, 41.3 kPa and 68.9 kPa, which the authors considered to be relevant confining pressures for ballast in railway tracks. The static triaxial tests were used to obtain information on the admissible stress values to perform the cyclic tests. The ballast material is a uniformly graded taprock with maximum particle size of 38 mm. The triaxial apparatus had a diameter $D = 254$ mm and height $H = 645$ mm and the specimen was compacted in eight layers. Further details on the experimental tests can be obtained in the original publications (Suiker and de Borst, 2003, Suiker et al., 2005). The experimental results of the static triaxial tests on ballast are represented in Figure 4.3.

Within the considered axial strains the maximum deviatoric stresses are 62 kPa, 237 kPa and 352 kPa for the confining pressures of 10.3 kPa, 41.3 kPa and 68.9 kPa respectively. From the deviatoric stress results, an estimation is obtained on the Young's modulus using the initial results:

$$E \approx \frac{q}{\varepsilon_a} \tag{4.28}$$

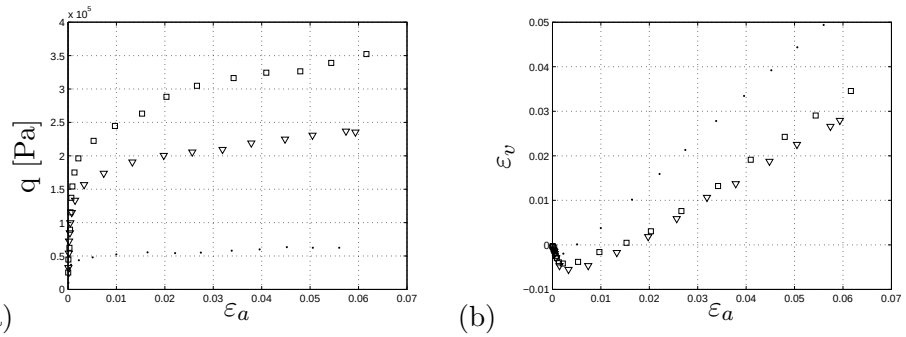

Figure 4.3: Experimental results of ballast triaxial testing, a) deviatoric and b) volumetric response at confining pressure: 10.3 kPa (•), 41.3 kPa (▽) and 68.9 kPa (□) (adapted from Suiker et al. (2005)).

which determines an initial value of 230 MPa. The volumetric results show that the ballast presents an initial compaction followed by an inversion to dilatational behaviour. There is no clear trend to co-relate the volumetric extensions obtained in the three confining pressures because at the confining pressure of 41.3 kPa the material presents more compaction than at 68.9 kPa or 10.3 kPa. One explanation for this relates to plastic deformations due to the isotropic compression stress, with increasing confining pressure the material naturally shows higher compaction, however, this may reverse when plastic strains are developed due to the isotropic compression stress. As such at confining pressure of 68.9 kPa the plastic strains developed induced a more dilatational behaviour even though the material is more compacted than at 41.3 kPa. Other explanation is that the volumetric strains are obtained from the average radial strains measured at 1/3, 1/2 and 2/3 height of the specimen. However, in some cases there were considerable differences in the radial strains obtained for the same specimen at different heights which the authors explained as resulting from the presence of some friction at the specimen top and bottom.

There is an increasing q/p ratio with increasing confining pressure for the ballast material (Figure 4.4). From the q/p ratio an estimate of the friction angle can be done through equation (4.7). The friction angle is estimated as varying from 37.5° to 48.6°, which corresponds to a variation of $\sin\phi$ between 0.58 and 0.75. These estimations provide initial values for the calibration procedure.

The calibration is carried on using the procedures described in subsection 4.2.3. Equal weighting factors are defined for the volumetric and deviatoric behaviour as well as for all the confining pressures. The initial values for the Young's modulus and the variation of $\sin\phi$ are those previously estimated from the experimental results. Figure 4.5 presents the comparison of experimental and numeric results after the calibration of the

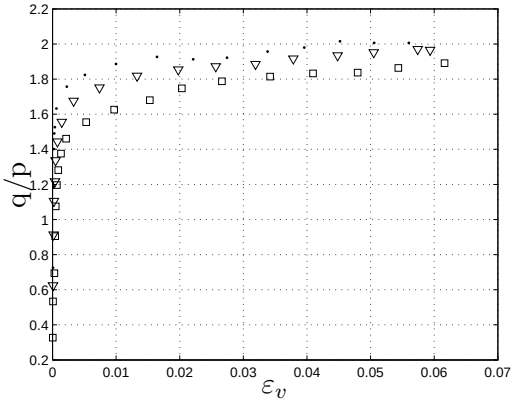

Figure 4.4: Representation of the ballast response in q/p-ε_v space at: 10.3 kPa (•), 41.3 kPa ($\bigtriangledown$) and 68.9 kPa (□) (adapted from Suiker et al. (2005)).

Modified Mohr Coulomb model.

A good calibration is obtained for both the deviatoric and volumetric behaviours. At 10.3 kPa and 41.3 kPa the correspondence of stress invariant q is very good, the numeric model predicts slightly lower stress values than the experimental values. At the highest confining pressure there is a noticeable difference between numeric and experimental values, even though the correspondence is still good. Such approximations in the calibration procedure of complex material models are usual (Cekerevac et al., 2006, Araújo, 2011). Concerning the volumetric strains, a very good approximation is obtained at two confining pressures: 10.3 kPa and 68.9 kPa. For 41.3 kPa the volumetric response obtained in the numeric analysis is not very accurate, but as previously stated there is some uncertainty in the results obtained from averaging the radial response at three points. Therefore, a broader tolerance for the volumetric response calibration is adopted. The calibrated parameters that correspond to the triaxial behaviour demonstrated in Figure 4.5 are presented in tables 4.1 and 4.2.

The value of the Young's modulus obtained is 293.8 MPa. This is larger than the value previously estimated although still relatively close. As there are no available results for small strain response, this Young's modulus may not be very accurate. Considering the ballast material, the values of the Young's modulus obtained in other simulations present in the literature (Suiker et al., 2005, Paderno, 2009, Araújo, 2011) range from 97 MPa to 277 MPa. In that regard, the value herein obtained may be considered a stiff ballast but nevertheless not far from the values usually obtained.

For the Poisson's ratio a value of 0.15 is obtained, considering that most

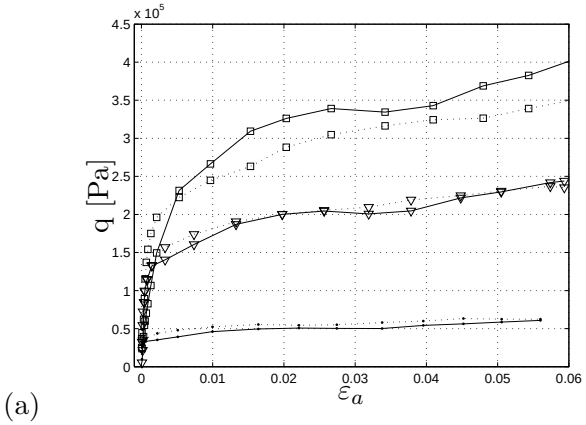

(a)

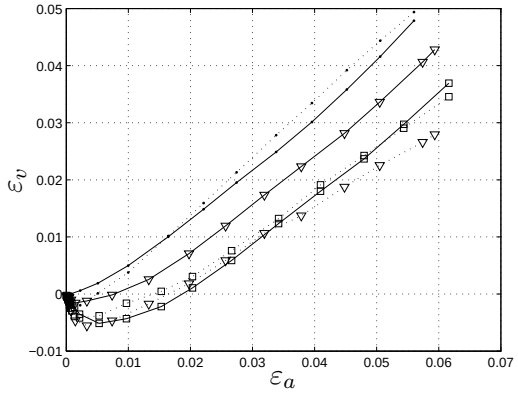

(b)

Figure 4.5: Experimental (dotted) and numerical (black) response of the ballast after calibration: a) deviatoric response and b) volumetric response at 10.3 kPa (•), 41.3 kPa (▽) and 68.9 kPa (□) (adapted from Suiker et al. (2005)).

Table 4.1: Calibrated modified Mohr-Coulomb parameters.

Parameter	value
E	293.8 MPa
ν	0.15
p_c	87980 Pa
Γ	0.00851
p_{ref}	227658.6 Pa
$\sin\phi_{cv}$	0.520
$\sin\phi_0$	0.613

Table 4.2: Calibrated values of the hardening curve of the yield surface.

κ	$\sin\phi$
0.01	0.688
0.02	0.707
0.03	0.713
0.04	0.705
0.05	0.726
0.06	0.735
0.07	0.747

of the analysis consider the Poisson's ratio ranging from 0.09 to 0.20 the value obtained is well within the acceptable range.

The pre-consolidation stress p_c obtained corresponds to 87.98 kPa. At the consolidation stage none of the triaxial tests reaches this mean stress. It is possible, however, that during the triaxial compression the $p : q$ state may reach the compression cap. For the internal variables Γ and p_{ref} the values calibrated are 0.00851 and 227.7 kPa, respectively.

The sine of the friction angle obtained varies from the initial value of 0.613 to 0.747 at an equivalent plastic shear strain of 0.07. This corresponds to a variation of the friction angle ϕ between 37.8° and 48.3° which corresponds to common values usually obtained for the friction angle of ballast material. This also corresponds well with the initial estimative made of a friction angle variation between 37.5° to 48.6°.

In retrospect, the calibration procedure is successful in the sense that it allowed to adjust the proposed non-linear material model to the deviatoric and volumetric response of the ballast material and that the parameter values obtained correspond to usual values for ballasted track, although the Young's modulus deviates slightly from the usual values. In the deviatoric stress a good correspondence is obtained for the three confining pressures while the volumetric response at 41.4 kPa is not very satisfactory, however, since there is some uncertainty related to the measurements, the obtained response is accepted. It must be regarded that the utilization of a pressure dependent Young's modulus could result in better correspondence between numeric and experimental values, however, the utilization of that behaviour presents much instability with the non-linear calculation diverging multiple times, and in that regard, even if the model allows that definition, it is not considered initially.

The parametric study in Figure 4.6 allows to better understand the influence of some of calibrated variables in the calibration procedure. The parametric studies are conducted with all variables constant and equal to

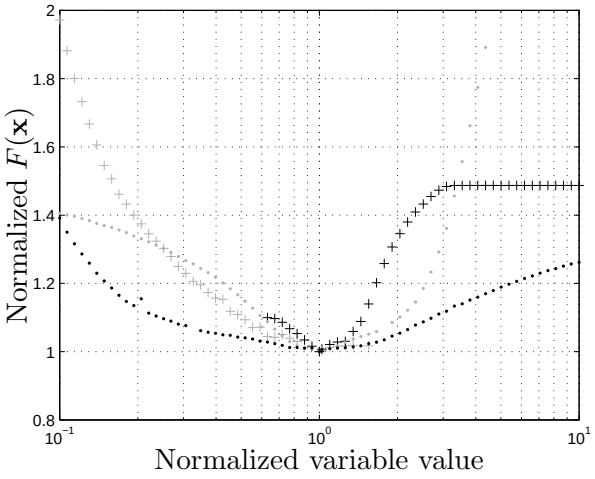

Figure 4.6: Normalized variation of the objective function with calibrated variable values of Young's modulus (+ grey), p_c (+ black), Γ (. grey) and p_{ref} (. black).

the calibrated value, except the variable in study which varies from 0.1 to 10 times its calibrated value. For each time the variable is changed the triaxial test in Diana is simulated and the objective function is determined.

All studied variables exhibit distinct influence in the objective function value. Expectedly, all variables converge for the minimum value of the objective function obtained in the calibration process when they assume their respective calibrated value. It is also apparent that none of the variables allows to obtain a normalized objective function value lower than 1. This is a necessary condition (although not sufficient) to assume that the global minimum is obtained.

It can be observed that not all the variables exhibit a normalized value of the objective function $F(\mathbf{x})$ value in all the parametric domain. The missing points correspond to numeric triaxial tests for which the iterative computation did not reach convergence.

The Young's modulus has high influence in the objective function, the value of the objective function is 1.97 for Young's modulus of 0.1 its calibrated value. As the Young's modulus approaches the calibrated value from the lower end, the objective function presents a monotonically decreasing variation. When the Young's modulus increases to values higher than the calibrated value, the variation of the objective function is much less pronounced with the normalized objective function increasing to 1.02 for a Young's modulus 1.55 higher than the calibrated value. At higher values of the Young's modulus the numeric triaxial simulations do not converge.

Since the step size of the triaxial simulation is already very small, the function has passed its decreasing behaviour and the obtained value is already on par with some of the highest values for the ballast Young's modulus; it is reasonable to assume that there is no need to further explore the domain.

The pre-consolidation pressure p_c has a very distinct influence in the normalized objective function. It is evident that for very low values it will not allow the models to converge. Such can be seen as there is no convergence until the normalized pre-consolidation pressure reaches 0.631, which corresponds to 55.5 kPa. For this pre-consolidation value the third triaxial test already reaches the compression cap with the application of the confining pressure. When the pre-consolidation stress is higher than the calibrated value, the objective function starts to increase rapidly due to the decrease of plastic strain in the models. For $p_c = 291\,\text{kPa}$ the cap is positioned at a point that neither one of the triaxial specimens reach and thus there is no influence of the compression cap in the response. Consequently for any higher values of the pre-consolidation stress the objective function remains constant.

Interpretation of the p_{ref} and Γ influence in the objective function is not so straightforward. These are internal variables that shape the hardening of the compression cap and their physical meaning is not easy to grasp. From equation (4.16) the p_{ref} is a reference pressure around which the pre-consolidation stress will change. This variation is scaled in function of the ratio between the reference pressure and the initial pressure, to this value a fraction is subtracted that depends on the variables m (0.5 by default), Γ, and the plastic volumetric strain ε_v^p. It then becomes evident that the term $-\frac{m}{\Gamma}\Delta\varepsilon_v^p$ scales the influence of the reference pre-consolidation stress since when this term is 0, equation (4.16) becomes:

$$p_c = p_{ref}\frac{p_{c0}}{p_{ref}} \Leftrightarrow p_c = p_{c0} \tag{4.29}$$

the implication being that the compression cap does not move at all. As stated previously the variable m is stated by default in the software and is not changed. Consequently the only variable that will influence the length of the step variation (represent by the second term) will be Γ.

Figure 4.6 confirms the high influence this variable has in the hardening of the compression cap, which influences the objective function. For low values of Γ a large variation of the position of the compression cap occurs. Consequently it re-positions at high compression values and its influence is reduced. Consequently the initial variation of the objective function is minimal. For increasing values of Γ the compression cap moves less and thus the parameter will start to have increasing influence in the value of the objective function. Thus, when the value of Γ approaches the calibrated value the normalized objective function tends to 1 at an increasing ratio.

Furthermore, for higher values of Γ the objective function increases at a seemingly exponential rate due to the fact that the compression cap moves less and its influence in the material behaviour increases.

The influence of the reference pre-consolidation stress p_{ref} is less pronounced, nevertheless a 40% variation of the objective function is obtained in the whole domain.

4.2.5 Case study

To study the non-linear response of the ballast material a study case is defined for which a rail track on foundation soil is simulated using the FEM software. Prior to the simulations in non-linear ballast behaviour, the FEM mesh is validated with a published case in which the track response was measured.

Galvín and Domínguez (2009) presented the results obtained experimentally during certification testing of a new high-speed train line between Córdoba and Málaga. These tests were done by the Spanish Railway Infrastructure Administrator and consisted in recording vibration levels produced by passing trains, in the rails and sleepers, as well as at selected points on the soil surface and in the steel structures supporting the contact line.

The Córdoba - Málaga HST track is a double track ballasted line with UIC 60 rails and mono-block concrete sleepers with length $l_{\mathrm{sl}} = 2.60\,\mathrm{m}$, width $b_{\mathrm{sl}} = 0.6\,\mathrm{m}$, height $h_{\mathrm{sl}} = 0.265\,\mathrm{m}$ (under the rail) and mass $m_{\mathrm{sl}} = 300\,\mathrm{kg}$. The sleeper spacing is $d_{\mathrm{sl}} = 0.6\,\mathrm{m}$. The dynamic soil properties were obtained from a SASW campaign and the inversion procedure corresponded well with the results obtained previously from boring tests. The soil profile was then estimated as containing an upper layer of silt and gravel with a thickness of 1.2 m and a shear wave velocity $C_{\mathrm{s}} = 150\,\mathrm{m/s}$, followed by an intermediate layer of clay with sand-like qualities having a thickness of 2.5 m and shear wave velocity $C_{\mathrm{s}} = 408.4\,\mathrm{m/s}$ resting on a half-space with shear wave velocity $C_{\mathrm{s}} = 635.0\,\mathrm{m/s}$ consisting of very dense sand and blue loam. The soil damping coefficient of 0.02 was estimated using a homogeneous soil equation (Barkan, 1962) and assuming a Poisson's ratio of $\nu = 0.3$.

The measurements used for the verification of the FE mesh were done during the passage of a Ave-Alstrom high-speed train at 298 km/h. The full train configuration was composed of 11 wagons of which 2 locomotives with total mass per axle of $m_{\mathrm{axl}} = 17000\,\mathrm{kg}$, 2 end wagons with mass per axle of $m_{\mathrm{axl}} = 14500\,\mathrm{kg}$, 1 laboratory wagon with mass per axle of $m_{\mathrm{axl}} = 10875\,\mathrm{kg}$ and 6 middle wagons with mass per axle of $m_{\mathrm{axl}} = 17000\,\mathrm{kg}$. The configuration of the Ave-Alstrom high-speed train is represented in Figure 4.7

The FE mesh used to simulate this study case is shown in Figure 4.8 The model has a total length of 50 m and width of 60 m (symmetry conditions), the soil is simulated to a depth of 10m. The rail is modelled with beam

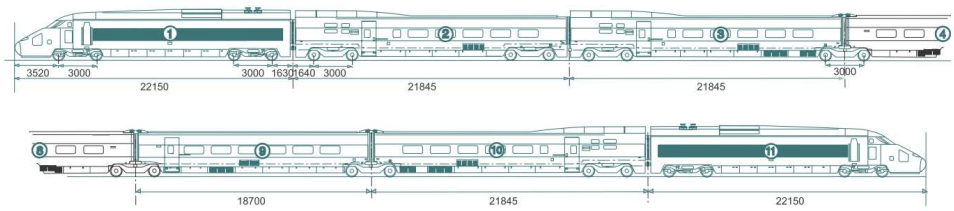

Figure 4.7: Configuration of the Ave-Alstrom high-speed train: locomotives (wagons 1 and 11), laboratory wagon (2), end wagons (3 and 10) and middle wagons (4 to 9), (Galvín and Domínguez, 2009).

elements of three nodes, the interface is modelled with spring-dashpot elements connecting the rail and the sleeper. The sleeper, ballast and soil are modelled with solid prismatic elements. Considering that in non-linear analysis elements with linear interpolation may present numeric shortcomings such as parasitic shear and volumetric locking (TNO, 2005), higher order elements are used comprising 3 nodes per edge for a total of 20 nodes in each prismatic element. Because of this, the total number of elements is kept to a minimum to reduce the elevated number of degrees of freedom. The final mesh is composed of 19108 elements of which 63 are beam elements, 21 are spring-dashpot elements, 1202 are absorbing elements and 17822 brick elements. The total number of nodes is 80265.

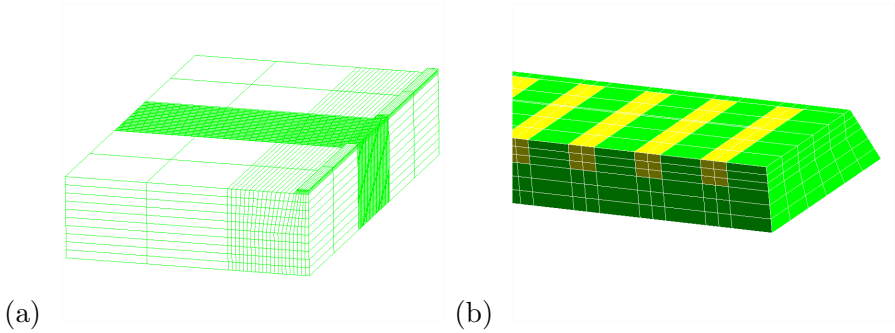

Figure 4.8: FE mesh for non-linear evaluation of ballast response: a) overall model and b) detail of ballast and sleepers.

Because the FE mesh in this case is modified to use second order elements, which implies a reduction of the number of elements and changes in the element size, it is adequate to perform another verification of the model. This comparison allows to validate the FE mesh, reinforcing the validation with experimental results in section 3.3 and the validation with

another numerical model in section 3.5. Even if the study case to be used for non-linear ballast behaviour does not entirely correspond to the case herein simulated, the comparison made with experimental results allows to proceed to non-linear analysis with the confidence that the FE mesh is adequate to simulate the phenomena at hand and that reliable results are obtained.

Since the track uses the same UIC 60 rail of the previously simulated cases, the properties used in the FE simulation are assumed to be the same: bending stiffness $E_{\mathrm{r}}I_{\mathrm{r}} = 6.45 \times 10^{6}\mathrm{Nm}^2$, mass per unit length $\rho_{\mathrm{r}}A_{\mathrm{r}} = 60.3\,\mathrm{kg/m}$ for each rail. For the ballast there are no indications of mechanical properties, consequently the properties obtained from the calibration of the modified Mohr-Coulomb model are admitted, with linear behaviour: ballast Young's modulus $E_{\mathrm{b}} = 293.8\,\mathrm{MPa}$, Poisson's ratio $\nu = 0.3$.

Galvín and Domínguez (2007) conducted numerical studies for a point load moving on the surface of a layered medium and found out that the surface response of the soil was almost the same as that of a homogeneous half-space with the dynamic properties of the upper layer. Following that experiment, they used the same method to simulate the experimental case herein presented, obtaining good correspondence between measurements and numerical results (Galvín and Domínguez, 2009). It should be noted that, as demonstrated in sub-section 3.4, the soil response at low frequencies tends to reach its peak values for velocities close to the shear wave velocity of the semi-infinite lower layer. Therefore, the simplification of considering only the properties of the upper layer may not be a a reasonable approximation for all cases. Nevertheless, in order to verify the method, in the FEM the soil is also simulated as a homogeneous half-space with the dynamic properties of the upper layer, the Rayleigh damping coefficients $\alpha = 2.2707$ and $\beta = 4.3001 \times 10^{-5}$ are obtained from an optimization problem where the frequency dependent damping is approximated do 0.02 in the low frequency range. The transient analysis is conducted using a time step $\Delta t = 2 \times 10^{-3}\,s$ simulating the passage of a single axle load. From the single axle response, the full train response is obtained from the known relative distance and mass of the Ave-Alstrom axles (Figure 4.9).

The track response is very well simulated in the numerical model. The time history of the vertical velocities corresponds very well with the experimental values, with special emphasis on the upwards velocities, the downward velocities are somewhat overestimated in the numerical case. From the frequency content it can be observed that in the low-frequency range (0-50 Hz) the numerical model predicts peak velocities at the correct frequencies although in some cases it is overestimated. As in the experimental case, the model predicts peak velocities in the bogie passing frequency $f = 4.43\,\mathrm{Hz}$ and corresponding high-order harmonic frequencies; also peaks occur in the axle passing frequency $f = 27.59\,\mathrm{Hz}$ and corresponding high-order harmonic frequencies. As Galvín and Domínguez (2009) remarked, the velocities obtained in the frequency range of 40-80 Hz are associated with wheel and rail

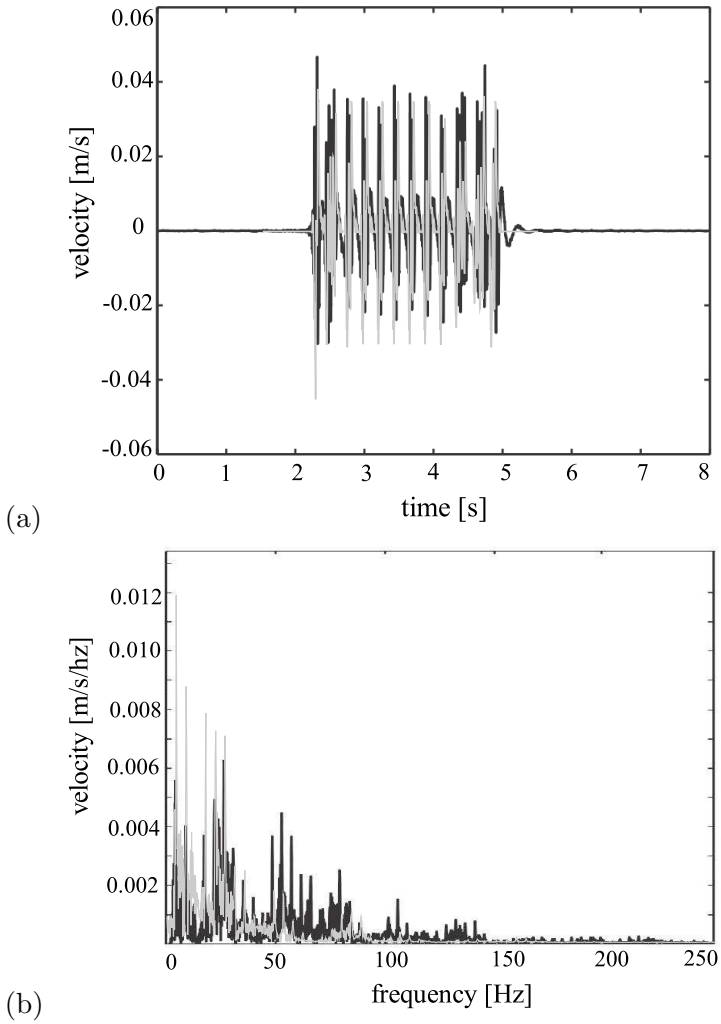

Figure 4.9: Experimental (black) and numerical (grey) vertical velocity in the sleeper: a) time history and b) frequency content.

irregularities, it is natural then that the numerical model underestimated the velocities in these frequencies as these irregularities are not accounted for.

4.2.6 Numerical simulation

From the validated mesh, a similar study case is defined. The study case corresponds to the same ballasted railway track with UIC 60 rails supported every 0.60 m by rubber pads on mono-block concrete sleepers. The track is supported by a ballast layer whose material properties corresponds to the

calibrated values of sub-section 4.2.4. The ballast layer has a height $h_\mathrm{b} = 0.35\,\mathrm{m}$ and density $\rho = 1700\,\mathrm{kg/m^3}$. Below the ballast, the soil is uniform corresponding to an infinite half-space with Young's modulus $E = 350\,MPa$, Poisson's ratio $\nu = 0.3$ and density $\rho = 2000\,\mathrm{kg/m^3}$. In the upper ballast crib and shoulder the continuous modelling approach tends to estimate very low compressive or even tensile stresses, to avoid numerical instabilities these portions of the ballast are simulated considering linear elastic behaviour.

The load corresponds to the passage of a single axle of the Thalys high-speed train ($2 \times 85\,\mathrm{kN}$) at $300\,\mathrm{km/h}$. Due to the limited assumption of constant Young's Modulus in the modified Mohr-Coulomb model, the error this assumption may cause in the FE analysis is further on studied. Two analyses of the track response are computed in which this effect is accounted for. For that matter, a pressure dependent bulk modulus, K is considered, described by the equation:

$$K = K_{ref} \left(\frac{p}{p_{ref}} \right)^n \tag{4.30}$$

in which p is the mean stress (considering the mean stress approximately equal to the coffining stress), n is a material dependent parameter, p_{ref} and K_{ref} are reference confining pressure and bulk modulus, respectively. For the ballast material tested by Suiker et al. (2005), Suiker and de Borst (2003), the reference pressure considered is the lowest confining pressure of 10.3 kPa of the triaxial tests, and the corresponding bulk modulus is estimated from the experimental results $K_{ref} = 54.27\,\mathrm{MPa}$. From the experimental results the bulk modulus at 41.3 kPa is 97.22 MPa and at 68.9 kPa the corresponding bulk modulus is 120.52 MPa. From these values, the variable n in equation (4.30) is estimated $n \approx 0.4198$. Considering the relation:

$$E = 3K(1 - 2\nu) \tag{4.31}$$

these bulk modulus correspond to Young's modulus of 97.68 MPa, 174.98 MPa and 216.94 MPa, at confining pressures of 10.3 kPa , 41.3 kPa and 68.9 kPa respectively. These values obtained are lower than the initial estimation of the Young's Modulus by the calibration procedure $E = 293.8\,\mathrm{Mpa}$, which illustrates the difficulty in determining the threshold between linear behaviour and shear yield when using the large strain triaxial results.

With the definition of parameters p_{ref}, K_{ref} and n, equations (4.30) and (4.31) can be used to determine the Young's modulus at any confining pressure, providing that it is confined between 10.3 kPa and 68.9 kPa. Equivalent linear analyses are defined in which the Young's Modulus depend upon the confining pressure, according to equations (4.30) and (4.31). For the update procedure the ballast is divided into 3 zones (Figure 4.10)

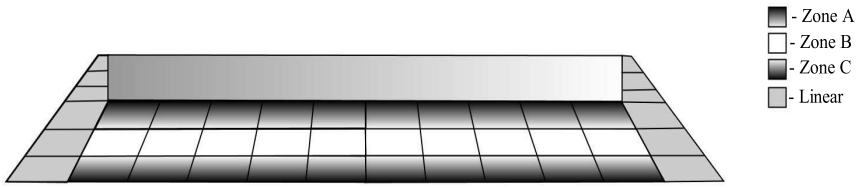

Figure 4.10: Definition of zones A, B and C across the ballast mesh.

The zones A, B and C represent the horizontal layering defined for the ballast material. For each zone, during computation of the axle load passage, the mean stress p is determined and the corresponding Young's modulus is updated. The mean stress p_i of iteration i is compared with the mean stress from the previous iterations p_{i-1} and if the variation is lower than 3% for the three zones, the procedure is complete. Otherwise, another iteration is done using the updated Young's modulus. This procedure is done for two cases: equivalent linear analysis and equivalent non-linear analysis, using the modified Mohr-Coulomb model with equivalent variable Young's Modulus. These analyses complement the linear analysis and the modified Mohr-Coulomb analysis. For easier reference, table 4.3 presents the characteristics and designation of each analysis.

Table 4.3: Characteristics of the numerical models.

Analysis Designation	**Young's modulus**	**Material model**
Linear	Constant	Linear
Non-linear	Constant	Modified Mohr-Coulomb
Equivalent linear	Pressure dependent	Linear
Equivalent non-linear	Pressure dependent	Modified Mohr-Coulomb

Tables 4.4 and 4.5 present the outline of the iteration procedure.

The equivalent linear analysis achieves convergence after 3 iterations. There is a considerable reduction in the mean stress from the initial analysis to the final iteration. The mean stresses range from 28.6 kPa to 36.1 kPa in the initial analysis and are reduced to almost half, varying from 15.4 kPa to 22.4 kPa in the last iteration. The values of the mean stresses obtained are concentrated between the confining stresses of the triaxial experiments of 10.3 kPa and 41.3 kPa. Therefore, the assumption by Suiker et al. (2005), Suiker and de Borst (2003) that their triaxial experiments were adapted for realistic in service confining pressures is herein confirmed. Concerning the final values for the Young's modulus in the ballast, a drastic reduction from

Table 4.4: Iterative procedure for the equivalent linear analysis.

Iteration	Zone	Initial E (MPa)	p (Pa)	$\frac{p_i}{p_{i-1}}$
Initial analysis	A	293.8	36060	-
	B	293.8	31380	-
	C	293.8	28580	-
1^{st} Iteration	A	192.9	22600	0.62
	B	181.9	15860	0.50
	C	174.9	13638	0.48
2^{nd} Iteration	A	158.5	22140	0.98
	B	136.6	17100	1.08
	C	128.2	15860	1.16
3^{rd} Iteration	A	157.2	22360	1.01
	B	141.0	17020	1.00
	C	136.6	15410	0.97

the initially calibrated value is obtained. This is explained by several factors, the previously mentioned difficulty in determining a small strain property from large strain results and the fact that even though the initial calibration is done for the three coffining pressures, a calibration considering only the first two would be more relevant for the case presented.

Table 4.5: Iterative procedure for the equivalent non-linear analysis.

Iteration	Zone	Initial E (MPa)	p (Pa)	$\frac{p_i}{p_{i-1}}$
Initial analysis	A	293.8	36060	-
	B	293.8	31380	-
	C	293.8	28580	-
1^{st} Iteration	A	192.9	32040	0.89
	B	181.9	28660	0.91
	C	174.9	26600	0.93
2^{nd} Iteration	A	183.5	31780	0.99
	B	175.1	28520	1.00
	C	169.7	26500	1.00

In the non-linear iteration procedure much lower differences in the mean stresses occur. The yield surface and the impossibility of the model to develop tensile stresses clearly affects the stress state in the ballast, particularly the mean stress. This is similar to the remarks by Nguyen et al. (2003) that found approximately 15% higher compressive stresses in the ballast when

this was simulated using a no-tension model. Therefore, the consideration or not of yield conditions may have an important influence in the stiffness of the ballast. In this case the final Young's modulus are higher than those of the equivalent linear analysis, although still quite distant from that obtained in the calibration procedure.

The vertical displacements and velocities in the rail and sleeper due to the passage of the Thalys axle at 300 km/h are presented in Figure 4.11 and Figure 4.12. Table 4.6 lists the peak displacements of the four analyses.

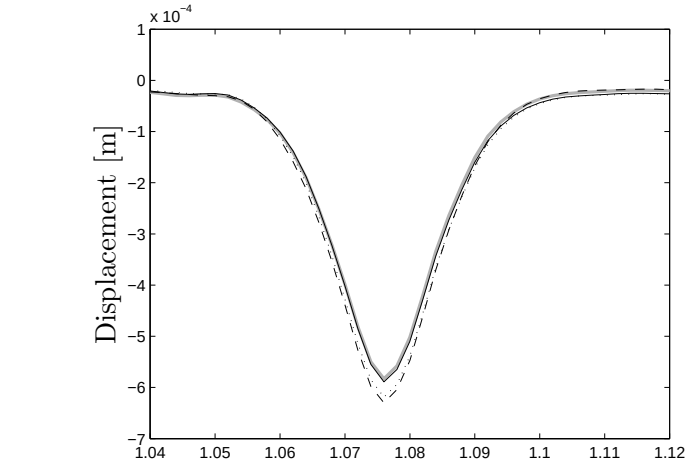

(a)

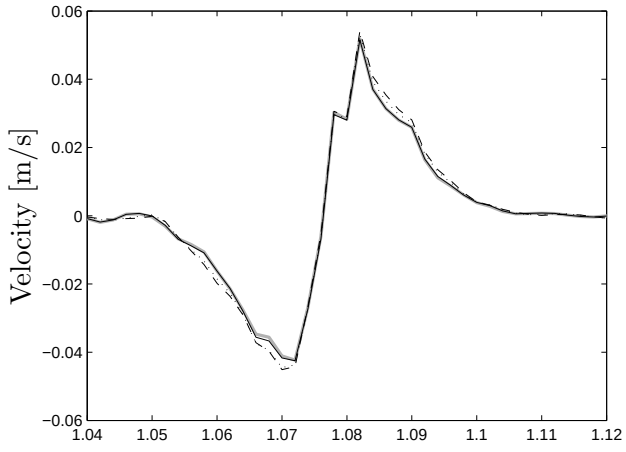

(b)

Figure 4.11: Vertical a) displacements and b) velocities in the rail from single axle passage using ballast models: linear (grey), non-linear (black), equivalent linear (dashed) and equivalent non-linear (dotted).

The consideration of pressure-dependent Young's Modulus does have sig-

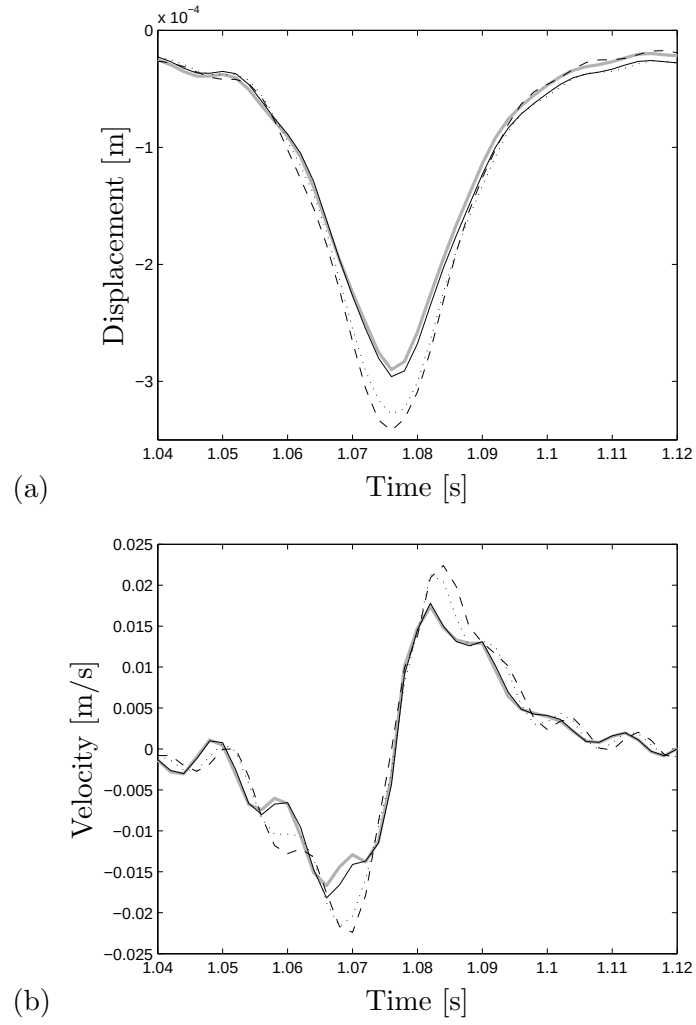

Figure 4.12: Vertical a) displacement and b) velocity in the sleeper from single axle passage using ballast models: linear (grey), non-linear (black), equivalent linear (dashed) and equivalent non-linear (dotted).

nificant influence in the computed rail response. From all the 4 analyses, those whose difference is the consideration of pressure dependent Young's modulus present higher differences in the track response than those in which the difference is the material model. It is also worthwhile to notice that in the models that consider pressure independent Young's modulus the difference between linear and modified Mohr-Coulomb is smaller than in the models that consider pressure dependent Young's modulus. Furthermore there is an inversion in the tendency: when permanent Young's Modulus is considered, the non-linear model presents higher peak displacements than

the linear model; on the other hand, if pressure dependent Young's modulus is considered, the equivalent non-linear model predicts lower peak displacements than the equivalent linear model. Therefore, there is an interaction between the two mechanisms that lead to the development of higher mean stresses (see tables 4.4 and 4.5), correspondingly higher ballast stiffness and lower peak displacements. Therefore, by considering the yield, compression and tensile caps higher mean stresses will develop, resulting in higher ballast stiffness and consequently lower peak displacements.

Table 4.6: Peak displacements of the analyses. ($m \times 10^{-4}$)

	Lin	Nlin	EqLin	EqNlin
rail	5.83	5.89	6.30	6.19
sleeper	2.90	2.96	3.42	3.28

The permanent settlements in the linear or equivalent linear naturally tend to 0, while the extended Mohr-Coulomb and the equivalent extended Mohr-Coulomb tend to predict similar values. Therefore, the consideration of pressure-dependent Young's Modulus seems to bare little influence in this regard. The velocities in the rail and sleeper are influenced in a similar way as the displacements.

The consideration of these different ballast behaviours has more influence in the sleeper response than in the rail. In the rail response the difference in the peak displacement from the linear to the equivalent linear analysis is 8%, while the peak displacement in the non-linear and equivalent non-linear analyses varied 5%. However, higher variations occur in the sleeper with a 18% variation from the linear to the equivalent linear models, and a variation of 11% in the non-linear and non-linear equivalent model. Also, if we account for the influence of the non-linear behaviour, the linear and non-linear models differ 1% in the rail peak displacement and 2% in the sleeper displacement. The iterative analyses have a 2% variation in the rails peak displacement and a 4% variation in the sleeper peak displacement. In conclusion, irrespective of the change that is considered in the ballast behaviour, the relative displacement variation of the sleeper is always approximately twice that of the rail. The sleeper resting directly upon the ballast is more susceptible to any change of its behaviour than the rail which still has the rail pad separating it from the sleeper.

From the analysis of this study case and the 4 different considerations of ballast behaviour it is possible to conclude that the correct determination of the Young's modulus is of much importance to the track response. Although the deviatoric behaviour obtained from the triaxial tests in the literature has an important role in providing higher accuracy to the computations, the mis-

take that may be done by disregarding the deviatoric behaviour seems less important than a mistake in the estimation of the Young's modulus or disregard of its variation with mean stress. Therefore, from the observations and conclusions obtained in this study, it is suggested that future experiments for the determination of track ballast behaviour should include the measurements at very low strains ($< 1 \times 10^{-4}$) to determine the Young's modulus, as well as the large strain measurements.

4.2.7 Stress-strain ballast response

The stress-strain ballast response in the 4 analyses is studied and compared. The analyses are compared taking into account the time history and the stress and strain distribution in the ballast during the axle passage. Since the 3D FE models consider the discrete rails support, the longitudinal as well as the transversal stress distribution is studied. Two transversal sections are further on referred, the "sleeper section" refers to a ballast section directly below the sleeper, the "crib section" refers to a ballast section at mid-length between two sleepers (Figure 4.13).

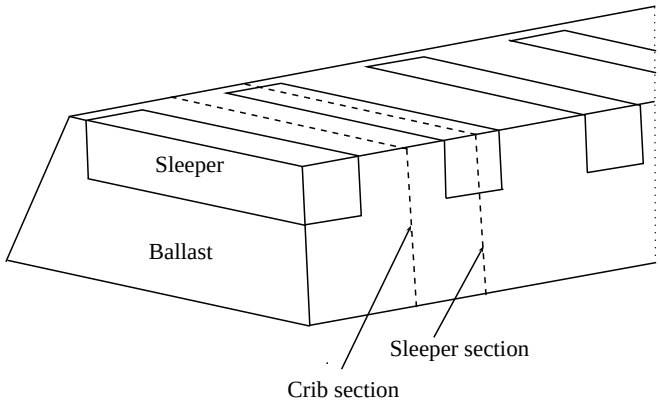

Figure 4.13: Representation of the ballast "Sleeper section" and "Crib section".

Figure 4.14 presents the distribution of the vertical stress σ_{yy} in the "sleeper section" at the time of the passage of the axle load.

The stress distribution is qualitatively similar in the linear and non-linear cases although in the linear case there is a larger concentration of stresses directly below the rail. In the non-linear case a maximum vertical stress of 8.1×10^4 Pa occurs directly below the rail, while almost no stress occurs at the top of the ballast shoulder. Concerning only the ballast material directly below the sleeper, the stresses vary from the mentioned maximum of 8.1×10^4 Pa to a minimum of approximately 2.8×10^4 Pa. It is noticeable that the ballast is reducing the stress levels for the lower layers, at the bottom of the ballast the highest vertical stress is approximately 75% the value of the

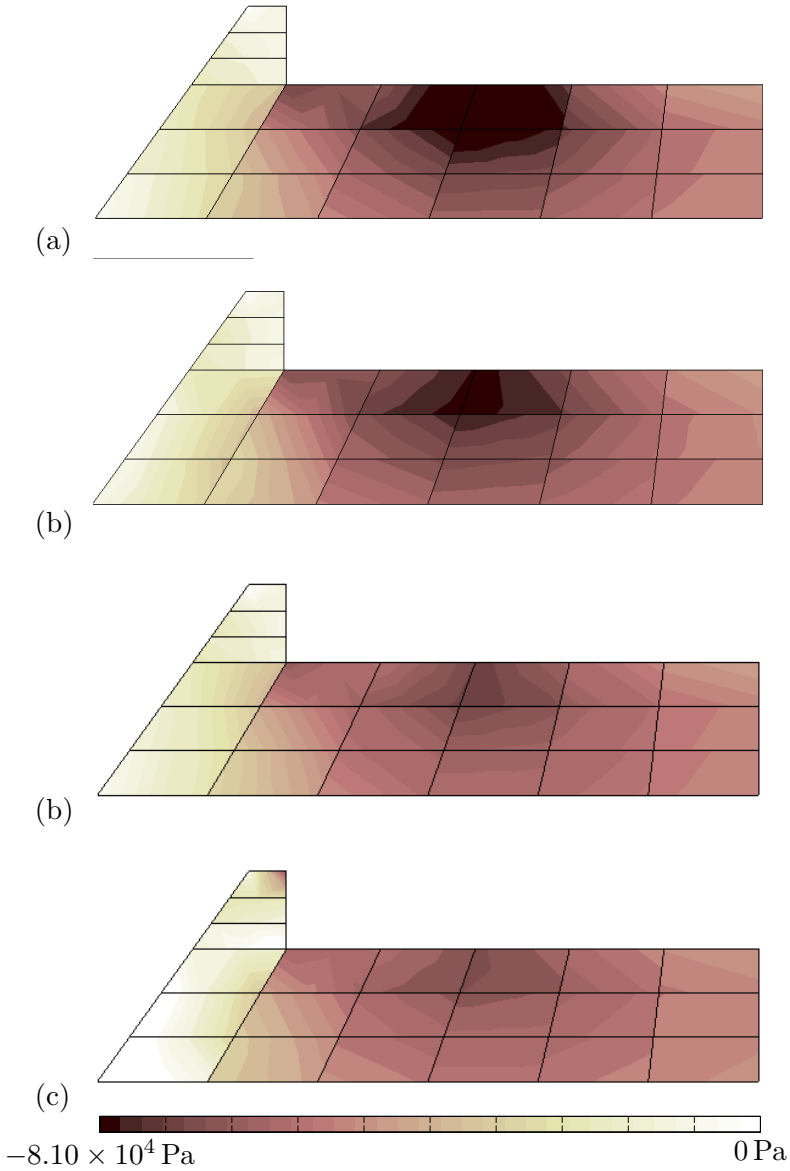

Figure 4.14: Transversal distribution of the vertical stress σ_{yy} in the ballast with a) linear, b) modified Mohr-Coulomb, c) equivalent linear and d) equivalent modified Mohr-Coulomb.

top vertical stress. The quantification of pressure dependent Young's modulus leads to the development of considerably lower vertical stresses in the equivalent linear and equivalent non-linear models. These analyses present very similar stress distributions, either qualitatively or quantitatively. Once again the highest differences in the response occurs between analysis that

include different consideration of Young's modulus.

The stresses in the ballast shoulder are far lower than directly below the sleeper. This portion of ballast material has very limited influence in the layer's overall performance, which confirms that the consideration of linear elastic behaviour in this zone has no influence in the accuracy of the model. In the ballast shoulder the stress distribution is qualitatively similar in all cases.

The vertical strain ε_{yy} obtained in the linear and non-linear cases is compared in Figure 4.15. Qualitatively, there are some minor differences in the deformation pattern of the linear and non-linear cases. In the linear model the deformation is distributed in concentric rings around the point where the most stress from the sleeper is transmitted to the ballast. In the non-linear case the distribution is not as concentric, with high deformation values occurring at mid-high, close to the ballast shoulder.

Quantitatively, the non-linear analysis naturally presents higher strain values of almost 3.0×10^{-4}, although the minimum strains found in each case is nearly the same, approximately 1.2×10^{-4}. The strains in the ballast shoulder are similar qualitatively and quantitatively in both cases. In the models that consider pressure dependent Young's modulus the vertical strains are considerably higher, reaching 4×10^{-4} in the equivalent non-linear model, in either case the top ballast material resting directly below the rail is subject to the higher stresses and strains. Even though the sleeper has a considerable stiffness (30 GPa) it does not distribute the axle load to the ballast in a uniform manner.

Figure 4.16 presents the vertical stresses in the crib section of the ballast at the time the axle load is passing directly above it. There are some noticeable differences between linear and non-linear models concerning the peak stresses in the ballast. There is a substantial decrease in the peak stress of the non-linear model, in comparison with the linear model. The equivalent linear and equivalent non-linear models present again very subtle differences, with highest stresses very similar but occurring at larger zones in the equivalent non-linear model. The stress distribution is surprisingly similar to that of the sleeper section even though the stress is not transmitted from above but from the two adjacent sleepers. The highest vertical stiffness in the sleeper sections occurs at the sleeper-ballast interface, and are transmitted horizontally in the longitudinal direction to the crib section.

The distribution of these stresses from the sleeper sections to the crib sections are better understood with the aid of Figure 4.17. This figure presents a longitudinal cut of the ballast through a vertical plane containing the rail. In it, the distribution of the vertical stresses σ_{yy} in the equivalent non-linear analysis is represented in two different time steps. For better observation of the ballast response, the sleepers are not represented. Therefore, the "sleeper sections" are identifiable as those in which the mesh presents an apparent hole. When the load is passing directly above the sleeper (Figure

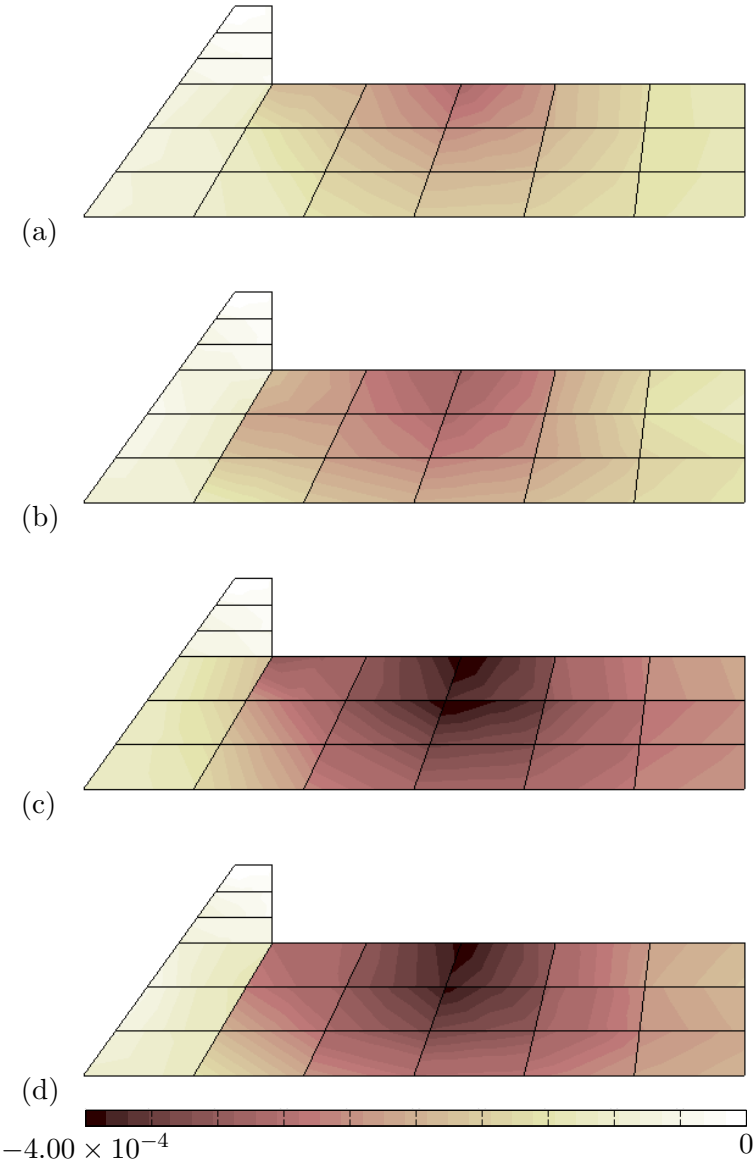

Figure 4.15: Transversal distribution of the vertical strain ε_{yy} in the ballast with a) linear, b) modified Mohr-Coulomb, c) equivalent linear and d) equivalent modified Mohr-Coulomb.

4.17a), most of the stress is transmitted directly to it and through the sleeper to the ballast below. From this contact point between the sleeper and the ballast, the stress is distributed in a radial pattern both in the transversal and the longitudinal directions. Largest strains are transmitted vertically than horizontally, regardless of that, a considerable stress distribution in the

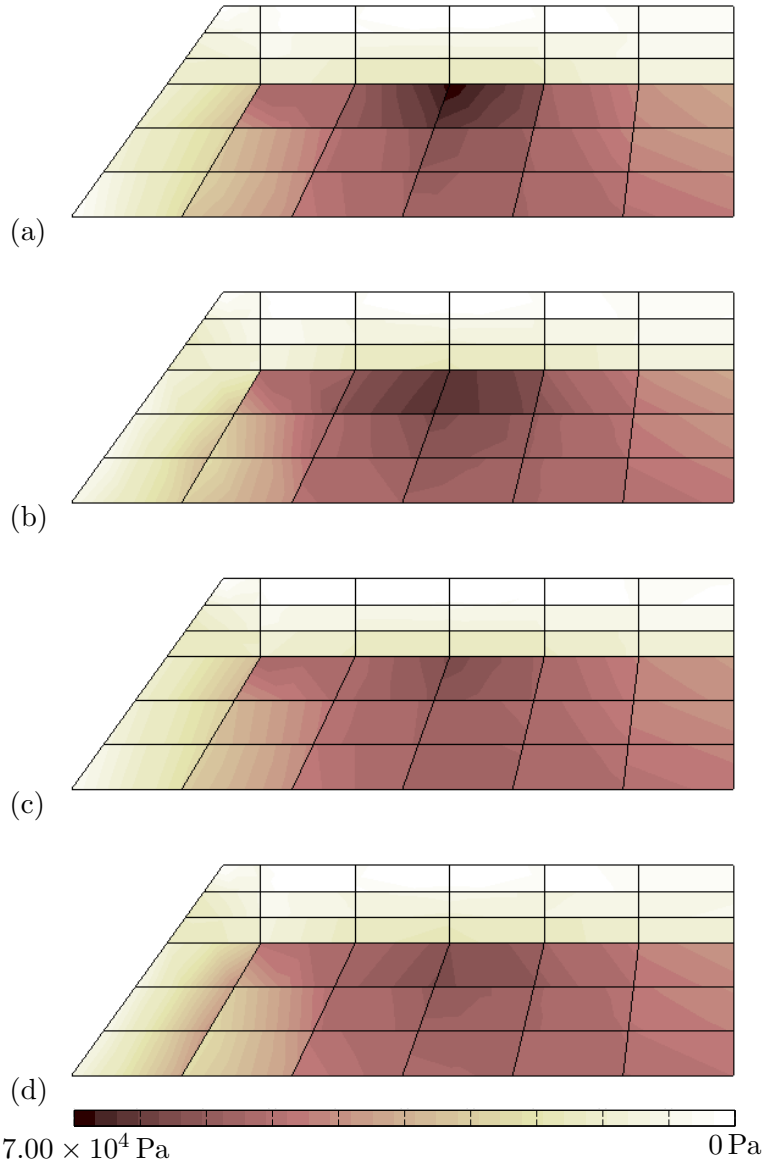

Figure 4.16: Transversal distribution of the vertical stress σ_{yy} in the ballast crib with a) linear, b) modified Mohr-Coulomb, c) equivalent linear and d) equivalent modified Mohr-Coulomb.

longitudinal direction occurs. When the axle load is passing directly above the crib section (Figure 4.17b), the vertical load is transmitted through the rails to the two closest sleepers, each receiving approximately 50% of the load. From these, the loads are distributed to the ballast as usual and radially transmitted. In this time instant the crib section is in the immediate

vicinity of the two loaded sleepers. Consequently, it will be subject also to high stresses transmitted from both. Although these ballast portions are not directly loaded they are still subject to high stresses and their role should not be disregarded. The stresses in the sleeper sections are nevertheless higher than in the crib section, even if the axle load is in the mid-span of the rail (Figure 4.18).

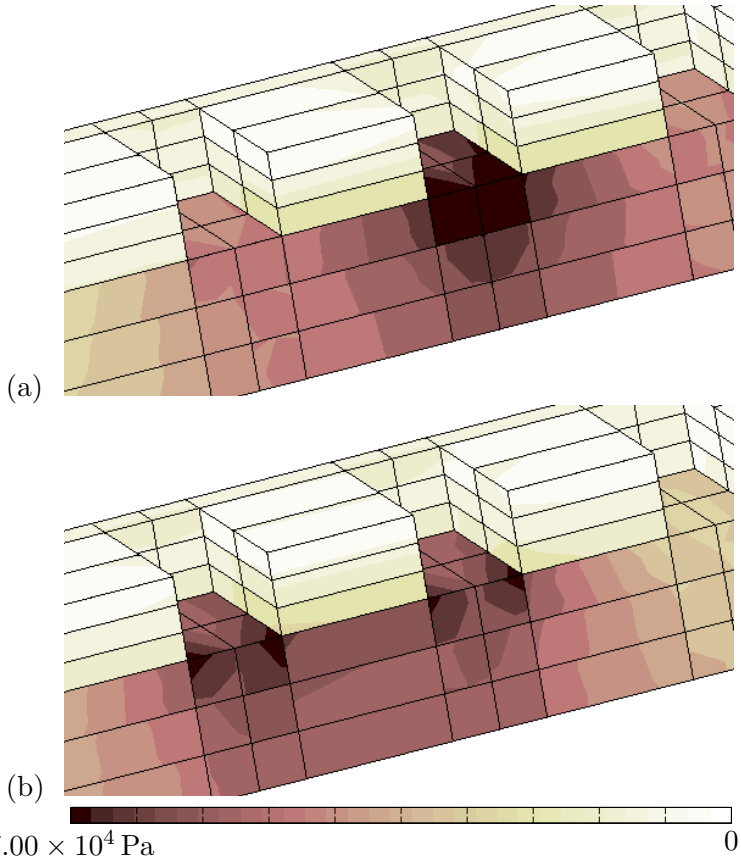

Figure 4.17: Longitudinal distribution of the vertical stress σ_{yy} in the ballast when the load is a) directly over the sleeper, b) at mid-span between two sleepers.

The crib section in study is immediately "after" the sleeper section, in the direction of the moving axle load. As the axle load passes directly above the sleeper section at $t = 1.076\,\mathrm{s}$ the ballast is subject to a peak stress $\sigma_{yy} = 72.1\,\mathrm{kPa}$, in the crib section the stress is increasing as the axle load is only $0.3\,\mathrm{m}$ away but a substantial lower stress is nevertheless present ($\sigma_{yy} = 50.0\,\mathrm{kPa}$). When the axle load passes directly above the crib section ($t = 1.080\,\mathrm{s}$) its vertical stress reaches a peak value $\sigma_{yy} = 54.5\,\mathrm{kPa}$ but still lower than the stress at the ballast below the sleeper ($\sigma_{yy} = 62.5\,\mathrm{kPa}$). With

the continuing axle movement the stress in the sleeper section diminishes as the load is being transmitted mainly to the next sleeper, however, the crib section is in the vicinity of the next sleeper and thus is subject to higher stresses than the sleeper section.

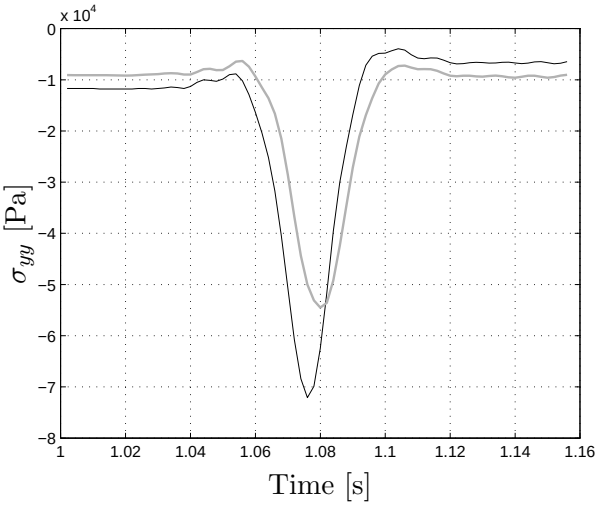

Figure 4.18: Time history of the vertical stress σ_{yy} in the midle of the ballast layer in the sleeper section (black) and crib section (grey) obtained in the equivalent non-linear model.

The stress-paths in the ballast of the equivalent non-linear model are analysed in four different points (Figure 4.19). The four points correspond to the nodes most directly below the axle load in the sleeper section and the corresponding nodes in the crib section. Point A is at the contact between the ballast and the sleeper, while points B, C and D are 0.11 m, 0.23 m and 0.35 m below the sleeper, respectively. The stress paths in the sleeper section are very similar qualitatively (Figure 4.20). Quantitatively the upper ballast points are subject to lower initial stresses ($p_{A0} = 5.3\,\text{kPa}$, $q_{A0} = 7.4\,\text{kPa}$ and $p_{D0} = 8.7\,\text{kPa}$, $q_{D0} = 12.6\,\text{kPa}$) due to the less weight they are subject to. However, these are subject to higher variations of p and q reaching higher maximum values of isotropic and deviatoric stresses ($p_{A\text{max}} = 36.5\,\text{kPa}$, $q_{A\text{max}} = 53.8\,\text{kPa}$ and $p_{D\text{max}} = 28.4\,\text{kPa}$, $q_{D\text{max}} = 43.7\,\text{kPa}$). These variations ($\Delta p_A = 31.2\,\text{kPa}$, $\Delta q_A = 46.4\,\text{kPa}$ and $\Delta p_D = 19.7\,\text{kPa}$, $\Delta q_D = 31.1\,\text{kPa}$) are similar to those obtained by Araújo (2011) in the ballast for a different case study, using Mohr-Coulomb and Hujeux material models, even though in that case the ballast was subject to an initial pressure of 20 kPa in its top. The stress paths in the upper crib section are different due to the fact that the stresses are transmitted to them almost horizontally during the passage of the axle load. Therefore,

these stresses are mostly of the deviatoric kind. Because of this, the upper ballast portions in the crib may be subject to the highest mobilized friction of angle. The crib ballast near the base has stress paths similar in shape and size to the sleeper section base ballast due to the fact that in that part the principal stress is closer to vertical and the local effect of the discontinuous rail support is dissipated. Concerning the mean stress, it is never lower than 3.3 kPa in the upper crib section or higher than 36.5 kPa in the upper ballast directly below the sleeper.

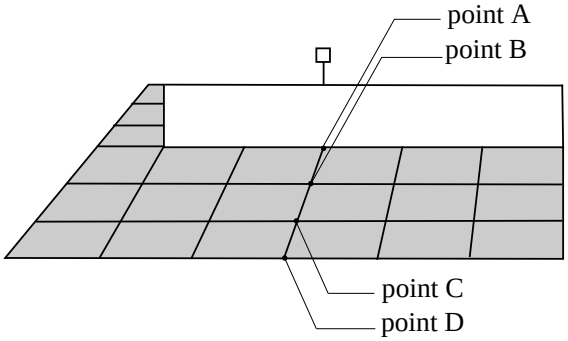

Figure 4.19: Definition of ballast points A to D.

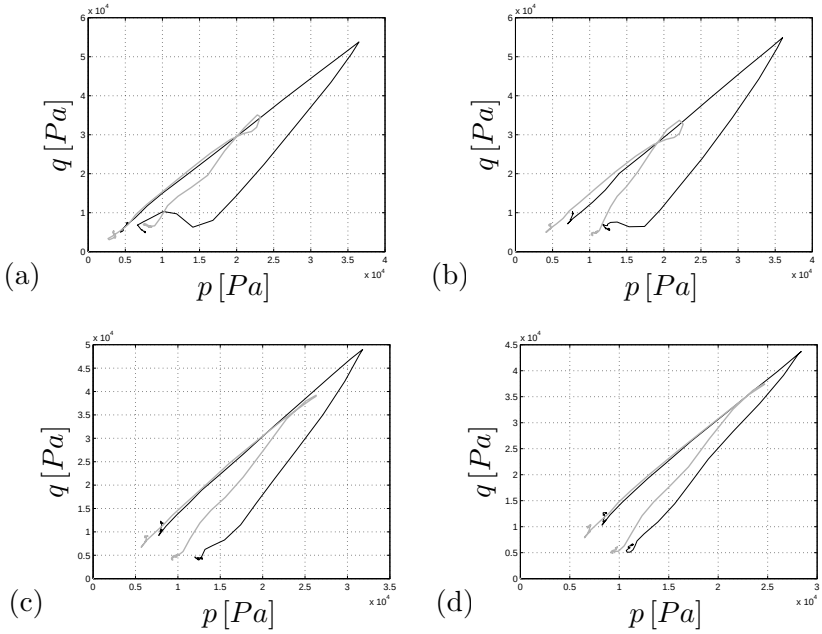

Figure 4.20: Stress path in the ballast sleeper section (black) and crib section (grey) in: a) point A, b) point B, c) point C and d) point D.

It is shown that for real representation of the ballast stress conditions the discrete ballast support must be considered and to this effect only 3D

models (either full 3D or periodic) are suitable. The prospect evolution from this work, regarding stress distribution in the ballast from axle passage, would be the definition of 3D DE models for a more accurate determination of the stresses in the crib sections. The large computational cost of DE models prevents the simulation of a full 3D track with moving loads in the rail. Current models found in the literature focus in the reproduction of the sleeper sections with a single point load with variable magnitude. This loading scheme may be suitable for sleeper sections study but do not represent well the conditions of the crib sections in service. It is foreseeable that the continuous improvement in computing power will in the future allow the definition of more complex models, namely more refined 3D FE meshes and 3D DE-FE models to reproduce a rail track. Therefore, more elaborate numerical studies may be developed in the future regarding the distinct roles of the "sleeper" ballast and "crib" ballast.

4.2.8 Partial remarks

The section presented the study of the non-linear ballast behaviour. The deviatoric ballast behaviour was obtained from experimental data (Suiker and de Borst, 2003). The non-linear material model used is a modified Mohr-Coulomb with hardening/softening of the yield cap as well as a compression cap with hardening. Due to numeric instabilities it was not possible to include pressure-dependent stiffness, however, this was accounted for in equivalent analyses. Four different ballast behaviour possibilities were defined, ranging from the linear elastic to the equivalent non-linear. A study case was defined and the passage of an axle load was simulated considering the four different definitions of ballast behaviour.

The results suggest that the consideration of pressure-dependent Young's modulus of the ballast has more influence in the track response than the definition of yield and compressive caps. To these conclusions contribute the fact that the Young's modulus of the ballast was calibrated to the experimental results of 10.3 kPa, 41.3 kPa and 68.9 kPa whereas the ballast material is only subject to isotropic pressures close to the first two values, and that the Young's modulus is not easily determined from large strain results.

From the analysis of these results it is suggested that in future experimental campaigns on track ballast the Young's modulus is directly determined experimentally and the deviatoric behaviour is obtained for several confining pressures between 5 kPa and 50 kPa. These seem to be the values of the mean stresses the ballast is subject to in service conditions.

Results also suggest that the crib ballast is subject to significant stresses, close to those that occur below the sleeper. Future studies with, for instance, 3D DE analyses could confirm these results to ensure that the continuous modelling of the ballast material is not provoking excessive transmission of stresses from the sleeper ballast to the crib ballast.

4.3 Non-linear soil behaviour

4.3.1 Cyclic response

In the consideration of traffic load the soil takes an important role in the track response. It is well established that the deformation characteristics of soils depend heavily on the level of shear strain to which soils are subjected. Soils respond linearly for very small shear strains and in an increasingly non-linear way with increasing shear strains, the failure takes place normally at a strain level of a few percent.

The majority of soils subject to symmetric cyclic loading present a typical response such as the one shown in Figure 4.21. It represents the typical response to the first load (dashed curve O-A) followed by the unloading A-B-C and finalized by the reloading C-D-A. This representation is ideal because it is symmetric and the diagram closes at point A, and so any stiffness degradation through the cycle is neglected.

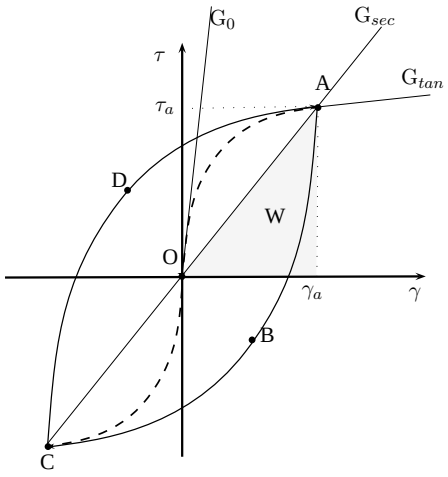

Figure 4.21: Typical stress-strain response of soils to cyclic loading.

The dashed curve O-A is the backbone curve. Starting from point O, the beginning of the backbone curve curve is almost linear, and for very small strains the stress-strain ($\tau - \gamma$) relation can be defined by the initial shear modulus G_0. As the shear strain increases the response of the soil follows the backbone curve and the consideration of linear relation between shear and strain becomes decreasingly accurate. If the shear strain increases monotonically from 0 to γ_a and then decreases, the unload will not follow the backbone curve but will follow the curve A-B-C presenting permanent deformation when the shear stress changes signal. From point C a new reversal in the deformation will follow the curve C-D-A. Upon returning to point A, the soil will continue along the backbone curve if the shear strain

does not reverse again. In rigour, the reload may not return exactly to the point A. For now this effect is neglected and thus it is considered that the hysteresis curve closes at point A.

For the load-reload cycle presented in Figure 4.21 a secant shear modulus can be computed to relate the shear strain γ_a and the shear stress τ_a:

$$G_{sec} = \frac{\tau_a}{\gamma_a} \tag{4.32}$$

where G_{sec} is the shear modulus of the soil at the shear strain γ_a. The size of the curve can be conveniently defined through its area, which is a measurement of the energy dissipation, and is therefore related with the damping coefficient:

$$\xi = \frac{\Delta W}{4\pi W} \tag{4.33}$$

ΔW is the area of the curve, and W is the energy imposed by the strain γ_a:

$$W = \frac{G_{sec}\gamma_a^2}{2} \tag{4.34}$$

and thus:

$$\xi = \frac{\Delta W}{2G_{sec}\gamma_a^2} \tag{4.35}$$

ξ is the damping ratio that the soil exhibits for a shear strain level γ_a. It is then clear that by knowing the backbone curve of a soil and the rules that shape the unload and reload curves, it is possible to know the secant shear modulus G_{sec} and the damping ratio ξ that correspond to any shear strain level γ_a. Then, curves like the ones shown in Figure 4.22 can be traced where the variation of shear modulus and damping are plotted.

As it is known that the deformation characteristics of the soils are heavily dependent on the deformation level, experiments have been done to properly determine the strain dependent variation of shear modulus and damping in a great number of different soils. As stated previously, for small strains the shear modulus remains practically unchanged and it is considered that the soil is in its elastic state. The shear strain at which the stress-strain relation becomes markedly non-linear changes from soil to soil, and can change in a soil depending on some factors.

It has been noted that for sands an increasing confining stress results in a larger linear shear strain threshold (Kokusho, 1980). Similarly, the damping shows smaller variation with shear strain when the confining stress is higher.

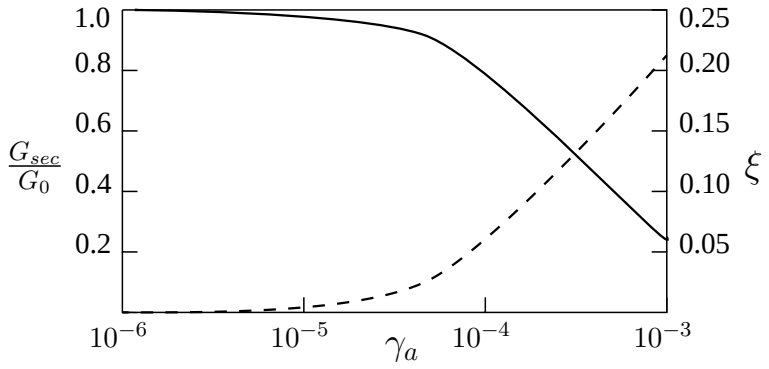

Figure 4.22: Typical soil variation of stiffness (full) and damping (dashed) with shear strain.

Vucetic and Dobry (1991) gathered data from 16 publications that studied the influence of various parameters in the variation of shear modulus and damping with shear strain (Figure 4.23). It was noticed that the plasticity index highly influenced the shape of the modulus reduction and damping increase curves. Highly plastic soils show less variation of the shear modulus, consequently the linear threshold shear strain can be much higher for these soils than for low plasticity soils. It has been also documented that the over-consolidation ratio does not significantly influence the secant shear modulus G_{sec} or damping ratio ξ.

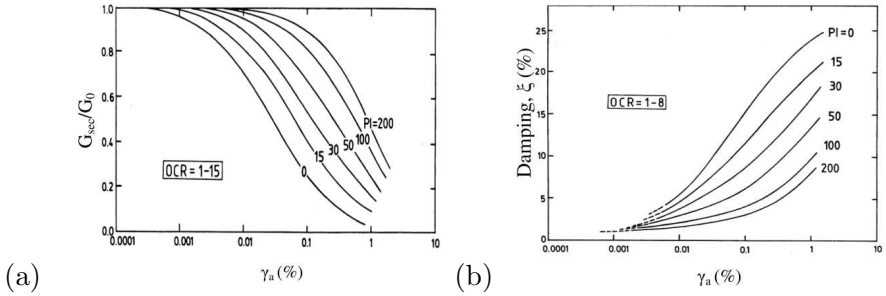

(a) (b)

Figure 4.23: Relation of cyclic shear strain with a) normalized shear modulus and b) damping (Vucetic and Dobry, 1991).

Ishibashi (1992) studied the effect of the mean effective shear stress on the modulus reduction curves of non-plastic and plastic soils (Figure 4.24). In this study, the triaxial tests were done for a variable mean effective stress between $1\,\mathrm{kN/m^2}$ and $400\,\mathrm{kN/m^2}$. The modulus reduction curve is much less sensible to the mean effective stress on soils of higher plasticity index.

The results of experimental studies conducted by many authors were

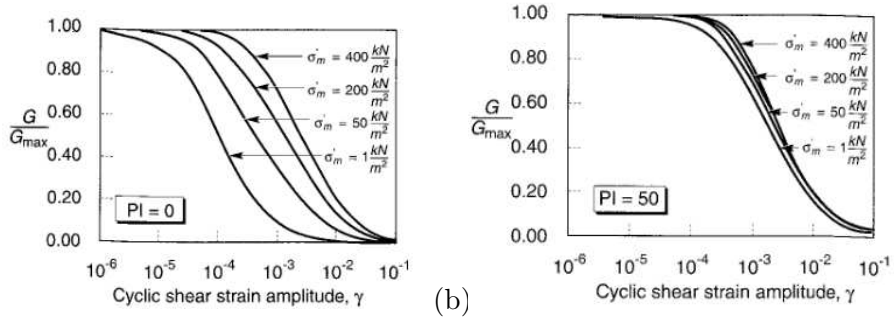

Figure 4.24: Influence of mean effective confining pressure on modulus reduction curves for a) non-plastic and b) plastic soil (after Kramer (1996) and Ishibashi (1992)).

compiled by Ishibashi and Zhang (1993) and they suggested the following relations:

$$\frac{G_{sec}}{G_0} = K(\gamma_a, PI)(\sigma'_m)^{m(\gamma_a,PI)-m_0} \tag{4.36}$$

where:

$$K(\gamma, PI) = 0.5\left\{1 + \tanh\left[\ln\left(\frac{0.000102 + n(PI)}{\gamma_a}\right)^{0.492}\right]\right\} \tag{4.37}$$

$$m(\gamma_a, PI) - m_0 = 0.272\left\{1 - \tanh\left[\ln\left(\frac{0.000556}{\gamma_a}\right)^{0.4}\right]\right\}\exp(-0.0145PI^{1.3}) \tag{4.38}$$

$$n(PI) = \begin{cases} 0 & \text{if } PI = 0 \\ 3.37 \times 10^{-6} PI^{1.404} & \text{if } 0 < PI \leq 15 \\ 7.0 \times 10^{-7} PI^{1.976} & \text{if } 15 < PI \leq 70 \\ 2.7 \times 10^{-5} PI^{1.115} & \text{if } PI > 70 \end{cases} \tag{4.39}$$

γ_a is the shear strain amplitude and PI is the plasticity index

When subject to undrained cyclic loading, the backbone curve of the soil can degrade with the number of cycles. This occurs when the shear strain surpasses a threshold cyclic strain, usually between 0.01% and 0.1% (Figure 4.25).

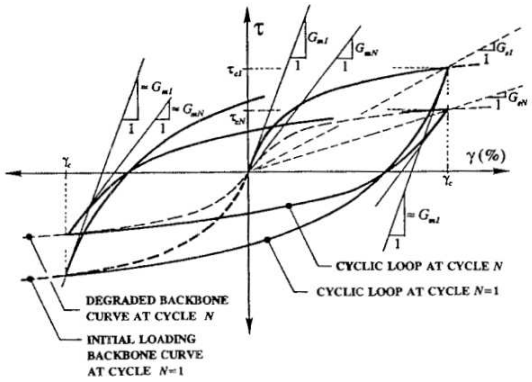

Figure 4.25: Representation of the backbone curve degradation with number of cycles (Matasovic and Vucetic, 1995).

The quantification of this degradation has been introduced by Idriss et al. (1978), by the definition of a degradation index δ that relates the secant shear modulus of the first cycle G_{sec1} with the secant shear modulus of cycle N, G_{secN}:

$$\delta = \frac{G_{secN}}{G_{sec1}} \tag{4.40}$$

it was observed that the relation of $\log \delta$ with $\log N$ is approximately constant (Figure 4.26), and thus the concept of degradation parameter t_N was created:

$$t_N = -\frac{\log \delta}{\log N} = N^{-t} \tag{4.41}$$

4.3.2 Stress-strain models for cyclically loaded soils

The realization that the soil deformation characteristics can be highly influenced by the induced level of shear strain has led to the development of models that can simulate this effect. When modelling soils which are cyclic or randomly loaded, it is important to incorporate a material model that is accurate to simulate the material at the shear strain level that is expected. When the soil behaviour is expected to remain within the small strain range, linear elastic models may be accurate. For higher strain values, usually more complex models should be used.

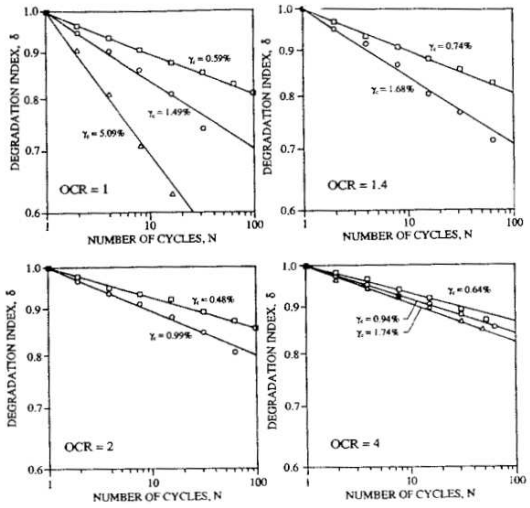

Figure 4.26: Relation of degradation index and the number of cycles for a VPN clay (Matasovic and Vucetic, 1995).

Linear visco elastic models

For small strains the linear relation between stress and strain may be accurate, however, it is known that there is always a certain degree of damping in the soils and this can lead to important variations in the soil's response. One way to overcome this is to recur to linear viscoelastic models. These models consider the linear stress-strain relation, but by including a viscous component provide the necessary energy dissipation to simulate damping in the soil. These models can be represented by a spring-dashpot element of which the Kelvin and Maxwell models are prime examples. One drawback of these models is that the viscous component of the tension is dependent of the frequency: in the Kelvin model the damping increases with increasing frequency while in the Maxwell model the inverse relation is found. Because of this, the application of any spring-dashpot model to real cases should be restricted to those where the relevant frequency range is very limited. Models are also available in which this short come is addressed. These rely on the similar consideration of spring-dashpot systems, but in which the dashpot reaction is independent of the frequency. The consideration of a rate-independent dashpot has been questioned and it does not have any physical correspondence (Ishihara, 1996), but it serves the purpose of providing a numerical approximation of viscoelastic models to soil behaviour. The application of a rate-independent dashpot to the Kelvin model results in the non viscous type Kelvin model.

Equivalent linear models

One way to incorporate the modulus and damping dependence of shear strain in soils is by the utilization of linear models in which the deformation characteristics are consistent with the induced shear strain. In equivalent linear models the procedure consists in running the simulation in a linear elastic model, the shear strain level in the soil is then determined, G_{sec} and ξ are updated to be consistent with the shear strain level and the simulation is done again to compute the new strain levels and check if the variation from the previous iteration stays within an adopted tolerance. The iterative procedure attempts to achieve a linear model in which the deformation characteristics are equivalent to those of the non-linear soil response. One problem with this approach is that in dynamic simulations the shear strain induced in the soil can have large variations in the time span that is simulated, therefore, an objective function is needed to define to which shear strain level are G_{sec} and ξ updated. For most laboratory tests in which the modulus reduction and damping variation curves are defined, the solicitations are harmonic and the shear strain level is characterized by the maximum shear strain amplitude, however, for transient loading originating from traffic or earthquake, the time history of shear strain can be highly irregular and the peak strain is not representative of the strain history of the soil. It is then adequate to determine an effective shear strain that better represents the soil response. In earthquake engineering the effective shear strain has been empirically found to be between 50% and 70% of the shear strain peak value. Since the soil response is little sensitive to variations within these percentages it is common to define the effective shear strain as 65% of the peak shear strain amplitude. Idriss and Sun used a more rigorous approach in which the effective shear strain to maximum shear strain ratio R_γ is computed considering the earthquake magnitude M:

$$R_\gamma = \frac{M-1}{10} \tag{4.42}$$

For transient loads resulting from traffic, no similar suggestions were found in the literature to compute the effective shear strain ratio. Therefore, authors tend to consider the empirical consideration used in earthquake engineering (Costa et al., 2010).

Although the procedure allows to approximate the soil response taking into account the modulus reduction and damping variation with shear strain, it must be noted that the resulting final simulation is still a linear elastic calculation. This implies that the soil properties, although adequately updated, remain constant through the time history of the dynamic simulation and permanent deformations or failure of the soil are not considered.

The advantages of this approach are its simple implementation within any linear calculation and the possibility of using directly the modulus re-

duction and damping variation curves to adjust the model. Because the calculation is ultimately linear, the approach can be implemented in models that are computed in the frequency domain, usually these have numerical advantages over models in the time domain and allow for a quicker computation.

This method has been adapted into a highly used one-dimensional soil response analysis called SHAKE (Schnabel et al., 1972). Other programs for 2D and 3D soil seismic response where the equivalent linear approach is employed were developed, such as the FLUSH (Lysmer et al., 1975) and GROUND 2D (Deng et al., 1995).

It has been noted that equivalent linear techniques tend to overestimate the damping of the soils. Since the damping is updated for the representative shear level, it does not account for the fact that the higher frequency component can be considerable and thus the smaller cycles at these frequencies contribute with lower damping. Acknowledging these short comes, some authors have proposed frequency dependent algorithms for equivalent linear models with good comparison with measured site responses (Furumoto et al., 2000, Assimaki and Kausel, 2002).

Cyclic non-linear models

Despite the convenience and simplicity of the equivalent linear models, these are still simplifications that provide only a generic approximation of the soil behaviour. To better reproduce the soil's response it is necessary to define non-linear models computed in a time integration scheme such as the famous Newmark method.

In cyclic non-linear models the hysteresis curve is incorporated in the model's response and the shear strain and damping variations result implicitly from the fact that the model follows the hysteresis curve, in the same way that occurs in practical cases.

Most of these models are distinguished by the way that they represent the backbone curve and the stress reversal curves, but they usually follow a set of rules called the extended Masing Rules:

1. For the initial load, the stress-strain curve follows the backbone curve.

2. If a stress reversal occurs at a point defined by (γ_a, τ_a) the stress-strain curve follows a path given by

$$\frac{\tau - \tau_a}{2} = F_{bb}\left(\frac{\gamma - \gamma_a}{2}\right) \tag{4.43}$$

   where F_{bb} is the function of the backbone curve. This means that the unloading and reloading curves will have the same shape as the

backbone curve but enlarged by a factor of 2 and with the origin translated to the point where the stress is reversed.

3. If the unloading or reloading curve exceeds the past maximum strain and intercepts the backbone curve, it will follow the backbone curve onwards.

4. If the unloading or reloading curve crosses an unloading or reloading curve of the previous cycle, it will follow the unloading or reloading curve of the previous cycle onwards.

Models that comply with these rules are called extended Masing models. Figure 4.27 shows an example of the variation of shear stress with time and the resulting stress-strain behaviour according to the Masing rules.

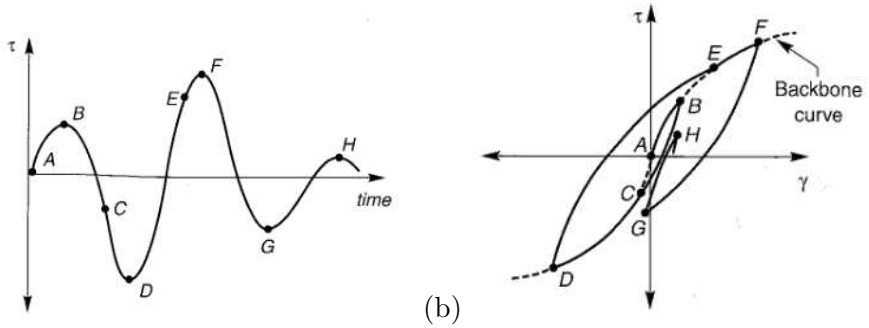

Figure 4.27: Soil response according to the Masing rules: a) variation of shear stress in time and b) corresponding stress-strain behaviour (Kramer, 1996).

At zero shear stress, the shear strain is not necessarily zero, meaning that these models have the ability to present permanent deformation, which is an advantage over the equivalent linear models. Many extended Masing models have been developed and used throughout the years, a few examples are presented in the following.

The hyperbolic model defines, as the name states, the backbone curve as a hyperbola. The backbone curve is bounded by two lines that are tangent to it at small and large strains (Figure 4.28 a). The numerical representation of the hyperbolic curve is given by:

$$F_{bb} = \frac{G_0}{1 + \left(\frac{|\gamma_a|}{\gamma_r}\right)} \tag{4.44}$$

in which γ_r is the reference strain, the strain that would occur at failure stress if the soil behaviour was linear. In Figure 4.28 b) the modulus reduction

and damping variation with shear strain is plotted against the shear strain normalized to the reference strain.

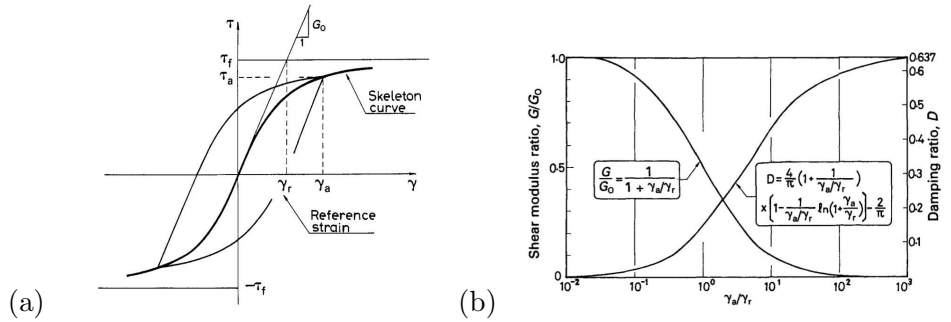

Figure 4.28: Hyperbolic model: a) definition of reference strain and b) variation of shear modulus and damping with normalized shear strain (Ishihara, 1996).

Since the variation of G_{sec} and ξ are correlated to the same variable, they can be correlated with each other. In Figure 4.29 this correlation is plotted with an approximated range where the majority of test data was obtained.

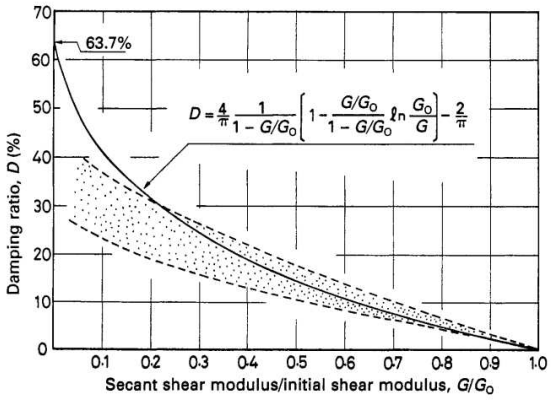

Figure 4.29: Relation between damping ratio and shear modulus ratio for the hyperbolic model (Ishihara, 1996).

The Ramberg-Osgood model defines the backbone curve using the following relation:

$$\frac{\gamma}{\gamma_y} = \frac{\tau}{\tau_y}\left[1 + \alpha_r \left|\frac{\tau}{\tau_y}\right|^{r-1}\right] \tag{4.45}$$

where τ_y and γ_y are carefully chosen stress and strain, α_r and r are also user defined parameters that can be calibrated in order to better suit the desired soil behaviour. Usually τ_y and γ_y are set as the maximum stress τ_f and reference strain γ_r. This changes equation (4.45) into:

$$\frac{G}{G_0} = \frac{1}{1 + \alpha \left| \frac{G}{G_0} \frac{\gamma_a}{\gamma_0} \right|^{r-1}} \tag{4.46}$$

from this, the damping is obtained:

$$\xi = \frac{2}{\pi} \frac{r-1}{r+1} \alpha \frac{\left| \frac{G}{G_0} \frac{\gamma_a}{\gamma_r} \right|^{r-1}}{1 + \alpha \left| \frac{G}{G_0} \frac{\gamma_a}{\gamma_r} \right|^{r-1}} \tag{4.47}$$

The Iwan model (Iwan, 1967) relies on the assumption that a hysteretic system can be constructed by a large number of elasto-plastic elements with different yield levels. The model consists in a series of spring-slip elements disposed in either a series or parallel combination. Unlike other models that define a function for the backbone curve and the unloading-reloading curves separately, this model implicitly complies with the Masing rules and by simply defining the appropriate backbone curve it will ensure that the unloading and reloading are accurate.

There are some limitations of the Masing models in the reproduction of the hysteretic damping at high strains, at which these models tend to increasingly overestimate the damping. Therefore, if a model is to be applied in a simulation where repeated cycling at very large strains is expected then a Masing model is not suitable. The short come of these models in reproducing damping at high strains has been attributed mainly to the second Masing rule which models unloading and reloading (Figure 4.30).

Realising this limitation, several authors have proposed alterations to the models or to the Masing rules. Pyke (1979) suggested an alternative to the second Masing rule in which the factor correlating the backbone curve and the reload/unload curves is not constantly 2 but rather dependent upon the shear strain. Similarly, other authors suggested formulations that somehow recur to a damping reduction factor (Darendeli, 2001, Phillips and Hashash, 2009). On the other hand Ishihara et al. (1985) suggested that shaping the unload/reload curves with the backbone curve is too restrictive and suggested a model in which two distinct backbone curves are defined, one shapes the initial soil response and the other shapes the stress reversal curves.

4.3.3 Case study

A case study is defined to study the non-linear subgrade behaviour under high-speed trains. It relies on the simulation of a hypothetical case of the

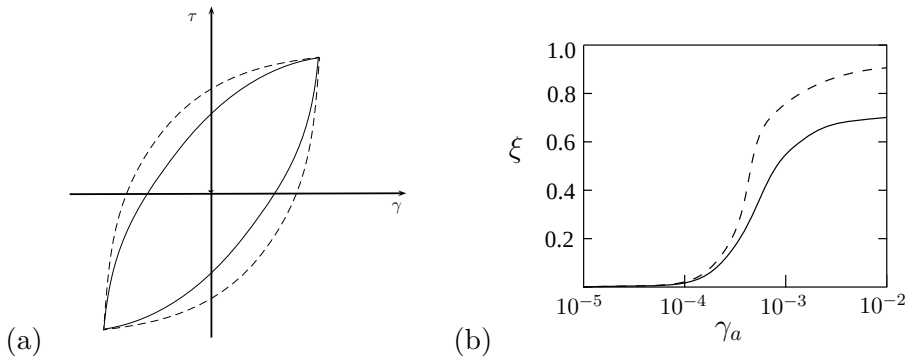

Figure 4.30: Comparison of experimental (full) and Masing (dashed) a) hysteresis curve at high strains and b) damping curve.

railway track from section 3.4.4 over a soil material for which the strain dependent characteristics are known, this experimental data is obtained from the literature. To study this, a 3D FE mesh is used with different material models: a linear analysis considers solely the small strain properties of the soil; an equivalent linear analysis iteratively updates the soil's properties to account for the non-linear behaviour and a non-linear analysis requiring the implementation of a cyclic non-linear model in the FE software.

Wang and Kuwano (1999) preformed a series of cyclic triaxial tests on clayey sands in order to determine the strain dependency of shear modulus and damping ratio of these soils. This was motivated by the lack of knowledge of the influence of the fine content in the dependency of shear modulus and damping with shear strain. For that, the clayey sands were prepared by mixing Kawasaki clay and Toyoura sand obtaining several mixtures with Plasticity Index of 2, 5, 10 and 30. The specimens of each mixture, with 50 mm in diameter and 125 mm in height were fully saturated and consolidated in confining stresses of 98, 196 and 392 kPa. After consolidation the cyclic triaxial tests were done in undrained conditions by the application of axial stress. According to the Japanese Standard, the shear modulus and damping were obtained and the 10^{th} of 12 cycles. The shear modulus at the 10^{th} cycle is obtained using equations (4.32) and (4.33). For each mixture and consolidation stress, 10 different amplitudes of axial stress were applied in order to obtain the shear modulus and damping at different shear strain amplitudes. It is easily demonstrated that for the case of triaxial tests, the shear stress τ and shear strain γ can be obtained from the axial stress σ_a and axial strain ε_a using

$$\tau = \Delta\tau = \frac{\Delta\sigma_a}{2} \tag{4.48}$$

$$\gamma = \Delta\gamma = \Delta\varepsilon_a(1 + \upsilon) \tag{4.49}$$

Figure 4.31 shows the results for the mixture M10 (i.e. with Plasticity Index of 10) .

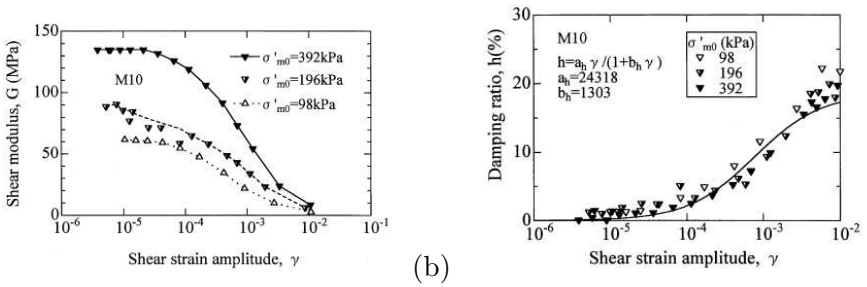

(a) (b)

Figure 4.31: Experimental results of the M10 clayey sand, cyclic shear strain dependence of a) shear modulus and b) damping (Wang and Kuwano, 1999).

The synthetic case study herein defined considers that the railway track rests upon a homogeneous subgrade of M10 clayey sand with properties obtained by Wang and Kuwano (1999).

4.3.4 Linear and equivalent linear analyses

The linear analysis considers the small strain properties of the soil and serves as the initial iteration for the equivalent linear analysis. Complementing the linear and non-linear analysis, an equivalent linear analysis is done in order to understand how much of an improvement it provides upon the linear case, and how well it simulates the non-linear behaviour. The equivalent linear analysis is done in the following way:

1. The iterative procedure begins with the linear analysis using the small strain soil properties. The soil mesh is divided into nine layers, the first 8 layers of 1 m each are subject to update of stiffness and damping, the last layer of 2 m has permanent small strain properties.

2. The computation is done for the passage of a Thalys axle passage and the shear strains in the finite elements directly below the track are monitored. For each finite element the peak shear strain is obtained and the average peak strains upon each soil layer are computed. From these, the effective shear strain is determined as 65% of the average peak strain in each layer.

3. For each layer the convergence is checked using the ratio of the effective shear strain obtained to the effective shear strain considered in the previous iteration. A 5% convergence criterion is considered.

4. If convergence is obtained in all the layers then the iterative procedure stops. Otherwise G_{sec} and ξ are updated for all layers by interpolating the experimental results for the effective shear strain in each layer and a new iteration is started, returning the procedure to step 2.

Table 4.7 presents the iterative procedure until convergence is achieved.

Large variations of the shear modulus are obtained from the initial analysis to the final iteration. Naturally as the depth increases the induced shear strains decrease and the final shear modulus is closer to the initial modulus. The 5^{th} layer has a stiffness variation until convergence of less than 5%, therefore, it is reasonable to conclude that it could have been considered as a layer with permanent small strain properties and also that the layers below it did not need to be updated. Therefore, the initial consideration that at more than 8 m the soil does not need to be updated is completely acceptable. Even though the stiffness almost didn't change, the final effective shear strain in that 5^{th} layer is almost 27% higher than the effective shear strain in the initial analysis. This demonstrates that even at depths where the linear behaviour is acceptable, the shear strains may be highly influenced by the non-linear behaviour of the soil above it. A more in depth look upon the equivalent linear model response is taken in sub-section 4.3.8 where the results obtained from the linear, equivalent linear and non-linear analysis are discussed.

4.3.5 Non-linear model of the soil

The purpose of this task is to simulate the hysteretic behaviour of the soil represented generically by Figure 4.21 and to determine whether the consideration of this behaviour results in a considerably different track-soil response due to the passage of a train, when compared with what is obtained considering linear behaviour. The aim is to simulate materials where the hysteretic behaviour is previously known from the literature and to simulate the soil for the same conditions. Also, taking into account the large computational effort demanded by the track-soil FE mesh, it is necessary to limit the complexity of the non-linear model of the soil. Because of this, the utilization of advanced constitutive models, where a more detailed soil behaviour can be modelled, is not considered.

The non-linear model of the soil implemented in Diana is a cyclic non-linear model based on the Iwan equation. The Iwan model relies on the assumption that a hysteretic system can be constructed by a large number of elasto-plastic elements with different yield levels. The original parallel

Table 4.7: Iterative procedure of the equivalent linear method.

Iteration	Layer	Initial G (MPa)	γ_{eff}	$\frac{\gamma_i}{\gamma_{i-1}}$
Initial analysis	1	61.42	1.72×10^{-4}	–
	2	61.42	1.06×10^{-4}	–
	3	61.42	6.19×10^{-5}	–
	4	61.42	3.80×10^{-5}	–
	5	61.42	2.89×10^{-5}	–
	6	61.42	2.41×10^{-5}	–
	7	61.42	1.90×10^{-5}	–
	8	61.42	1.35×10^{-5}	–
1^{st} iteration	1	47.53	2.16×10^{-4}	1.25
	2	52.80	1.27×10^{-4}	1.20
	3	57.12	6.94×10^{-5}	1.12
	4	59.67	4.15×10^{-5}	1.08
	5	60.30	3.50×10^{-5}	1.08
	6	60.62	2.80×10^{-5}	1.16
	7	60.85	2.15×10^{-5}	1.13
	8	61.19	1.46×10^{-5}	1.07
2^{nd} iteration	1	45.35	2.26×10^{-4}	1.05
	2	51.08	1.32×10^{-4}	1.04
	3	56.25	7.04×10^{-5}	1.02
	4	59.44	4.22×10^{-5}	1.04
	5	59.88	3.64×10^{-5}	1.02
	6	60.36	2.86×10^{-5}	1.02
	7	60.74	2.19×10^{-5}	1.02
	8	61.11	1.47×10^{-5}	1.01
3^{rd} iteration	1	44.87	2.28×10^{-4}	1.01
	2	50.67	1.34×10^{-4}	1.01
	3	56.13	7.06×10^{-5}	1.00
	4	59.38	4.24×10^{-5}	1.00
	5	59.78	3.67×10^{-5}	1.01
	6	60.32	2.87×10^{-5}	1.00
	7	60.72	2.21×10^{-5}	1.01
	8	61.09	1.48×10^{-5}	1.00

Iwan model (Iwan, 1967) is explained in the following. Figure 4.32 shows a representation of the Iwan parallel model with four elements.

Each element consists in a linear spring with stiffness k_i in series with a slip damper with a maximum allowed force τ_i. Usually all the elements have the same elastic stiffness k, and different slip stress τ_i. The initial loading

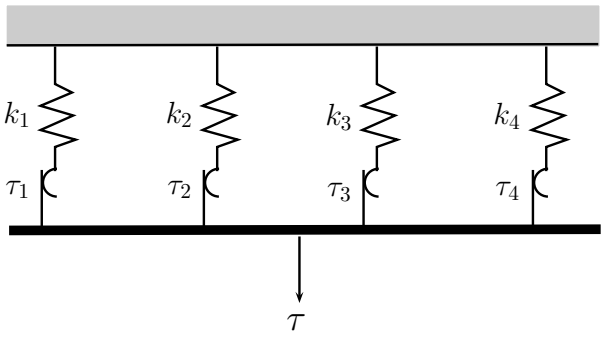

Figure 4.32: Representation of the Iwan parallel model with 4 elements.

curve is given by:

$$\tau = \sum_{i=1}^{n} k\gamma + \sum_{i=n+1}^{n_\mathrm{k}} \tau_i \tag{4.50}$$

where n_k is the total number of elements and n is the number of elements that remain elastic for the strain γ. Before the first yield stress is achieved, the model behaves linearly. When the first yield stress is achieved, the respective element no longer resists to deformation and from there onwards the overall stiffness of the model is reduced by k until the next yield stress is achieved or an inversion of the load occurs. In fact, the Iwan model approximates the stress-strain curve by a series of line segments (Figure 4.33).

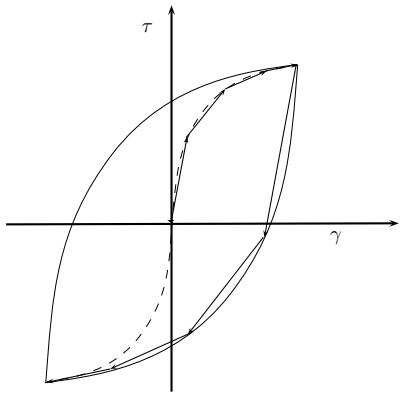

Figure 4.33: Behaviour of the parallel Iwan model.

When the model is unloaded, the elements that had slipped become active again because the model is now loading in the opposite direction, this means that the model stiffness K at the beginning of the unload is the same as in the beginning of the first load and the elements will unload until they

reach 0 stress. The model is therefore not elastic. In unload, the elements will then start loading in the opposite direction, this means that to reach the yield stiffness each element much be loaded twice the stress that was needed at the backbone curve in the opposite direction. Since it was demonstrated that the combined stiffness K is the same as in the original loading case, the shear strain must also be the double and thus the Masing rule for unload is respected.

The cyclic non-linear model based on the Iwan equation has the advantage of simulating the hysteretic behaviour of the soil with the correct load and unload behaviour without the definition of complex mechanisms such as yield surfaces, hardening laws and flow rules. The calibration of such a model is simplified by the fact that in its core it is governed by an equation that reproduces the backbone curve of the soil and thus the calibration can be restricted to fitting the Iwan curve to the backbone curve obtained experimentally.

The Iwan curve has also been adapted to account for the backbone curve degradation with number of cycles (Lee et al., 2009). This is a feature that can result in interesting studies in the future, and although this degradation is not currently considered, the possibility of its implementation has also motivated the choice of this model.

4.3.6 Implementation of the non-linear model

The Diana software provides a framework in which the user can implement a material model. This material model is supplied as a Fortran routine that updates the stress vector $\boldsymbol{\sigma}$, the user state variables $\boldsymbol{\alpha}$ and the constitutive matrix $\mathbf{D}$.

The Diana software uses these variables computed in the external routine to assemble the global tangent stiffness matrix $\mathbf{K}_{\tan}$ and the vector of internal forces $\mathbf{f}^{\text{int}}$. These are applied in the non-linear scheme (Newton-Raphson, p.e.) to compute the non-linear response of the model.

At any iteration step k the software Diana computes for each Gauss point the strain vector at the end of the last step $\boldsymbol{\varepsilon}_{n+1}^{k\text{-}1}$, the strain increment vector $\Delta\boldsymbol{\varepsilon}^{k}$ and the stress vector at the end of the last iterative step $\boldsymbol{\sigma}_{n+1}^{k\text{-}1}$. For simplicity, the counter for the Gauss point is omitted in the present formulation, as it is clear that the proceeding is repeated for all Gauss points in each finite element. These values are outputted to the external user defined routine that should determine the updated state variables vector $\boldsymbol{\alpha}_{n+1}^{k}$, the updated stress vector $\boldsymbol{\sigma}_{n+1}^{k}$ and the updated constitutive matrix $\mathbf{D}_{n+1}^{k}$. The update procedure for these variables, in the context of the implementation of the Iwan parallel model is explained in the following (and further detailed in Annex A).

The non-linear model is implemented as a Hooke isotropic model with variable modulus. The instant modulus is determined using the Iwan equa-

tion.

The parameters of the model are the Young's modulus E, the Poisson's ratio ν, the volumetric mass ρ, the number of spring/slip elements n_{k} and the slip-stress of each element $\tau_1, \tau_2, ...\tau_{n_{\mathrm{k}}}$. An equal stiffness for all spring/slip elements is assumed

$$k = \frac{G_0}{n_{\mathrm{k}}} \tag{4.51}$$

where k is the stiffness of the spring/slip elements.

Initially, the iterative strain vector $\boldsymbol{\varepsilon}_{n+1}^{k}$ is determined

$$\boldsymbol{\varepsilon}_{n+1}^{k} = \boldsymbol{\varepsilon}_{n+1}^{k\text{-}1} + \Delta\boldsymbol{\varepsilon}^{k} \tag{4.52}$$

The Iwan equation (4.50) determines the relation between effective shear strain, γ_{eff} and effective shear stress τ_{eff} of the material. From the experimental results, the stiffness and damping variation curves are generally determined by considering that the effective shear strain and the effective shear stress correspond to the maximum shear stress and maximum shear strain of the load cycle. Consequently, the maximum shear strain is computed from the iterative strain vector:

$$\gamma_{\mathrm{eff}} = \gamma_{n+1}^{k} = \frac{\varepsilon_1 - \varepsilon_3}{2} \tag{4.53}$$

in which ε_1 and ε_3 are, respectively, the major and minor principal strains of the strain state represented by $\boldsymbol{\varepsilon}_{n+1}^{k}$. The principal strains are determined as the eigenvalues of the strain tensor. These eigenvalues are computed using a QR decomposition method with Householder reflectors (Annex B).

The Iwan model is updated for the effective shear strain γ_{eff}. The shear stress τ is updated with the Iwan model as well as the vector of state variables $\boldsymbol{\alpha}$ that contains information on the tension in each spring/slip element of the Iwan model as well as its status (contributing to the stiffness of the model or slipping). From the shear stress and shear strain variation over k, a secant shear modulus is computed (Figure 4.34).

$$G_{\mathrm{sec}} = \frac{(\tau_{n+1}^{k} - \tau_{n+1}^{k\text{-}1})}{(\gamma_{n+1}^{k} - \gamma_{n+1}^{k\text{-}1})} \tag{4.54}$$

A reduction factor of the secant shear modulus G_{sec} from the initial shear modulus G_0 is determined:

$$f_{\mathrm{sec}} = \frac{G_{\mathrm{sec}}}{G_0} \tag{4.55}$$

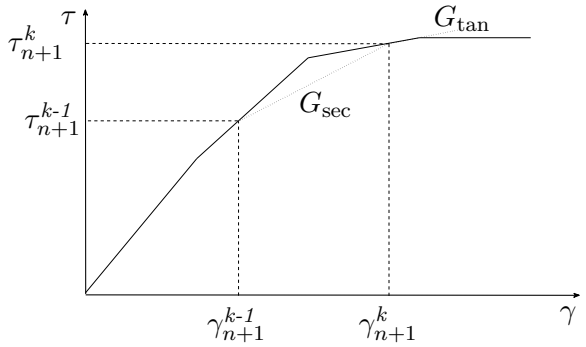

Figure 4.34: Determination of $G_{\sec}$ and $G_{\tan}$ in the non-linear model.

and a secant matrix $\mathbf{D}_{\sec}$ is computed

$$\mathbf{D}_{\sec} = \mathbf{D} f_{\sec} \tag{4.56}$$

The updated stress tensor is determined:

$$\boldsymbol{\sigma}_{n+1}^{k} = \boldsymbol{\sigma}_{n+1}^{k-1} + \mathbf{D}_{\sec} \Delta \boldsymbol{\varepsilon}^{k} \tag{4.57}$$

From the state variables vector $\boldsymbol{\alpha}_{n+1}^{k}$ the number of active elements determines the tangent shear modulus $G_{\tan}$ at the end of step k.

The modified Lamé coefficients are computed:

$$\mu' = G_{\tan} \tag{4.58}$$

$$\lambda' = \lambda \frac{G_{\tan}}{G_0} \tag{4.59}$$

And the new constitutive matrix is computed from the modified Lamé coefficients:

$$\mathbf{D}_{\tan} = \begin{bmatrix} \lambda'+2\mu' & \lambda' & \lambda' & 0 & 0 & 0 \\ \lambda' & \lambda'+2\mu' & \lambda' & 0 & 0 & 0 \\ \lambda' & \lambda' & \lambda'+2\mu' & 0 & 0 & 0 \\ 0 & 0 & 0 & \mu' & 0 & 0 \\ 0 & 0 & 0 & 0 & \mu' & 0 \\ 0 & 0 & 0 & 0 & 0 & \mu' \end{bmatrix}$$

4.3.7 Calibration

M10 clayey sand at 392 kPa

The M10 clayey sand (Wang and Kuwano, 1999) is simulated with the cyclic non-linear model. The experimental values obtained with a confining pressure of 392 kPa (Figure 4.35) are used to calibrate the parameters of the Iwan curve using a least squares optimization procedure. For that purpose, the results are initially transformed from the representation of shear modulus to shear stress using equation (4.32). Considering that each elasto-plastic element has equal stiffness k, the experimental results are used to calibrate the slip stress of each element in the Iwan load curve (4.50) in order to simulate the same stiffness degradation. The calibration is repeated for a different number of elasto-plastic elements in order to obtain the best correspondence.

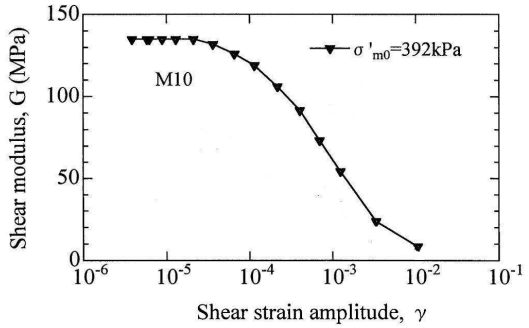

Figure 4.35: Experimental stiffness reduction with shear strain of the M10 clayey sand at confining pressure of 392 kPa (adapted from Wang and Kuwano (1999)).

By a carefully choice of the number of elements in the Iwan model and of the initial values of the slip stress to perform the curve fitting procedure, it seems that any curve that follows the typical stiffness degradation curves of soils (Figure 4.21) can be represented by this model. This is an important verification because the consideration of equal stiffness k for all the elements of the Iwan model could have led to a restriction of the soil behaviour preventing an accurate calibration of the model. In this work, the number of slip elements is roughly estimated using:

$$n_k \approx \frac{G_0}{G_{tan\gamma}} \tag{4.60}$$

where $G_{tan\gamma_a}$ is the tangent shear modulus at the maximum shear strain of the experimental results. This estimation is based on the consideration

that at the maximum shear strain at least one element must still contribute to the global stiffness of the model (i.e. at least one element must still be subject to stress lower than its slip stress). The stiffness of that element (and therefore of all the others) should then be equal to $G_{tan\gamma_a}$

$$k = G_{tan\gamma_a} \tag{4.61}$$

replacing (4.60) in (4.51) results in equation (4.61).

For the M10 clayey sand with confining pressure of 392 kPa, the best correspondence is obtained with a Iwan model comprised of $n_k = 20$ elasto-plastic elements with stiffness $\frac{G_0}{n_k}$, the slip stress of each element is presented in table 4.8.

Table 4.8: Slip stress of the elements (M10 at 392 kPa).

Element	k_1	k_2	k_3	k_4	k_5	k_6	k_7
Slip Stress (Pa)	179	203	352	625	656	1020	1161
Element	k_8	k_9	k_{10}	k_{11}	k_{12}	k_{13}	k_{14}
Slip Stress (Pa)	1246	1370	2707	2786	3020	3533	3891
Element	k_{15}	k_{16}	k_{17}	k_{18}	k_{19}	k_{20}	-
Slip Stress (Pa)	6228	6344	6630	7645	8311	45766	-

Figure 4.36 compares the experimental shear stress and the numerical shear stress obtained with the Iwan equation (4.50) using the parameters of table 4.8.

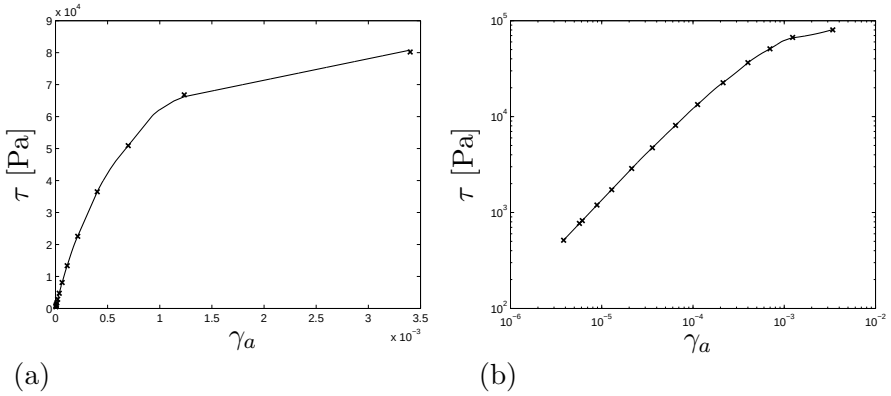

(a) (b)

Figure 4.36: Stress-strain behaviour of the clayey sand, experimental (x) and Iwan (full) values in a) decimal and b) log scale.

The Iwan curve represents well the experimental results that determine the stiffness degradation with shear stress. In the range of shear strain

the experimental results and the Iwan results correspond very well. In the following the implemented model, with the calibrated values, is used in the numerical reproduction of the triaxial tests. This allows to compare the experimental and numerical results and to verify whether the Iwan curve that, as shown in Figure 4.36, represents well the soil's stiffness degradation with shear strain, is accurately applied by the model that is implemented in Diana. The simulations are done using a single 3D brick element. As in the experimental cases, the specimen is subject to axial stress variation in order to induce a defined level of shear strain. An initial axial stress is induced in the specimen followed by a cycle of a determined amplitude. Six triaxial tests are done with varying axial stress amplitude in order to recreate the shear strain amplitude of the experimental data (Figure 4.35). Table 4.9 shows the maximum axial stress applied in the numerical cyclic triaxial tests.

Table 4.9: Peak axial stress of the triaxial simulations (M10 at 392 kPa).

Triaxial test	1	2	3	4	5	6
Peak axial stress (kPa)	9.5	16.2	26.7	45.1	73.0	101.9

Figure 4.37 represents hysteresis curves obtained in the triaxial test simulations. At low level of shear strain the model behaves almost linearly as would be expected. In the first triaxial simulation the unload and reload curves follow almost the same path as the initial load. In this triaxial test the model is already behaving in a non-linear way although very slightly. The hysteretic curve has very small area thus the damping is reduced, but there is already some hysteretic damping occurring at this shear strain level. On the other hand, in the 6^{th} triaxial test it can be seen that the initial linear behaviour becomes increasingly non-linear with the increase in the shear strain. This also means that the unload and reload curves are more distant to the backbone curve and consequently the damping is significantly higher.

Using the numerical results of the triaxial simulations (Figure 4.37), the stiffness degradation and damping variation with shear strain are computed using equations (4.32) and (4.33). Figure 4.38 presents the experimental and numerical variation of shear modulus and damping with shear strain.

The shear modulus degradation with shear strain is very well simulated and all the numerical triaxial tests reproduce very well the experimental results. It can be concluded that the calibrated Iwan curve is accurately implemented in the Diana environment and that the model does not present any numerical inaccuracy. The damping is not so accurately simulated by the model. At shear strains lower than 10^{-4} the numerical results correspond well. At higher shear strain amplitudes the implemented model tends to increasingly overestimate the damping. This tendency to overestimate the

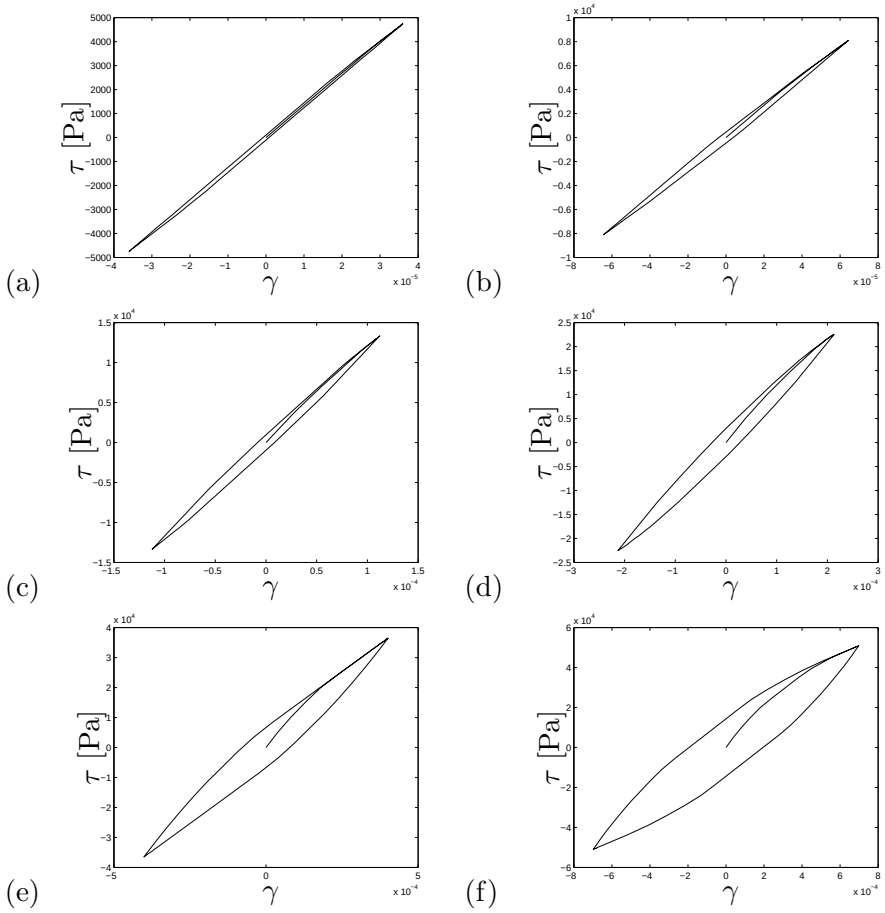

Figure 4.37: Hysteresis curves of the M10 clayey sand at confining pressure of 392 kPa obtained with the numeric cyclic triaxial tests with peak axial stress of a) 9.5 kPa, b) 16.2 kPa, c) 26.7 kPa, d) 45.1 kPa, e) 73.0 kPa and f) 101.9 kPa.

damping at high shear strains has also been found in other models that follow the Masing rules (Lopez-Caballero et al., 2004). This is related to the previously referred limitation of the models that follow the Masing rules and has been mainly appointed to the reload/unload conditions. These models can be adapted by the adoption of a coefficient that affects the slope of the unload and reload curves and reduces the area of the hysteresis curve of the soil. However, this adjustment requires the knowledge of the exact shape of the hysteresis curve at these high strain levels, which in the case of these literature results (as in the majority of literature works) is not provided.

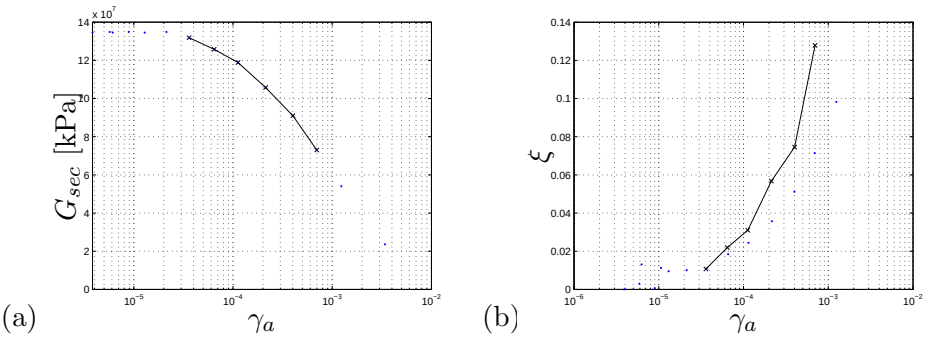

Figure 4.38: M10 Clayey sand at confining pressure of 392 kPa, shear strain dependency of a) shear modulus and b) damping, comparison of experimental (.) and numerical (x) results.

M10 clayey sand at 98 kPa

The non-linear model is also used to recreate the experimental results of the M10 clayey sand obtained with confining pressure of 98 kPa. Figure 4.39 presents the experimental results of the stiffness degradation with shear strain. Due to the difference in the confining pressure, there is a significant difference in the stiffness of this specimen and the one subject to 392 kPa.

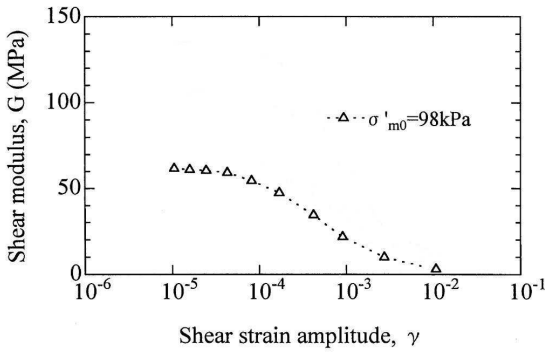

Figure 4.39: Experimental stiffness reduction with shear strain of the M10 clayey sand at confining pressure of 98 kPa (adapted from Wang and Kuwano (1999)).

The calibration procedure is repeated for this specimen. The experimental values obtained with a confining pressure of 98 kPa (Figure 4.39) are used to calibrate the parameters of the Iwan curve using a least squares optimization procedure. The numerical fitting of the Iwan curve and the experimental results is again repeated for a different number of elasto-plastic elements in order to obtain the best correspondence. For the M10 clayey

sand with confining pressure of 98 kPa, the best correspondence is obtained with a Iwan model comprised of $n_k = 14$ elasto-plastic elements, the slip stress of each element is presented in Table 4.10.

Table 4.10: Slip stress of the elements (M10 at 98 kPa).

Element	k_1	k_2	k_3	k_4	k_5	k_6	k_7
Slip Stress (Pa)	94	194	247	436	483	680	1189
Element	k_8	k_9	k_{10}	k_{11}	k_{12}	k_{13}	k_{14}
Slip Stress (Pa)	1219	1356	1632	1797	3111	4618	24697

Figure 4.40 compares the experimental shear stress and the numeric shear stress obtained with the Iwan curve (4.50) using the parameters of table 4.10. Again, it is shown that the Iwan curve can be calibrated to pro-

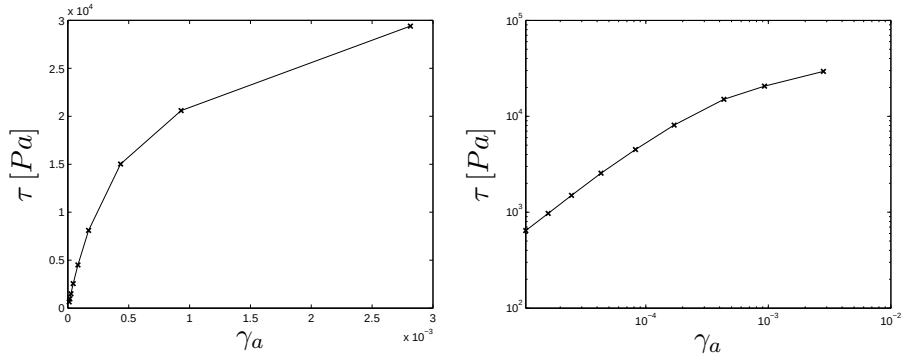

(a) (b)

Figure 4.40: Stress-strain behaviour of the M10 clayey sand with confining pressure of 98 kPa, experimental (x) and Iwan (full) values in a) decimal and b) log scale.

vide very accurate reproduction of the experimental behaviour of the clayey sand. Therefore, the consideration of constant stiffness k for all elements of the Iwan model is not a restrictive consideration.

Afterwards, the implemented model with the calibrated values is used in the numerical reproduction of the triaxial tests. In this case nine triaxial tests are done to obtain the response at the same shear strain of the experimental results, in a range of 1.05×10^{-5} to 2.8×10^{-3}. Table 4.11 presents the maximum axial stress applied in the numerical cyclic triaxial tests.

The triaxial tests are again very promising as they show that for very low shear strain amplitudes the model remains linear (Figures 4.41a and 4.41b) while for very high shear strain amplitudes the model shows a clear degradation of the shear modulus, which is demonstrated by the slope of

the backbone curve in Figures 4.41g, and 4.41h. At these very high shear strain amplitudes the area of the hysteresis curve in the specimen response is large, thus following the experimental results that suggest an increase of damping at high shear strains.

Table 4.11: Peak axial stress of the triaxial simulations (M10 at 98 kPa).

Triaxial test	1	2	3	4	5	6	7	8	9
Peak axial stress (kPa)	1.3	1.9	3	5.1	9	16.2	30.1	41.2	58.8

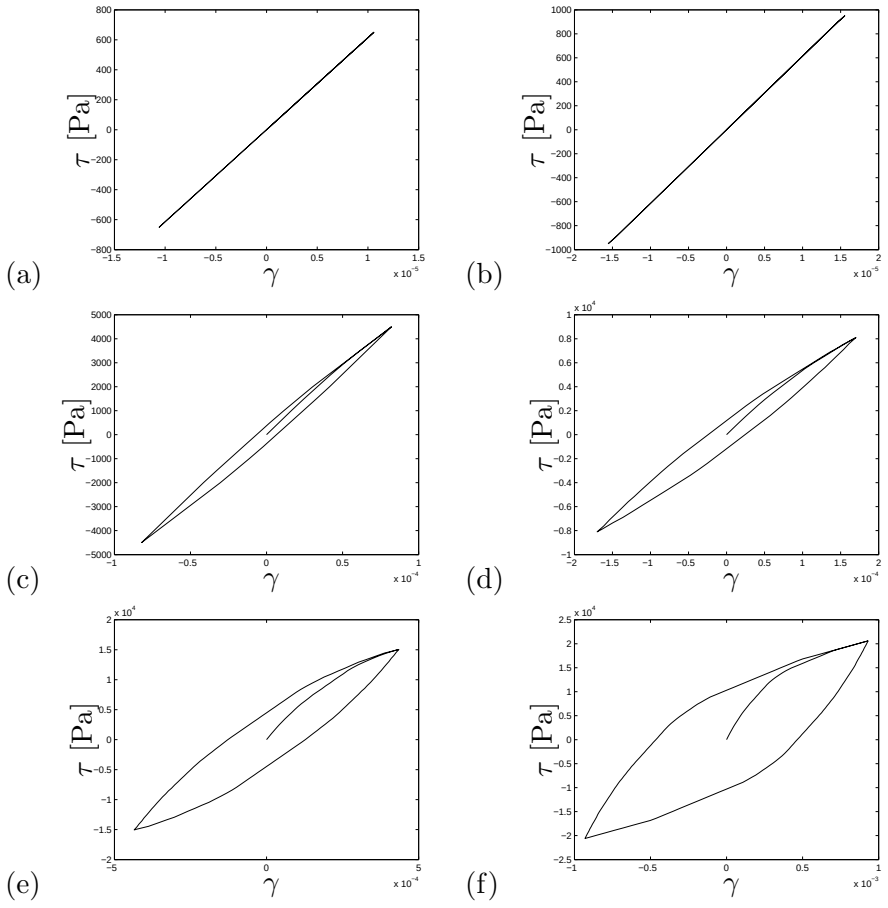

Figure 4.41: Hysteresis curves of the M10 clayey sand at confining pressure of 98 kPa obtained with numeric cyclic triaxial tests with peak axial stress of a) 1.3 kPa, b) 1.9 kPa, c) 9 kPa, d) 16.2, e) 30.1 kPa and f) 41.2 kPa.

The experimental and numerical shear modulus and damping variation

with shear strain are compared in Figure 4.42.

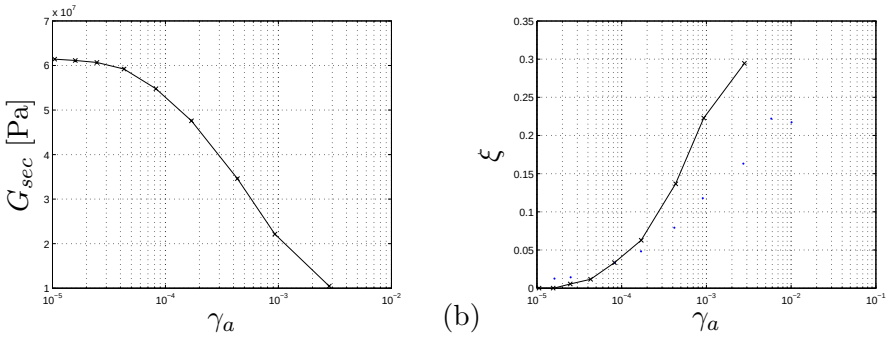

(a) (b)

Figure 4.42: M10 clayey sand at confining pressure of 98 kPa shear strain dependency of a) shear modulus and b) damping in experimental (.) and numerical (x).

The shear modulus degradation with shear strain is very well simulated. Figure 4.42a shows that there is almost no noticeable difference between the experimental results and the numerical simulations. These results would be expected since the Iwan curve that is in the core of the non-linear model was calibrated with the experimental shear modulus degradation. However, numerical inaccuracies could lead to some differences in the 3D specimen response, nevertheless that is not the case herein presented. The comparison of the numerical and experimental results of the triaxial tests of this clayey sand at confining pressures of 392 kPa and of 98 kPa are both very good thus it can be concluded that the implemented model simulates with very good accuracy the shear modulus degradation with shear strain. The damping is again increasingly overestimated at shear strain amplitudes higher than 10^{-4}.

It is worthwhile to recall that the implemented model is not an advanced constitutive model but rather a cyclic non-linear model. Because of this, it is numerically less expensive but it does not simulate the soil at varying conditions. In it's current state the model does not account for variations in the confining pressure or pore pressure development. Because of this the non-linear model has to be calibrated for each confining pressure, like in the presented examples.

4.3.8 Results discussion

The calibrated model of the M10 clayey sand is used as foundation soil in the non-linear numerical simulation of the track response. The simulation is done for the confining pressure of 98 kPa because it is a more realistic confining pressure for the soil at low depths. The situation simulated is the passage of a single axle of the Thalys high-speed train at 300 km/h. These

are inevitably elaborate models and computationally demanding, easily ascending to hundreds of thousands degrees of freedom. Because of this, much care must be taken into the mesh refinement so that no more computational effort is taken than the necessary.

Using the information obtained from the equivalent linear model, the non-linear behaviour is only considered for the upper 5 m of subgrade. For the lower soil layer the small strain properties of the clayey sand are considered (Figure 4.43).

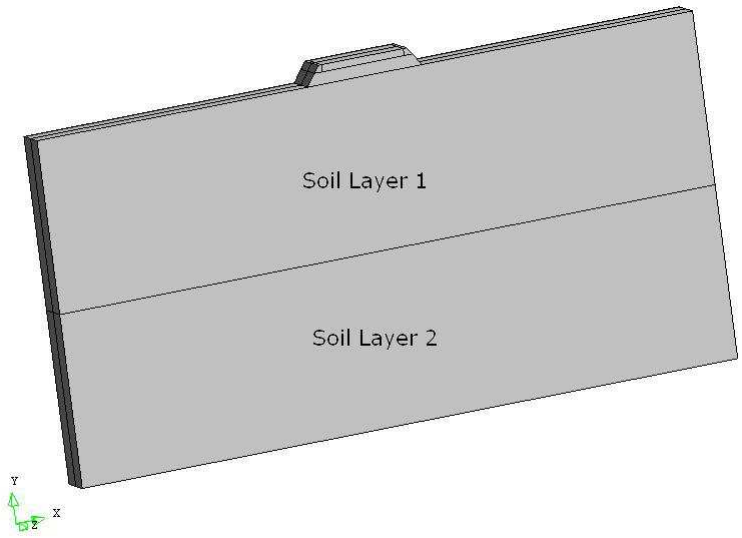

Figure 4.43: Division of the soil in two layers.

Figure 4.44 presents the stiffness reduction obtained in the equivalent linear model and the non-linear model at the moment of the passage of the train axle in a transversal section directly below the sleeper. It should be noted that only half the soil is represented as symmetry is assumed. All points at $x = -0.75$ m are vertically aligned with the rail and all represented points at $x > -1.75$ m are directly below the track.

The most glaring observation that can be made is that a much higher soil stiffness reduction occurs in the non-linear case than in the equivalent linear, even if that occurs in a very small zone. Since the soil has a low initial shear modulus, high shear strains result from the solicitation and these high shear strains lead to high stiffness reductions. In the track-soil interface directly below the track, the soil can reduce to slightly less than 50% its original stiffness, which represents a considerable reduction that can affect the stiffness distribution through the soil, even though this occurs in a very small portion of soil, there is also a considerable reduction of 10% stiffness that can occur as deep as 3.5 m.

Generally speaking, the stiffness reduction found in the equivalent lin-

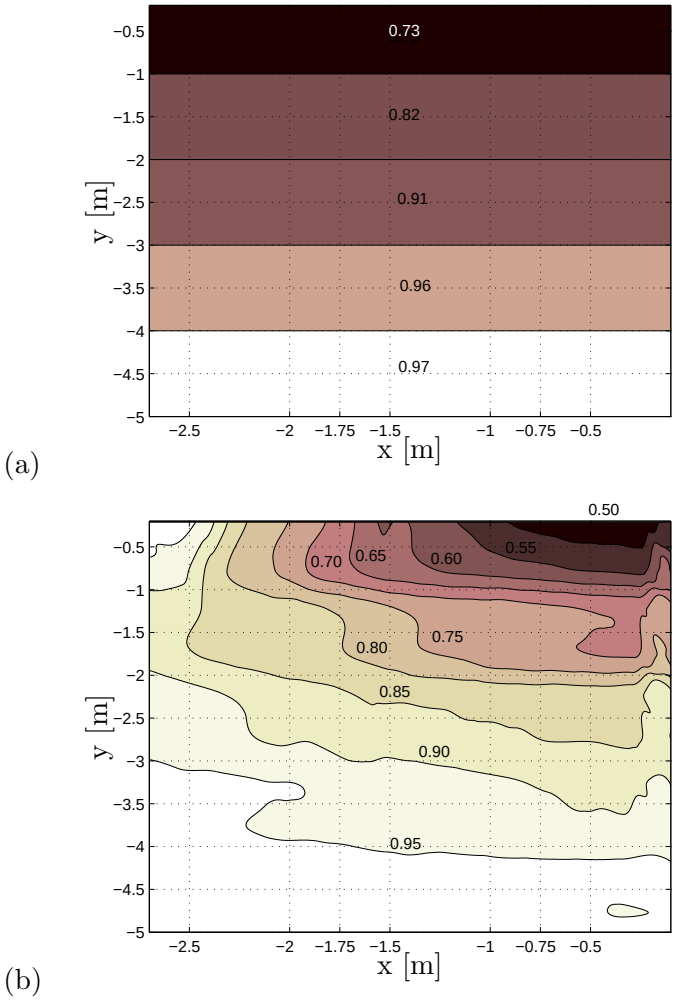

Figure 4.44: Transversal distribution of the stiffness reduction ($\frac{G}{G_0}$) of the subgrade in the a) equivalent linear and b) non-linear model.

ear case is consistent with that found in the non-linear case, especially at increasing depths where the iso-lines of the non-linear simulation present an almost horizontal layering. At depths around 1 m or less the horizontal layering seems to be less acceptable as large differences occur between the soil stiffness in the horizontal direction. Figure 4.45 presents a novel look at the soil stiffness reduction from the non-linear model, considering both its spacial and its time distribution. The figure presents the iso-lines of stiffness reduction $\frac{G_{sec}}{G_0}$, but instead of presenting only the time instant at which the axle load is passing through the transversal section ($t = 0.116\,\mathrm{s}$), it presents their time history.

The soil degradation starts only when the axle load is already very close

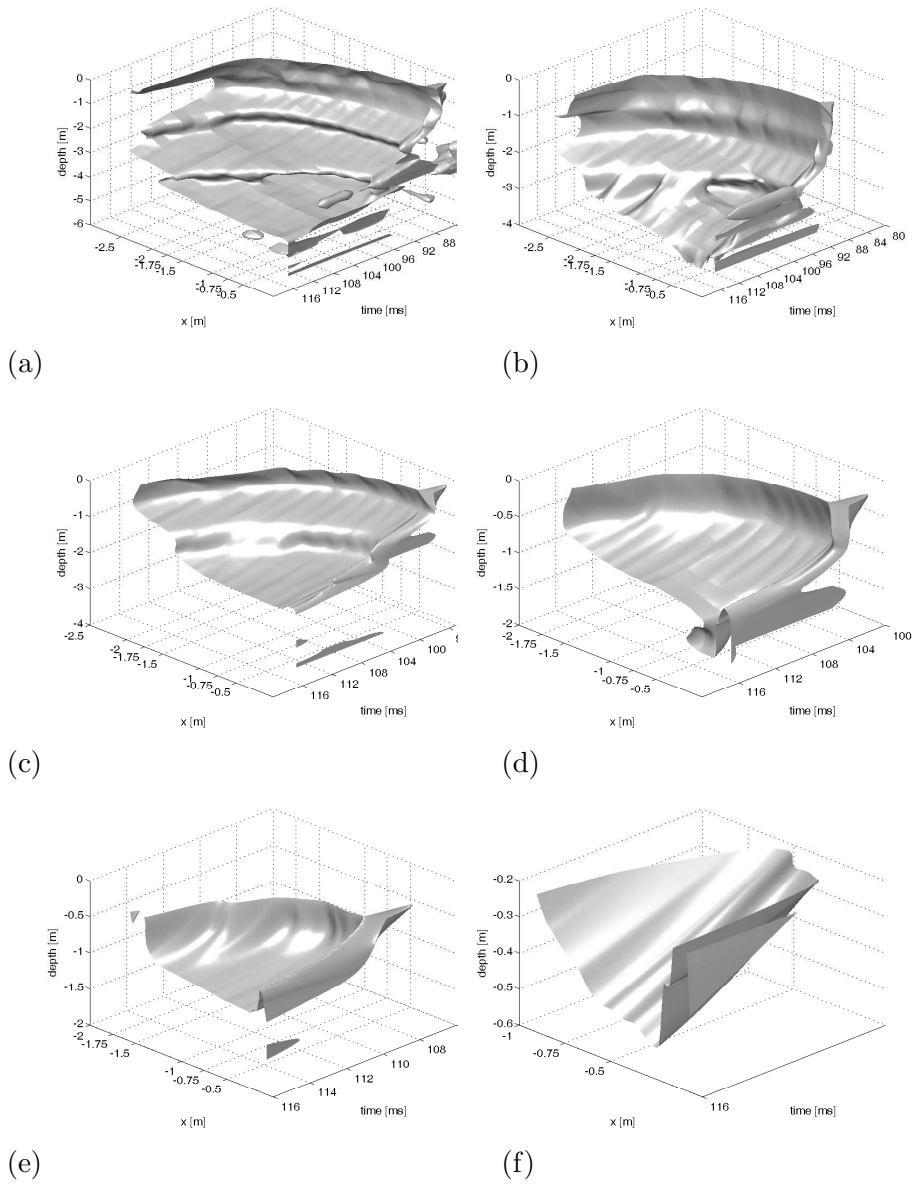

Figure 4.45: Time history of the subgrade stiffness reduction iso-lines: a) 0.95, b) 0.90, c) 0.80, d) 0.70, e) 0.60 and f) 0.50.

to the transversal section. In Figure 4.45 a) it is shown that a 5% reduction starts to occur at a time $t \approx 0.086\,\mathrm{s}$ which is only 0.03 s before the passage of the train axle. So the first soil stiffness reduction occurs when the axle load is less than 2.5 m from the section in study. A 10% reduction only starts occurring at $t = 0.090\,\mathrm{s}$ when the axle load is approximately 2 m away. The 0.50 iso-line that enclosures a soil portion with a considerable

stiffness reduction is limited to a very small time and space span. It appears only at the time step in which the axle load is passing through the soil section. Naturally, all iso-lines appear initially at the soil surface, and very localized, further they expand in the horizontal direction and descend along the subgrade. Taking as example the 0.95 iso-line, it evolves from the soil-track interface and a horizontal span of 0.5 m at $t = 0.086$ s to a depth of approximately 5 m and a horizontal span of more than 2.5 m when the load is passing directly above the section in study. In short, the stiffness reduction of the soil is very confined in time, but expands rapidly in space as the axle load approximates. The shear strain induced in the soil (Figure 4.46) is slightly different in the three cases. The shear strain can surpass 3.6×10^{-4} in the soil close to the soil-track interface, especially directly bellow the rail. However, the linear and equivalent linear models predict considerably lower peak values of 2×10^{-4} and 2.4×10^{-4} respectively. These major differences are found mainly directly below the rail and less than 1 m depth. Both the linear and equivalent linear models have very good prediction of the shear strain in the soil at larger depths than 2 m, where the iso-lines of shear strain follow approximately the same path as the the iso-lines in the non-linear case.

From the comparison of the shear strain distribution it is fair to conclude that the equivalent linear model is indeed an improvement upon the linear model, as it better represents the shear strains in a range of 1 m to 2 m depth. From the observed shear strain distributions in the soil, some preliminary observations can be made. The shear strain in the soil, which is the main parameter that determines the soil's stiffness degradation and damping variation is concentrated mainly below the track at low depths. Both the linear and equivalent linear models provide a good estimation of the shear strain in the soil except for very low depths. A fairly good shear strain prediction is done by these models in zones where stiffness reductions as large as 10% occur. Therefore, they seem to be good tools to estimate the boundaries between linear and non-linear response.

The iso-line of 4×10^{-5} shear strain is the only that is similar in all three models and it is plausible that for lower strains the linear model has good accuracy. The iso-line of 8×10^{-5} obtained in the linear model is considerably different than those obtained in the equivalent linear and non-linear models. For higher strains the soil behaves increasingly non-linearly so it is only natural that the linear model does not provide an accurate strain response. The equivalent linear model obtains good predictions of the iso-lines up to 2×10^{-4} which is a considerable improvement upon the linear model. Only in the upper soil layer can it be said that there are large differences in the shear strains determined in the equivalent linear and non-linear models. The non-linear response presents shear stresses reaching 10 kPa, while in the linear and equivalent linear cases, the model reaches slightly higher shear stresses of 12 kPa (Figure 4.47). This is a hint that

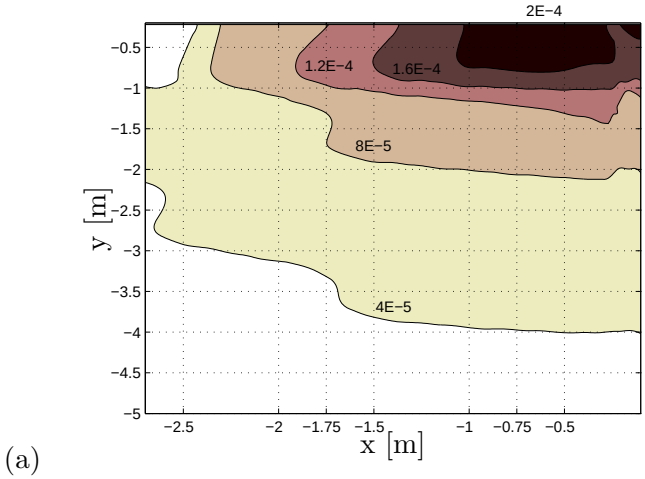

(a)

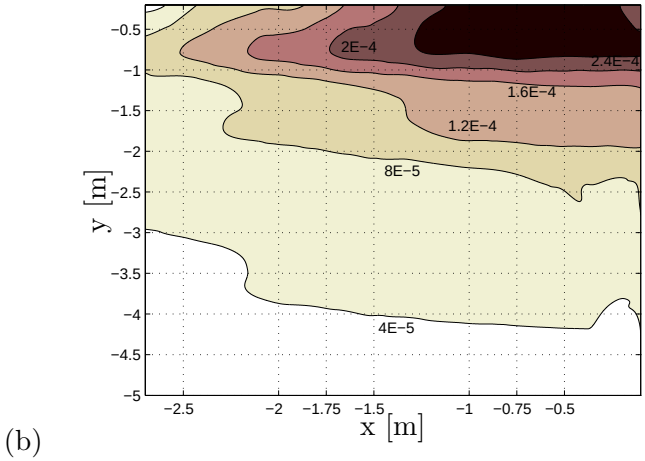

(b)

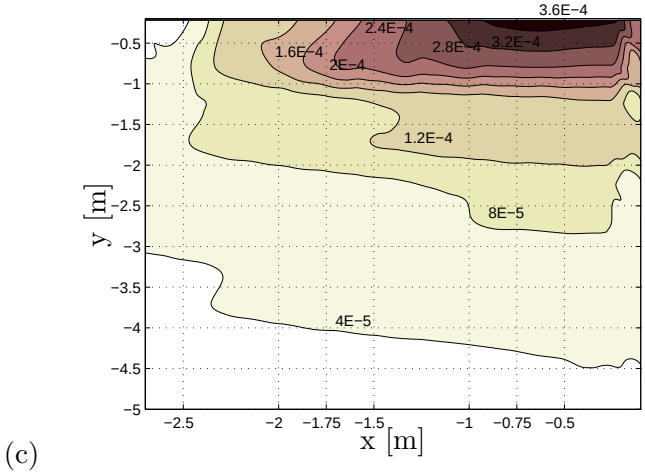

(c)

Figure 4.46: Transversal distribution of the shear strain in the subgrade computed with the a) linear b) equivalent linear and c) non-linear models.

when the soil degrades near the track occurs a redistribution of stresses to stiffer portions of soil. The consequence is that the degraded portion of soil is subject to lower stresses than linear models predict. There is a zone very close to the track, at less than 1.5 m depth and less than 1.5 m from the centre of the track, where the stress distribution is not very accurate in the linear and equivalent linear cases. Nevertheless, the stress distribution is remarkably accurate for the most part, even in the linear case. Again it is hinted that the equivalent linear case presents an upgrade in accuracy from the linear case and in many cases may be a very important tool to predict stress and strain of the subgrade. It seems that the method for the equivalent linear analysis is adequate, although it would be interesting to study if different reduction factors for the computation of the effective shear strain would be more adequate. Regardless of that, it seems that for the most part, the horizontal layering of the soil is an acceptable simplification except for the top 1 to 2 m, where a horizontal division of the soil would very likely lead to better representation of the soil degradation.

The analysis of the track response in the three cases (Figure 4.48) suggests similar conclusions to those obtained from the stress-strain state of the soil. The displacement of the rail increases significantly when considering the non-linear behaviour. Again, considering the differences between the linear and non-linear cases, the equivalent linear analysis presents a middle ground that approximates the behaviour of the non-linear analysis, although without the complexity nor the accuracy of the later. The non-linear behaviour has in this case undeniable influence in the track response, especially the rail peak displacement. The shape of the time response does not change much. This is confirmed by the analysis of it's time derivative, in which the velocity corresponds very well in the three cases.

Naturally, the linear and equivalent linear models do not have the capability to present permanent settlements and after the passage of the axle load the rail response returns to 0, in the non-linear case that does not happen, indicating that some permanent deformations in the soil occur.

4.3.9 Partial remarks

This section presented the numerical modelling of the effect of the hysteretic behaviour of the foundation soil in the performance of the railway track. The section began by presenting a general outline of the hysteretic behaviour of granular materials and the influence of some of the material characteristics in this behaviour.

The experimental results obtained by Wang and Kuwano (1999) were used define a case study. For the consideration of the soil three different computation models representing the same study case were developed: a linear model, an equivalent linear model and a non-linear model. The linear model simply considered the 3D FE response of the soil using the small

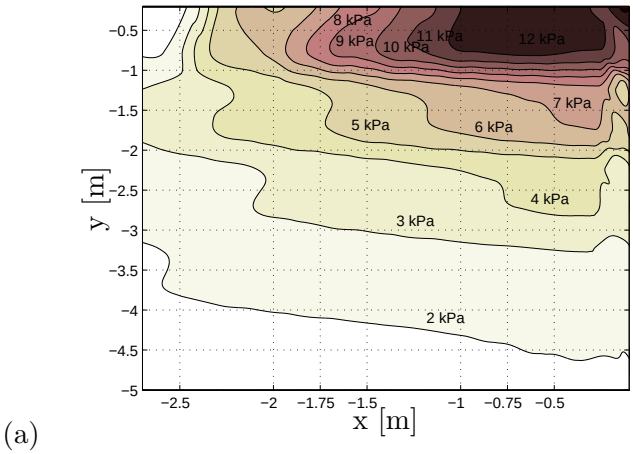

(a)

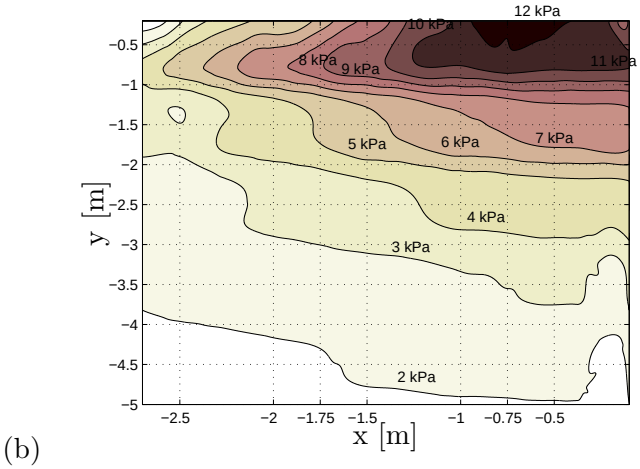

(b)

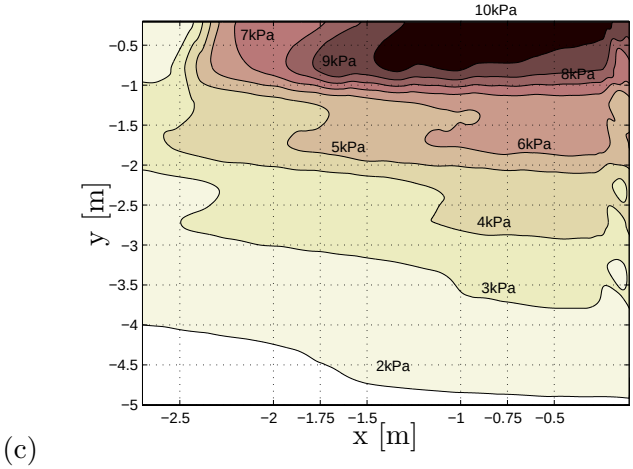

(c)

Figure 4.47: Transversal distribution of the shear stress (Pa) in the M10 clayey sand at 98 kPa computed with the a) linear b) equivalent linear and c) non-linear model.

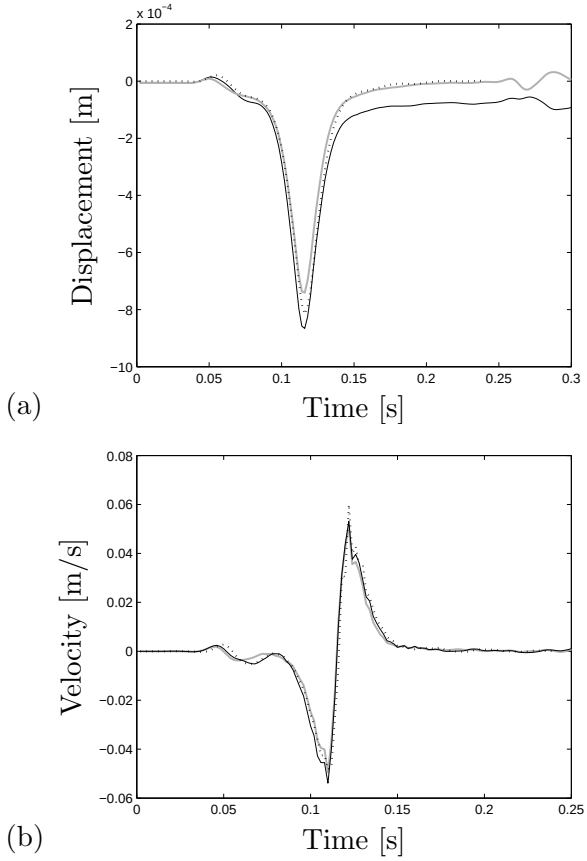

Figure 4.48: Rail response of the linear (grey), equivalent linear (dotted) and non-linear (full) M10 material model at 98 kPa: a) displacements, b) velocities.

strains characteristics of the clayey sand. The equivalent linear model used the experimental results of Wang and Kuwano (1999) to update the stiffness and damping of the soil according to the shear strain obtained in the calculation. The non-linear model required the implementation in the Diana software of the Iwan parallel model, which implicitly complies with the Masing rules. This model follows the Iwan equation that approximates the backbone curve with a set of parallel elastoplastic elements with the same stiffness but different slip stress. Whenever a stress reversal occurs the combined behaviour of the elastoplastic elements follows what was described by the rules of Masing.

After calibration, the obtained values were used in the cyclic non-linear model to reproduce the hysteretic behaviour of the material in several cyclic triaxial simulations. The hysteretic curves that were obtained present the same shape as would be expected. The comparison between the experimental and numerical stiffness reduction is very good, which suggests that the

model is numerically well implemented. Regarding damping variation with shear strain, the numerical model follows the same trend of other Masing models which also suggests that the model is numerically efficient in reproducing the Masing rules, although it is known that they do not represent well the soil damping at high strains.

After validation of the cyclic model, the influence of the hysteretic behaviour of the soils in the behaviour of a high speed track was simulated using the previously validated FE mesh, with the passage of an axle load at 300 km/h. Only the relevant calibrated case of 98 kPa confining pressure was considered.

The non-linear simulation showed that there is a considerable stiffness reduction in the soil, which may reduce to less than 50% its initial value in a small portion directly below the rail. The stiffness reduction is very confined in time, with relevant variations of stiffness starting only 0.03 s before the axle passage. Regarding the track response there are some noticeable differences in the rail displacement when non-linear behaviour is considered, with a considerable increase in the peak displacement and a permanent settlement. However, in terms of velocities the responses are almost the same in the three cases.

The equivalent linear simulation presented an improvement over the linear method in all the results analysed. It is capable of more accurately predicting the non-linear response in terms of stress and strain in the soil, as well as obtain a better approximation of the rail displacements. Although it is unclear if a different reduction factor would improve the equivalent linear method, it seems plausible to conclude that a more refined division of the soil in homogeneous update zones in the upper 1 m would result in more accuracy in the representation of the non-linear model. Despite this, the horizontal layering is still an acceptable simplification and the presented equivalent linear analysis is an adequate tool to estimate the non-linear soil response.

4.4 Integrated analysis

4.4.1 Introduction

The final analysis uses the knowledge obtained in all the previous analyses, with special emphasis on the non-linear analyses, in order to do an integrated analyses of the track response. This takes into account the relevant behaviour at the embankment as well as the soil in order to perform a detailed evaluation of the track response. A very well documented case is chosen to perform this analysis as it has been extensively used to study and validate other numerical tools (Kaynia et al., 2000, Takemiya, 2003, Karlström and Boström, 2006, Costa et al., 2010). The response of the track is very well known as are the track and subgrade properties. Therefore, it is an excellent case to once more validate the numerical tools allowing also to study the influence of velocity in the non-linear response.

4.4.2 Case study

The case study is the Ledsgard track site in southern Sweden along the West Coast between Gothenburg and Malmö. This site gained some attention in railway engineering when, in 1997, shortly after beginning operation the circulation speeds had to be reduced due to excessive vibrations in the track and in its vicinity. What followed was an extensive experimental campaign aimed at measuring the track response and the properties of the track and soil in order to determine the causes of these anomalies in the track behaviour. This experimental campaign was promoted by the Swedish National Rail Administration (Banverket) and had cooperation of several other institutes.

The experimental measurements in the track were performed by 20 test runs, northward and southward, using an X-2000 (Figure 4.50) passenger train consisting of an engine and four cars at speeds varying from 10 km/h to 204 km/h. During these test runs the response in the track was recorded using displacement transducers and accelerometers, the subgrade response was recorded using accelerometers and seismometers located at several depths and at several horizontal distances from the track. The experimental results showed that for circulation speeds lower than 70 km/h the displacements are quasi-static. However, for higher circulation speeds, the peak displacements increase drastically (Figure 4.49).

The geotechnical investigation campaign consisted in cross-hole, down hole and SASW in situ tests as well as cyclic triaxial tests on undisturbed samples. These tests revealed that the soil is characterized by dry crust of 1.1 m on top of an organic clay layer with approximately 3 m thickness. Under these, lies a layer of soft marine clay with increasing stiffness down to the bedrock at approximately 70 m depth. The configuration and small

strain properties considered for the subgrade by Kaynia et al. (2000) are presented in table 4.12.

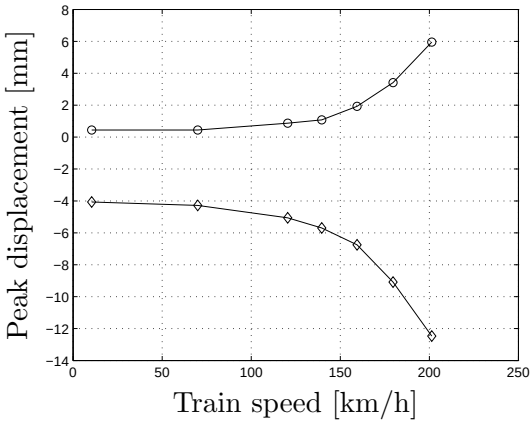

Figure 4.49: Experimental peak sleeper displacements at Ledsgard (adapted from Kaynia et al. (2000)).

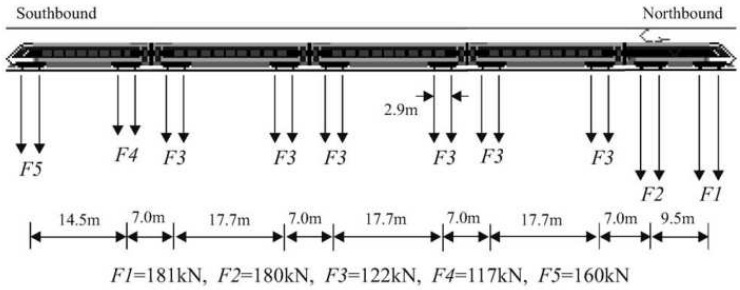

Figure 4.50: Configuration of the X-2000 test train (Karlström and Boström, 2006).

The Ledsgard line is composed of tree tracks (Figure 4.51a), the X-2000 train circulates on the western track only. For the FE simulations a simplification is made to simulate only the western track considering symmetry conditions (Figure 4.51b). The rails are the usual UIC 60 rails spaced every 0.67 m, the geometry and properties of the rails, rail pads and sleepers are the same considered for the previous analyses.

4.4.3 3D FE modelling

The non-linear subgrade behaviour is accounted for using the implemented Iwan parallel model. The small strain properties presented in table 4.12 are

Table 4.12: Dynamic soil characteristics.

Layer	d [m]	C_s [m/s]	C_p [m/s]	ρ [kg/m^3]	ξ [-]
Dry crust	1.1	72	500	1500	0.04
Organic clay	3.0	41	500	1260	0.02
Clay 1	4.5	65	1500	1475	0.05
Clay 2	6.0	87	1500	1475	0.05
Clay 3	∞	100	1500	1475	0.05

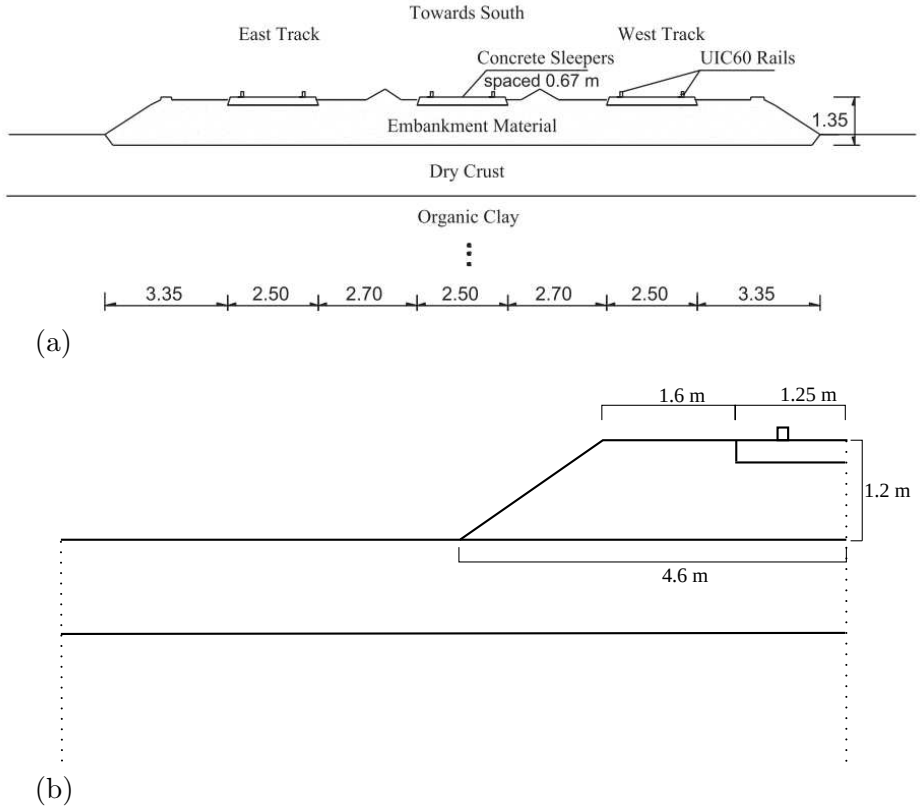

Figure 4.51: Geometry of the Ledsgard site: a) actual geometry (Costa et al., 2010) and b) considered geometry in the 3D FE simulations.

considered for the initial stiffness and damping of the layers. The evolution of the secant shear modulus of the organic clay was obtained in cyclic triaxial tests in laboratory. The results are obtained from Costa et al. (2010) and used in a least squares optimization procedure in order to obtain the Iwan

parallel model parameters that best correspond to the experimental results of the variation of the secant shear modulus. The curves of the other layers is obtained from the relations 4.36 and 4.37 published by Ishibashi and Zhang (1993) and the corresponding Iwan parallel properties are obtained in a least squares optimization procedure. For the dry crust a Plasticity Index of 30 is considered, while for the Clay layers a higher Plasticity Index of 50 is considered. Since for these values of the Plasticity Index the curves are little sensible to the coffining pressure, the same value of 50 kPa is considered for the dry crust and the clays. The variations of the secant shear modulus and damping with shear strain in the calibrated Iwan parallel model are presented in Figure 4.52. The experimentally obtained results of the stiffness reduction with shear strain for the organic clay are well averaged by the calibrated model, the damping is higher than experimental results, as usual with this model.

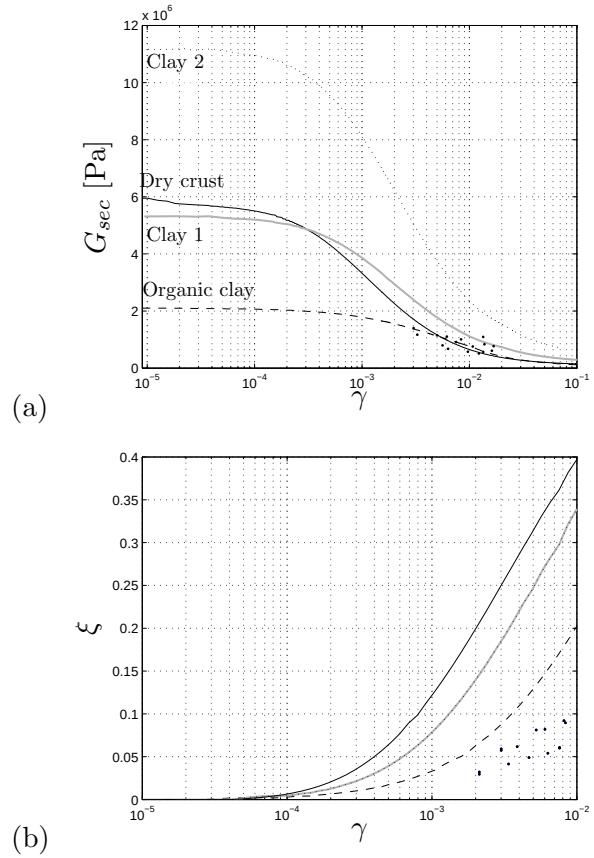

Figure 4.52: Adopted G_{sec} and ξ variation curves in the subgrade with the Iwan parallel model, dots represent experimental results for the organic clay.

Concerning the embankment behaviour, the small strain properties consist shear wave velocity $C_s = 210\,\mathrm{m/s}$ and dilatational wave veloc-

ity $C_p = 340\,\mathrm{m/s}$ (Costa et al., 2010); whereas the volumetric weight is $\rho = 1800\,\mathrm{kg/m^3}$,. These correspond to a Poisson's ratio $\nu = 0.19$ and a Young's modulus $E = 189\,\mathrm{MPa}$. The non-linear behaviour of the embankment is accounted for using the non-linear equivalent modified Mohr-Coulomb, with lack of better information the parameters that shape the non-linear behaviour are the same obtained in sub-section 4.2.4. It is not possible to simulate the passage of the full X-2000 high-speed train as this would require the simulation of a very long track stretch. Moreover, due to the high non-linear behaviour of the full model, the computations require several days to complete, with some time steps requiring a large number of iterations to converge. Therefore, these integrated non-linear models should spare as much as possible in the computational requirements. For this case a similar to the previous 3D FE meshes is used in which 30 m stretch of track is simulated. In non-linear behaviour it does not make sense to superpose the response of a single axle to obtain the response to the passage of the full train. Therefore, a study is done to check the validity of simulating a single axle passage, by comparing the non-linear response to the passage of the first axle and the first bogie of the X-2000 train circulating in the southbound direction at 204 km/h (Figure 4.53).

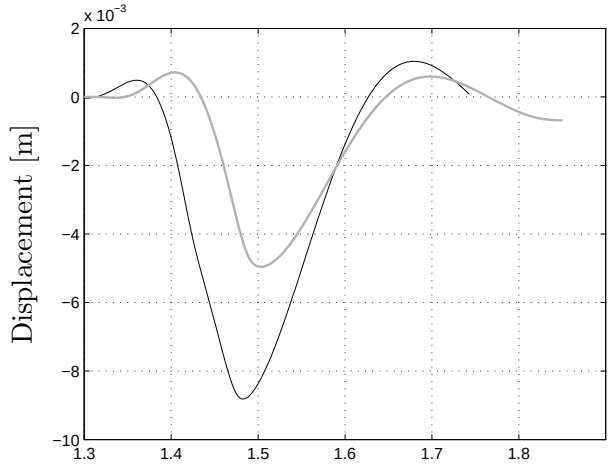

(a)

Figure 4.53: Time history of the sleeper response to the passage of the first X-2000 axle (grey) and first bogie (black) at 204 km/h in the non-linear model.

Since the two axles in the same bogie are separated by 2.9 m the peak response obtained in the simulation of the bogie occurs due to the influence of both axles. Therefore, it is not possible to separate the influence of each and at this speed, the shape of the response to the bogie passage is similar

to the shape of a single axle passage, although with higher peak values and larger duration in time. On the other hand, from the train configuration (Figure 4.50) the second bogie in the southbound direction is distant by 14.5 m so it is safe to assume that the response to the passage of the first bogie not significantly affected by the following bogies. From this knowledge, the following simulations are done by simulating the passage of the first bogie of the X-2000 train, in the linear analyses the response is superposed to obtain the response of the full train passage; in the non-linear analyses only the passage of the first bogie is studied.

4.4.4 Results discussion

Three cases are simulated: the cases involving speeds of 70 km/h and 204 km/h are compared with measurements; a third case that involves a low speed of 10 km/h is also simulated to observe the influence of the dynamic effects in the other two cases. In both comparisons of measurements, the non-linear analysis presents greater accuracy than the linear analysis (Figure 4.54).

Velocity was also observed to intensify the non-linear effects. For the 70 km/h simulation, the linear analysis presents a suitable prediction of the sleeper displacements. The non-linear analysis of the 70 km/h simulation improves the prediction of the first axle passage, but not significantly because the linear simulation is markedly accurate. For the 204 km/h simulation, the non-linear responses of the track and soil are higher, therefore, the linear analysis is less accurate for predicting the peak displacement of the passage of the first bogie. Moreover, the non-linear dynamic effects are more discernible when the response to the passage of the subsequent carriages is observed. There is a substantial increase in the upward and downward peak displacements, which the linear analysis does not predict. The non-linear analysis presents a substantial improvement in the prediction of the passage of the first bogie. Similar conclusions were obtained by Costa et al. (2010), when simulating the same track by using linear and linear equivalent models. The authors remarked that for low velocities, the linear analysis could present discrepancies as low as 10% with experimental measurements whereas at higher speeds this error could be higher than 100%. Banimahd and Woodward (2007) also reached similar conclusions for a different case study when considering non-linear elastic subgrade behaviour.

Considering the assumptions made about the non-linear behaviour of the materials, the agreement between measurements and numerical predictions is good. This analysis allows to again validate the 3D FE mesh and show that the non-linear response of the materials can significantly impact track response. Although these results were already demonstrated in sections 4.2 and 4.3 with synthetic cases, they are demonstrated here again using the

case of a real track.

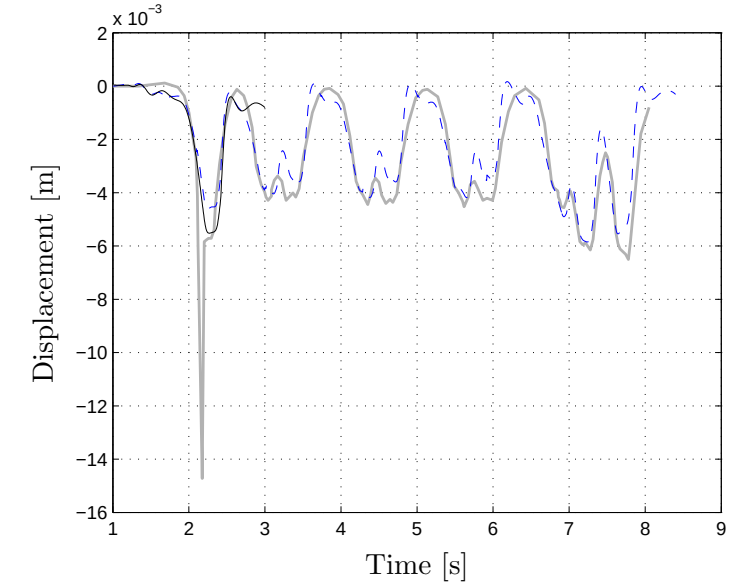

(a)

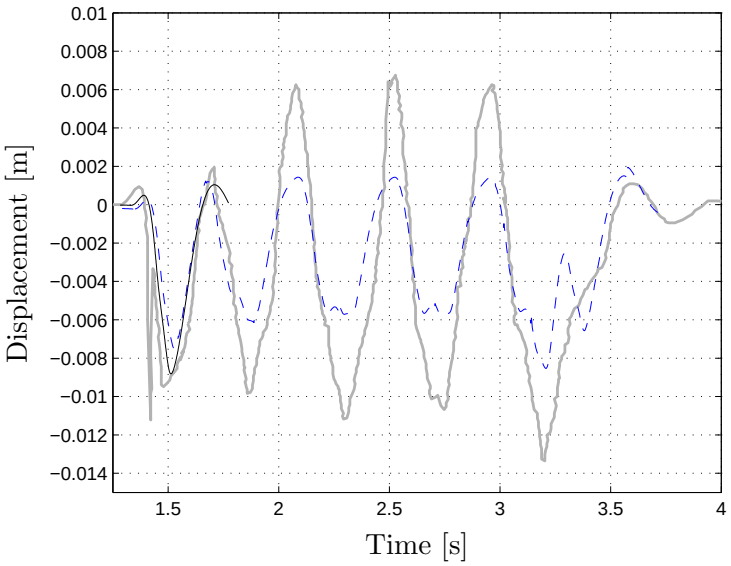

(b)

Figure 4.54: Time history of the sleeper displacements obtained in experimental (grey), numerical linear (dashed) and numerical non-linear (black) analyses at circulation speeds of a) 70 km/h and b) 204 km/h.

Figure 4.55 presents the frequency content of the experimental, linear and non-linear numerical analyses. Because only the first bogie response is computed in the non-linear analyses, the frequency content of the experi-

mental measurements is computed using the truncated time response, which corresponds to the same time frame as for the non-linear response.

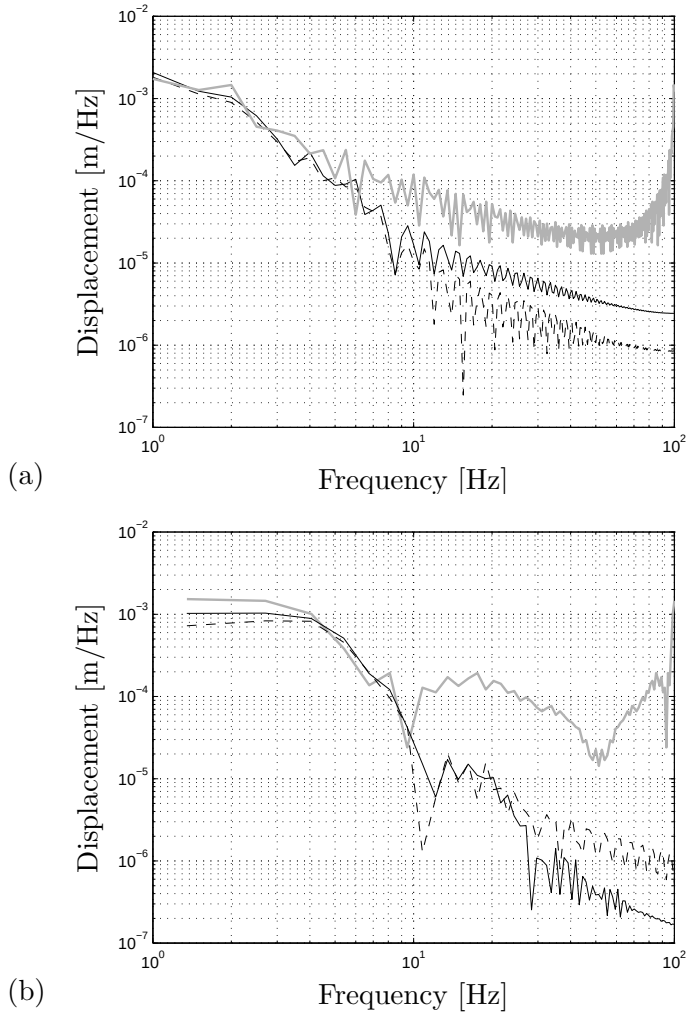

Figure 4.55: Frequency content of experimental (grey), numerical linear (dashed) and numerical non-linear (black) sleeper displacements at circulation speeds of a) 70 km/h and b) 204 km/h.

The quasi-static response is dominant in both cases, with the response rapidly decaying with increasing frequency. In both cases, the amplitude measured decays to less than 10% from 1 Hz to 10 Hz. In the numerical models, this reduction is exacerbated because the models do not consider the dynamic component of the load and, as demonstrated in section 3.5, the accuracy is diminished for high frequencies due to the size of the finite elements. For a circulation speed of 70 km/h, good agreement is obtained at

low frequencies; however, this agreement quickly weakens. For a circulation speed of 204 km/h, there is good agreement up to 10 Hz; accuracy is also diminished for higher frequencies in the non-linear model. Regardless of these inaccuracies at increasing frequencies, the dominant response is well simulated in both cases, which is evident in the comparison of the time histories of the sleeper displacements.

The linear and non-linear analyses exhibit good agreement for circulation speeds of 70 km/h at the dominating frequency range. However, for circulation speeds of 204 km/h, there is a considerable loss of accuracy in the linear analyses at the lowest frequencies.

The degradation of the subgrade stiffness is mapped in Figure 4.56 for a transversal section directly below the sleeper. The points at $x = -0.75\,\mathrm{m}$ are located below the rail and all points at $x > -4.6\,\mathrm{m}$ are below the track.

Beginning at the limit velocity, the circulation speed significantly affects the stiffness reduction in the soil. However, for lower speeds there is a slight change in dynamic behaviour with increasing velocity. This condition is evident from a comparison of the degradation of shear modulus at the circulation speeds of 10 km/h and 70 km/h, in which few changes are perceptible; change is observed primarily at the top soil below the track. This finding is consistent with the measured peak displacements (Figure 4.49) that slightly increase from 10 km/h to 70 km/h. For higher circulation speeds, the peak displacements begin to increase significantly and the same result occurs for the stiffness degradation. For a circulation speed of 204 km/h, greater stiffness variations occur in the soil. Assuming that the 95% iso-line separates the zones between linear and non-linear behaviour, the portion of soil in which non-linear behaviour must be considered is similar for low circulation speeds but increases significantly for the circulation speed of 204 km/h. This occurrence is more prominent in the horizontal direction: at the soil surface, a 5% stiffness degradation occurs 8.8 m from the track centre for circulation speeds of 70 km/h, whereas this distance increases to 14.5 m for circulation speeds of 204 km/h. The variation in depth for which non-linear behaviour occurs is not as drastic. Qualitatively, Costa et al. (2010) discovered similar variations in the nonlinear boundaries in the horizontal direction for high speeds; in the vertical direction, the increase in depth in the non-linear zone was higher. Note that the stiffness reduction, as presented by the authors, results from an update in the stiffness for a representative shear strain to the passage of the full train; this stiffness reduction is constant throughout the analysis, whereas in the analysis in this study, the stiffness reduction presented is the peak reduction due to the passage of the first bogie. Regardless of the differences in the consideration of non-linear behaviour, this analysis confirms the conclusions obtained by Costa et al. (2010).

It is also apparent that the track distributes stresses and strains in the transversal direction because the iso-lines present nearly horizontal directions at points below the track ($x > -4.6\,\mathrm{m}$) and at depths higher than 1 m.

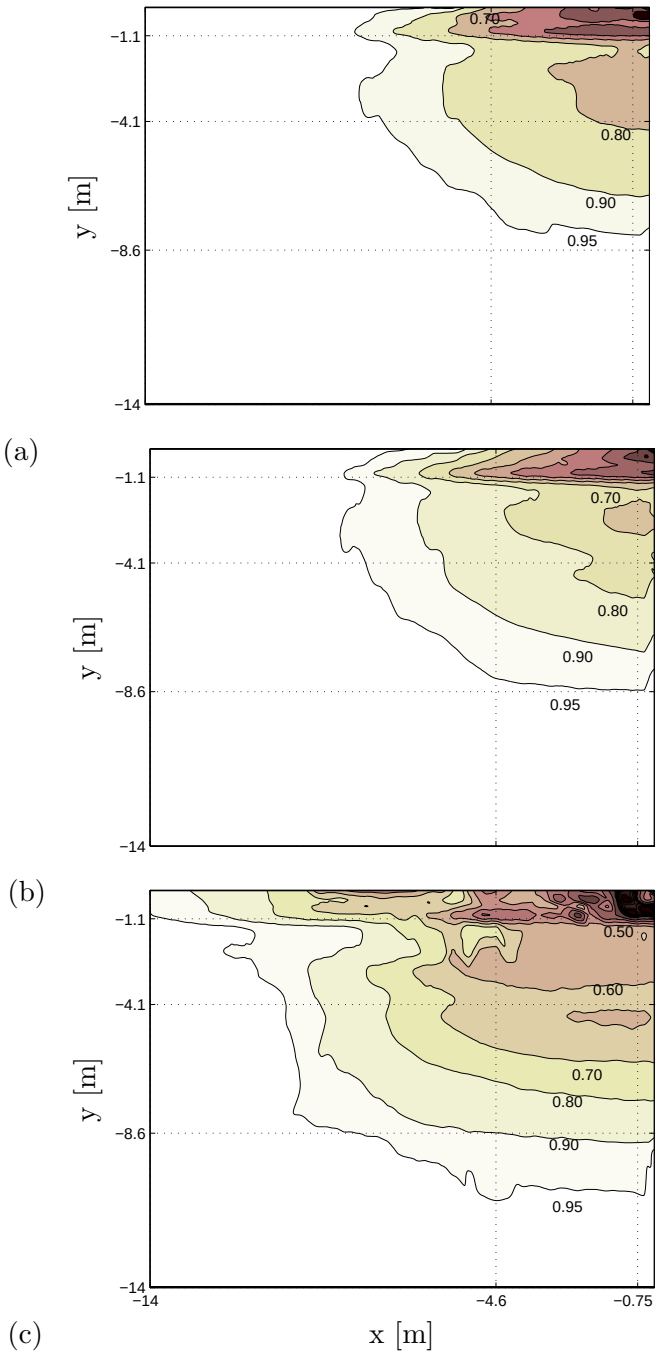

Figure 4.56: Peak stiffness reductions $\frac{G_{sec}}{G_0}$ due to the passage of the X-2000 front bogie at a) 10 km/h, b) 70 km/h and c) 204 km/h.

For the dry crust layer, the soil portions directly below the rail are subject to maximum non-linear behaviour; however, for the other layers the variation in non-linear behaviour with horizontal position is extremely limited for all portions directly below the track. The stress and strain variations in the soil are also analysed (Figure 4.57).

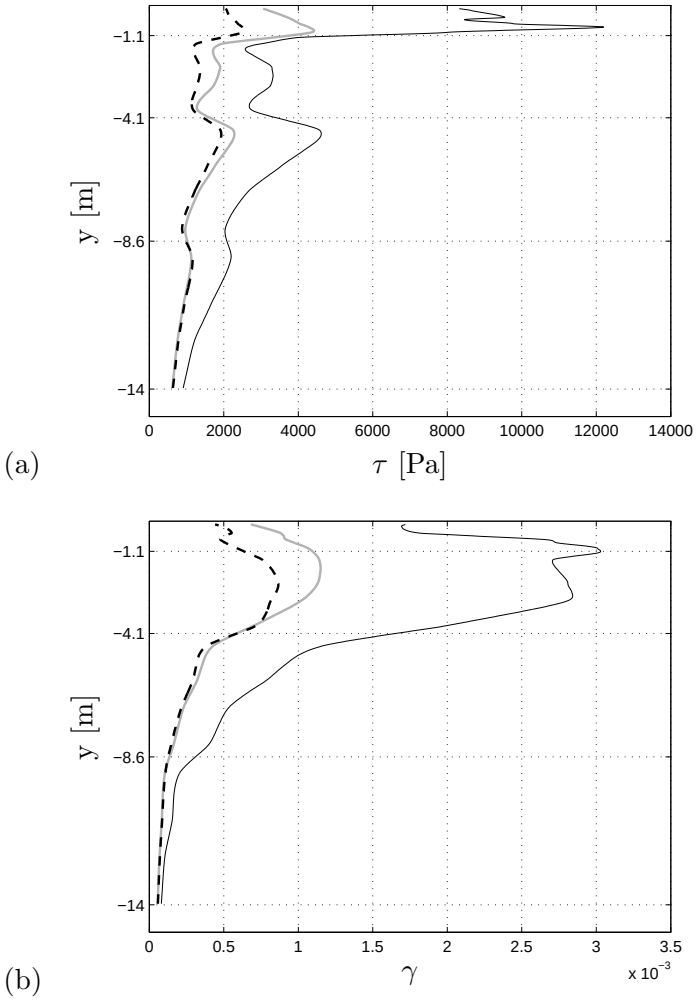

Figure 4.57: Variation with depth of a) shear stress τ and b) shear strain γ in the soil directly below the rail for circulation velocity of 10 km/h (dashed), 70 km/h (grey) and 204 km/h (black).

Few changes occur in the soil due to the increase in speeds from 10 km/h to 70 km/h, with the most prominent changes appearing at the top. As expected, substantially higher stress and strain variations occur in the soil at circulation speeds of 204 km/h. These differences are significant at

low depths and reduce with increasing depth, whereas non-linear behaviour becomes less relevant. Nevertheless, even at 14 m depth, the stresses and strains are higher for circulation speeds of 204 km/h. There is also a tendency of the stresses and strains to increase in the vicinity of the interface between the different layers. The stresses in the dry crust layer (0 m to 1.1 m depth) are approximately 3 times higher for the circulation speed of 204 km/h than at 70 km/h, this is where the highest differences between both circulation speeds occur. Conversely, the average shear strains in the organic clay are higher than the average shear strains in the dry crust for both circulation speeds because this layer exhibits much lower initial stiffness than any other layer.

Figures 4.58 and 4.59 present the variation of shear stresses and strains in the soil directly below the rail, for circulation speeds of 70 km/h and 204 km/h.

When non-linear behaviour is considered, there is a considerable reduction in stress at the dry crust for circulation speeds of 70 km/h because this is where most stiffness degradation occurs and the stresses are redistributed to the remaining layers, whose stiffness is more similar to low strain stiffness. This result, however, does not occur at 204 km/h because a larger portion of the soil presents stiffness degradation. Consequently, the stress can be distributed to fewer zones.

At the top layers, there is a significant difference between shear strains in the linear and non-linear analyses for circulation speeds of 70 km/h; this difference reflects the resulting soil degradation. However, for speeds of 204 km/h, the differences in shear strain are much greater, which further highlights that non-linear behaviour is more relevant for increasing circulation speeds and, therefore, the linear analyses are less accurate.

4.4.5 Partial remarks

This section presents the analysis of a railway track by integrating the non-linear behaviour of embankment and subgrade. In the case studied, the non-linear response of the track leads to extreme vibrations and, therefore, the consideration of non-linearity is necessary to obtain adequate predictions.

Due to the limitations of the track size and required computational resources, the non-linear analysis incorporated only the simulation of the first train bogie. The simulations confirmed that non-linear behaviour plays an important role in track response. Beginning with a certain velocity, the magnitude of the non-linear response increases with increased train circulation. At 70 km/h, the linear analysis demonstrates considerable accuracy in the prediction of the sleeper displacements. At 204 km/h, the results of the linear analysis are very inaccurate, whereas the non-linear analysis yield significant improvement. The stiffness degradation is very similar for circu-

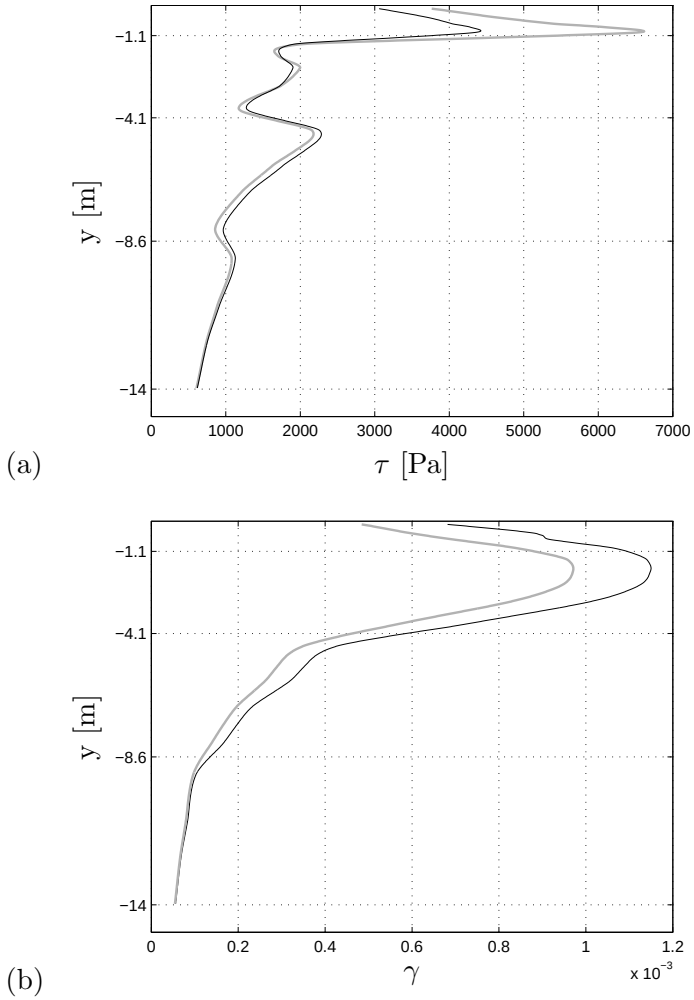

Figure 4.58: Variation with depth of a) shear stress τ and b) shear strain γ in the soil directly below the rail for circulation velocity of 70 km/h in the linear (grey) and non-linear (black) analysis.

lation speeds of 10 km/h and 70 km/h; however, at 204 km/h, substantial differences are obtained with a considerable increase in the zone in which non-linear behaviour is obtained. The study of the stresses and strains in the soil provide similar conclusions because these values are very similar for the two lowest circulation speeds at most depths. However, considerably higher stresses and strains occur at the highest circulation speed to depths of 10 m.

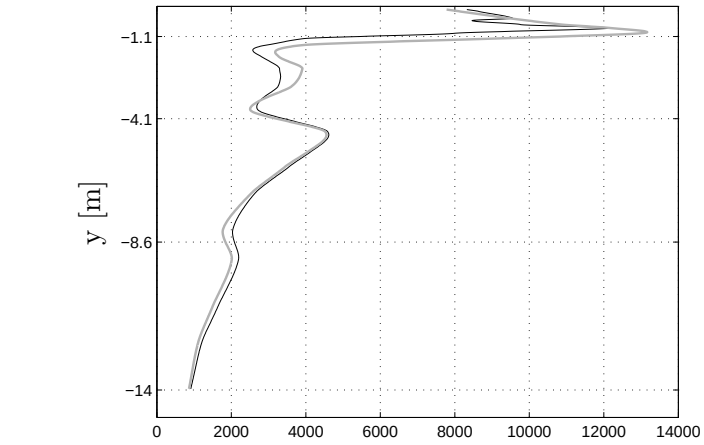

(a)

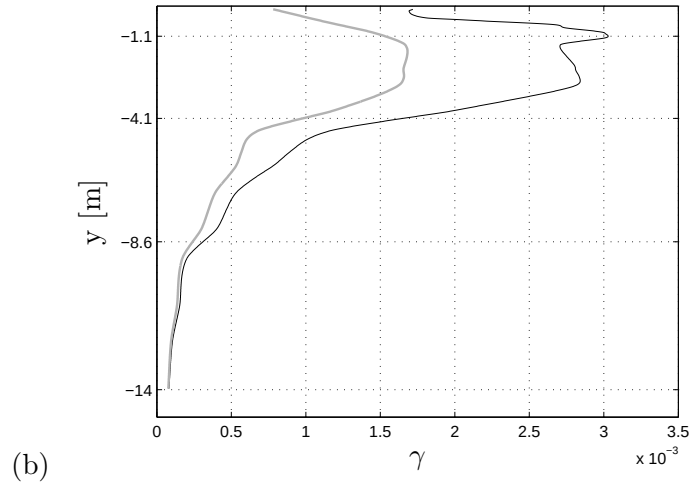

(b)

Figure 4.59: Variation with depth of a) shear stress τ and b) shear strain γ in the soil directly below the rail for circulation velocity of 204 km/h in the linear (grey) and non-linear (black) analysis.

4.5 Conclusions

This chapter presents the isolated studies of non-linear ballast and subgrade modelling, with an emphasis on their influence in track response and the integration of non-linearity in a railway track simulation. The ballast was modelled using a modified Mohr-Coulomb constitutive model with shear, tensile and compressive caps, and hardening/softening of the shear and compressive caps. The non-linear behaviour of the subgrade was obtained using a cyclic non-linear model that follows the hysteresis curve of the soil behaviour by using Iwan's parallel model. In both cases, comparisons between the results obtained with the linear models are presented.

In the study of non-linear behaviour of ballast, it was demonstrated that ballast has significant influence in track response, especially if the definition of its small strain stiffness is unclear or its variation with isotropic stress is not considered. The definition of limiting caps in the $p : q$ space is also advisable; even though its influence seems lower than the influence of the pressure dependent stiffness. The results of this study, and the results obtained by Araújo (2011) indicate that the isotropic pressure of the ballast in service falls predominantly between 5 kPa and 50 kPa. Therefore, it is suggested that future experimental studies of track ballast focus mainly on its behaviour within this range. In both cases, the track peak displacements may be considerably influenced by the consideration of non-linearity, but the peak particle velocities are less influenced by the consideration of non-linearity.

In the case of the subgrade, stiffness reductions greater than 50% of the small strain value may occur in the soil immediately below the track. These large stiffness reductions are very localised in time and space. The linear and equivalent linear analyses may provide an estimation of the subgrade zone in which non-linear behaviour occurs. In addition, the accuracy of the linear equivalent behaviour analyses are improved compared with the linear cases.

The study of the Ledsgard site is a rare case in which nonlinear embankment and subgrade are considered in the simulation of a track stretch. As concluded by Costa et al. (2010) and Banimahd and Woodward (2007), this consideration of the importance of non-linear behaviour of track response increases significantly with circulation speed. This notion, however, is only valid when the circulation speed surpasses a threshold value. At lower speeds, only slight changes in non-linear behaviour are evident. At higher circulation speeds, the stiffness reduction in the soil and the zone in which non-linear behaviour occurs increase significantly. The obtained results indicate that the non-linear 3D FE can be an accurate tool for predicting track response to train passage. However, simulation of non-linear behaviour of the full train was not possible.

Summarizing the contributions of this chapter, the influence of non-

linear behaviour of ballast and subgrade on track response was examined. In this study, relevant information about stress and strain distributions in the track and soil were obtained, in the transversal and longitudinal directions of the track. The implementation of the cyclic non-linear model is an important contribution that provides the first 3D simulation of a railway track with cyclic non-linear soil response, which complements the equivalent linear analyses of Costa et al. (2010) and non-linear elastic analyses of Banimahd and Woodward (2007). Although the model can be improved in some regards, it is an invaluable tool that performs innovative analyses. The integrated simulation of the Ledsgard railway track, in which the non-linear track response is accurately predicted, presents an important contribution as a 3D FE methodology. This simulation facilitates the study of the influence of circulation speed on stiffness degradation of the soil and the distribution of stresses and strains with depth.

Chapter 5

Main Summary

5.1 Main conclusions and contributions

This thesis presents a study of the numerical prediction of railway track response to the passage of high-speed trains. It is mainly focused on the influence of non-linear material behaviour on track ballast and subgrade. This study is conducted using 3D FE models, which generated another focus of the thesis: to emphasise the advantages and disadvantages of this numerical method for this type of simulation.

In Chapter 2, the most common numerical methods and the knowledge gained about railway response were explored. It was concluded that non-linear behaviour is seldom considered in these simulations, especially for those simulations in which the full track-soil system is modelled. The objectives of this thesis were formulated.

Chapter 3 has a twofold objective: to study the elastodynamics of the linear soil-track system and validate the adopted FE simulation methodology. It was confirmed that although the track simulation may be accurate considering only the quasi-static moving load, the response away from the track requires the consideration of the dynamic components of the load. It was concluded that the FEM obtained accurate transfer functions to the free field; however, this required a very refined mesh which was only accomplished using a 2D mesh with axisymmetry. When a 3D FE mesh was employed, an increased element side had to be adopted that diminished accuracy at high frequencies. In spite of this result, the 3D FE mesh obtained rail receptances and transfer functions between the track and the nearby subgrade that were similar to those computed by the validated 2.5D models. This finding indicates that the mesh is well suited for modelling railway track response. The 3D FE also obtains a similar rail response to the passage of a moving load, which validates the methodology that was adopted to simulate moving loads.

Chapter 4 considers non-linear behaviour of the ballast and soil due to

high-speed train circulation. This main contribution is derived from the fact that non-linear behaviour has seldom been considered in railway track simulation, especially in 3D simulations and large-track models. This innovative study allowed to formulate the following remarks:

- The non-linear ballast behaviour influences track response with higher peak displacements and velocities than predicted by linear models.
- Simultaneously considering non-linear ballast behaviour and stress-dependent stiffness predicts distinct results than when considering these characteristics separately. Therefore, the consideration of both characteristics is essential for obtaining more accurate ballast responses.
- An accurate determination of the small strain properties of ballast and the consideration of pressure-dependent stiffness may more significantly influence model response than by the consideration of non-linear behaviour.
- Stresses and strains in ballast are primarily concentrated directly below the rail at the contact point with the sleeper, and diminish radially from this point.
- Stresses in ballast portions between two sleepers are significantly analogous to the stresses in portions directly below the sleepers. The transversal distribution of the stresses is also similar in both cases.
- The main differences between the stress paths of crib ballast and sleeper ballast are discovered at the top of the layer. At the bottom layer, the stress paths are very similar.
- A cyclic non-linear model was implemented that allows the FE simulated soil to follow the hysteresis loops. This model follows Iwan's parallel model and the Masing rules to determine the relationship between shear stress and shear strain in the material.
- The implemented model obtains a perfect reproduction of the stiffness reduction with shear strain. The Masing rules imply that an incorrect damping formulation occurs for shear strains of 1×10^{-4} and higher; the model also does not consider the variation of material behaviour with mean stress.
- The non-linear simulation showed that there is a considerable reduction in stiffness of the soil, which may be less than 50% of its initial value. The greatest reduction in stiffness is confined to a very small soil portion and a very restricted time span.

- For the equivalent linear analysis, the horizontal layering of soil stiffness distribution is sufficient for nearly all soil depths, except for the top 1 to 2 m, in which a more refined distribution below the track is more appropriate.
- Both the linear and equivalent linear models present a fairly accurate estimation of the boundaries between linear and non-linear soil behaviour.
- The equivalent linear analysis is an improvement upon the linear case, and allows for an interesting approximation of the results of the non-linear approaches, with much less complexity.
- Consideration of the effective shear strain as 65% of the peak shear strain results in a good estimation of the soil stiffness reduction.
- The simulation of the Ledsgard railway track demonstrates that there are cases in which the consideration of non-linear behaviour is essential to obtain adequate prediction of track response.
- The presented non-linear 3D FE methodology accurately predicts railway track response. However, due to the high computational needs of the model, only the response to the passage of the first bogie was computed.
- The relevance of non-linear behaviour increases with circulation speed. Consequently, for low circulation speeds, the linear analyses present good accuracy in railway track response, which is not the case for higher speeds where non-linear analyses are required.
- The stiffness degradation profile in the soil is also highly influenced by circulation speed.

5.2 Future developments

The development of these analyses and the interpretation of the results leads to the realisation that further investigation of this subject is needed. Some of these new evaluations will eventually become possible as expanded computational capabilities facilitate enhanced complexity of the models. Although this thesis proves that the 3D FE models can be used to accurately simulate railway track behaviour, the models still require further understanding, optimisation, computational resources and computational time to deem them fully functional for works other than research. On the other hand, 2.5D models are much more computationally effective and provide equally accurate predictions of the track displacements, and are definitely better suited to predict propagation of waves to the free field. However, these models do

not allow for such a detailed study of the ballast response as the one done in this thesis. Even though non-linear behaviour can be simulated with the equivalent linear analyses, real non-linear behaviour with prediction of permanent deformations is not possible. Moreover, if available in commercial packs these are not so user friendly as some FE software. It is the opinion of the author that with the referred increasing capacity of computers, most disadvantages of 3D FE computations may fade away making it the best option for railway track response prediction. Accounting for these improvements in the computational resources, it is suggested the following future works:

- Utilization of increasingly large 3D FE meshes allowing for the modelling of the full train passage in non-linear behaviour of ballast and soil.
- Study of the increasing accuracy in the track response prediction occurring from the utilization of similar mesh geometry but with much more refinement.
- Study of non-linear track and soil response due to the quasi-static and dynamic train loads. These would result from the increase of accuracy at higher frequencies due to improved mesh refinement.
- Comparison between 3D FEM and 3D DEM non-linear ballast response to moving loads and train circulation. This requires the simulation of a representative track stretch.
- 3D DEM study of the differences between inter-particle forces occurring in a ballast portion directly below the sleeper and a ballast portion between sleepers.

Other developments stemming from the presented works can be suggested that do not depend upon the increase of computational resources:

- Simulation of damping evolution at high strains of the implemented cyclic non-linear model. This requires the abandonment of the Masing rule for reload/unload and could be achieved by the utilization of a factor dependent upon the shear strain level that would scale the stiffness of the Iwan elements when a stress reversal occurs.
- Study of the possibility to include stress dependent small strain properties in the implemented cyclic non-linear model, as well as stress dependent stiffness reduction curves and consequently damping variation curves. A power law relating the mean stress and stiffness of the Iwan elements should be sufficient for modelling the low strain stiffness. However, to obtain equally accurate stiffness reduction curves, it could require the definition of a second law relating the mean pressure and the slip-stress of the elements.

- Parametric study of the accuracy of equivalent linear analyses for a representative effective shear strain.
- Study of the long-term track behaviour. This development can lead to very important considerations regarding the influence of the track properties in the maintenance frequency, leading to direct implications in the design and long-term cost of new tracks and consequently in life cycle cost analyses.

Bibliography

J.D. Achenbach. *Wave propagation in elastic solids*, volume 16 of *North-Holland Series in Applied Mathematics and Mechanics*. North-Holland, Amsterdam, The Netherlands, 1973.

M. Adam, G. Pflanz, and G. Schmid. Two- and three-dimensional modelling of half-space and train-track embankment under dynamic loading. *Soil Dynamics and Earthquake Engineering*, 19:559–573, 2000.

A. Al Shaer, D. Duhamel, K. Sab, G. Foret, and L. Schmitt. Experimental settlement and dynamic behavior of a portion of ballasted railway track under high speed trains. *Journal of Sound and Vibration*, (316), 2008.

L. Andersen and S.R.K. Nielsen. Reduction of ground vibration by means of barriers or soil improvement along a railway track. *Soil Dynamics and Earthquake Engineering*, 25:701–716, 2005.

N. Araújo. *High-speed trains on ballasted railway track - Dynamic stress field analysis*. PhD thesis, Universidade do Minho, Guimarães, Portugal, 2011.

D. Assimaki and E Kausel. An equivalent linear algorithm with frequency- and pressure-dependent moduli and damping for the seismic analysis of deep sites. *Soil Dynamics and Earthquake Engineering*, 22:959–965, 2002.

M. Banimahd and P.K. Woodward. Numerical study of train speed effect on railway track response. In *Proceedings of the 9th International Conference in Railway Engineering*, London, United Kingdom, 2007.

D.D. Barkan. *Dynamics of bases and foundations.* McGraw-Hill, New York, 1962.

G. A. Beckey and S.F. Masri. Random search techniques for optimisation of nonlinear systems with many parameters. *Math Comput Simulation*, 25: 210–213, 1983.

J.P. Bérenger. A perfectly matched layer for the absorption of electromagnetic waves. *Journal of Computational Physics*, 41:115–135, 1994.

P. Bettess. *Infinite elements*. Penshaw Press, Sunderland, United Kingdom, 1992.

M.A. Biot. Bending of infinite beams on an elastic foundation. *Journal of Applied Mechanics, Transactions of the ASME*, 59:A1–A7, 1937.

F. B. Bonnett. *Practical Railway Engineering*. Imperial College Press, London, 2005.

H. Brandl. Geotechnical aspects for high-speed railways. In *Proceedings of the International Seminar on Geotechnics in Pavement and Railway Design and Construction*, Rotterdam, Netherlands, 2004.

S. F. Brown and F. L. Hyde. Significance of cyclic confining stress in repeated-load triaxial testing of granular material. *Transportation Research Record*, 537:49–58, 1975.

C. Cekerevac, S. Girardin, G. Klubertanz, and L. Laloui. Calibration of an elasto-plastic constitutive model by a constrained optimisation procedure. *Computers and Geotechnics*, 33:432–443, 2006.

E. Celebi. Three-dimensional modelling of train-track and sub-soil analysis for surface vibrations due to moving loads. *Applied Mathematics and Computation*, 179:209–230, 2006.

P. Chatterjee, G. Degrande, D. Clouteau, T. Al-Hussaini, M. Arnst, and R. Othman. Numerical modelling of ground borne vibrations from underground railway traffic. In *Proceedings of the 6th National Congress on Theoretical and Applied Mechanics*, Ghent, Belgium, May 2003. National Committee for Theoretical and Applied Mechanics.

H. Chebli, D. Clouteau, and L. Schmitt. Dynamic response of high-speed ballasted railway tracks: 3D periodic model and in situ measurements. *Soil Dynamics and Earthquake Engineering*, 28:118–131, 2008.

Y.P. Cheng, Y. Nakata, and M.B. Bolton. Discrete element simulation of crushable soil. *Geotechnique*, 53(7):19–29, 2003.

W.C. Chew and Q.H. Liu. Perfectly matched layers for elastodynamics: A new absorbing boundary condition. *Journal of Computational Acoustics*, 4(4):341–359, 1996.

D. Clouteau, M.L. Elhabre, and D. Aubry. Periodic BEM and FEM-BEM coupling: application to seismic behaviour of very long structures. *Computational Mechanics*, 25:567–577, 2000.

D. Clouteau, G. Degrande, and G. Lombaert. Numerical modelling of traffic induced vibrations. *Meccanica*, 36(4):401–420, 2001. URL `http://dx.doi.org/10.1023/A:1015005410628`.

D. Clouteau, R. Othman, M. Arnst, H. Chebli, G. Degrande, R. Klein, P. Chatterjee, and B. Janssens. A numerical model for ground-borne vibrations from underground railway traffic based on a periodic FE-BE formulation. In D. Thompson and C. Jones, editors, *8th International Workshop on Railway Noise*, volume 1, pages 167–178, Buxton, UK, September 2004.

T. F. Coleman and Y. Li. On the convergence of reflective Newton methods for large-scale nonlinear minimization subject to bounds. *Mathematical Programming*, 67(2):189–224, 1994.

T. F. Coleman and Y. Li. An interior, trust region approach for nonlinear minimization subject to bounds. *SIAM Journal on Optimization*, 6:418–445, 1996.

F. Collino and C. Tsogka. Application of the perfectly matched absorbing layer model to the linear elastodynamic problem in anisotropic heterogeneous media. *Geophysics*, 66, 2001.

A.P. Costa, R. Calçada, S. A. Cardoso, and A. Bodare. Influence of soil non-linearity on the dynamic response of high-speed railway tracks. *Soil Dynamics and Earthquake Engineering*, 30:221–235, 2010.

A.P. Costa, R. Calçada, and S. A. Cardoso. Trackground vibrations induced by railway traffic: In-situ measurements and validation of a 2.5D FEM-BEM model. *Soil Dynamics and Earthquake Engineering*, 32:111–128, 2012.

T. Dahlberg. Railway track dynamics - a survey. Technical report, Solid Mechanics/IKP, Linkping University, 2003.

M.B. Darendeli. *Development of a new family of normalized modulus reduction and material damping*. PhD thesis, University of Texas, Austin, 2001.

T.M. Dawn and C.G. Stanworth. Ground vibrations from passing trains. *Journal of Sound and Vibration*, 66(3):355–362, 1979.

G. Degrande and G. Lombaert. High-speed train induced free field vibrations: in situ measurements and numerical modelling. In N. Chouw and G. Schmid, editors, *Proceedings of the International Workshop Wave 2000, Wave propagation, Moving load, Vibration reduction*, pages 29–41, Ruhr University Bochum, Germany, December 2000. A.A. Balkema, Rotterdam. URL `../papers/degrip00b.pdf`.

G. Degrande and L. Schillemans. Free field vibrations during the passage of a Thalys high-speed train at variable speed.

Journal of Sound and Vibration, 247(1):131–144, 2001. URL http://dx.doi.org/10.1006/jsvi.2001.3718.

G. Degrande, P. Chatterjee, D. Clouteau, T. Al-Hussaini, M. Arnst, and R. Othman. A numerical prediction model for ground-borne vibrations from underground railway traffic using a coupled periodic FEM-BEM approach. In *10th International Congress on Sound and Vibration*, Stockholm, Sweden, July 2003. CD-ROM.

N. Deng, S.A. Ashford, and J. Lysmer. Ground2d: A two-dimensional seismic site response analysis program. Technical report, Earthquake Engineering Research Center, University of California, Berkeley, 1995.

J. Domínguez. *Boundary elements in dynamics*. Computational Mechanics Publications and Elsevier Applied Science, Southampton, United Kingdom, 1993.

G. Eason. The stresses produced in a semi-infinite solid by a moving surface force. *International Journal of Engineering Science*, 2:581–609, 1965.

T. Ekevid and N. Wiberg. Wave propagation related to high-speed train. A scaled boundary FE-approach for unbounded domains. *Computer Methods in Applied Mechanics and Engineering*, 191:3947–3964, 2002.

C. Esveld. *Modern Railway Track*. MRT Productions, Duisburg, West Germany, 1989.

W.M. Ewing, W.S. Jardetzky, and F. Press. *Elastic waves in layered media*. McGraw-Hill, New York, Toronto, London, 1957.

P. Fiala, G. Degrande, and F. Augusztinovicz. Numerical modelling of ground borne noise and vibration in buildings due to surface rail traffic. *Journal of Sound and Vibration*, 301(3-5):718–738, 2007. URL http://dx.doi.org/10.1016/j.jsv.2006.10.019.

S. François, M. Schevenels, and G. Degrande. *BEMFUN: MATLAB toolbox for boundary elements in elastodynamics. Version 2.1 Build 16. User's guide*. Department of Civil Engineering, KU Leuven.

S. François, M. Schevenels, P. Galvin, G. Lombaert, and G. Degrande. A 2.5D coupled FE-BE methodology for the dynamic interaction between longitudinally invariant structures and a layered halfspace. *Computer Methods in Applied Mechanics and Engineering*, 199(23-24), 2010.

L. Fryba. *Vibration of solids and structures under moving loads*. Noordhoff International Publishing, Groningen, 1973.

Y. Furumoto, M. Sugito, and A. Yashima. Frequency-dependent equivalent linearized technique for FEM response analysis of ground. In *Proceedings of the 12th World Conference in Earthquake Engineering (CD-ROM)*, Auckland,New Zealand, 2000.

P. Galvín and J. Domínguez. High-speed train-induced ground motion and interaction with structures. *Journal of Sound and Vibration*, 307:755–777, 2007.

P. Galvín and J. Domínguez. Experimental and numerical analyses of vibrations induced by high-speed trains on the CórdobaMálaga line. *Electronic Journal of Geotechnical Engineering*, 29:641–657, 2009.

P. Galvín, S. François, M. Schenevels, E. Bongini, G. Degrande, and G. Lombaert. A 2.5D coupled FE-BE model for the prediction of railway induced vibrations. *Soil Dynamics and Earthquake Engineering*, 30(12), 2010.

W. Gardien and H.G. Stuit. Modelling of soil vibrations from railway tunnels. *Journal of Sound and Vibration*, 267:605–619, 2003.

P.E. Gill, W. Murray, and M.H. Wright. *Practical Optimization*. Academic Press: London, 1981.

C. González-Nicieza, M.I. Álvarez Fernández, A. Menéndez-Díaz, A.E. Álvarez Vigil, and F. Ariznavarreta-Fernández. Failure analysis of concrete sleepers in heavy haul railway tracks. *Engineering Failure Analysis*, 15:90–117, 2008.

K.F. Graff. *Wave motion in elastic solids*. Ohio State University, 1975.

A. E. Groen. Elastoplastic modelling of sand using a conventional model. Technical report, Delft University of Technology, 1995.

S. Gupta, G. Degrande, H. Chebli, D. Clouteau, M.F.M. Hussein, and H.E.M. Hunt. A numerical model for prediction of vibration from underground railways. In *7th World Congress on Computational Mechanics*, Los Angeles, California, USA, July 2006a.

S. Gupta, P. Fiala, M.F.M. Hussein, H. Chebli, G. Degrande, F. Augusztinovicz, H.E.M. Hunt, and D. Clouteau. A numerical model for groundborne vibrations and re-radiated noise in buildings from underground railways. In P. Sas and M. De Munck, editors, *Proceedings of ISMA2006 International Conference on Noise and Vibration Engineering*, pages 1741–1756, Leuven, Belgium, September 2006b.

T.G. Gutowski and C.L. Dym. Propagation of ground vibration: A review. *Journal of Sound and Vibration*, 2(49):179–193, 1976.

W. Haegeman. In situ tests Retie-Waremme-Lincent. Report RUG IV.1.16.3, Soil Mechanics Laboratory, Ghent University, September 2001. STWW Programme Technology and Economy, Project IWT-000152.

L. Hall. Simulations and analyses of train-induced ground vibrations in finite element models. *Soil Dynamics and Earthquake Engineering*, 23:403–413, 2003.

M. Heelis, A. Dawson, A. Collop, D. Chapman, and V. Krylov. Resilient modulus of soft soil beneath high-speed rail lines. *Transportation Research Record*, 1687:39–46, 1999.

G. Holm, B. Andréasson, P. Bengtsson, A. Bodare, and H. Eriksson. Mitigation of track and ground vibrations by high speed trains at Ledsgård, Sweden. Technical report, Swedish Deep Stabilization Research Centre, 2002.

Z. Hossain, B. Indraratna, F. Darve, and P. K. Thakur. DEM analysis of angular ballast breakage under cyclic loading. *Geomechanics and Geotechnical Engineering*, 2(3), 2007.

D. V. Hutton. *Fundamentals of finite element analysis.* McGraw-Hill, New York, 2004.

I.M. Idriss and J.I. Sun. *SHAKE91: a computer program for conducting equivalent linear seismic response analysis of horizontally layered deposits. Users Guide.* University of California.

I.M. Idriss, D. Dobry, and R.D. Singh. Nonlinear behavior of soft clays during cyclic loading. *Journal of Geotechnical Engineering, Proceedings of the ASCE*, 104(12):1427–1447, 1978.

B. Indraratna and S. Nimbalkar. Implications of ballast breakage on ballasted railway track based on numerical modelling. In *Proceedings of the , 13th International Conference of the International Association for Computer Methods and Advances in Geomechanics*, Melbourne, Australia, 2011.

B. Indraratna, L. S. S. Wijewardena, and A. S. Balasubramaniam. Large-scale triaxial testing of graywacke rockfill. *Geotechnique*, 43(1):37–51, 1993.

B. Indraratna, D. Ionescu, and H. D. Christie. Shear behaviour of railway ballast based on large-scale triaxial tests. *Journal of Geotechnical and Geoenvironmental Engineering, Proceedings of the ASCE*, 124(5):439–449, 1998.

B. Indraratna, J. Lackenby, and D. Christie. Effect of confining pressure on the degradation of ballast under cyclic loading. *Geotechnique*, 55(4): 325–328, 2005a.

B. Indraratna, J. S. Vindod, and J. Lackenby. Influence of particle breakage on the resilient modulus of railway ballast. *Geotechnique*, 59(7):643–646, 2005b.

I. Ishibashi. Discussion of "Effect of soil plasticity on cyclic response" by M. Vucetic and R. Dobry. *Journal of Geotechnical Engineering, Proceedings of the ASCE*, 118(5):830–832, 1992.

I. Ishibashi and X. Zhang. Unified dynamic shear moduli and damping ratios of sand and clay. *Soils and Foundations*, 33(1):182–191, 1993.

K. Ishihara. *Soil behaviour in earthquake geotechnics*, volume 46 of *Oxford Engineering Science Series*. Clarendon Press, Oxford, United Kingdom, 1996.

K. Ishihara, N. Yoshida, and S. Tsujino. Modelling of stress strain relations of soils. In *Proceedings, Fifth International Conference on Numerical Methods in Geomechanics*, Nagoya, Japan, 1985.

Itasca. *PFC 2D. Particle Flow Code in 3 Dimensions. Online Manual Table of Contents*. http://www.itascacg.com/.

W.D. Iwan. On a class of models for the yielding behaviour of continuous and composit systems. *Journal of Applied Mechanics, Transactions of the ASME*, 34:612–617, 1967.

S.H. Ju, J.R. Liao, and Y.L. Ye. Behavior of ground vibrations induced by trains moving on embankments with rail roughness. *Soil Dynamics and Earthquake Engineering*, 30:1237–1249, 2010.

A. Karlström and A. Boström. An analytical model for train-induced ground vibrations from railways. *Journal of Sound and Vibration*, 292:221–241, 2006.

E. Kausel. An explicit solution for the Green functions for dynamic loads in layered media. Technical report, Massachusetts Institute of Technology, 1981.

E. Kausel and J.M. Roësset. Stiffness matrices for layered soils. *Bulletin of the Seismological Society of America*, 71(6):1743–1761, 1981.

A.M. Kaynia, C. Madshus, and P. Zackrisson. Ground vibration from high speed trains: prediction and countermeasure. *Journal of Geotechnical and Geoenvironmental Engineering, Proceedings of the ASCE*, 126(6):531–537, 2000.

T. Kokusho. A cyclic triaxial test of dynamic soil properties for wide strain range. *Soils and Foundations*, 20:45–60, 1980.

A. Kouby, E. Burgeois, and F. Rocher-Lacoste. Subgrade improvement method for existing railway lines an experimental and numerical study. *Electronic Journal of Geotechnical Engineering*, 15:461–494, 2010.

G. Kouroussis, O. Verlinden, and C. Conti. Free field vibrations caused by high-speed lines: Measurement and time domain simulation. *Soil Dynamics and Earthquake Engineering*, 31:692–707, 2011.

S.L. Kramer. *Geotechnical earthquake engineering*. Prentice-Hall, Upper Saddle River, New Jersey, 1996.

J. Lackenby, B. Indraratna, G. McDowell, and D. Christie. Effect of confining pressure on ballast degradation and deformation under cyclic triaxial loading. *Geotechnique*, 57(6):527–536, 2007.

H. Lamb. On the propagation of tremors over the surface of an elastic solid. *Philosophical Transactions of the Royal Society*, A203:1–42, 1904.

J.S. Lee, Y.W. Choo, and D.S. Kim. A modified parallel IWAN model for cyclic hardening behavior of sand. *Soil Dynamics and Earthquake Engineering*, 29(4):630–640, 2009.

F. Lekarp, U. Isacsson, and A. Dawson. State of the art. I: Resilient response of unbound aggregates. *Journal of Transportation Engineering, Proceedings of the ASCE*, 126(1):66–75, 2000a.

F. Lekarp, U. Isacsson, and A. Dawson. State of the art. II: Permanent strain response of unbound aggregates. *Journal of Transportation Engineering, Proceedings of the ASCE*, 126(1):76–83, 2000b.

W.L. Lim. *Mechanics of Railway Ballast Behaviour*. PhD thesis, University of Nottingham, Nottingham, United Kingdom, 2004.

W.L. Lim and G.R. McDowell. Discrete element modelling of railway ballast. *Granular Matter*, (7):19–29, 2005.

S. Lobo-Guerrero and L. E. Vallejo. Discrete element method analysis of railtrack ballast degradation during cyclic loading. *Granular Matter*, 8: 195–204, 2006.

G. Lombaert. *Development and experimental validation of a numerical model for the free field vibrations induced by road traffic*. PhD thesis, Department of Civil Engineering, K.U.Leuven, 2001. URL `../papers/lomb01a.pdf`.

G. Lombaert and G. Degrande. Ground-borne vibration due to static and dynamic axle loads of intercity and high-speed trains. *Journal of Sound and Vibration*, 319:1036–1066, 2009.

G. Lombaert, G. Degrande, J. Kogut, and S. François. The experimental validation of a numerical model for the prediction of railway induced vibrations. *Journal of Sound and Vibration*, 297(3-5):512–535, 2006. URL `http://dx.doi.org/10.1016/j.jsv.2006.03.048`.

F. Lopez-Caballero, A. Modaressi, and S. D'Aguiar. Amélioration du modéle de comportement non linéaire existant dans le logiciel CyberQuake. Technical report, École Centrale Paris, 2004.

M. Lu and G. R. McDowell. The importance of modelling ballast particle shape in the discrete element method. *Granular Matter*, 9:69–80, 2007.

M. Lu and G. R. McDowell. Discrete element modelling of railway ballast under triaxial conditions. *Geomechanics and Geotechnical Engineering*, 3 (4), 2008.

J. Lysmer and R.L. Kuhlemeyer. Finite dynamic model for infinite media. *Journal of the Engineering Mechanics Division, Proceedings of the ASCE*, 95(EM4):859–877, 1969.

J. Lysmer, T. Udaka, C.F. Tsai, and H.B. Seed. Flush: a computer program for approximate 3D analysis of soil-structure interaction problems. Technical report, Earthquake Engineering Research Center, University of California, Berkeley, 1975.

C. Madshus and A.M. Kaynia. High-speed railway lines on soft ground: dynamic behaviour at critical train speed. *Journal of Sound and Vibration*, 231(3):689–701, 2000.

J. Martins, A. Gomes Correia, L.F. Ramos, J. Marcelino, L. Caldeira, and J. Delgado. Measurement of vibrations induced by high-speed trains. In *Proceedings of the Eighth International Conference on the Bearing Capacity of Roads, Railways and Airfields*, Champaign, Illinois, USA, 2009.

N. Matasovic and M. Vucetic. Generalized cyclic-degradation pore-pressure generation model for clays. *Journal of Geotechnical Engineering, Proceedings of the ASCE*, 121(1):33–42, 1995.

Matlab 7.6.0.324. The Mathworks Inc., 2005.

J.J. More and D.C. Sorensen. Computing a trust region step. *SIAM Journal on Scientific and Statistical Computing*, 23:553–572, 1983.

A. Nataatmajda. Significance of cyclic confining stress in repeated load triaxial test: a reconsideration. In *Proceedings of the 2nd International Conference on Road and Airfield Pavement Technology, Vol.2*, Singapore, 1995.

S. Nazarian and M.R. Desai. Automated surface wave method: field testing. *Journal of Geotechnical Engineering, Proceedings of the ASCE*, 119(7): 1094–1111, 1993.

V. Nguyen, D. Duhamel, and B. Nedjar. A continuum model for granular materials taking into account the no-tension effect. *Mechanics of Materials*, (35), 2003.

J. O'Brien and D.C. Rizos. A 3D FEM-BEM methodology for simulation of high speed train induced vibrations. *Soil Dynamics and Earthquake Engineering*, 25:289–301, 2005.

C. Paderno. Simulation of ballast behaviour under traffic and tamping process. In *9th Swiss Transport Research Conference*, Lausanne, Switzerland, 2009.

C. Phillips and Y.M.A. Hashash. Damping formulation for nonlinear 1D site response analyses. *Soil Dynamics and Earthquake Engineering*, 29: 1143–1158, 2009.

L. Pronzato, E. Walter., A. Venot, and J-F. Lebruchec. A general purpose global optimiser: implementation and applicaitons. *Math Comput Simulation*, 26:412–422, 1984.

R.M. Pyke. Nonlinear soil models for irregular cyclic loadings. *Journal of the Geotechnical Engineering Division*, 105(6), 1979.

L. Pyl and G. Degrande. Determination of the dynamic soil characteristics with the SASW method at a site in Lincent. Report BWM-2001-02, Department of Civil Engineering, K.U.Leuven, August 2001. STWW Programme Technology and Economy, Project IWT-000152.

G. P. Raymond and J. R. Davies. Triaxial test on dolomite railroad ballast. *Journal of the Soil Mechanics and Foundation Division, Proceedings of the ASCE*, 104(6):737–751, 1978.

P.K. Robertson, R.G. Campanella, D. Gillespie, and A. Rice. Seismic CPT to measure in situ shear wave velocity. *Journal of the Soil Mechanics and Foundation Division, Proceedings of the ASCE*, 112(8):791–803, 1986.

P.W. Rowe. The stress-dilatancy relation for static equilibrium of an assembly of particles in contact. In *Proceedings of the Royal Society of London. Series A, Mathematical and Physical Sciences*, pages 500–527, 1962.

J. Sadrekarimi and M. Akbarzad. Comparative study of methods of determination of coefficient of subgrade reaction. *Electronic Journal of Geotechnical Engineering*, 14, 2009.

G. Saussine, C. Cholet, P.E. Gautier, F. Dubois, C. Bohatier, and J.J. Moreau. Modelling ballast behaviour under dynamic loading. Part 1: A 2D polygonal discrete element method approach. *Comput. Methods Appl. Mech. Engrg.*, 195:2841–2859, 2006.

M. Schevenels, G. Degrande, and S. François. EDT: an ElastoDynamics Toolbox for Matlab. In *Proceedings of the Inaugural International Conference of the Engineering Mechanics Institute (EM08)*, Minneapolis, Minnesota, U.S.A., May 2008.

P.B. Schnabel, J. Lysmer, and H.B. Seed. Shake: a computer program for earthquake response analysis of horizontally layered sites. Technical report, Earthquake Engineering Research Center, University of California, Berkeley, 1972.

E.T. Selig and J.M. Waters. *Track Geotechnology and Substructure Management.* Thomas Telford, London, 1994.

X. Sheng, C.J.C. Jones, and M. Petyt. Ground vibration generated by a harmonic load acting on a railway track. *Journal of Sound and Vibration*, 225(1):3–28, 1999.

X. Sheng, C.J.C. Jones, and D.J. Thompson. A comparison of a theoretical model for quasi-statically and dynamically induced environmental vibration from trains with measurements. *Journal of Sound and Vibration*, 267 (3):621–635, 2003.

X. Sheng, C.J.C. Jones, and D.J. Thompson. A theoretical model for ground vibration from trains generated by vertical track irregularities. *Journal of Sound and Vibration*, 272(3-5):937–965, 2004.

X. Sheng, C.J.C. Jones, and D.J. Thompson. Prediction of ground vibration from trains using the wavenumber finite and boundary element methods. *Journal of Sound and Vibration*, 293:575–586, 2006.

L. Shuangyang, L. Yuanming, Z. Shujuan, Y. Yugui, and Y. Wenbing. Dynamic responses of Qinghai-Tibet railway embankment subjected to train loading in different seasons. *Soil Dynamics and Earthquake Engineering*, 32:1–14, 2012.

A.S.J. Suiker. *The mechanical behaviour of ballasted railway tracks.* PhD thesis, Delft University of Technology, 2002.

A.S.J. Suiker and R. de Borst. A numerical model for the cyclic deterioration of railway tracks. *International Journal for Numerical Methods in Engineering*, 57(4):441–470, 2003.

A.S.J. Suiker, R. de Borst, and C. Esveld. Critical behaviour of a timoshenko beam half-plane system under a moving load. *Archive of Applied Mechanics*, 68:158–168, 1998.

A.S.J. Suiker, E.T. Selig, and R. Frenkel. Static and cyclic triaxial testing of ballast and subballast. *Journal of Geotechnical and Geoenvironmental Engineering, Proceedings of the ASCE*, pages 771–782, 2005.

H. Takemiya. Simulation of track-ground vibrations due to a high-speed train: the case of X-2000 at Ledsgard. *Journal of Sound and Vibration*, 261:503–526, 2003.

K.V. Terzaghi. Evaluation of coefficient of subgrade reaction. *Geotechnique*, 5:297–326, 1955.

TNO. *Diana 9*. http://tnodiana.com/, 2005.

E. Tutumluer, H. Huang, and Y.M.A. Hashash. Discrete element modeling of railroad ballast settlement. In *Proceedings of the AREMA 2007 Annual Conferences*, Chicago, Illinois, USA, 2007.

E. Tutumluer, H. Huang, Y.M.A. Hashash, and J. Ghaboussi. Arema gradations affecting ballast performance using discrete element modeling (dem) approach. In *Proceedings of the AREMA 2009 Annual Conference & Exposition*, Chicago, Illinois, USA, 2009.

M. Vucetic and R. Dobry. Effect of soil plasticity on cyclic response. *Journal of Geotechnical Engineering, Proceedings of the ASCE*, 117(1):89–107, 1991.

G.X. Wang and J. Kuwano. Modeling of strain dependency of shear modulus and damping of clayey sand. *Soil Dynamics and Earthquake Engineering*, 18:463–471, 1999.

D.S. Watkins. *Fundamentals of Matrix Computations*. John Wiley & Sons, Inc., New York, 2002.

W. White, S. Valliappan, and I.K. Lee. Unified boundary for finite dynamic models. *Journal of the Engineering Mechanics Division, Proceedings of the ASCE*, 103(EM5):949–964, 1977.

J.P. Wolf and C. Song. *Finite-element modelling of unbounded media*. John Wiley and Sons, 1996.

S.E. Wright. Damage caused to ballast by mechanical maintenance techniques. Technical report, British Rail Research Technical Memorandum, 1983.

Y.B. Yang, H.H. Hung, and D.W. Chang. Train-induced wave propagation in layered soils using finite/infinite element simulation. *Soil Dynamics and Earthquake Engineering*, 23:263–278, 2003.

Z. Yang and A. Elgamal. Application of unconstrained optimization and sensitivity analysis to calibration of a soil constitutive model. *International Journal for Numerical and Analytical Methods in Geomechanics*, 27:1277–1297, 2003.

D. Yuan and S. Nazarian. Automated surface wave method: inversion technique. *Journal of Geotechnical Engineering, Proceedings of the ASCE*, 119(7):1112–1126, 1993.

Appendix A

Iwan parallel model

The definition of the material properties in the implemented Iwan material model is defined in a data file which is read by the Diana software. An example of such a material model is shown here:

```
5  YOUNG     1.5969E+08
   POISON    3.000000E-01
   DENSIT    2.000000E+03
   RAYLEI    3.4060  6.4501e-005
   USRMAT
   USRVAL    1.5969E+08 3.00E-01  4.3872E6 14
   USRSTA    0 0 0 0 0 0 0 0 0 0 0 0 0 0 0 0 1 1 1
             1 1 1 1 1 1 1 1 1 1 1
   USRIND    94  194 247 436 483 680 1189 1219 1356
             1632 1797 3111 4618 24697
```

The first four lines refer to the usual definition of a linear elastic material model in Diana software (TNO, 2005). All variables defined in this field are used in Diana software for the initial predictions of the material behaviour, the external sub-routine does not have access to these values. The first number is a referral to the material model, in this case all elements with material model 5 will behave according to the parameters described above. The first to fourth parameters are the material Young's modulus, Poisson's ratio, volumetric mass and Rayleigh damping coefficients respectively. In this case the units used all SI.

The fifth line refers that the following parameters are to be used in an external, user defined, material model. The Diana software is oblivious to the meaning of these parameters, it only communicates with the external routine the values of these parameters at the beginning of the integration and receives (and stores) values of the variables at the end of the iteration. The first set of parameters is a set of constant values, in this case as the external routine doesn't have access to the small strain properties defined

in the previous field it is necessary to repeat some of them, therefore USRVAL(1) and USRVAL(2) correspond to the small strain Young's modulus and Poisson's ratio. USRVAL(3) corresponds to the stiffness of each Iwan element k and USRVAL(4) corresponds to the number of Iwan elements n_k. The USRSTA field corresponds to a set of user state variables. These variables will change throughout the computation according to the state of the material model, and is up to the Diana software to store their values and transmit to the external routine the user state values of each Gauss point in each element. In the case of this material model the number of user state variables is $2 \times n_k + 2$. USRSTA(1) and USRSTA(2) correspond to the maximum shear strain and maximum shear stress at the end of the previous iteration, respectively. USRSTA(3) to USRSTA($2 + n_k$) correspond to the stress in each of the Iwan elements at the end of the previous iteration. USRSTA($3 + n_k$) to USRSTA($2 \times n_k + 2$) correspond to boolean variables in which it is stated whether the corresponding element was active (1) or inactive (0) at the end of the previous iteration. Finally, USRIND(1) to USRIND(n_k) correspond to a set of constants that contain the slip-stress of each Iwan element.

Using these variables and with the method described in sub-section4.3.6, the Fortran code of the implemented Iwan cyclic non-linear model is presented in the following.

```
!!!!!!!!!!!!!!!!!!!!!!!!!!!!!! DEFINITION !!!!!!!!!!!!!!!!!!!!!!!!!
  nk=USRVAL(4)
  k=USRVAL(3)

  n=1
  do while (n<=nk)
  st(n)=USRIND(n)
  n=n+1
  end do

  PreviousGamma=USRSTA(1) !START 0
  previousTau=USRSTA(2) !START 0

  n=1
  do while (n<=nk)
  sTau(n)=USRSTA(2+n)
  n=n+1
  end do

  n=1
  do while (n<=nk)
```

```
  bol(n)=USRSTA(2+nk+n)
  n=n+1
  end do

  tempTau=USRSTA(2)


!!!!!!!!!!!!!!!!!!!!!!!!!!!COMPUTE DELTAGAMMA!!!!!!!!!!!!!!!!!!!


  ma(1,1)=DEPS(1)+EPS0(1)
  ma(2,1)=DEPS(4)/2+EPS0(4)/2
  ma(3,1)=DEPS(6)/2+EPS0(6)/2
  ma(1,2)=DEPS(4)/2+EPS0(4)/2
  ma(2,2)=DEPS(2)+EPS0(2)
  ma(3,2)=DEPS(5)/2+EPS0(5)/2
  ma(1,3)=DEPS(6)/2+EPS0(6)/2
  ma(2,3)=DEPS(5)/2+EPS0(5)/2
  ma(3,3)=DEPS(3)+EPS0(3)

  call qrmet(ma, princi)

  sigma1=maxval(princi)
  sigma3=minval(princi)
  DeltaGamma=sign(1.00,princi(1)*princi(2)*princi(3))*
 $             (sigma1-sigma3)-PreviousGamma

  tempDeltaGamma=DeltaGamma

!!!!!!!!!!!!!!!!!!!!!!!!!!!COMPUTE MAIN !!!!!!!!!!!!!!!!!!!!!

  s=1
  do while (s<=nk)

     if (abs(sTau(s))<st(s) .OR. sTau(s)*tempDeltaGamma<0) then
        dTaus=sTau(s)+tempDeltaGamma*k

       if (dTaus>=st(s)) then
     tautoblow=st(s)-sTau(s)
         tempDeltaGamma=tempDeltaGamma-(tautoblow)/k
         c=s

            do while (c<=nk)
                 sTau(c)=sTau(c)+tautoblow
```

```
                c=c+1
            end do
            bol(s)=0

        elseif (dTaus<=-st(s)) then
        tautoblow=-st(s)-(stau(s))
        tempDeltaGamma=tempDeltaGamma-(tautoblow)/k
            c=s

           do while (c<=nk)
                sTau(c)=sTau(c)+tautoblow
                 c=c+1
            end do
                bol(s)=0
        else
            sTau(s)=dTaus
            bol(s)=1
        endif
    else
        bol(s)=0
    endif

    s=s+1
 end do

!!!!!!!!!! COMPUTE UPDATED STIFFNESS MATRIX !!!!!!!!!!!!!!!!


 redfac=sum(bol)/nk


  YOUNG=USRVAL(1)*redfac
  POIS=USRVAL(2)
  G=YOUNG/(2*(1+POIS))
  LAMDA=YOUNG*POIS/((1+POIS)*(1-2*POIS))

  STIFFN=STIFFN*0
  STIFFN(1,1)=LAMDA+2*G
  STIFFN(2,2)=STIFFN(1,1)
  STIFFN(3,3)=STIFFN(1,1)
  STIFFN(2,1)=LAMDA
  STIFFN(1,2)=STIFFN(2,1)
  STIFFN(1,3)=STIFFN(2,1)
```

```
  STIFFN(3,1)=STIFFN(2,1)
  STIFFN(2,3)=STIFFN(2,1)
  STIFFN(3,2)=STIFFN(2,1)
  STIFFN(4,4)=G
  STIFFN(5,5)=G
  STIFFN(6,6)=G


!!!!!!!!!!!! COMPUTE UPDATED STRESS VECTOR !!!!!!!!!!!!!!!!!

  Tau=sum(sTau)

  G2=(Tau-previousTau)/(DeltaGamma)
  G0=USRVAL(1)/(2*(1+POIS))
  redfac2=G2/G0
  YOUNG2=USRVAL(1)*redfac2
  LAMDA2=YOUNG2*POIS/((1+POIS)*(1-2*POIS))

  SECMAT=SECMAT*0
  SECMAT(1,1)=LAMDA2+2*G2
  SECMAT(2,2)=SECMAT(1,1)
  SECMAT(3,3)=SECMAT(1,1)
  SECMAT(2,1)=LAMDA2
  SECMAT(1,2)=SECMAT(2,1)
  SECMAT(1,3)=SECMAT(2,1)
  SECMAT(3,1)=SECMAT(2,1)
  SECMAT(2,3)=SECMAT(2,1)
  SECMAT(3,2)=SECMAT(2,1)
  SECMAT(4,4)=G2
  SECMAT(5,5)=G2
  SECMAT(6,6)=G2

!!!!!!!!!!!!!!!!!!! UPDATE VARIABLES !!!!!!!!!!!!!!!!!!!!!!!!

  SIG = SIG + MATMUL(SECMAT, DEPS)
  STIFF=STIFFN

  USRSTA(1)=sign(1.00,princi(1)*princi(2)*princi(3))*
 $             (sigma1-sigma3)
  USRSTA(2)=Tau

  n=1
  do while (n<=nk)
  USRSTA(2+n)=sTau(n)
```

```
n=n+1
end do

n=1
do while (n<=nk)
 USRSTA(2+nk+n)=bol(n)
 n=n+1
end do



RETURN
END
```

Appendix B

The matrix eigenvalue problem

B.1 Introduction

The eigenvalue problem has been studied by many researchers for many decades. In the scope of numeric determination of the eigenvalues of a given matrix, it has been proved by Abel's theorem that it is not possible to solve the eigenvalue problem using a direct method. Consequently all methods to determine the eigenvalues are iterative methods Watkins (2002).

The QR decomposition of a matrix is one of the most important operations in linear algebra being used to invert a matrix to solve a set of simulation operations or in numerous applications in scientific calculation. The decomposition's purpose is fairly simple: given a matrix A, decompose it into two matrices Q and R such that Q is an orthogonal matrix $Q^T \times Q = I$, R is an upper diagonal matrix and $Q \times R = A$. The advantage of producing such a decomposition of matrix A is that by inverting the the multiplication of Q and R the result is a matrix A_1 that is unitarily similar to A and consequently they have the same eigenvalues. This in itself does not solve the problem as the eigenvalues of A_1 are also unknown. The biggest gain in this procedure is that matrix A_1 is slightly closer to an upper-diagonal form than the original matrix A, consequently if the QR decomposition and multiplication $R \times Q$ are consecutively applied to matrices $A_1, A_2, ...A_n$ the final result will be a matrix which is upper triangular (the values of the elements bellow the diagonal are neglectable) and whose eigenvalues appear in the main diagonal in descending order of magnitude.

B.2 Householder reflectors

There are several methods for doing the QR decomposition such as the Grand-Schmitt orthonormalization, Householder reflectors or Givens rota-

tions. Each of them has advantages and disadvantages depending on the type of problems involved. It is evident that the QR method converges more rapidly when using matrices in the Hessenberg form instead of full matrices. The Householder reflectors allow to compute the Q matrix in an Hessenberg form in order to improve the convergence of the QR method.

The Householder reflection may be described with aid of a 2D example (Figure B.1). Considering a line l passing through the origin it is pretended to reflect any given vector through that line. A rotation of the coordinate system may be conveniently chosen such that one of the axes v coincides with l and the other u is perpendicular to l. Assuming that there is a vector x that can be written with vectors v and u

$$x = \alpha u + \beta v \tag{B.1}$$

its reflection w through line l will be

$$w = -\alpha u + \beta v \tag{B.2}$$

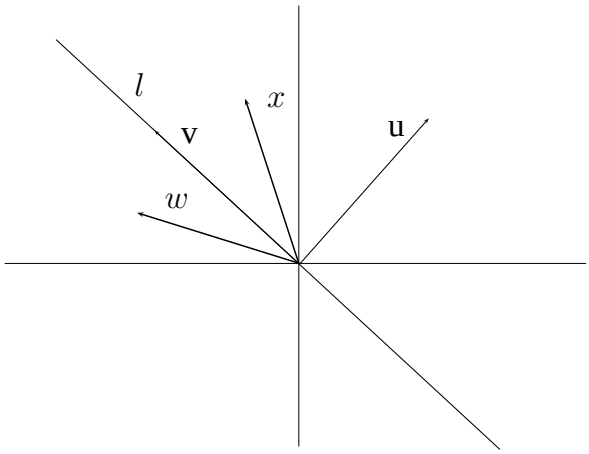

Figure B.1: Reflection of vector x along the line l.

assuming a reflector operator Q it must satisfy:

$$Q\left(\alpha u + \beta v\right) = -\alpha u + \beta v \tag{B.3}$$

A the method by which a solution is obtained is beyond the scope of this work, however a solution for the reflector operator is:

$$Q = \mathrm{I} - \gamma u u^T \tag{B.4}$$

in which I is the identity matrix, γ is given by:

$$\gamma = \frac{2}{\|u\|_2^2} \tag{B.5}$$

and u is given by:

$$u = x - \alpha \tag{B.6}$$

in which $\alpha = [\sigma 00]$ and $\sigma = \|u\|_2$. Equation B.13 can be reorganized:

$$Q = \mathrm{I} - 2\frac{u}{\|u\|_2}\frac{u^T}{\|u\|_2} \tag{B.7}$$

B.3 Wilkinson Shift

In many cases it is numerically advantageous to shift the computation of the QR algorithm from the Matrix A to a matrix $A - \mu\mathrm{I}$. If the value of μ is criteriously chosen the convergence of the QR algorithm may be largely improved. For the shifted QR algorithm the computation of A_1 may be derived:

$$A - \mu\mathrm{I} = Q \times R \tag{B.8}$$
$$\Leftrightarrow A_1 = R \times Q + \mu\mathrm{I} \tag{B.9}$$
$$\Leftrightarrow A_1 = Q^t(A - \mu\mathrm{I})Q + \mu\mathrm{I} \tag{B.10}$$
$$\Leftrightarrow A_1 = Q^t \times A \times Q \tag{B.11}$$

For the consideration of μ must be taken into account the types of matrices whose eigenvalues are to be computed and the advantages of each of the shifts that are available. To ensure the stability of the process, the Wilkinson shift was chosen. This shift has quadratic convergence in the worst case scenarios but ensures that convergence is always achieved. For the interpretation of the problem, consider a matrix B that corresponds to the lower-right 2×2 sub-matrix of A:

$$\mathbf{B} = \begin{bmatrix} \mathrm{b}_{11} & \mathrm{b}_{12} \\ \mathrm{b}_{21} & \mathrm{b}_{22} \end{bmatrix}$$

The Wilkinson shift corresponds to the eigenvalue of B that is closer to b_{22}. The Wilkinson shift may be stably computed using:

$$\mu = \mathrm{b}_{22} - \frac{\mathrm{sign}(\delta)\mathrm{b}_{12}^2}{(|\delta| + \sqrt{\delta^2 + \mathrm{b}_{12}^2})} \tag{B.12}$$

where

$$\delta = \frac{b_{11} - b_{22}}{2} \tag{B.13}$$

B.4 Algorithms

The previous sections intended to do an introduction to the numerical tools that were implemented. Having a superficial knowledge of these tools allows to better understand the algorithms that are presented in this section.

The eigenvalue computation was implemented in two main algorithms: **qrmet** and **qrdec**. The dimensions of the matrix and number of eigenvalues are referred because they are fixed values. Given the limited purpose of the implementation it was decided not to waste efforts on making the algorithms more generic to allow square matrices of any dimensions and compute the corresponding number of eigenvalues.

The **qrmet** is the most general algorithm, it receives the 3×3 matrix A and outputs the vector *eigen* which contains the 3 eigenvalues of A. It performs the Wilkinson shift on matrix A_{i-1} and calls the function **qrdec** to obtain the QR decomposition of the shifted matrix S. It computes the new matrix A_i and determines whether the sum of the non-diagonal elements of A_i is less than 2% of the sum of the diagonal elements. If this criterion is fulfilled then it is considered that convergence has been achieved and the diagonal elements of A_i correspond to the eigenvalues of A. Otherwise the process is repeated for A_i.

Algorithm 1 qrmet

load matrix A
$f = 0$; start counter $i = 1$
$A_{i-1} = A$
while $f \leq 50$ **do**
  $\mathbf{B} = \begin{bmatrix} b_{11} & b_{12} \\ b_{21} & b_{22} \end{bmatrix} = \begin{bmatrix} a_{i-1_{22}} & a_{i-1_{23}} \\ a_{i-1_{32}} & a_{i-1_{33}} \end{bmatrix}$
  $\delta = \frac{b_{11}-b_{22}}{2}$
  $\mu = b_{22} - \frac{\text{sign}(\delta) b_{12}^2}{(|\delta| + \sqrt{\delta^2 + b_{12}^2})}$
  $S = A_{i-1} - I\mu$
  qrdec(S)
  $A_i = Q_i^T \times A_{i-1} \times Q_i$
  $f = \frac{a_{i_{11}} + a_{i_{22}} + a_{i_{11}}}{a_{i_{12}} + a_{i_{21}} + a_{i_{13}} + a_{i_{31}} + a_{i_{23}} + a_{i_{32}}}$
  $i = i + 1$
end while
$eigenval = \begin{bmatrix} a_{i11} & a_{i22} & a_{i33} \end{bmatrix}$

The **qrdec** algorithm performs the QR decomposition of a 3×3 matrix.

Algorithm 2 qrdec

load matrix S
$X = \begin{bmatrix} s_{11} & s_{12} & s_{13} \end{bmatrix}^T$
$\alpha = \sqrt{x_1^2 + x_2^2 + x_3^2}$
$e = \begin{bmatrix} 1 & 0 & 0 \end{bmatrix}^T$
$u = X - \alpha e$
$v = \frac{u}{\|u\|_2}$
clear X; α ; e;u and v
$Q_A = I - 2 \times vv^T$
$R_A = Q_A \times S$
$R_B = \begin{bmatrix} r_{b_{11}} & r_{b_{12}} \\ r_{b_{21}} & r_{b_{22}} \end{bmatrix}$
$X = \begin{bmatrix} r_{b11} & r_{b11} \end{bmatrix}^T$
$\alpha = \sqrt{x_1^2 + x_2^2}$
$e = \begin{bmatrix} 1 & 0 \end{bmatrix}^T$
$u = X - \alpha e$
$v = \frac{u}{\|u\|_2}$
$Q_b = I - 2 \times vv^T$